

Design, Synthesis and Pharmacological evaluation of novel Cathepsin S inhibitors

THESIS

Submitted in partial fulfilment
of the requirements for the degree of
DOCTOR OF PHILOSOPHY

by

MADHU BABU BATTU

ID No 2011PHXF022H

Under the Supervision of
Prof. P. YOGEE SWARI



BITS Pilani

Pilani | Dubai | Goa | Hyderabad

BIRLA INSTITUTE OF TECHNOLOGY AND SCIENCE, PILANI

2014

BIRLA INSTITUTE OF TECHNOLOGY AND SCIENCE, PILANI

CERTIFICATE

This is to certify that the thesis entitled “**Design, Synthesis and Pharmacological evaluation of novel Cathepsin S inhibitors**” and submitted by **MADHU BABU BATTU** ID No. **2011PHXF022H** for award of Ph.D. of the Institute embodies original work done by him under my supervision.

Signature of the Supervisor:

Name in capital letters : **P.YOGEE SWARI**

Designation : **Professor**

Date:

“Pain is temporary. Quitting lasts forever”

Lance Armstrong

ACKNOWLEDGEMENT

*First and foremost I would like to thank **God Almighty** who has given me this opportunity.*

*I would like to give bundles of thanks to my supervisor, **Prof.P.Yogeeswari**, Professor and Associate Dean (Sponsored Research and Consultancy Division), Department of Pharmacy, BITS-Pilani Hyderabad Campus for her continuous guidance, suggestions and support. She was always an inspiration to me for my work. I am thankful for her enthusiasm, patience and love for research. She was always an inspiration to me in research. The work environment given to me under her, the experiences gained from her and her creative working culture is treasured and will be remembered throughout my life.*

*I deeply acknowledge and heartfelt thanks to **Prof.D.Sriram**, Professor, Department of Pharmacy, BITS-Pilani Hyderabad Campus for his valuable suggestions, guidance offered to me during this period.*

*I am thankful to acknowledge my DAC member **Dr.Arati Dhar**, for her support and encouragement during this period.*

*I am grateful to **Prof.Bijendra N. Jain**, Vice-Chancellor, BITS-Pilani Campus and **Prof.V.S.Rao**, Director, BITS-Pilani Hyderabad Campus for allowing me to carry out my doctoral research work in the institute.*

*I am thankful to **Prof.M.M.S.Anand**, Registrar and **Prof.S.K.Verma**, Dean, Academic Research (Ph.D. Programme), BITS-Pilani for their support to do my research work.*

*I would like to **Prof.M.B.Srinivas**, Dean, Administration and **Prof.Vidya Rajesh**, Associate Dean, Academic Research (Ph.D Programme), BITS-Pilani Hyderabad Campus for their continuous support and encouragement during my research work.*

*I would like to express my gratitude to **Dr.Srikanth Charde**, Assistant Professor & Head, Department of Pharmacy, BITS-Pilani Hyderabad Campus for providing me with all necessary laboratory facilities and for having helped me at various stages of my research work.*

*I sincerely acknowledge the help rendered by **Dr.Punna Rao**, **Dr.Sajeli Begum**, and other **Faculty members**, Department of Pharmacy, BITS-Pilani Hyderabad Campus.*

*I am grateful to express my sincere thanks to all my friends **Dr. Monika, Dr. Mallika, Aditya, Jean, Patrisha, Rahul, Praveen, Srikanth, Rukkaiyya, Mahibalan, Shailender, Brindha, Koushik, Manoj, Reshma.A, Shalini, Ganesh.S, Saketh, Gangadhar, Poorna, Ganesh.P, Santhosh, Brahmam, Renuka, Priyanka.S, Radhika, Vijay, Suman, Bobesh, Anup, Sridevi, Preeti, Hasitha, Omkar, Peter, Bomba, Reshma.L, Priyanka.P, Eddie, Glaecia, Abik, late Thimmappa and late Srividya** for the time they had spent for me and helped me to complete my work.*

*I am very much thankful to the post graduate students **Ramesh, Sridevi, Madhuri, Jagadeesh** for their help in setting up the experiments.*

*I express my thanks to our laboratory attenders and demonstrators **Mr. Rajesh, Mr.Venkat, Mr.Seenu, Ms.Saritha and Ms.Rekha** for all their support.*

I deeply acknowledge the Council of Scientific and Industrial Research New Delhi, India for CSIR SRF award [09/1026(0006)/2012.EMR-I] and their financial assistances during international travel grant to attend a conference at Florence, Italy.

*I would like to thank my close relatives, uncle late **Gabriel**, and grand parents' late **chinnappa, Mrs. Bhagyamma, Mr.Sanjeeva Rao, Mrs. Anasuyamma** for all their support and prayers.*

*At the end, but from my heart, I thank and deeply appreciate my family **Mr. Mariyanna and Mrs. Vijaya kumari**, my brother **Mr. Rajasekhar** and Uncle **Dr. Jayaraju** for their faith in me and allowing me to be as ambitious as I wanted. It was under their watchful eye that I gained so much drive and an ability to tackle challenges head on. No words can express how grateful I am for your love and support. You made my world beautiful.*

ABSTRACT

Neuropathic pain is a complex clinical syndrome, which may be intractable in several distinct common neurological disorders such as diabetic neuropathy, herpes zoster, trigeminal neuralgia, radiculopathies, cancer, spinal cord injury, multiple sclerosis and stroke. Several extensive research reports revealed that, Cathepsin S has crucial role in inflammatory neuropathic pain, where, extracellular Cathepsin S released from microglial cells due to p38 mitogen-activated protein kinase pathway, liberates soluble fractalkine from DRG neurons, which further induces the release of inflammatory mediators that activate neurons, which signals pain to the higher centers leading to neuropathic pain.

In the present study, a diverse set of molecules as CatS inhibitors were initially identified using lead identification strategies of ligand based and structure based drug design methods. Lead molecules obtained from the lead identification strategies, were further experimentally evaluated with *in vitro* enzymatic assays, where, the most active lead compound was found to be Lead **9** with IC₅₀ of 3.09 μM, but later failed in glioblastoma growth inhibition studies. Further, second most active compound **Lead 8** showed good enzyme inhibition (6.58 μM) and with GIC₅₀ of 0.477 μM and with >100 fold selectivity index as well as with low cytotoxicity on normal cells. Thus, **Lead 8** was selected as final lead molecule to proceed for synthesis and biological evaluation as a step for lead optimization.

All the synthesized molecules from the **Lead 8** (1,2,4-triazol thiol arylacetamide moiety) were interpreted with the SAR studies with help of binding interaction patterns and atom based QSAR predictions in relation with enzymatic and biological evaluations. However, all the compounds were forwarded to the preliminary neuropathic pain *in vivo* animal screening. In the preliminary behavioral assessments on CCI animal models, 18 compounds along with parent compound **Lead 8** were further analyzed to understand the ED₅₀ values. Among all the compounds, compound **8-n** exhibited better ED₅₀ value (< 3.000) in cold allodynia and also with adequate mechanical hyperalgesia with low ED₅₀ value (8.407) and revealed remarkable activity in tactile allodynia with values of 5.9 ± 1.2 gm, 2.8 ± 0.8 gm, 0.4 ± 0.3 gm PWT for 30, 10 and 3

mg/kg dosing respectively. Compound **8-n** also showed good enzymatic and glioblastoma inhibition activity when compared to other similarly neuropathic pain active compounds, in the *in vitro* enzymatic and biological evaluation studies (5.217 and 0.002 μ M respectively). Thus, compound **8-n** was further estimated for gene and protein expression levels of neuro-inflammatory mediators involved in neuropathic pain. Relative normalized expression of NF κ B, ERK1, IL-1 β , IL-6 and TNF- α in *in vivo* samples of brain, spinal cord and sciatic nerve was found to be attenuated significantly (from $p < 0.05$ to < 0.001) in all three tissues examined, in comparison with standard GBP group. Compound **8-n** also showed similar (NF κ B, ERK1, IL-1 β , IL-6 and TNF- α) gene expression reduction in the *ex vivo* brain samples.

Table of contents

	<i>Page No.</i>
<i>Certificate</i>	<i>i</i>
<i>Acknowledgements</i>	<i>iii</i>
<i>Abstract</i>	<i>v</i>
<i>List of Tables</i>	<i>xii</i>
<i>List of Figures</i>	<i>xiv</i>
<i>List of Abbreviations</i>	<i>xvi</i>
CHAPTER 1 - Introduction to Neuropathic pain and methods of drug design	1-14
1.1. Neuropathic pain	1
1.2. Management and diagnosis of neuropathic pain	2
1.3. Pathophysiological mechanisms in neuropathic pain	5
1.3.1. Mechanisms of central sensitization following nerve injury	5
1.3.2. Micro glial activation mechanism in the dorsal horn	6
1.3.2.1. Glial activation following nerve injury	6
1.3.2.2. Cross talk among neurons, microglia, and astrocytes in the dorsal Horn	9
1.3.2.3. Toll-like receptors and opioid resistance in the conditions of neuropathic Pain	9
1.3.3. Propriospinal and supraspinal neuroimmune signaling mechanism	10
1.3.3.1. Neuroimmune signaling in spinal cord injury	10
1.3.3.2. Glia-neuron interactions and descending of pain facilitation	11
1.4. Cancer related neuropathic pain	11
1.5. Introduction on drug discovery pipeline using computer-aided drug design (CADD)	12

CHAPTER 2 - Review of literature	16-36
2.1. Therapeutic molecular target cathepsin S	16
2.2. Cathepsins and their importance	18
2.3. Role of cathepsin S in MHC class II mediated antigen presentation	22
2.4. Cathepsin S and autoimmune diseases	23
2.5. Cathepsin S and asthma	24
2.6. Pro-nociceptive mechanism of CatS and microglia in progression of neuropathic Pain	25
2.7. Role of CatS in neoplastic cancer progression	27
2.8. Cathepsin S inhibitors	27
2.8.1. Carbonyl compounds	28
2.8.1.1. Furanones	28
2.8.1.2. Keto-heterocycles	29
2.8.1.3. Ketoamides	30
2.8.1.4. Non-peptidyl aldehydes	31
2.8.2. Nitrile compounds	31
2.8.2.1. Peptidyl nitriles	31
2.8.2.2. Non-peptidyl nitriles	32
2.8.3. Non-covalent inhibitors	33
CHAPTER 3 - Objectives and plan of work	37-39
3.1. Objectives	37
3.2. Plan of Work	38
CHAPTER 4 - Materials and methods	40-58
4.1. Computational details	40
4.2. Ligand based pharmacophore generation and 3D QSAR mapping	40

4.2.1. Data Set and molecular modeling	40
4.2.2. Development of pharmacophore models and 3D QSAR	41
4.2.3. Pharmacophore validation	41
4.2.4. PLS analysis and validation	42
4.2.5. External statistical validation	43
4.3. Structure based pharmacophore modelling	44
4.3.1. e-Pharmacophore model development	44
4.3.2. Pharmacophore validation	45
4.3.3 Atom based 3D QSAR	46
4.4. Docking based virtual screening and ADME prediction studies	46
4.5. Enzymatic assay	46
4.6. Cell culture	47
4.6.1. Growth inhibition and cell viability assay	47
4.7. Chemistry	48
4.7.1. General procedure for the synthesis	48
4.7.2 HPLC method development for the purity analysis	52
4.8. Pharmacology	52
4.8.1. Animals	52
4.8.2. Chronic constriction injury (CCI) method	53
4.8.3. Drug administration	53
4.8.4. Cold allodynia behavioral assessment	53
4.8.5. Mechanical hyperalgesia behavioral assessment	54
4.8.6. Tactile allodynia behavioral assessment	54
4.8.7. Locomotor activity assessment	55
4.8.8. RNA extraction and cDNA synthesis	55

4.8.9. Real-time quantitative polymerase chain reaction	56
4.8.10. Western blotting analysis	57
4.8.11. Brain slice preparation for <i>ex vivo</i> studies	57
4.9. Statistical analysis	58
CHAPTER 5 - Lead identification: Drug design and biological evaluation	59-121
5.1. Ligand based drug design	60
5.1.1. Determination of pharmacophore and validation	62
5.1.2. 3D QSAR model generation and PLS analysis	92
5.1.3. Analysis of external statistical validation	94
5.1.4. Analysis of 3D contour maps	98
5.2. Structure based drug design	102
5.2.1. e-Pharmacophore modeling and validation	104
5.3. Virtual screening and docking	108
5.3.1. ADME predictions	111
5.4. Preliminary enzymatic assay studies	111
5.5. Cell - based assays for lead molecules	115
5.6. Relationships between the binding poses and activity	118
5.7. Summary and conclusions	121
CHAPTER 6 - Lead optimization and structure activity relationships	122-166
6.1. Lead optimization	122
6.1.1. Synthesis and analysis of Lead-8 series compounds	122
6.1.2. Purity analysis	141
6.2. Biological Evaluation	143
6.2.1. Structure activity relationships based on enzyme inhibition and docking Interactions	150

6.2.2. Binding pattern relationships with co-crystal ligand	158
6.2.3. Structure activity relationships based on growth inhibition of glioblastoma cell lines	160
6.2.4. Selectivity index analysis	160
6.3. Atom based QSAR contour map analysis	163
6.4. Summary and conclusions	166
CHAPTER 7 - Neuropharmacological interventions	167-187
7.1. Pharmacology	167
7.1.1. Behavioral assessment of chronic constriction injury model	168
7.1.1.1. Cold allodynia	169
7.1.1.2. Mechanical hyperalgesia	171
7.1.1.3. Tactile allodynia	174
7.1.2. Neurotoxicity	177
7.1.3. Structure activity relationships	177
7.1.4. Gene expression studies from <i>in vivo</i> samples	179
7.1.5. Western blot analysis	183
7.1.6. Gene expression studies from <i>ex vivo</i> samples	185
7.2. Summary and conclusions	187
CHAPTER 8 - Recapitulation and Future perspectives	188-190
References	191-209
APPENDIX	210-213
List of publications	210
Papers presented at national/international conferences	211
Biography of the candidate	212
Biography of the supervisor	213

List of Tables

Table No	Description	Page No
Table 1.1	Assessment of negative and positive sensory symptoms in NP	4
Table 5.1	Selected best pharmacophore hypotheses and their internal scores	63
Table 5.2	Pharmacophore statistical validation for top 5 hypotheses	64
Table 5.3	Trifluoroethylamine compounds for 3D QSAR study and their experimental and predicted biological activity	67
Table 5.4	Dipeptide nitriles with morpholine moiety for 3D QSAR study and their experimental and predicted biological activity	68
Table 5.5	Dipeptide nitrile compounds for 3D QSAR study and their experimental and predicted biological activity	69
Table 5.6	Cyanopyrimidine compounds for 3D QSAR study and their experimental and predicted biological activity	70
Table 5.7	Succinyl-nitrile compounds for 3D QSAR study and their experimental and predicted biological activity	71
Table 5.8	Dipeptidyl nitriles with alkylamide moiety for 3D QSAR study and their experimental and predicted biological activity	72
Table 5.9	Tetrahydropyrido-pyrazole thioether amine compounds for 3D QSAR study and their experimental and predicted biological activity	73
Table 5.10	Ketobenzimidazole compounds for 3D QSAR study and their experimental and predicted biological activity	74
Table 5.11	Pyrrolopyrimidine compounds for 3D QSAR study and their experimental and predicted biological activity	76
Table 5.12	Cyanopyrimidine compounds for 3D QSAR study and their experimental and predicted biological activity	77
Table 5.13	Arylalkyne compounds for 3D QSAR study and their experimental and predicted biological activity	78
Table 5.14	Bicyclic piperidine compounds for 3D QSAR study and their experimental and predicted biological activity	80
Table 5.15	Tetrahydropyrido pyrazole compounds for 3D QSAR study and their experimental and predicted biological activity	81
Table 5.16	N-sulphonyl tetrahydropyridopyrazole compounds for 3D QSAR study and their experimental and predicted biological activity	82
Table 5.17	Pyrimidopyrrolo nitrile compounds for 3D QSAR study and their experimental and predicted biological activity	83

Table 5.18	N-substituted tetrahydropyrido pyrazole compounds for 3D QSAR study and their experimental and predicted biological activity	85
Table 5.19	Pyrimido nitriles compounds for 3D QSAR study and their experimental and predicted biological activity	86
Table 5.20	Various CatS inhibitors from research and patent literature used for 3D QSAR study and their experimental and predicted biological activity	87
Table 5.21	PLS internal validation of best five hypotheses, evolved after 3D QSAR model building	93
Table 5.22	External statistical validation results of 3D QSAR model for the Hypothesis 1 (AAADH. 1)	95
Table 5.23	Pharmacophore enrichment validation of all four-combination hypotheses	106
Table 5.24	Hit molecules found from both ligand and structure based pharmacophores with their Glide and QikProp scores and the selected final lead molecules.	112
Table 5.25	All lead compound's IC ₅₀ values of enzyme inhibition, glioblastoma cell growth inhibition (GIC ₅₀) and cytotoxicity (CC ₅₀) and their selectivity index	116
Table 6.1	Structural representation and enzyme inhibition (IC ₅₀), glioblastoma cell growth inhibition (GIC ₅₀) and HEK293 cytotoxicity (CC ₅₀) of synthesized, compound Lead-8 and 1 st and 2 nd generation series compounds and their selectivity index	145
Table 6.2	Structural representation and enzyme inhibition (IC ₅₀), glioblastoma cell growth inhibition (GIC ₅₀) and HEK293 cytotoxicity (CC ₅₀) of synthesized 2 nd generation extension series compounds and standard drugs and their selectivity index	149
Table 7.1	Percentage reversal of PWD values (Mean ± SEM) of CA for compounds tested from 1 st and 2 nd generation series at 30 mg/kg post injection	170
Table 7.2	Percentage reversal of PWT values (Mean ± SEM) in MH for compounds tested from 1 st and 2 nd generation series at 30 mg/kg post injection	172
Table 7.3	50% PWT (grams) variance values in TA for compounds tested from 1 st and 2 nd generation series at 1 h post injection in different doses (30, 10 and 3 mg/kg)	175
Table 7.4	ED ₅₀ values of selected compounds based on methods CA and MH and their respective percentage of neurotoxicity values represented in Mean±SEM	178
Table 7.5	Quantitative mRNA relative to normalized expression (10 ⁴) of NFκB, ERK1, IL-1β, IL-6 and TNF-α in brain, spinal cord and sciatic nerve expressed as Mean±SEM	182

List of Figures

Figure No	DESCRIPTION	Page No
Figure 1.1	Cross talks among neurons, microglia, and astrocytes and dorsal horn sensitization	8
Figure 2.1	Illustration of the catalytic mechanism of peptide hydrolysis catalyzed by cysteine proteases	19
Figure 2.2	Role of cathepsin S in MHC class II mediated antigen presentation	23
Figure 2.3	Schematic representation of proposed pro-nociceptive mechanism of CatS	26
Scheme 4.1	Synthetic protocol for 1,2,4-triazol thiol arylacetamide analogues	49
Figure 5.1	Schematic workflow of ligand based pharmacophore generation and validation	61
Figure 5.2	Pharmacophore hypothesis (Hypothesis 1) and distance between the pharmacophoric sites are in pink dotted lines. All the distances are in Å unit	65
Figure 5.3	Scatter plot between predicted vs. experimental activity of CatS inhibition by the 3D QSAR model	96
Figure 5.4	Illustration of alignment pattern of 161 diverse scaffold molecules on ligand based pharmacophore hypothesis while building 3D QSAR model	97
Figure 5.5	Illustration of 3D QSAR contour map on most (a1, b1) and least active (a2, b2) compounds	99
Figure 5.6	Illustration of the 3D QSAR contour map for hydrophobic visualization and docking poses of most (a1) and least active compound (a2)	101
Figure 5.7	Schematic workflow of structure based pharmacophore generation and validation	103
Figure 5.8	Possible four-combination hypotheses from the evolved e-Pharmacophore model	105
Figure 5.9	Illustration of four point e-pharmacophore hypothesis (DARH. 4) derived from CatS crystal structure data (2F1G)	107
Figure 5.10	Virtual-screening workflow from both ligand and structure based drug designing	109
Figure 5.11	Illustration of the co-crystal ligand (2F1G) interacted with active site of CatS represented in three dimensional binding pose	110
Figure 5.12	Structures of 26 lead molecules identified after virtual screening and enzymatic assay along with structure of crystal ligand (2F1G)	114
Figure 5.13	Ligand interaction pictures of lead molecules from Lead 1 to 12	119
Figure 5.14	Ligand interaction pictures of lead molecules from Lead 13 to 26	120

Figure 6.1	Spectral representation ¹ H NMR spectra of compound 8-a	136
Figure 6.2	MASS spectra of compound 8-a	137
Figure 6.3	Spectral representation ¹ H NMR spectra of most active compound 8-n	138
Figure 6.4	Spectral representation ¹³ C NMR spectra of most active compound 8-n	139
Figure 6.5	MASS spectra of compound 8-n	140
Figure 6.6	HPLC chromatogram of most active compound 8-n with 98.986% purity, generated by chromatograph system with channels 1&2 (a) and overlay picture (b) of compound 8-n and blank (ACN)	142
Figure 6.7	Binding poses with hydrogen and hydrophobic interactions of compounds from 8-a to 8-h	154
Figure 6.8	Binding poses with hydrogen and hydrophobic interactions of compounds 8-i to 8-o and 8-3n	155
Figure 6.9	Binding poses with hydrogen and hydrophobic interactions of compounds from 8-2a to 8-2h	156
Figure 6.10	Binding poses with hydrogen and hydrophobic interactions of compounds from 8-2i to 8-2o and 8-4j	157
Figure 6.11	Illustrations of docking binding patterns of crystal ligand (a) compound lead-8 (b) compound 8-n (c) and compound 8-2l (d).	159
Figure 6.12	Scatter plot to locate the most and least active compounds lied in safety index.	162
Figure 6.13	Contour mapping on most active compound 8-2l (a, c, e) and least active compound 8-d (b, d, f) based on atom based QSAR model	165
Figure 7.1	Efficacy of selected compounds in CA from 1 st generation series (a) and 2 nd generation series (c), MH from 1 st generation series (b) and 2 nd generation series (d) at dose 30 mg/kg	173
Figure 7.2	Efficacy of selected compounds in TA from 1 st generation series (a) and 2 nd generation series (b) compounds at 1hr post injection in different doses (30, 10 and 3 mg/kg).	176
Figure 7.3	Effect of treatment of compound 8-n and GBP on quantitative mRNA levels of NFκB (a) ERK1 (b) IL-1β (c) IL-6 (d) and TNF-α (e) in brain, spinal cord and sciatic nerve	181
Figure 7.4	Western blot on the in vivo samples with their relative quantity of pERK expression measured by Image J application	184
Figure 7.5	Quantitative mRNA level estimation of IL-6, IL-1β, TNF-α, NFκB and ERK1 in LPS treated <i>ex vivo</i> brain samples in the presence of compound 8-n and GBP	186

ABBREVIATIONS

5-HT3	:	5-hydroxytryptamine 3
A	:	Acceptor
ACN	:	Acetonitrile
ADME	:	Absorption, Distribution, Metabolism and Excretion
AMPA	:	α -Amino-3-hydroxy-5- methyl-4-isoxazole propionic acid
ANOVA	:	Analysis of variance
APC	:	Antigen Presenting Cell
ATP	:	Adenosine Triphosphate
BALF	:	Broncho Alveolar Lavage Fluid
BDNF	:	Brain Derived Neurotrophic Factor
BEDROC	:	Boltzman enhanced discrimination receiver operating characteristic
CA	:	Cold Allodynia
CADD	:	Computer-Aided Drug Design
CatS	:	Cathepsin S
CC ₅₀	:	Cell Cytotoxicity 50%
CCI	:	Chronic Constriction Injury
CCL2	:	Cysteine-Cysteine Chemokine Ligand
CCR2	:	Chemokine (C-C motif) Receptor type 2
CD4	:	Cluster of Differentiation 4
cDNA	:	complementary Deoxy ribonucleic acid
CLIP	:	Class II associated Invariant chain Peptide
CNS	:	Central Nervous System
CREB	:	Cyclic adenosine monophosphate Response Element Binding protein
CRPS	:	Complex Regional Pain Syndromes
CX3CL1	:	Extracellular transmembrane chemokine fractalkine
CXCR3	:	CXC chemokine receptor 3
Cys	:	Cysteine
D	:	Donor
DC	:	Dendritic Cells
DIPEA	:	N,N-Di-IsoPropylEthyl Amine
DMSO	:	Dimethyl Sulphoxide
dNTP	:	Deoxyribonucleotide
DRG	:	Dorsal Root Ganglion
DTT	:	Dithiothreitol
EC	:	Endothelial Cell
ECL	:	Enhanced Chemiluminescence
ECM	:	Extra Cellular Matrix
ED ₅₀	:	Effective Dose 50%
EDTA	:	Ethylene Diamine Tetraacetic acid

EF	:	Enrichment factor
EFNS	:	European Federation of Neurological Societies
EI-MS	:	Electron Ionization-Mass Spectroscopy
ERK	:	Extracellular signal Regulated Kinase
ESI-MS	:	Electro spray ionization-mass spectroscopy
FKN	:	Fractalkine
GABA	:	Gamma Amino Butyric Acid
GAPDH	:	Glyceraldehyde 3-Phosphate Dehydrogenase
GBP	:	Gabapentin
GH	:	Goodness of Hit
GIC ₅₀	:	Growth Inhibitory Concentration 50%
Glide	:	Grid based Ligand Docking with Energetics
H	:	Hydrophobic
HCV	:	Hepatitis C Virus
HEK293	:	Human Embryonic Kidney 293
hERG	:	Human Ether-à-go-go-Related Gene
HIV	:	Human Immuno Deficiency Virus
HLA-DM	:	Human leukocyte antigen DM
HPLC	:	High-Performance Liquid Chromatography
HRP	:	Horse Radish Peroxidase
HTVS	:	High Throughput Virtual Screening
HZ	:	Herpes Zoster
IC ₅₀	:	Inhibitory Concentration 50%
IENFD	:	Intraepidermal Nerve Fiber Density
Ii	:	Invariant chain
IL- 1 β	:	Interleukin-1 β
IL-6	:	Interleukin-6
JNK	:	c-Jun-N-terminal kinase
KCC2	:	Potassium-Chloride transporter member
KCC2	:	Potassium Chloride co transporter
Ki	:	Dissociation constant
KMnO ₄	:	Potassium permanganate
LCMS	:	Liquid Chromatography–Mass Spectrometry
LEP	:	Laser-Evoked Potential
L-Glu	:	L-Glutamate
LHVS	:	Morpholinylurea-Leucyl-Homophenyl-Vinyl sulfone phenyl
log K _p	:	Skin permeation rate
log p MDCK	:	Predicted apparent MDCK cell permeability in nm/sec using Predicted apparent MDCK cell permeability in nm/sec using the Affymax scale
LOO	:	Leave One-Out
LPS	:	Lipopolysaccharide
MAPK	:	p38 Mitogen-Activated Protein Kinase
MBP	:	Myelin Basic Protein

MCP-1	:	Monocyte Chemoattractant Protein-1
MEM	:	Minimal Essential Medium
MG	:	Myasthenia Gravis
MH	:	Mechanical Hyperalgesia
MHC	:	Major Histocompatibility Complex
MHz	:	Megahertz
MMP	:	Matrix Metalloprotease
mRNA	:	Messenger Ribonucleic Acid
MS	:	Multiple Sclerosis
NF κ B	:	Nuclear Factor Kappa B
NK-1R	:	Neurokinin-1 Receptor
nM	:	Nanomolar
nm	:	Nanometers
NMDA	:	N-Methyl-D-Aspartate
nMec	:	Methylcoumarin
NMR	:	Nuclear Magnetic Resonance
NO	:	Nitric Oxide
NP	:	Neuropathic pain
NSAID	:	Non-Steroidal Anti-Inflammatory Drug
Oligo-dT	:	Short sequence of deoxy-thymine nucleotides
OPLS_2005	:	Optimized Potential for Liquid Simulations_2005
P2X receptor	:	Purinergic 2X receptor
PAGE	:	Polyacrylamide Gel Electrophoresis
PCR	:	Polymerase Chain Reaction
pERK	:	Phospho-ERK
PGS	:	Prostaglandins
PHASE	:	Pharmacophore Search Engine
pIC ₅₀	:	$-\log IC_{50}$
PKC	:	Protein Kinase C
PLS	:	Partial Least-Squares
PRESS	:	Predictive Residual Sum Of Squares
PTSA	:	4-Phenyl-1,2,4-Triazol Sulfanyl Acetamide
PWD	:	Paw withdrawal duration
PWT	:	Paw withdrawal thresholds
QPlogBB	:	Predicted brain/blood partition coefficient
QPlogPo/w	:	Predicted octanol/water partition coefficient
QPPCaco	:	Predicted apparent Caco-2 cell permeability in nm/sec using the Boehringer-Ingelheim scale
QSAR	:	Quantitative Structure-Activity Relationship
QST	:	Quantitative Sensory Testing
R	:	Ring Aromatic
RA	:	Rheumatoid Arthritis
RAM	:	Random-Access Memory

RIE	:	Robust Initial Enhancement
RMSD	:	Root Mean Square Deviation
RMSE	:	Root Mean Square Error
RNA	:	Ribonucleic acid
ROS	:	Reactive Oxygen Species
RPMI	:	Roswell Park Memorial Institute medium
RT Enhancer	:	Reverse transcriptase enhancer
RT-qPCR	:	Real Time quantitative PCR
RVM	:	Rostral Ventromedial Medulla
SAR	:	Structure Activity Relationship
SCI	:	Spinal Cord Injury
SD	:	Squared Deviation
SDS	:	Sodium Dodecyl Sulfate
SEM	:	Standard error of mean
SI	:	Selectivity Index
SP	:	Glide standard precision
SubP	:	Substance P
TA	:	Tactile Allodynia
TBST	:	Tris-Buffered Saline Tween-20
Th1	:	T helper type 1
TLR4	:	Toll-Like Receptor 4
TMS	:	Trimethyl Silane
TNFR	:	Tumor Necrosis Factor Receptor
TNF α	:	Tumor Necrosis Factor α
TPSA	:	4-Phenyl-1,2,4-triazol sulfanyl acetamide
TRI reagent	:	TRIZOL reagent
TRP	:	Transient Receptor Potential
TRPA	:	Transient Receptor Potential A Subfamily
TRPV1	:	Transient Receptor Potential V1 Subfamily
VPL	:	Ventropostero Lateral Nucleus Of The Thalamus
WHO	:	World Health Organization
XP	:	Glide extra precision
ZVVR-AMC	:	Benzyloxycarbonyl- valine- valine-arginine-7-amido-4-methylcoumarin
μ M	:	Micro molar

CHAPTER 1

Introduction to neuropathic pain and methods of drug design

CHAPTER 1

Introduction to neuropathic pain and methods of drug design

1.1. Neuropathic pain

Pain is a complex sensation which strongly accompanied by various ailments, severe diseases and cognitive influences. To date, fundamental origin of various pain sensations and underlying pathophysiological mechanisms in patients remains a challenge for pain specialists. [Crucchi G., *et al.*, 2010] Particularly, Neuropathic pain (NP) is a complex clinical syndrome which may be intractable in several distinct common neurological disorders such as diabetic neuropathy, herpes zoster (HZ), trigeminal neuralgia, radiculopathies, cancer, spinal cord injury, multiple sclerosis and stroke are some of most common causes. It is characterized by the presence of positive as well as negative signs and symptoms, including spontaneous pain (often described as lancinating, sharp, shooting), abnormal sensations (tingling, burning, crawling ants, etc.), loss of sensation (numbness), allodynia (pain in response to non-painful stimuli like touch), and hyperalgesia (exaggerated pain in response to painful stimuli) [Mohan V., 2008]. NP tends to be severe, chronic, and has a hugely negative impact on the physical and social functioning, emotional health, and overall well-being of the patient.

NP varied in its nature characterized by increased sensitivity to thermal and/or mechanical stimuli that may or may not be accompanied by the phenomenon of spontaneous or aberrant pain sensations. A range of disorders of the peripheral nervous system such as trigeminal neuralgia, postherpetic neuralgia, nerve lesions, post-amputation pain and series of neuropathies are all consider various kinds of nociceptive pain inducers [Jensen TS., *et al.*, 2014]. Various ailments caused by lesions or disease of the parts of the nervous system that usually signal somatosensory information to the higher centers of the brain progressive to NP [Jensen TS., *et al.*, 2011]. In chronic NP conditions, despite, differences in etiology, many of these conditions share common clinical phenomena. In particular, conditions of postherpetic neuralgia and painful diabetic neuropathy signs are similar with sensation of touch-evoked pain. Conversely, different signs

and symptoms can observe in the same disease such as pain paroxysms and stimulus-evoked abnormalities in postherpetic neuralgia. General classification based on clinical implications include four broad classes: peripheral focal and multifocal nerve lesions (inflammatory or ischemic, traumatic), peripheral generalized polyneuropathies (inflammatory, metabolic, toxic), CNS lesions (e.g. stroke, multiple sclerosis, spinal cord injury), and complex neuropathic disorders (complex regional pain syndromes [CRPSs]) [Baron R., *et al.*, 2006]. Where, CRPSs, formerly called reflex sympathetic dystrophies, Sudeck's atrophy or causalgia are painful disorders that can develop as a uneven consequence of trauma, and typically affect the limbs [Jänig W., *et al.*, 2003].

NP remains under diagnosed and undertreated problem in third world countries. There are well-established estimates of the overall population prevalence of NP based on estimates of the main etiological conditions in developed countries, where about 1% prevalence in the United Kingdom [Bowsher D., *et al.*, 1991] and about 2% in the United States [Bennett G., *et al.*, 1997]. Most of the NP cases are associated with the prevalence of diabetes which is about 2.8% worldwide, the lifetime incidence of HZ approximately being 24% around the globe [Bowsher D., *et al.*, 1999], and the global prevalence of HIV (with 34 million people affected in 2010) [www.who.int.]. Some studies showed us that the major proportion of individuals with these conditions experienced neuropathic pain. For instance, about 26.4% of those with type 2 diabetes had painful peripheral diabetic neuropathy [Davies M., *et al.*, 2006], 8% of those diagnosed with HZ infection had postherpetic neuralgia after 30 days [Choo PW., *et al.*, 1997], and 37% of those with chronic low back pain had a predominantly neuropathic component to their pain [Freyenhagen R., *et al.*, 2006]. Treatment strategies existed until date and were fully based on symptomatic conditions and to mask pain sensations. Moreover, the most common pharmacological agents prescribed for NP are tricyclic antidepressants, anticonvulsants, opioids and non-steroidal anti-inflammatory drugs (NSAIDs) [Jain P., *et al.*, 2009].

1.2. Management and diagnosis of neuropathic pain

Patients with neuropathic pain demonstrate distinct sensory symptoms that can coexist in various combinations. Bedside sensory examination includes touch, pinprick, pressure, cold, heat, vibration and temporal summation [Jänig W., *et al.*, 2003; Bouhassira D., *et al.*, 2004] (Table 1.1). Responses can be graded as normal, decreased and increased to determine whether negative or positive sensory phenomena. The stimulus-evoked (positive) pain types are classified as

dysesthetic, allodynic, or hyperalgesic and according to the dynamic or static character of the stimulus [Crucchi G., *et al.*, 2004]. Measurement of signs are usually checked with the touch and can be assessed by gently applying cotton wool to the skin, pinprick sensation by the response to sharp pinprick stimuli, and deep pain by gentle pressure on muscles and joints. Cold and heat sensations are generally assessed by measuring the response to acetone spray and thermo rollers kept at 20 °C and at 45 °C. Vibration induced sensations can be assessed by a tuning fork placed at strategic points (inter phalangeal joints). Abnormal temporal summation is a clinical equivalent of increasing neuronal activity following repetitive C-fiber stimulation at >0.3 Hz. This wind-up-like pain can be produced by mechanical and thermal stimuli [Baron R., *et al.*, 2006]. There are distinct terms and assessments that existed for the diagnosis of specific NP sensory symptoms or signs as presented in Table 1.1.

The majority of previous recommendations by European Federation of Neurological Societies (EFNS) guidelines were reinforced by recent studies and asserted relevant methods for the assessments of pathophysiological conditions of NP [Rasmussen PV., *et al.*, 2004]. A new definition of NP recommended by EFNS and the diagnostic grading system will probably lead to more accurate diagnosis in clinical practice and research studies. A number of new validated tools has now resolved the previous lack of questionnaires (to assess NP in patients) and screening tools explicitly dedicated to NP. Laboratory techniques that were restricted to research, such as quantitative sensory testing (QST), laser-evoked potentials (LEPs) and Intraepidermal Nerve Fiber Density (IENFD) are now being used more widely in clinical practice and trials. Amongst these methods of assessment, QST seen to be the best for provoked pain and responses to treatment; LEPs are the best for A δ pathways, and IENFD for C-fibre loss in distal axonal neuropathies. In addition, it is generally agreed that assessment should be carried out in the area of maximal pain, using the contralateral area as control [Baron R., *et al.*, 2006; Rasmussen PV., *et al.*, 2004]. Quantitative assessments while comparing the contralateral control with sensory testing tools as well as validated questionnaires are the most successful current diagnostic strategies. Whereas, profound research need to be focus on biochemical analysis of several sensory mediators involved in NP, where it helps to treat the root causes of NP rather than conventional symptomatic treatments.

Table 1.1 Assessment of negative and positive sensory symptoms in NP [Baron R., *et al.*, 2006].

Symptom/sign	Definition	Assessment	Expected pathological response
Negative signs and symptoms			
Hypoesthesia	Reduced sensation to non-painful stimuli	Touch skin with painter's brush, cotton swab or gauze	Reduced perception, numbness
Pallhypoesthesia	Reduced sensation to vibration	Apply tuning fork to bone or joint	Reduced perception threshold
Hypoalgesia	Reduced sensation to painful stimuli	Prick skin with single pin stimulus	Reduced perception, numbness
Thermohypoesthesia	Reduced sensation to cold or warm stimuli	Touch skin with objects of 10°C and touch skin with objects of 45°C	Reduced perception
Spontaneous sensations/pain			
Paraesthesia	Non-painful ongoing sensation (ant crawling)	Grade intensity (0–10) Area in cm ²	-
Paroxysmal pain	Shooting electrical attacks for seconds	Number per episode Grade intensity (0–10) Threshold for evocation	-
Superficial pain	Painful ongoing sensation, often of burning quality	Grade intensity (0–10) Area in cm ²	-
Evoked pain			
Mechanical dynamic Allodynia	Normally non-painful light-pressure moving stimuli on skin evoke pain	Stroking skin with painter's brush, cotton swab or gauze	Sharp burning pain in the primary affected zone, spreading into unaffected skin areas (2° zone)
Mechanical static allodynia	Normally non-painful static pressure stimuli on skin evoke pain	Manual gentle mechanical pressure to the skin	Dull pain in the area of affected (damaged or sensitized) primary afferent nerve endings (1° zone)
Mechanical punctate or pinprick hyperalgesia	Normally stinging-but-notpainful stimuli evoke pain	Manual pricking of the skin with a safety pin, sharp stick or stiff von Frey hair	Sharp superficial pain in the primary affected zone, spreading into unaffected skin areas (2° zone)
Temporal summation	Repetitive application of identical single noxious stimuli is perceived as more pain sensation (wind-up-like pain)	Pricking the skin with safety pin at <3 s intervals for 30 s	Sharp superficial pain of increasing intensity
Cold allodynia	Normally non-painful cold stimuli evoke pain	Touch skin with objects of 20 °C (metal roller, glass of water, coolants like acetone) Control: touch skin with objects of skin temperature	Painful, often burning, temperature sensation in the area of affected (damaged or sensitized) primary afferent nerve endings (1° zone)
Heat allodynia	Normally non-painful heat stimuli evoke pain	Touch skin with objects of 40 °C (metal roller, glass of water) Control: touch skin with objects of skin temperature	Painful burning temperature sensation in the area of affected (sensitized) primary afferent nerve endings (1° zone)
Mechanical deep somatic allodynia	Non-painful pressure on somatic tissues evoke pain	Manual light pressure at joints or muscle	Deep pain in joints or muscles

1.3. Pathophysiological mechanisms in neuropathic pain

Most of the current ideas regarding the pathophysiology of neuropathic pain originated from experimental work on animal models. These studies delineated a series of partially independent pathophysiological mechanisms. Pain sensations are normally elicited by activity in nociceptive neurons of the DRG with unmyelinated (C-) and thinly myelinated (A δ -) primary afferent neurons that activate different types of neurons in the dorsal horn, particularly in lamina I and lamina V, which project via parallel pathways to the thalamus and to the brainstem [Benarroch EE., *et al.*, 2010]. The primary DRG afferents also activate excitatory and inhibitory interneurons in lamina II that exert local control on nociceptive transmission [Latremoliere A., *et al.*, 2009; Basbaum AI., *et al.*, 2009; D'Mello R., *et al.*, 2008]. These nociceptors are usually silent in the absence of normal stimulation, and respond best to potentially noxious stimuli. The DRG neurons express different types of voltage-gated sodium (Na⁺) channels (particularly Nav1.7, Nav1.8, and Nav1.9), acid-sensitive channels, serotonin 5-HT₃ receptors, purinergic P2X receptors and transient receptor potential (TRP) channels (including TRPV1 and TRPA) that are activated by noxious chemical or mechanical stimuli [Basbaum AI., *et al.*, 2009]. However, activation of A δ and C-fiber nociceptors in normal conditions, lead to glutamate release from the primary afferent nerve terminals, resulting in short term activation of α -amino-3-hydroxy-5-methyl-4-isoxazole propionic acid (AMPA) receptors in the dorsal horn neurons. Local inhibitory mechanisms, mediated by gamma aminobutyric acid (GABA) and glycine, as well as other signals such as opioids and adenosine, presynaptically regulate neurotransmitter release from primary afferents and prevent excessive excitation of dorsal horn projection neurons. During normal transmission of nociceptive afferent signals in the dorsal horn astrocytes or microglia are usually not activated [Milligan ED., *et al.*, 2009].

1.3.1. Mechanisms of central sensitization following nerve injury

Studies on several experimental models in rodents, such as chronic constriction, partial nerve ligation, or transection of the sciatic nerve or chronic compression of the L4-L5 roots, have provided a large amount of information regarding the cellular, chemical, and molecular changes underlying neuropathic pain [Latremoliere A., *et al.*, 2009; Basbaum AI., *et al.*, 2009; Costigan M., *et al.*, 2009]. These studies showed that peripheral nerve injury and tissue inflammation elicit several plastic changes in nociceptors, including upregulation of Na⁺ and TRP channels, which result in reduced threshold for activation and repetitive firing of DRG neurons in response to

nociceptive stimuli (peripheral sensitization). This altered activity of primary afferents triggers plastic changes in both local and projection neurons in the dorsal horn, resulting in central sensitization of the spinothalamic system [Drdla R., *et al.*, 2008]. After nerve injury, repetitive firing of DRG neurons triggered release of L-glutamate and primary neurotransmitter, and also neuropeptides such as substance P (SubP) and adenosine triphosphate (ATP), calcitonin gene-related peptide, brain-derived neurotrophic factor (BDNF), and several chemokines and cytokines. These multiple signals lead, directly or indirectly, to plastic changes resulting in increased excitability of dorsal horn projection neurons [Latremoliere A., *et al.*, 2009; Basbaum AI., *et al.*, 2009; Drdla R., *et al.*, 2008]. For instance, SubP elicits membrane depolarization neurokinin-1 receptors and thus removes the magnesium (Mg^{2+}) blockade of the glutamate NMDA receptors, allowing calcium (Ca^{2+}) influx via this channel as well as via voltage-gated Ca^{2+} channels. Calcium release from intracellular stores in response to activation of metabotropic glutamate receptors further increase cytosolic Ca^{2+} concentration. And also, calcium activates several downstream transduction cascades, including phosphorylation pathways such as extracellular signal regulated kinase (ERK), protein kinase C, and calmodulin kinase II as well as nitric oxide (NO) synthase and cyclooxygenase. These transduction pathways elicit plastic changes in dorsal horn neurons that increase their responsiveness to afferent inputs. For example, phosphorylation by calmodulin kinase II or ERK increases surface expression and open probability of AMPA and NMDA receptors, whereas phosphorylation of the transcription factor cyclic adenosine monophosphate response element binding protein (CREB) upregulates expression of several synaptic proteins and other nociceptive signals [Latremoliere A., *et al.*, 2009; Basbaum AI., *et al.*, 2009; Drdla R., *et al.*, 2008].

1.3.2. Microglial activation mechanism in the dorsal horn

During normal transmission of nociceptive signals, astrocytes or microglia are not activated. Whereas, after peripheral nerve injury both types of glial cells proliferate and release a variety of chemical mediators that contribute to altered synaptic transmission in the dorsal horn and increased excitability of the projection neurons.

1.3.2.1. Glial activation following nerve injury

Several *in vitro* studies indicate that the responses of microglia and astrocytes vary with the type of stimulus [McMahon SB., *et al.*, 2009]. There were several differences in the responses of

microglia and astrocytes after peripheral nerve injury. Microglial activation occurs in the early phase of stimulus due to cell death and may occur in the absence of axonal degeneration. In contrast, the astrocyte response occurs in later stages after axonal degeneration, and is involved in persistence of neuropathic pain. The sequential activation of microglia and astrocytes following nerve injury involves mitogen-activated kinase p38 in microglia, and c-jun-N terminal kinase in astrocytes, resulting in activation of nuclear factor κ B (NF κ B), which promoted transcription of several inflammatory mediators [Milligan ED., *et al.*, 2009; Inoue K., *et al.*, 2009].

Several *in vitro* and *in vivo* models indicated that several chemical signals released from microglia and astrocytes after nerve injury contributed to increase in pain transmission in the dorsal horn [Milligan ED., *et al.*, 2009; McMahon SB., *et al.*, 2009]. These include interleukin-1 β (IL-1 β), tumor necrosis factor α (TNF α), chemokines, excitatory amino acids, ATP, BDNF, D-serine, NO, reactive oxygen species (ROS), arachidonic acid, and prostaglandins (PGS) (Figure1.1). These chemical signals contribute to central sensitization by several multiple mechanisms, including neurotransmitter release and increased primary afferent excitability. Potentiation of glutamate-mediated depolarization and impaired local GABAergic inhibition also occur as a part of the mechanism. For example, both TNF α and IL-1 β increase excitability of DRG neurons by increasing Na⁺ influx via Nav1.8 channels and upregulate the number and function of NMDA and neurokinin-1 receptors (NK-1R) in projection neurons [Milligan ED., *et al.*, 2009; Guo W., *et al.*, 2007], TNF α downregulates expression of amino acid transporter 2 involved in glutamate uptake by astrocytes [Boycott HE., *et al.*, 2008]. Activated microglia release BDNF, which reduces expression of the chloride (Cl⁻) transporter KCC2, rendering the effects of GABA_A receptors excitatory rather than inhibitory [Coull JA., *et al.*, 2005].

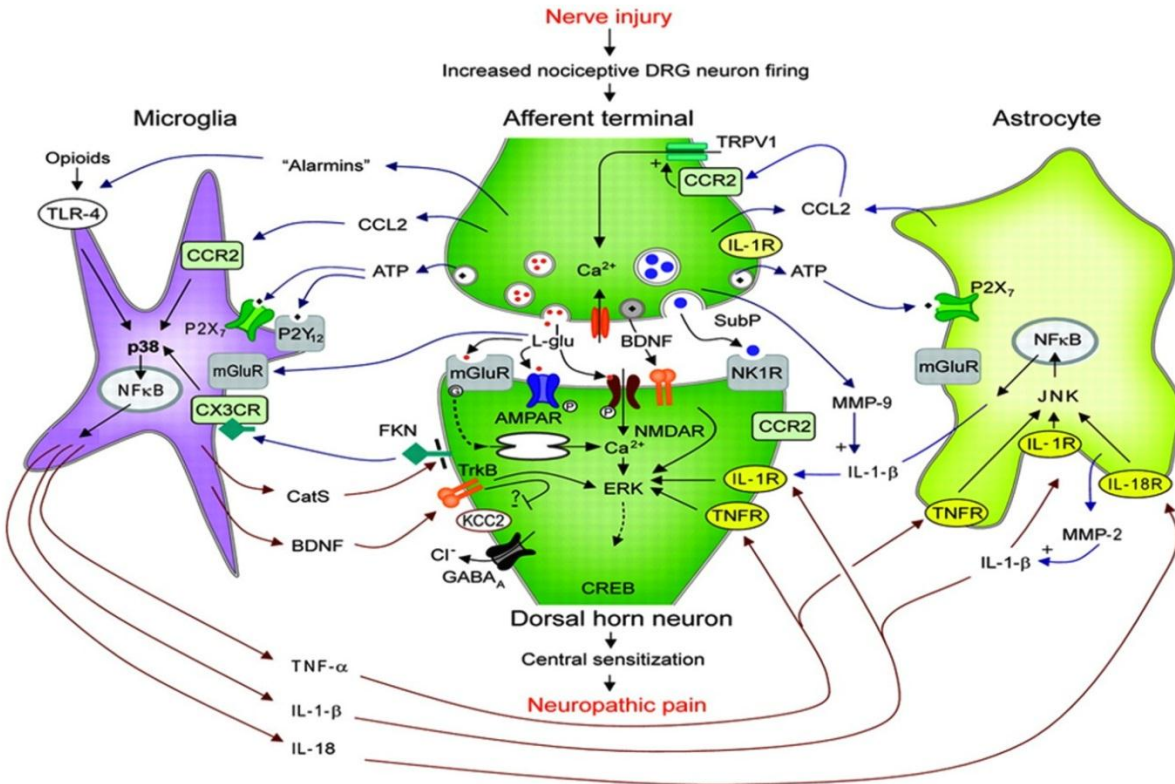


Figure 1.1 Cross talks among neurons, microglia, and astrocytes and dorsal horn sensitization [Benarroch EE., et al., 2010]

After nerve injury, repetitive firing of DRG neurons triggers release of L-glutamate (l-glu), SubP, ATP, BDNF, and the cysteine-cysteine chemokine ligand CCL2. These multiple signals lead to increased neurotransmitter release from primary afferents and increased excitability of dorsal horn projection neurons (central sensitization). SubP, acting via NK-1R, leads to neuronal depolarization, activation of NMDA receptors, and calcium (Ca^{2+}) influx. Calcium activates several phosphorylation pathways, including ERK, which increase surface expression of AMPA receptors and activate the transcription factor CREB. ATP activates astrocytes (via P2 \times 7 receptors) and microglia (via P2 \times 4, P2 \times 7, and P2Y12 receptors). Activation of microglia and astrocytes via mitogen-activated kinase p38 and c-jun-N terminal kinase (JNK) leads to activation of NFκB, which promotes transcription of several inflammatory mediators. IL-1β acting via its receptor IL-1R and TNFα acting via its receptor TNFR increase primary afferent excitability and potentiate glutamate-mediated excitation. BDNF released from activated microglia reduces expression of the chloride (Cl^-) transporter KCC2, rendering the effects of gamma aminobutyric acid (GABA_A) receptors excitatory. CCL2, acting via CCR2 receptors, promotes depolarization of nociceptive afferent astrocyte activation. Cathepsin S released from activated microglia elicit cleavage and release of fractalkine (FKN) which, in turn, activates microglia via CXCR3 receptors. Matrix metalloprotease (MMP)-9 released from damaged DRG neurons and MMP-2 released from astrocytes cleave and activate IL-1β. Peripheral nerve injury elicits the release of “endogenous danger signals” or “alarmins” from DRG neurons; these signals activate toll-like receptor 4 (TLR4) in microglia, resulting in release of inflammatory cytokines and inhibition of opioid-mediated analgesia.

1.3.2.2. Cross talk among neurons, microglia, and astrocytes in the dorsal horn

Several potential auto excitatory loops and cross talk among dorsal horn neurons, microglia, and astrocytes triggered by peripheral injury (Figure 1.1). These interactions further stimulate microglia and astrocytes and promote plastic changes in excitatory and inhibitory neurotransmission [Milligan ED., *et al.*, 2009; McMahon SB., *et al.*, 2009; Inoue K., *et al.*, 2009]. Glial activation reflects the effects of several chemical signals released from afferents of damaged DRG neurons or from neurons in the dorsal horn following nerve injury, including L-glutamate, ATP, substance P, BDNF, NO, and chemokines [Milligan ED., *et al.*, 2009; McMahon SB., *et al.*, 2009]. After release in the dorsal horn following activation of nociceptive afferents, both L-glutamate, acting via NMDA receptors, and substance P, acting via NK-1 receptors, activate microglia and astrocytes and promote release of proinflammatory cytokines. [McMahon SB., *et al.*, 2009] ATP released from damaged DRG afferents or sensitized dorsal horn neurons activates both astrocytes (via P2X7 receptors) and microglia (via P2X4, P2X7, and P2Y12 receptors) [Inoue K., *et al.*, 2009] Glial activation major release of chemokines. For example, in response to TNF α released from microglia, damaged DRG neurons and astrocytes upregulate expression of the cysteine-cysteine chemokine ligand CCL2 (also known as monocyte chemoattractant protein-1 (MCP-1)) and its receptor [White FA., *et al.*, 2009] CCL2, acting via its CCR2 receptors, elicit upregulation of TRPV1 channels and depolarization of nociceptive afferents [Dansereau MA., *et al.*, 2008] as well as astrocyte activation. [Thacker MA., *et al.*, 2009] Fractalkine (FKN), a transmembrane chemokine that is expressed in DRG and dorsal horn neurons [Cardona AE., *et al.*, 2008] cleaved and released by Cathepsin S (CatS). Where, CatS released from activated microglia elicits cleavage and release of FKN which, in turn, activates microglia via CXCR3 receptors [Clark AK., *et al.*, 2009]. Matrix metalloproteases (MMPs) are also implicated in chronic neuropathic pain [Ji RR., *et al.*, 2009]. Specifically, MMP-9, released from damaged DRG neurons, and MMP-2, released from activated astrocytes, cleave and activate IL-1 β released from microglia. All these studies have emphasized the complexity of chemical signaling in the dorsal horn in response to nerve injury.

1.3.2.3. Toll-like receptors and opioid resistance in the conditions of neuropathic pain

Peripheral nerve injury elicit release of “endogenous danger signals” or “alarmins,” which include degradation products of the extracellular matrix and substances released by stressed or dying DRG cells, such as heat shock proteins [Watkins LR., *et al.*, 2009]. These signals are

recognized by toll-like receptors (TLRs), such a TLR4, which trigger innate immune responses via several pathways resulting in release of inflammatory cytokines [Laird MH., *et al.*, 2009]. In the CNS, TLR4 is predominantly expressed in microglia, but its expression may also be unregulated in astrocytes during inflammation [Hutchinson MR., *et al.*, 2008]. Recent evidence indicated that activation of TLR4 in microglia has a key role in initiation and maintenance of neuropathic pain [Watkins LR., *et al.*, 2009]. Furthermore, activation of TLR4 receptors in microglia by opioids resulted in release of proinflammatory cytokines, which has been shown to antagonize the classic analgesic effects of opioids acting on μ -type receptors in neurons [Watkins LR., *et al.*, 2009].

1.3.3. Propriospinal and supraspinal neuroimmune signaling mechanism

1.3.3.1. Neuroimmune signaling in spinal cord injury

Peripheral nerve or spinal cord injury (SCI) is associated with exaggerated spontaneous rhythmic burst firing in the ventro postero lateral nucleus of the thalamus (VPL), which correlates with behavioral manifestations of neuropathic pain [Saab CY., *et al.*, 2009]. There is emerging evidence indicating that neuronal injury at one level of the spinal cord trigger remote signaling in the spinothalamic system that could alter nociceptive information processing at the level of the thalamus [Saab CY., *et al.*, 2009]. In a spinal contusion model in the rat, thoracic SCI elicited microglial activation and an altered neuronal activity both in the lumbar dorsal horn and in the VPL; this was associated with sensitization of lumbar dorsal horn and thalamic neurons and behavioral signs of allodynia and thermal hyperalgesia [Saab CY., *et al.*, 2009; Hulsebosch CE., *et al.*, 2008]. Activation of microglia at locations distant from the initial SCI may involve signaling via the cytokine CCL21 [Saab CY., *et al.*, 2009; Hulsebosch CE., *et al.*, 2008]. It has been hypothesized that CCL21 is upregulated in response to damage of lumbar spinothalamic axons as they pass by the thoracic SCI site; this cytokine might lead to local activation of microglia at the lumbar levels and served as a remote signal to the thalamus [Saab CY., *et al.*, 2009]. Upregulation of CCL21 in the terminal fields of lumbar spinothalamic axons lead to microglial activation and abnormal burst firing in thalamocortical neurons in the VPL, which was associated with hyperalgesia and allodynia. These affects are attenuated by interruption of the spinothalamic tract or neutralization of CCL21 signaling in the VPL [Saab CY., *et al.*, 2009; Hulsebosch CE., *et al.*, 2008].

1.3.3.2. Glia-neuron interactions and descending of pain facilitation

Neurons in the rostral ventromedial medulla (RVM) receive inputs from the periaqueductal gray, project to the dorsal horn, and are a major component of the descending pain modulation system, which may exert context-dependent antinociceptive or pronociceptive effects [Cunha TM., *et al.*, 2009]. Recent evidence indicated that supraspinal glial-neuronal interactions at the level of the RVM might promote descending pain facilitation following peripheral nerve injury. Studies by Wei F., *et al.*, [Wei F., *et al.*, 2008] showed that, after chronic constriction injury of the rat infraorbital nerve, there is both early and transient reaction of microglia and prolonged reaction of astrocytes in the RVM, associated with local elevations of IL-1 β and TNF α levels. These cytokines elicit phosphorylation and activation of NMDA receptors in RVM neurons; which was associated with behavioral manifestation of neuropathic pain [Wei F., *et al.*, 2008]. This indicated that pro-inflammatory cytokines released from activated glial cells act via NMDA receptors in RVM neurons promoting descending pain facilitation. Other signals, such as glutamate, ATP, substance P, and BDNF, might also elicit glial activation at the level of the RVM, thus promoting neuropathic pain [Cunha TM., *et al.*, 2009].

1.4. Cancer related neuropathic pain

According to the world health organization (WHO) analgesic ladder for cancer pain relief, 80% of cancer pain could usually be controlled. Therefore 20% of cancer pains are difficult to control [Laird B., *et al.*, 2008]. Neuropathic cancer pain is often in the uncontrolled cancer pain category and use of adjuvant analgesics such as amitriptyline and gabapentin (GBP) are important. Underlying mechanisms for cancer induced NP is obscure, whereas several inflammatory mediators, which are responsible for both diseases mainly in brain cancers, can cause additional effect on neuropathic nociceptive mechanisms. Active CatS in the extracellular environment of astrocytoma contribute to degradation of extra cellular matrix components thereby facilitating the invasive process in brain tumor, which has a major role in progression of neuropathic pain by cleavage of extracellular domain of FKN. However, several diagnostic methods also markedly reported that the chronic cancer pain was caused by nerve compression and immune-reactive and pronociceptive substances (such as CatS and BDNF) released from tumors [Hiroshi U., *et al.*, 2006], but the profound molecular mechanisms of these substances in cancer pain remain to be studied. Although, evidently several reports from rodent model studies have been demonstrated that the cancer invasion pain model induced by implantation of Meth A sarcoma cells around the

sciatic nerve in BALB/c mice [Shimoyama M., *et al.*, 2002], leads to development of allodynia, thermal hyperalgesia, and spontaneous pain [Shimoyama M., *et al.*, 2002; Walker K., *et al.*, 2002; Wacnik PW., *et al.*, 2001]. Moreover, neuropathies associated with specific chemotherapies used in cancer are with well-known mechanisms but still in conditions of clinical challenge. Development of single entity of drug candidate for a combination therapy could be a fruitful strategy to face the existing clinical management of cancer related NP.

1.5. Introduction on drug discovery using computer-aided drug design (CADD)

In a drug discovery campaign, major purposes, include filtering of large compound libraries into smaller sets of predicted active compounds that can be tested experimentally, optimization of lead compounds to increase its affinity or optimize drug metabolism and pharmacokinetics. As a part of drug discovery, design of novel compounds, by “growing” molecules with one functional group at a time or by piecing together fragments into novel chemotypes respectively are fruitful strategies [Sliwoski G., *et al.*, 2014]. All these drug discovery objectives could be very well applied in computer-aided drug design (CADD), which not only aims to explain the molecular basis of therapeutic activity but also to predict possible derivatives that would improve activity.

CADD can be classified into two general categories: structure-based and ligand-based drug design. Structure-based design relies on the knowledge of the target protein structure to calculate interaction energies for all compounds tested, whereas ligand-based design exploits the knowledge of known active and inactive molecules through chemical similarity searches or construction of predictive, quantitative structure-activity relation (QSAR) models [Kalyaanamoorthy S., *et al.*, 2011]. Structure-based drug design is generally preferred where high-resolution structural data of the target protein are available, i.e., for soluble proteins that can readily be crystallized. Ligand based drug design is generally preferred when there is no or little crystallized structural information, and depends on the previous reported ligand molecules of interest. A successful application of these methods will result in compounds that have been validated by *in vitro* and *in vivo* and its binding location has been confirmed, ideally through a co-crystal structure [Jorgensen WL., *et al.*, 2010].

One of the most common uses in CADD is the high throughput virtual screening (HTVS), where, screening of virtual compound libraries to test their biological activity of interest. HTVS comes in many forms, including chemical similarity searches by fingerprints or topology, selecting compounds by predicted biologic activity through 3D QSAR models or pharmacophore

mapping, and virtual docking of compounds into target of interest, known as structure based docking [Enyedy IJ., *et al.*, 2008]. These methods allow the ranking of “hits” from the virtual compound library for acquisition. Using of these computer-assisted methods will improve the quality of drug discovery by knowledge-based approaches and also to optimize lead compound within a limited time. However, pharmacophore approaches is vital for accelerating discovery efforts when more data that are extensive are available by providing a means of superimposing structures for 3D quantitative structure/activity relationship (QSAR) development, or by acting as a rapid prefilter on real or virtual libraries that are too large for routine treatment with more expensive structure-based techniques, such as docking.

The methodologies used by that time were relatively simple, employing a small number of physical chemical descriptors and statistical methods such as multiple linear regressions. QSAR modeling was viewed solely as a tool for lead optimization; i.e., it was employed to elucidate the relationship between structure and activity in relatively small congeneric compound series and predict relatively small structural modifications leading to enhanced activity. Rapid development of combinatorial chemistry and high throughput screening methods in recent years has significantly increased a bulk of experimental structure activity relationship (SAR) datasets. These developments have emphasized several reliable analytical methods for biological SAR data examination such as QSAR. QSAR has been traditionally perceived as a means of establishing correlations between trends in chemical structure modifications and respective changes of biological activity [Golbraikh A., *et al.*, 2002]. However, in many cases of chemical library design, the number of compounds that could be practically synthesized and tested is much smaller than the total size of exhaustive virtual chemical libraries. There is a need for developing virtual library screening tools, and QSAR modeling can be adapted to the task of targeted library design. However, the application of 3D QSAR models for virtual screening places a special emphasis on statistical significance and predictive ability of these models as their most crucial characteristics. Development and characterization of 3D QSAR methodologies were shown significant impact on drug designing and discovery. Understanding of large chemical entities and demonstrating the key structural features for the particular biological target is a prominent strategy of the ligand based 3D QSAR analysis. Precisely, mapping on the key structural domains of active compounds gives knowledge-based path to the researchers in designing and development of novel drug analogues.

Structure or receptor based drug designing grabbed recent interest among the researchers to discover new ligands for the biological targets. Considerable information on three-dimensional structure of receptors is available from x-ray crystallographic studies of receptors with bound complexes. Analyzing the active site could generate an interaction map of desirable features that a ligand should satisfy to adequately interact with receptor. In fact, this can other way call as generation of respective energies utilized for ligand interaction and converted to energy features. The features that could be generated include hydrogen bond donors, hydrogen bond acceptors, and lipophilic sites. Generation of 3D pharmacophore hypothesis based on evolved energies is also popularly called as e-pharmacophore. The generated hypotheses are employed for queries in searching a multi-conformational database of compounds with known activities to undergo validation. An analysis of the set of queries that “hit” or “reject” highly active compounds could help in understanding the 3D features essential for the activity. This strategy can build up several promising novel ligand molecules for any x-ray crystallographed protein targets.

CHAPTER 2

Review of literature

CHAPTER 2

Review of literature

2.1. Therapeutic molecular target Cathepsin S

In recent years, an improved genetic understanding of most of the metabolic and immune related diseases, fore fronting the treatment strategies towards rectified therapies by targeting specific molecular entities have been reported. Deliberation on therapeutic enzyme targets to determine the underlying molecular pathways has been the focus of recent interest in research. Hardly any single molecular target is involved in multiple disease pathways with either direct or indirect relevance of function. One of such pivotal molecular target generally crucial for regulating immune responses is Cathepsin S which belong to the papain subfamily of cysteine proteases found in lysosomal/endosomal vesicles of antigen presenting cells (APCs), such as macrophages, B cells and dendritic accessory cells, and also in adipocytes and smooth muscle cells. Moreover, expression of CatS is preferentially tissue-specific and is expressed in conditions of phagocytosis and antigen presentation. Evidently, high levels of CatS expressions are found in alveolar macrophages, dendritic cells (DC), vascular smooth muscle cells, spleen, lymph nodes, while moderate levels have been identified in bone marrow, appendix, and thymus [Heng X W., *et al.*, 2006; Shi G P., *et al.*, 1994].

Currently, CatS is considered as one of the primary targets for various immune system related diseases such as rheumatoid arthritis (RA), bronchial asthma, psoriasis, atherosclerosis, myasthenia gravis (MG), multiple sclerosis (MS), chronic obstructive pulmonary diseases and also other major diseases like neuropathic pain (NP), Alzheimer's disease, cancer and obesity [Gupta S., *et al.*, 2008; Wiener JJM., *et al.*, 2010; Alice LD., *et al.*, 2011; Marrack P, *et al.*, 2001]. As CatS has been implicated in the pathophysiology of a number of auto-immune and allergic conditions, where, its function relates to its role in antigen presentation by MHC class II to CD4⁺ T-cells, degradation of the extracellular matrix and also the pro-nociceptive role of extracellular transmembrane chemokine fractalkine (CX3CL1) release in neurons contribute towards initiation and propagation of respective diseases [Thurmond RL., *et al.*, 2005; Teupser

D., *et al.*, 2004; Sukhova GK., *et al.*, 2003]. In particular, both professional as well as nonprofessional APCs utilize CatS for MHC class II-mediated antigen presentation where CatS plays a key role in an independent manner of MHC class II transportation than other cathepsins [Lautwein A., *et al.*, 2004; Beers C., *et al.*, 2005]. Furthermore, studies on CatS deficient mice showed a reduced collagenolytic activity and defective microvessel development in microvascular endothelial cells during wound repair, displaying a crucial role in ECM degradation as well as in angiogenesis [Shi G P., *et al.*, 2003]. Several extensive studies from the group Clark *et al.*, [Clark AK., *et al.*, 2007] on inflammatory neuropathic pain revealed that the extracellular CatS released due to p38 mitogen-activated protein kinase (MAPK) pathway [Clark AK., *et al.*, 2010], liberates soluble FKN from neurons [Clark AK., *et al.*, 2007; Clark AK., *et al.*, 2009] which further induced the release of inflammatory mediators that activate neurons which signals pain to the higher centers. Recent reports from Wang *et al.*, revealed the role of CatS in angiogenic islet formation and growth of solid tumors in multi-stage murine pancreatic islet cell carcinogenesis mouse model [Wang B., *et al.*, 2006].

Since, the name cathepsin indicate digestion, all the cathepsins display protease activities most preferably at slightly acidic environment [Turk V., *et al.*, 2012]. Cathepsins were classified based on their proteolytic activity, as serine proteases (cathepsins A and G), aspartic proteases (cathepsins D and E) and lysosomal cysteine cathepsins (11 human cysteine cathepsins, i.e., B, C, F, H, K, L, O, S, V, X and W) [Rossi A., *et al.*, 2004]. Among these, CatS has been found to be peculiarly stable at a neutral or slightly alkaline pH [Kirschke H., *et al.*, 1989] (All other cathepsins are mostly unstable at neutral pH [Turk B., *et al.*, 1995]) and accordingly sustaining its activity. For instance, because of its stability at neutral pH and potential for broad proteolytic activity, airway epithelial ciliated cells are able to capture cathepsin S onto their surfaces to promote motility of their cilia. While CatS enzyme functions both intracellularly in degradation of endosomal protein bulk [Hermann B., *et al.*, 2001] and extracellularly in activation and degradation of membrane proteins and connective tissue matrix respectively to implicate progressive immune disease pathways, enticing toward generation of CatS inhibitors. A wide range of structural motifs have been discovered in their period, by using standard methods of x-ray crystallography, NMR as well as predictive molecular modeling methods of ligand-based and structure-based pharmacophore mapping and ligand based 3D QSAR analysis and docking based virtual screening methods. As yet, more than 15 chemotypes were designed and synthesized till

date as CatS inhibitors revealed through patent and research articles, which were conferred in a number of perpetual reviews [JM Wiener J., *et al.*, 2010; Alice LD., *et al.*, 2011; Thurmond RL., *et al.*, 2005; Link JO., *et al.*, 2006; Maryanoff BE., *et al.*, 2008] as well as in ligand and structure based drug design studies [Markt P., *et al.*, 2008].

2.2. Cathepsin S and its importance

Cathepsins are inactive preproenzymes, with their prosequence or signals necessary for the entry into the endoplasmic reticulum for subsequent proteolytic activation. These preproenzymes are then processed by signal peptidases to the mature forms in the acidic and reducing conditions of late endosomes or lysosomes. Moreover, the proteolytic activity of all these cysteine protease cathepsins result due to the presence of a cysteine (Cys) residue as a chief moiety in their enzyme active center (in CatS, Cys25). As described in Figure 2.1 for the catalytic mechanism of the archetypal cysteine protease papain, members of the lysosomal cathepsin family attack the substrate via a reactive crucial step of the catalytic process involves formation of a reactive thiolate/imidazolium ion pair (Cys-S⁻/His-Im⁺) from proton transfer between Cys25 and His159 (papain numbering) [Chang WW., *et al.*, 2007].

In principle, the thiolate of Cys residue attack on the carbonyl carbon atom of the scissile peptide bond of the substrate by making the carbonyl group of the amide group converted into negatively charged carbonyl oxygen (CO⁻). The oxygen thus carries a negative net charge, allowing formation of the first tetrahedral transition state. The oxyanion is stabilized by hydrogen bonding to the amide groups of Cys25 backbone and Gln19 side chain of CatS, resulting in the formation of an oxyanion hole. Subsequent rotation of the His residue enables the proton transfer from the imidazolium cation to the nitrogen of the amide bond being hydrolyzed. The amine group is released from the enzyme, and cleavage occurs [Menard R., *et al.*, 1991a; Menard R., *et al.*, 1991b; Menard R., *et al.*, 1995; Harrison MJ., *et al.*, 1997; Otto H., *et al.*, 1997; Rzychon M., *et al.*, 2004]. The newly formed substrate amine is hydrogen bonded to the His159 residue whereas carbonyl portion of the substrate gets linked to the Cys25 residue via a thioester bond, forming an acyl enzyme (Figure 2.1). In the next reaction step, amine portion of the substrate is dissociated and replaced with a water molecule. That in turn attacks the carbonyl carbon of acyl enzyme by imidazole nitrogen, which contributes to polarization of the water molecule followed by the formation of the second tetrahedral intermediate. At the final reaction step, thioester deacylation leads to reconstruction of the carboxyl group in the hydrolyzed substrate, which is

concerted with the release of an active enzyme [Menard R., *et al.*, 1991a; Menard R., *et al.*, 1991b; Menard R., *et al.*, 1995; Harrison MJ., *et al.*, 1997; Otto H., *et al.*, 1997; Rzychon M., *et al.*, 2004].

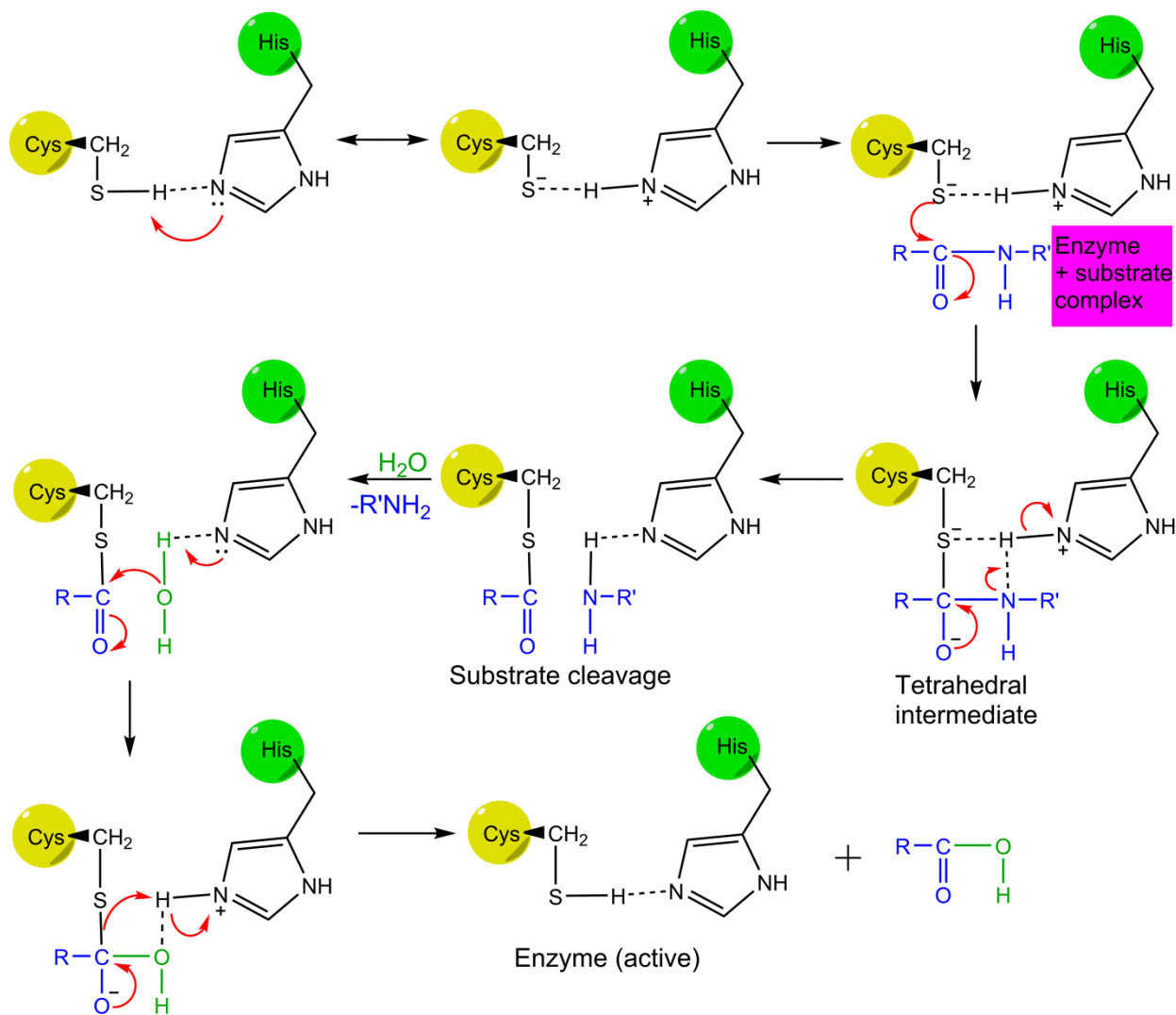


Figure 2.1. Illustration of the catalytic mechanism of peptide hydrolysis catalyzed by cysteine proteases

Due to their lysosomal localization, cathepsins were initially thought to be ‘housekeeping’ molecules that functioned exclusively as the cell’s garbage disposals. However, this view has changed as several cathepsin genes are now known to have distinctive patterns of expression, and have vital roles in specific physiological processes, and been linked to many severe genetic disorders [Rzychon M., *et al.*, 2004; Wolters PJ., *et al.*, 2000; Jedeszko C., *et al.*, 2004; Mohamed MM., *et al.*, 2006; Joyce JA., *et al.*, 2004; Toomes C., *et al.*, 1999]. Cathepsins such as cathepsins L, F and S are considered to be the major enzymes involved in the generation of MHC II (major histocompatibility complex class II molecules) - antigenic peptide complexes, and that cathepsins B and L indirectly activate the apoptotic caspases [Nakagawa TY., *et al.*, 1999]. Indeed, recent data demonstrate that lysosomal cathepsins can be translocated to the plasma membrane or secreted by tumor cells, most probably by alterations in receptor-mediated pathway(s) and/or in the alternative mannose-phosphate receptor independent trafficking. These observations indicate that the detection of cathepsins in extracellular fluids may permit quantification and monitoring of cancer treatment. Thus, understanding of this important group of proteinases and their cognate inhibitors is expected to provide significant diagnostic and prognostic information for cancer management [Krepela E., *et al.*, 2001; Sloane BF., *et al.*, 1984].

As discussed earlier, all papain-like cysteine proteases consist of a signal peptide or a propeptide and a catalytic domain for mature proteolytic enzyme activity (Figure 2.1). Signal peptides or propeptides, which are responsible for the translocation into the endoplasmic reticulum during mRNA translation, are with variable length on average between 10 and 20 amino acids in length. Initially, the propeptide executes protein folding of the catalytic domain by acting as a scaffold, later it proceeds as a chaperone for the transport of the proenzyme to the endosomal/lysosomal compartment and finally, it serves as a high-affinity reversible inhibitor preventing the premature activation of the catalytic domain. The catalytic domains of all human cathepsins are between 214 and 260 amino acids in length and contain the highly conserved active sites consisting of a cysteine, a histidine, and an asparagine residue.

As per the findings from the x-ray crystallography studies, the overall fold of cathepsins is highly conserved and consists of L and R domains of similar size where the active site cysteine residue is located in a center of structurally conserved α -helix of the L domain whereas the histidine residue is in the R domain. The propeptide or signal peptide is less structured and runs in inverse

orientation through the substrate-binding cleft. Five cathepsins are strict endopeptidases (cathepsins L, S, K, V, and F) and four cathepsins are exopeptidases (cathepsins B, C, X, and H). Current target, CatS shares its high sequence homology with other derived cathepsins such as K and L, where, there are distinct differences between the enzymes, specifically in their respective S2 and S3 sub sites of the active pocket as illustrated by their crystal structures, which have been taken advantage of in the quest for selective CatS inhibition [Pauly TA., *et al.*, 2003]. The S2 sub-pocket of CatS contains the following amino acids: Phe70, Gly137, Val162, Gly165 and Phe211 [Gauthier JY., *et al.*, 2007]. The two glycine residues serve as ‘gatekeepers’ and enable a wider sub site when compared with the S2 site of CatK. Whereas, at the bottom of the CatS S2 site, Phe211 is mobile and could accommodate an ‘open’ conformation, providing extra space between itself and Phe70 and enabling opportunistic π -stacking interactions with either or both phenylalanine residues. The S2 sub site of CatK features Tyr67, Ala133, Leu157, Ala160 and Leu209, thereby creating a narrower and shallow sub site without a corresponding ‘open’ form [Cai J., *et al.*, 2010]. While in case of cathepsin L, in place of the glycine gatekeepers of CatS S2 site, cathepsin L displays Ala135 and Gly164, also limiting the size to small groove that can accommodate smaller non-bulky groups into the site. However, S3 dissimilarities among the cathepsins can, at times, be less adeptly exploited. The major differences among Cathepsin K, L and S are the display of Asp61/Tyr67, Leu69/Glu63 and Phe70/ Lys64, respectively, which can contribute to electrostatic differences. However, taking advantage of the positively charged S3 of CatS with a complementary negatively charged moiety can lead to overall compound cell permeability issues [Irie O., *et al.*, 2008a]. Interesting point is that as CatS sub site S3 appears to be smaller than that of CatK, there is potential plasticity for Lys64 in CatS, which could re-orient its side chain to allow for larger substituents in this subsite [Liu H., *et al.*, 2005]. Moreover, supporting details by SAR results from various series reported in the literature have claimed that the S3 of CatK can accommodate larger functionality than that of CatS and vice versa [Gauthier JY., *et al.*, 2007; Liu H., *et al.*, 2005]. Additionally, the most important pocket for CatS activity and selectivity was reported to be S2. The conformational flexibility of CatS S2, due to Phe211, is a key for reaching selectivity over similar proteases. The CatS S2 pocket is also deeper and at the same time, its entrance is narrower. All of these differences could in principle be used in designing selective cathepsin S inhibitors.

2.3. Role of Cathepsin S in MHC class II mediated antigen presentation

The molecular mechanism leading to the formation of class II peptide complexes and presentation of antigen on the cell surface begins with the synthesis of the class II $\alpha\beta$ heterodimers in the endoplasmic reticulum. These dimers are assembled together with the assistance of the Ii chaperone molecule to form a nanomeric complex $\alpha\beta$ -Ii. This complex is then delivered to the endosomes where Ii is degraded in a stepwise fashion by the lysosomal proteases, allowing the antigen-binding site of MHC II to be exposed. In B-cells and dendritic cells, CatS is the single enzyme that cleaves the Ii p10, 10-kDa fragment of the lysosomal MHC II bound invariant chain to form 24 amino-acid CLIP (class II associated invariant chain peptide) fragments (Figure 2.2). HLA-DM in humans and H-2M in mice catalyze the replacement of the MHC II-bound CLIP peptide with an extracellularly derived antigenic peptide. Ruckrich et al. have recently identified two CatS cleavage sites (R78 – M79, K80 – L81) by which CatS could directly yield CLIP from its precursor [Ruckrich T., *et al.*, 2006]. In macrophages, CatS deficiency does not severely impair Ii degradation and antigen processing as cathepsin L can partially compensate for it [Nakagawa TY., *et al.*, 1999]. In addition, the lysosomal cysteine protease cathepsin F has also been suggested to contribute to degradation of Ii in macrophages [Shi GP., *et al.*, 2000]. CatS also plays a major role in MHC class II maturation and presentation *in vivo* in non-professional APC-like intestinal epithelial cells, despite the high expression of cathepsin L. CatS-deficient mice demonstrate a profound inhibition of Ii degradation in professional APC *in vivo*. Cathepsin L is active in other types of epithelium for example thymic epithelial cells and kidney epithelium [Nakagawa T., *et al.*, 1998].

Apart from its role in MHC II antigen presentation, CatS also has potent elastolytic activity that modulates connective tissue matrix degradation. Matrix remodeling can occur either intracellularly on phagocytosed matrix molecules or extracellularly after secretion of lysosomal cathepsin. Extracellular degradation of collagen can be incomplete, leaving fragments that are phagocytosed by fibroblasts, macrophages and smooth muscle cells. These phagosomes fuse with lysosomes containing cathepsins and complete the degradation. In addition to intracellular degradation of collagens, CatS also degrades matrix protein extracellularly. Cells found to release CatS include macrophages [Punturieri A., *et al.*, 2000], smooth muscle cells [Shi GP., *et al.*, 1999], tumor cells [Heidtmann HH., *et al.*, 1993] and EC [Shi GP., *et al.*, 2003].

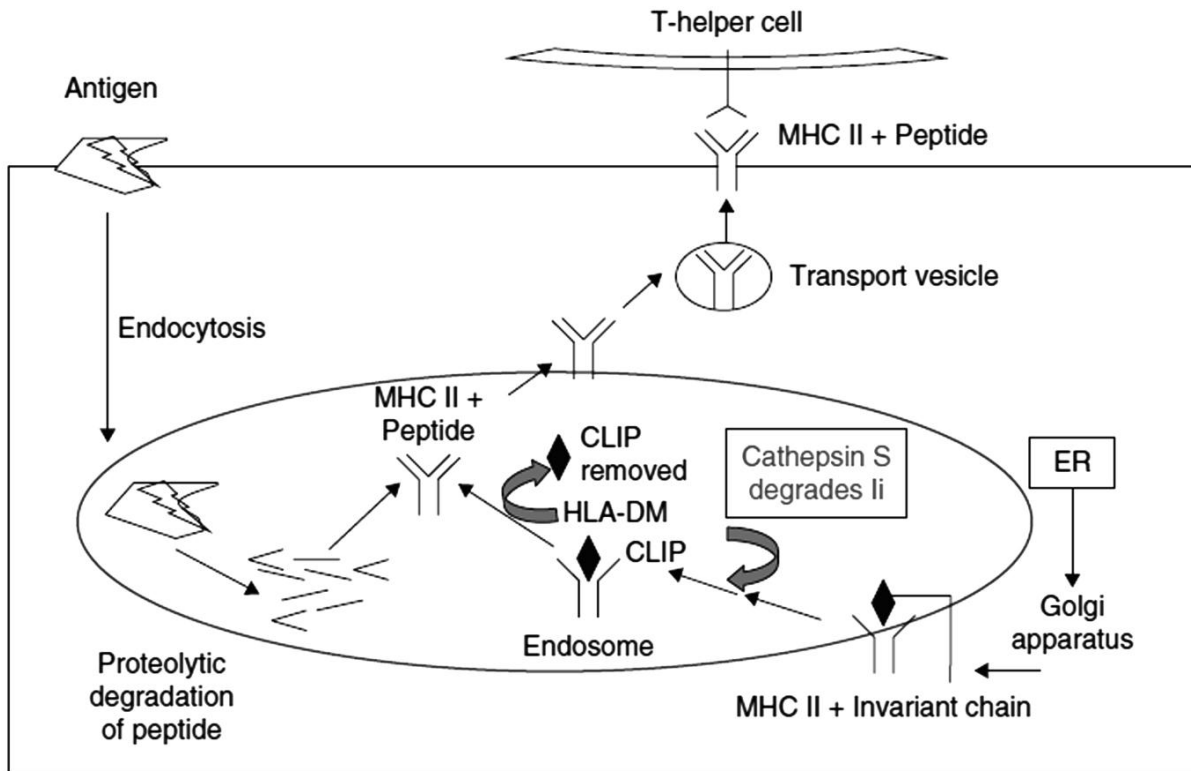


Figure 2.2 Role of cathepsin S in MHC class II mediated antigen presentation [Pettit AR., *et al.*, 1999].

Invariant chain (Ii) is associated with newly synthesized MHC class II molecules in the ER. CatS is involved in Ii cleavage, followed by removal of CLIP and antigen loading. CLIP: Class II associated invariant chain peptide; ER: Endoplasmic reticulum.

2.4 Cathepsin S and autoimmune diseases

Autoimmune diseases are believed to rise from a breakdown of tolerance and a deregulation of the ability of the immune system to discriminate effectively between ‘self’ and ‘non-self’. The production of autoantibodies against distinct ‘self’ proteins of the cell nucleus constitutes one of the autoimmune manifestations that characterize systemic autoimmunity. Processing and presentation of intracellular autoantigens to T cells constitutes a central issue in the generation of antigen-driven autoimmunity. **Rheumatoid arthritis (RA)** is a chronic inflammatory joint disorder involving autoimmune processes that result in destruction of the joint cartilage eventually leading to loss of joint function. DC mediated immune responses are thought to be most critical in RA. They contribute to the initiation and perpetuation of RA by presentation of artherogenic antigen to autoreactive T cells [Gupta S., *et al.*, 2008]. It has been previously

demonstrated that the infiltration of DC occurs early in disease pathology and that DC are enriched in the synovial tissue and synovial fluid of affected joints. CatS has been shown to be expressed in synovial macrophages in RA joints. CatS knockout mice were generally healthy and revealed a decreased susceptibility towards collagen-induced arthritis. The administration of a potent CatS inhibitor to mice resulted in inhibition of CatS and in failure to respond to ovalbumin stimulation [Nakagawa TY., *et al.*, 1999]. The observed inhibition of immune responses is thought to be caused primarily by the impairment of antigen presentation to CD4 helper cells. The positioning of this enzyme in the disease cascade offers it the distinct advantage of causing less marked side effects. **Multiple sclerosis** (MS) is another chronic inflammatory demyelinating disease of the central nervous system (CNS) which is characterized pathologically by lesions containing lymphocytes and macrophages. It is an autoimmune disease in which Th1 cells recognize components of the myelin sheath and initiate a self-propagating autodestructive process within the CNS. Myelin basic protein (MBP) is the potential autoantigen implicated in the pathogenesis of MS. MBP needs to be proteolytically processed before it is presented for an autoimmune response. CatS plays a role in the initiation of proteolytic processing of MBP [Beck H., *et al.*, 2001]. Thus, a therapy that nips the evil in the bud like CatS inhibitors would have an appreciable effect. **Psoriasis**, another autoimmune disease, is characterized by scaly skin lesions secondary to keratinocyte hyperplasia. Keratinocytes, which also function as non-professional antigen presenting cells, are stimulated by primed T cells. It has been documented that CatS is selectively upregulated along with MHC II, in response to a pro-inflammatory cytokine in psoriatic patients. These biological agents are ‘custom- designed’ molecules that are precisely targeted to interfere with the pathogenesis of psoriasis. Though their immunosuppressive effects are well directed, adverse events like decreased in CD4⁺ count with Alefacept, flu like symptoms and thrombocytopenia with Efalizumab and injection site reaction, demyelination disorder with etanercept have been reported [Koo J., *et al.*, 2005; Galadari I., *et al.*, 2005] . CatS inhibitors might offer a novel approach in the treatment of psoriasis as antigen presentation to CD4⁺ cells, which is the root cause, would be impaired.

2.5 Cathepsin S and asthma

Pulmonary hypersensitivity and inflammation with eosinophilic infiltration is a prominent feature of allergic airway diseases, including asthma. Activated eosinophils release several inflammatory mediators including cationic proteins, lipids and oxygen radicals that participate in

airway inflammation and injury. Recent studies also demonstrated that selective inhibition of cysteine proteases could be an additional potential strategy for modulating the immune response in class II-restricted disease processes. Several proteins have been identified by proteomic screening of lung tissue samples and broncho-alveolar lavage fluid (BALF), for proteins that displayed a clear increase during allergen-induced airway inflammation, including CatS. Interestingly, many of the proteins that were increased are known to be associated with hypoxia and cell stress, indicating a link between allergen-induced airway inflammation and increases in hypoxia-related gene products [Fajardo I., *et al.*, 2004]. The increase in CatS observed in allergen-challenged animals may be related to the actual immune response. In fact, it has been shown that inhibition of CatS results in an impaired immune response to the specific allergen. The increased levels of CatS may arise from inflammatory cells infiltrating the lung tissue. Certainly, the fact that CatS inhibitors can block the T cell proliferation induced by giant ragweed suggests that allergic conditions may be possible clinical indications. In summary, CatS could have beneficial effects in allergic airway inflammatory diseases by reducing collagen deposition and by interfering with antigen presentation respectively [Riese RJ., *et al.*, 1998].

2.6. Pro-nociceptive mechanism of CatS and microglia in progression of neuropathic pain

Besides its role in antigen processing and presentation, CatS retains proteolytic activity at extracellular neutral pH when released by macrophages and microglia. Indeed, the release of CatS from these cells is induced by pro-inflammatory stimuli [Liuzzo JP., *et al.*, 1999a; Liuzzo JP., *et al.*, 1999b; Petanceska S., *et al.*, 1996].

In the dorsal horn area innervated by damaged fibers, activated microglia leads to high concentrations of ATP, which in turn activate the P2X7 receptor. Determination of the intracellular signaling pathways downstream of P2X7 activation revealed that phospholipase C and phospholipase A2, as well as p38 MAPK are critical for ATP-induced release of CatS. CatS then liberates soluble FKN by converting membrane bound FKN from neurons. Later, FKN feeds back onto the microglial cells via the CX3CR1 receptor to further activate the p38 MAPK pathway (Figure 2.3). Finally, release of inflammatory mediators that further activates ERK, which increase surface expression of AMPA receptors and activate the transcription factor CREB in neurons and results in chronic pain. Notably, CatS released under these conditions is effective at degrading collagen extracellular matrix and has led to the suggestion that P2X7

receptor antagonists may reduce cancer cell invasiveness [Jelassi B., *et al.*, 201; Clark AK., *et al.*, 2012].

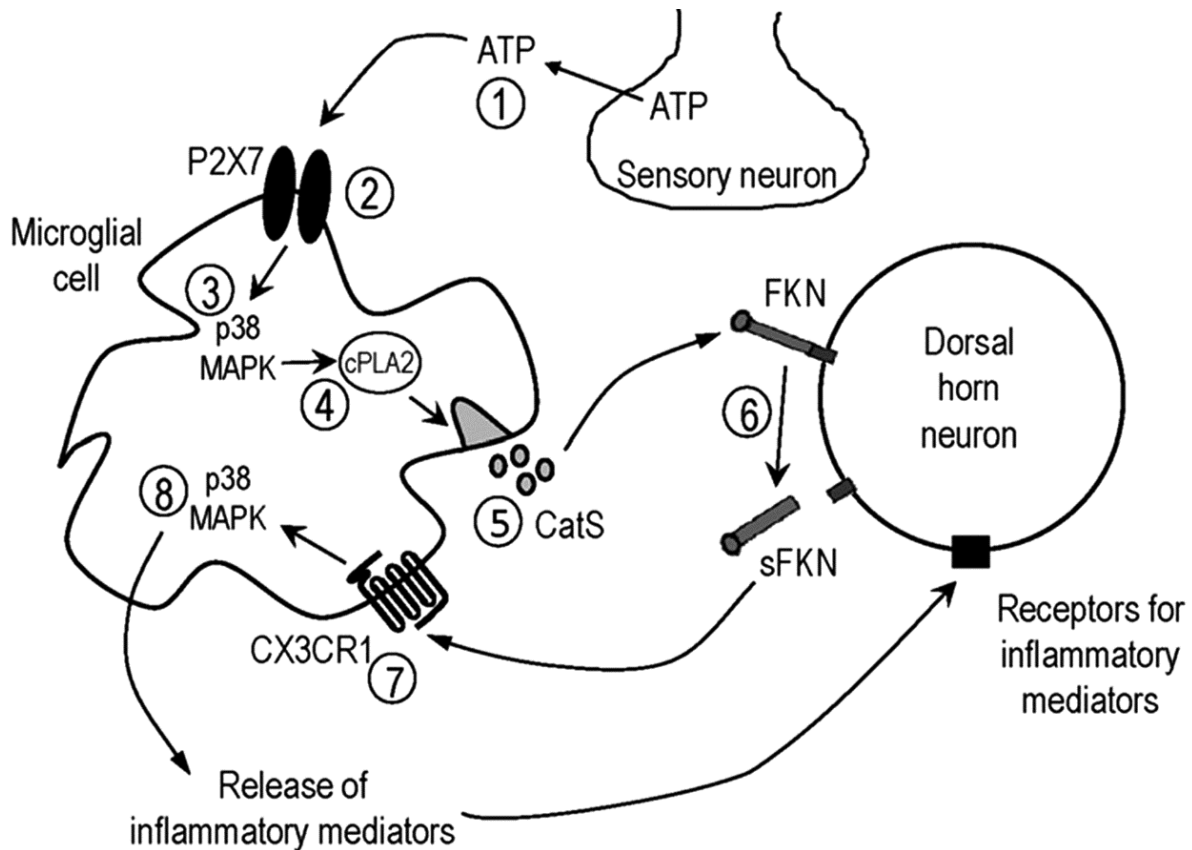


Figure 2.3. Schematic representation of proposed pro-nociceptive mechanism of CatS [Clark AK., *et al.*, 2012].

In the dorsal horn area innervated by damaged fibers, high concentrations of extracellular ATP (1) possibly released by primary afferent terminals, leads to P2X7 receptor activation on microglia (2) Following P2X7 activation intracellular signaling mechanisms including p38 MAPK (3) and phospholipase A2 (4) result in release of CatS (5) which then liberates soluble FKN from neurons (6). FKN feeds back onto the microglial cells via the CX3CR1 receptor (7) to further activate the p38 MAPK pathway (8) and release inflammatory mediators that activate neurons and result in chronic pain.

2.7. Role of CatS in neoplastic cancer progression

Ample clinical evidence showing that the up-regulation of CatS confers a poor prognosis in patients with a variety of malignancies [Flannery T., *et al.*, 2003; Rodriguez J., *et al.*, 2005; Tandon AK., *et al.*, 1990]. The excessive expression and activity of cathepsins not only help promote tumor growth but they also enhance the degradation of the ECM components that, subsequently, promote tumor cell invasion, metastasis and formation of secondary tumors. Understanding of the role of CatS and its activity in tumor malignancy may thus help clarify its molecular mechanism in regulating the presentation of tumor-associated antigens. Several clinical studies have shown that the expression level of CatS was different between tumor and adjacent control tissue cytosols. The expression of CatS was also found to be up regulated in astrocytomas, providing yet another evidence for a potential role of CatS in astrocytoma invasion [Flannery T., *et al.*, 2003]. Furthermore, the expression level of CatS is closely associated with tumor progression in glioblastomas, suggesting that CatS may serve as a useful prognostic indicator and potential target for anti-invasive therapy [Flannery T., *et al.*, 2006]. Recent immunofluorescence evidences from the works of Zhang L., *et al.*, [Zhang L., *et al.*, 2014] revealed that, the inhibition of CatS induces autophagy and apoptosis in human glioblastoma cell lines through ROS-mediated PI3K/AKT/mTOR/p70S6K and JNK signaling pathways. Therefore, CatS could be a novel therapeutic target for treating malignant glioblastoma and other cancers.

2.8. Cathepsin S inhibitors

Recently, considerable progress has been achieved in the design of inhibitors that specifically target CatS to avoid indiscriminate properties upon members of the cathepsin family. After the appearance of irreversible inhibitors (like the vinyl sulfone LHVS, compound 1), reversible and selective inhibitors of CatS have appeared. Like most cysteine protease inhibitors, their interaction with the target protease involves the formation of a covalent bond with the catalytic thiol. The functional group involved in that interaction is often called as 'warhead'. Reversible inhibitors represent a more attractive therapy than irreversible ones, as there is less opportunity for idiosyncratic toxicity. Indeed, irreversible compounds, even with high specificity for a particular protease, can bind and permanently inactivate a non-target enzyme, thus increasing the likelihood of toxicity.

Since 1990's copious drug design and biomolecular, research on cysteine proteases has been generated ample of novel CatS inhibitors mainly towards reversible, nonpeptidic and small molecule derivatives. Moreover, researchers around the globe continued to be pursuing large data of promising molecules due to increased interest in CatS is evident from the rise in patent literature since a decade. The number of CatS patents to date has surpassed that of most competitive homologs, cathepsin L and K. Due to profound focus on CatS as an enzyme target, thus far, there are research reports and patent literatures both peptidic and non-peptidic moieties with respective irreversible warheads as well as reversible selective inhibitors such as; nitriles, aliphatic ketones, ketoheterocycles, β -lactams, pyrazoles, furanones, ketoamides, benzimidazole piperidines, cyanopyrimidines, tetrahydropyridinepyrazoles, pyrrolopyrimidines, arylalkynes, amidofurans, benzoylhydrazones, trifluoroethylamines, bicyclic piperdines [Leroy V., et al., 2004; Alice LD., *et al.*, 2011].

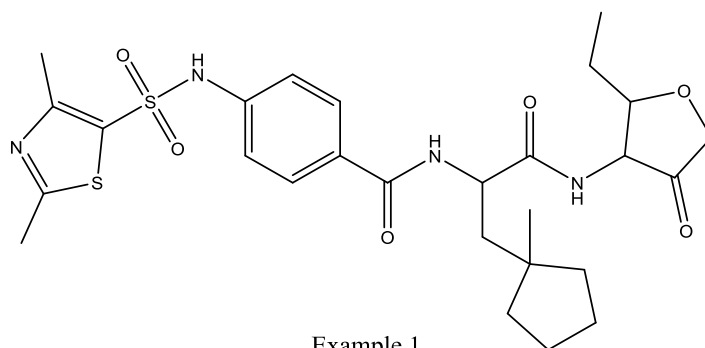
2.8.1. Carbonyl compounds

Since 2004, the carbonyl warhead, through its feature in furanones, keto-heterocycles and ketoamides, continued to be pursued by researchers from Medivir/Peptimmune, Amura Therapeutics (formerly Incenta Ltd), the Novartis Genomics Institute and Celera Genomics (formerly Axys Pharmaceuticals). Though small molecule discovery was suspended at Celera Genomics in 2006, Virobay has since picked up this program and maintained the investigation of small molecules, more recently as specific cathepsin inhibitors for cancer therapy [Elie BT., *et al.*, 2010]. Non-peptidyl compounds have also been disclosed by researchers at the University of California-Berkeley, discovered through a substrate-based fragment identification method.

2.8.1.1. Furanones

Furanones are comes under carbonyl warhead bearing CatS inhibitors. Several early reports on the use of peptidyl furanones as CatS inhibitors were reported and the patented literatures as from Medivir and Peptimmune [Ameriks MK., *et al.*, 2008]. Majority of these compounds maintained a methyl cyclopentyl alanine as the S2 binding element. Through structure-based and rational drug design efforts, example 1 was identified as a lead [Ayesa S., *et al.*, 2009]. Employment of solid-phase synthesis routes enabled the preparation of numerous compounds to explore P3 SAR. The results demonstrated that aromatic substitution in place of the methyl group on the sulfonamide would lead to increased CatS potency and selectivity over Cat K/L,

best exemplified by example 1 (CatS K_i = 0.7 nM, Cat K K_i = 1800 nM, Cat L K_i = 16,000 nM) [Ayesa S., *et al.*, 2009].

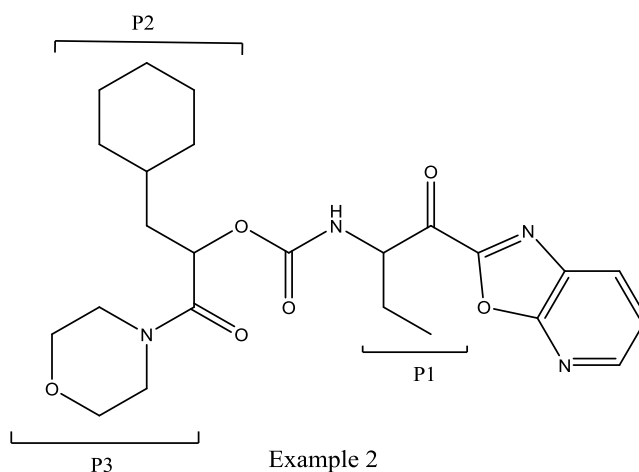


Example 1

2.8.1.2. Keto-heterocycles

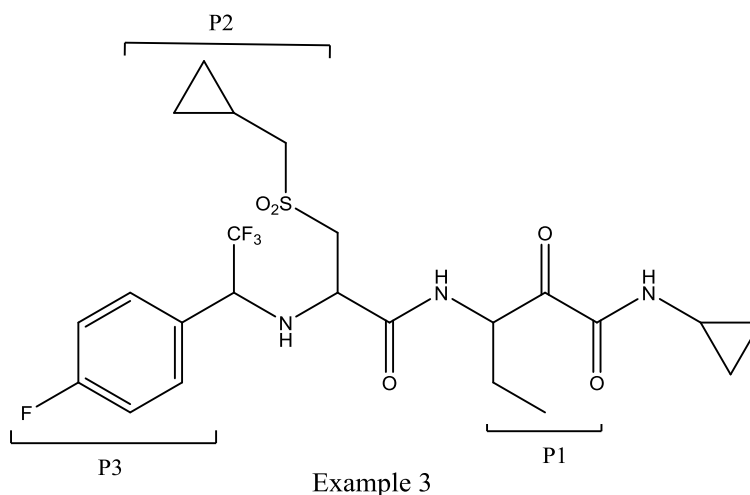
Ketoheterocycles have been reported as serine and cysteine protease inhibitors. Many of them are believed to be reversible inhibitors [Leroy V., *et al.*, 2004]. Several patented literatures from the companies Boehringer Ingelheim claimed keto heterocycles as potent, reversible inhibitors of cathepsin S for modulating auto-immune diseases such as rheumatoid arthritis. Axys and Aventis have claimed carbamate and amino derivatives of keto heterocycles, such as selective inhibitors of cathepsin S [Leroy V., *et al.*, 2004].

Where in 2005, Novartis Genomics Institute disclosed their work on peptidyl keto-benzoxazoles, with a handful of the 61 examples were nitriles and cyclic ketones [Alper PB., *et al.*, 2005]. The most active ketone (Example 2) demonstrated CatS K_i value of 0.4 nM, with good selectivity over the other cathepsins (650×CatK, 3200×CatL, 13,000×CatB) [Alper PB., *et al.*, 2005]. Specific substitutions such as the cyclohexylmethyl group at the P2 position (Example 2) enabled selectivity for CatS over the caspases and other cathepsins. In 2005, Celera Genomics published a number of patent applications on keto-heterocycles [Link JO., 2005].



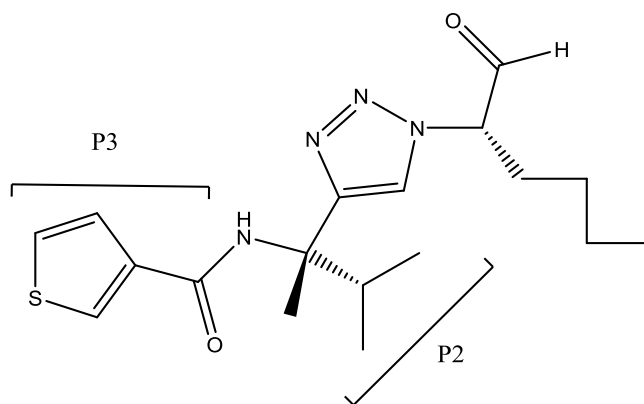
2.8.1.3. Ketoamides

In addition to the keto-heterocycles, with ample of patent literature, Celera Genomics disclosed a series of ketoamide cathepsin inhibitors, describing changes to the P1 alkyl group and P2 aliphatic sulfone as well as to the P3 amine, as seen in Example 3 [Graupe M., *et al.*, 2007; O LJ., 2006]. Where, from aforementioned keto-heterocycles of Celera Genomics group, the P3 carbonyl was removed in molecules and improved with ketoamides leads to improved cysteine protease inhibition. These compounds were reported to inhibit CatS at $K_i \leq 100$ nM (130 pM). A compound from this particular set (Example 3) was recently profiled by Virobay, exhibiting antitumor efficacy in pancreatic cancer model [Elie BT., *et al.*, 2010]. Virobay also used Ketoamides as dual CatS/HCV-replication inhibitors with the aim of treating hepatitis C, Alzheimer's disease and other autoimmune disorders [Holsinger LJ., *et al.*, 2009].



2.8.1.4. Non-peptidyl aldehydes

The application of novel substrate-based fragment identification and optimization method, called ‘substrate activity screening’, by Ellman and co-workers led to the initial preparation of N-acylated aminocoumarin fragments, with high enzyme affinity [Wood WJ., *et al.*, 2005; Patterson AW., *et al.*, 2007]. These groups were succeeded in development of core moieties with several modifications such as replacement of the aminocoumarin with hydrogen converted N-acylated aminocoumarin substrates into potent non-peptidyl inhibitors [Wood WJ., *et al.*, 2005; Patterson AW., *et al.*, 2007]. Moreover, modifications at the P2 position on these molecules (Example 4, $K_i = 9\text{nM}$) with alkyl substituents, which were capable of extending into S2 pocket was followed to increase in potency improvement and selectivity [Inagaki H., *et al.*, 2007].



Example 4

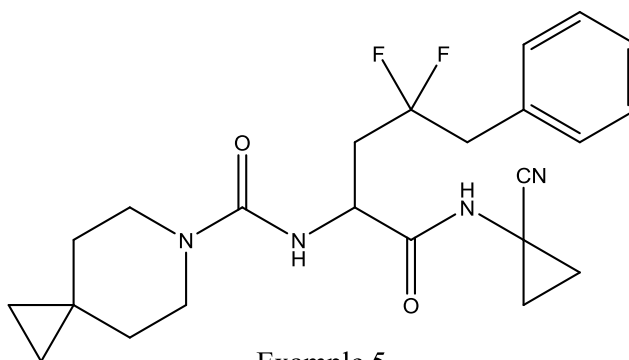
2.8.2. Nitrile compounds.

Nitrile derivatives has been known to be reversible inhibitors of cysteine proteases. Advantage of this warhead is that inhibitors do not usually interact with serine proteases. The catalytic thiol adds to the nitrile, reversibly forming a thioimidate derivative. Since 2000, a number of peptidic and non-peptidic nitrile derivatives has been claimed in the patent literature to be inhibitors of cathepsin S, B, K and L. The most active players targeting cathepsin S with nitrile-based inhibitors are AstraZeneca, Aventis [Leroy V., *et al.*, 2004].

2.8.2.1. Peptidyl nitriles

Ample of several patent literature on peptidyl nitriles as CatS inhibitors since 2000, with competitive and collaborated research efforts were progressed from different companies such as,

Sanofi-aventis, Celera Genomics, Merck Frosst, Virobay and Boehringer Ingelheim [Aldous DJ., et al., 2005]. Peptidyl nitriles were described as CatS, K and B inhibitors; only general CatS activity was described (CatS $K_i = 0.1$ to 100 nM) [Aldous DJ., et al., 2005]. From 2003 to 2006, Merck Frosst with Celera Genomics published a number of patent applications on peptidyl nitriles resulting in the discovery of odanacatib (MK-0822) which is currently in clinical trials. Analogs of odanacatib were reportedly used as a starting point for CatS selective molecules. These molecules took advantage of the larger P2 and smaller P3 moieties to favor CatS relative to Cat K [Alice LD., et al., 2011]. A patent application in 2007 on similar nitrile analogs focused on the alteration of the P3 urea using spirocyclic amines (Example 5, $K_i = 0.3$ nM) [Schudok M., et al., 2007; Schudok M., et al., 2009]. Notably, the SAR suggested that the smaller heterocyclic ring and the *ortho* nitrile substitution on the P3 aryl group were important for CatS selectivity. Unsurprisingly, P2 substitution was tolerant of branched alkyl (Val/Leu) as well as benzyl groups could be notable exceptions to improve the activity.



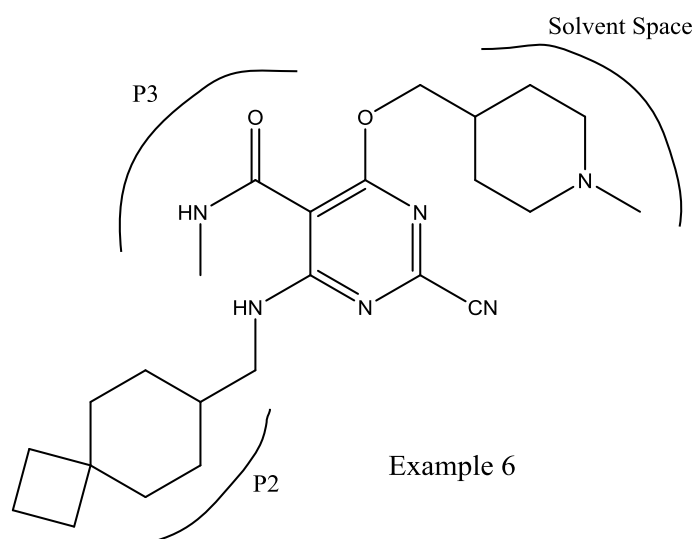
Example 5

2.8.2.2. Non-peptidyl nitriles

Researchers from different organizations have been working on non-peptidyl nitriles since 2000 and important core moieties includes 2-cyanopyrrolopyrimidines and 2-cyanopyrimidines by Novartis; triazine- and pyrimidine-2-carbonitriles as well as pyrrolo-/purine-pyrimidine carbonitriles as inhibitors of CatS by AstraZeneca; purine-6-carbonitriles, cyano-triazines and dioxo-triazines as CatS inhibitors from Organon Laboratories [Leroy V., et al., 2004; Alice LD., et al., 2011].

Majorly all the authors focused on differences in the S2 pocket size between the cathepsins were exploited to gain selectivity for CatS over CatK/L [Sunesis Pharmaceuticals., 2008]. Although the authors attempted to take advantage of the electrostatic differences in S3 for CatS selectivity, it was likely that the plasticity of Lys64 allowed for accommodation of large P3 substitution and

could have accounted for the additional selectivity observed in the SAR. Importantly, the smaller 2-cyanopyrimidines [Hart TW., *et al.*, 2006] from Novartis were researchers took advantage of the larger S2 pocket of CatS versus that of CatK, enlarging the P2 substituent of these analogs to allow for better selectivity over CatK. Introduction of polar substitution at the solvent-exposed 6-position of the pyrimidine ring (Example 6) led to improved hERG profiles [Irie O., *et al.*, 2008a]. Moreover, compound Example 6 exhibited promising results on evaluation in a murine experimental autoimmune encephalomyelitis model for MS and against neuropathic mechanical hyperalgesia (MH) in rats [Irie O., *et al.*, 2008a].

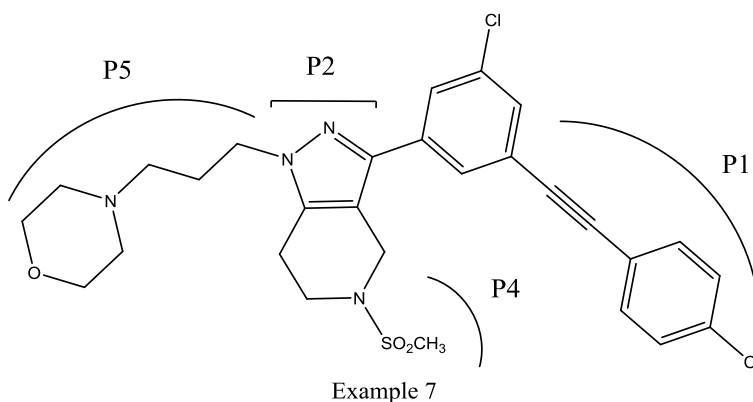


2.8.4. Non-covalent inhibitors

Initially, a patent disclosure in 2002 of novel, reversibly bound, non-covalent tetrahydropyrazolo-pyridine inhibitors, by researchers at J&J PRD, L.L.C., and later published number of patent applications in 2008 to follow-up on the earlier structures. These second-generation compounds featured greater exploration at the aryl ring pendant to the pyrazole core, with varied substitution such as functionalized alkynes/alkenes, thioethers, aryl rings, and amides/sulfonamides with or without an alkyl linker [Alice LD., *et al.*, 2011; Ameriks MK., *et al.*, 2008]. A crystal structure literatures of different pyrazole derivatives bound to a Cys25Ser mutant of CatS had elucidated that the pyrazole core served as the P2 element, the N-alkylated ‘headgroup’ attached to the pyrazole reached the S5 pocket and the tetrahydropyridine interacted with the S4 subsite, remaining solvent-exposed [Ameriks MK., *et al.*, 2009]. This binding mode

notably deviated from previously reported CatS inhibitors in the literature as there was no access to the S1, S1' or S3 pockets. Crystal structures of select second generation compounds bound to the Cys25Ser CatS mutant illustrated that these molecules maintained those earlier interactions with S5, S4 and S2 but now the newly added functionality occupied either the S1 or S3 pockets [Ameriks MK., *et al.*, 2009; Wiener DK., *et al.*, 2010; Ameriks MK., *et al.*, 2010; Alice LD., *et al.*, 2011].

During the optimization of the alkynes, it was found that improved affinity could be attained by incorporation of a terminal substituted aryl ring with concomitant truncation of the P5 functionality, the latter of which enabled sub-micromolar inhibition of mouse CatS, and eventually led to Example 7 [Ameriks MK., *et al.*, 2010] and its series. Sub-micromolar cellular activity was notably not achieved in this series until basic lipophilic groups were placed at the P1 arylalkyne or P5 region of the molecule (Example 7, $IC_{50} = 200$ nM) [Alice LD., *et al.*, 2011].

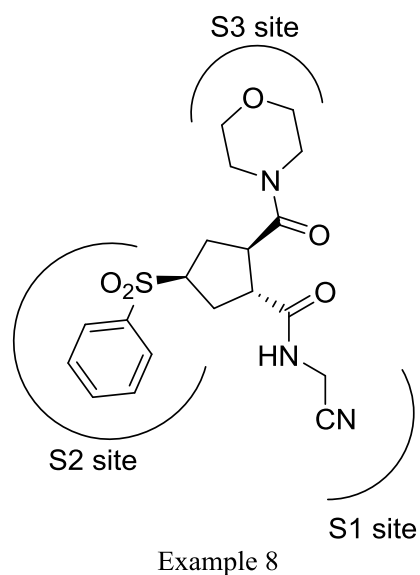


Several different patent literature applications were existed until date for the biaryl and amide/sulfonamide analogs, diazinones as P2 replacements for the pyrazole-based inhibitors, arylaminoethyl amines and amides [Alice LD., *et al.*, 2011].

Other than patent literatures there are ample of research publications on non-covalent CatS inhibitors, which were gathered to utilize in generation of ligand based pharmacophores to dig out novel moieties for CatS inhibition [Markt P., *et al.*, 2008]. Recent pharmacophore based 3D QSAR studies, [Markt P., *et al.*, 2008], represented several CatS inhibitors with diverse structural moieties and for the generation of ligand-based pharmacophore. Trifluoroethylamines from Gauthier JY., *et al.*, [Gauthier JY., *et al.*, 2007] were designed in prior consideration of CatS S2 subsite selectivity of the inhibitors, which was believed to be accepted as significantly larger

groups compared to the S2 subsite found in Cat K. This difference provided a key to achieving selectivity of the CatS by trifluoroethylamines.

Recent literature from Hilpert H., *et al.*, group [Hilpert H., *et al.*, 2013], have synthesized series of cyclopentanes, pyrrolidines and prolines derivatives in order to attain the selectivity in favor of CatS, 1,2,4-substituted five-membered scaffolds with three residues attached to the scaffold orientated toward the S1–S3 pockets of the CatS active site. Whereas, selectivity for CatS could be accomplished by an appropriate extended residue pointing into the S2 pocket of CatS, which is significantly smaller in CatK, revealed by the earlier reports. Among three derivatives cyclopentanes were achieved high enzyme inhibition and CatS selectivity. Initially with simple and no group substitution extending into the S2 pocket were turned out to be an unselective dual CatS/K inhibitor with modest activities. But later, with the cyclopropylmethyl sulfone residues for the S2 pocket interaction, resulted in an approximately 4-fold higher enzymatic inhibition of CatS but, more importantly, had a profound effect on increase in CatS selectivity, which improved >100-fold. Along with number of other alkylsulfone S2 substitutions, phenylsulfone substitution (Example 8) boosted the IC_{50} value into the subnano molar range ($IC_{50} = 0.0007 \mu\text{M}$) with the desired high selectivity of >20,000-fold versus CatK. With the help of SAR studies on cyclopentanes and other heterocyclic derivatives there is a clear observation that the rigidity of a cyclic scaffold can be of advantage to reduce the number of rotatable bonds, thereby making the inhibitors less prone for metabolic break down and more potent if the appropriate binding conformation is populated.



Therefore, with above all CatS literature on inhibitor development, it was very clear that as an important target for pharmaceutical industry and researchers, due to pleiotropic nature of CatS. Strong efforts have been made to identify potent and selective CatS inhibitors. Selectivity over other cathepsins is of high importance to evaluate the pharmacology of CatS inhibitors and to assess their therapeutic potential in the clinic. Many of the recent CatS inhibitors contain an electrophilic motif (e.g., a nitrile), which binds covalently and reversibly to cysteine in the active site, forming a thioimidate. This binding motif has been employed, for example, in the aminocyclopropane nitrile or in the succinamide derivative and more recent triazoles.

CatS inhibition in various kinds of disorders was exemplified as attractive therapeutic target for drug discovery and grabbed recent attention towards therapeutic intervention in a neuropathic pain [Clark AK., *et al.*, 2009]. Earlier in 2008, Markt *et al.* [Markt P., *et al.*, 2008] reported ligand-based and structure-based pharmacophore models utilizing covalent and non-covalent CatS inhibitors and explained the importance of the site specificity of CatS active site. In the present work, alignment of each ligand series from various scaffolds (ranges from 2 picomolar to 100 nanomolar) to find out responsible activity features by using ligand based pharmacophore generation studies. 3D QSAR mapping was done to validate generated pharmacophores as well as to attain contour maps to predict SAR. After all, with the above considerations revealed by earlier reports, current target CatS drug development objectives and work plans were preempted and constructed.

CHAPTER 3

Objectives and plan of work

CHAPTER 3

Objectives and plan of work

3.1. Objectives:

As previously mentioned, neuropathic pain is a complex clinical syndrome caused due to several distinct common neurological disorders affecting the global population both in developed and in developing countries. Conventionally, major research on developing drug candidates to treat NP was mainly focused on symptomatic and superficial management. Profound studies on molecular targets which are root causes for the disease progression and inter related common enzyme targets are necessary steps for the meticulous treatment. The crucial role of CatS in the regulation of the pathophysiology of a number of auto-immune conditions, by its role in antigen presentation (MHC class II to CD4⁺ T-cells), degradation of the extracellular matrix and also the pro-nociceptive role of releasing fractalkine (CX3CL1) in neurons. CatS existed with unique contribution as an enzyme target which involves, initiation and propagation of respective diseases such as NP and cancer as well as cancer induced NP.

After thorough review of the literature, design of small molecule inhibitors of human CatS was considered as prime objective of importance hence the below mentioned strategy has been followed.

I. Primary objective was to design new CatS inhibitors

- Development of ligand based and structure based pharmacophore models to explore the novel chemical entities for CatS inhibition.
- High throughput virtual screening of *in house* database (~500000 molecules) from the pharmacophore based screening to docking based virtual screening.

II. Synthesis of various analogues of CatS inhibitors based on virtual screening and the biological evaluation.

III. *In vitro* screening of synthesized molecules for understanding CatS inhibitory activity.

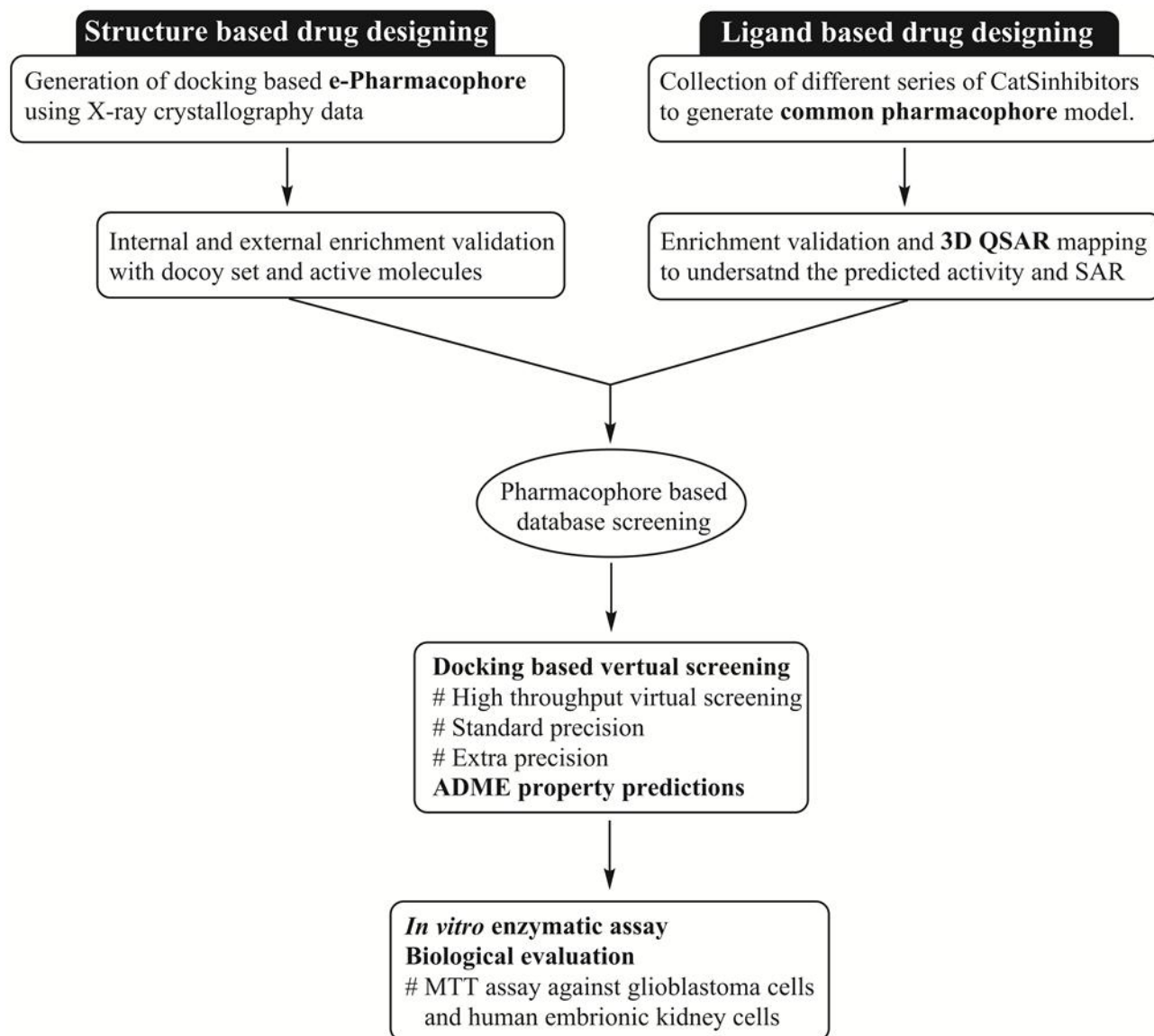
IV. *In vitro* cell lines studies for anticancer and activity.

V. *In vivo* behavioral and molecular pharmacological studies on disease induced animal models.

3.2. Plan of Work:

The plan of work was classified into the following categories

3.2.1. Design and development of new CatS inhibitors using computational methods



3.2.2. Synthesis of various analogues of lead molecule selected from biological evaluation.

3.2.3. *In vitro* CatS enzymatic assay using fluorescent CatS kit.

3.2.4. *In vitro* cytotoxicity studies on cell lines like U-87 MG and HEK293 cells.

3.2.5. Atom based QSAR analysis to understand the SAR.

3.2.6. *In vivo* neuropathic pain studies.

3.2.6.1. Behavioral rodent model studies on allodynia and hyperalgesia

3.2.6.2. Neurotoxicity assessment studies

3.2.7. Measurement of *in vivo* gene expression levels of various key regulators NF κ B, ERK1, IL-1 β , IL-6 and TNF- α using RT-qPCR.

3.2.8. Measurement of protein levels of key regulator ERK1 (associated with CatS in MAPK pathway) using western blot analysis.

3.2.9. Measurement of LPS treated brain tissue *ex vivo* gene expression levels of various key regulators NF κ B, ERK1, IL-1 β , IL-6 and TNF- α using RT-qPCR.

CHAPTER 4

Materials and methods

CHAPTER 4

Materials and methods

4.1. Computational details

An Intel Core i7 2600, 3.40GHz capacity processor with memory of 12GB RAM running with the CentOS 6.1 X86_64 bit operating system was used to carry out all the computations. The e-pharmacophore models were generated using Glide and PHASE applications implemented in the Maestro 9.3 software package (Schrodinger, LLC, New York, 2012). Finally, ADME prediction of molecules was checked with QikProp 3.5 (Maestro 9.3). 2D sketcher tab on Maestro graphical user interface was used to draw all structures. Structures were energetically minimized and stereo isomers generation were done at neutral pH 7 using ionizer subprogram of LigPrep 2.6 (Maestro 9.3).

4.2. Ligand based pharmacophore generation and 3D QSAR mapping

4.2.1. Data Set and molecular modeling

A data set comprising of 161 molecules reported as CatS inhibitors were collected from various literatures and were used in the present study. The various scaffolds employed in the current work consisted of derivatives of pyrrolopyrimidines [Irie O., *et al.*, 2008a], ketobenzimidazole piperidines [Thurmond RL., *et al.*, 2004], 4-amino-2-cyanopyrimidines [Irie O., *et al.*, 2008b], succinyl-nitriles [Bekkali Y., *et al.*, 2007], tetrahydropyridinepyrazoles [Ameriks MK., *et al.*, 2010], dipeptide nitriles [Ward YD., *et al.*, 2002; Asaad N., *et al.*, 2009], tetrahydropyridopyrazole thioether amines [JM Wiener J., *et al.*, 2010], ketobenzimidazoles [Gustin DJ., *et al.*, 2005], pyrrolopyrimidines [Irie O., *et al.*, 2008a], cyanopyrimidines [Irie O., *et al.*, 2008b], arylalkynes [Ameriks MK., *et al.*, 2009], amidofurans [Ayesa S., *et al.*, 2009], benzoylhydrazones [Cywin CL., *et al.*, 2003], trifluoroethylamines [Gauthier JY., *et al.*, 2007], bicyclic piperdines [Grice CA., *et al.*, 2006] as inhibitors of CatS and the respective IC₅₀ values were noted and further converted into pIC₅₀ (-logIC₅₀) values to develop pharmacophore. All

structures were drawn using 2D sketcher tab on Maestro graphical user interface. The LigPrep 2.5 [Schrodinger, LLC] application from Schrodinger package was utilized to build and energetically minimize structures and to add hydrogens and generate stereoisomers at neutral pH 7 (± 2) using ionizer subprogram. Canvas 1.4 [Sakkiah S., *et al.*, 2012] chemoinformatics package that clusters the molecules based on Tanimoto similarities between a set of linear fingerprint descriptors was used to determine the structural diversity among the compounds and to choose representative molecules from each cluster. Clustered molecules with structural diversity were utilized for 3D QSAR development.

4.2.2. Development of pharmacophore models and 3D QSAR

Pharmacophore model development followed by 3D QSAR approach and internal statistical validation analysis were performed using PHASE. From the total 161 molecules, 98 molecules were randomly chosen for training set and 63 (Tables 1- 18) were selected as test set, by using the “Automated Random Selection” option of PHASE application (Schrodinger, LLC, New York, NY). Conformer generation was carried out with the MacroModel (Schrodinger, LLC, New York, NY) torsion sampling and OPLS_2005 force field. Prepared ligands were exploited to build pharmacophore model, where, dataset was divided into active, moderately active and inactive to spot out the essential features.

For 3D QSAR development, molecular dataset was divided into training and test set. Where, training set molecules were later placed into regular grid of cubes, with each cube allotted zero or more “bits” to account for the different type of pharmacophore features in the training set that occupy the cube (1\AA^3). This representation gave rise to binary-valued occupation patterns that could be used as independent variables to create partial least squares (PLS) factors for 3D QSAR models.

4.2.3. Pharmacophore validation

For validating the reliability of the best five-pharmacophore hypotheses, enrichment calculation was performed. A decoy set molecules (contains no activity) were acquired from scrodinger online database, from which 990 decoy molecules were grouped with 60 known active molecules of CatS inhibitors (Total of 1050 molecules), compiled as a database. Further, decoy set database was utilized to check the hypothesis ability to discriminate the active CatS inhibitor compounds

from other molecules. Enrichment factor (EF) and goodness of fit (GH) was calculated using equations 1 and 2 [Sakkiah S., et al., 2012]:

$$EF = \frac{(H_a \times D)}{(H_t \times A)} \dots\dots\dots (1)$$

$$GH = \left(\left(\frac{H_a}{4H_tA} \right) \times (3A + H_t) \right) \times \left(1 - \left(\frac{H_t - H_a}{D - A} \right) \right) \dots\dots\dots (2)$$

Where

‘H_t’ was total number of compounds in the hit list; ‘H_a’ was the total number of active molecules in the hit list ‘A’ is the total number of actives in the decoy set and ‘D’ was the total number of molecules in the decoy set.

4.2.4. PLS analysis and validation

The predictive value of the models was evaluated by cross-validation analysis, which was performed using the leave one- out (LOO) cross-validation. The cross validated coefficient, r_{cv}² (also called as LOO-q²) was calculated using the following equation:

$$r_{cv}^2 = 1 - \frac{\sum(Y_{obs} - Y_{pred})^2}{\sum(Y_{obs} - Y_{mean})^2} \dots\dots\dots (3)$$

Where

Y_{obs}, Y_{pred}, and Y_{mean} were the observed, predicted, and mean values of the target property (pIC₅₀) of the training set, respectively. (Y_{obs} - Y_{mean})² was the predictive residual sum of squares (PRESS). The predictive correlation coefficient (r_{pred}²), based on molecules of test set could indicate the predictive power of models and hence for external test set was derived as bellow,

$$r_{pred}^2 = \frac{SD - PRESS}{SD} \dots\dots\dots (4)$$

Where SD was the sum of the squared deviations between the actual activities of the test set and mean activities of the training set molecules and PRESS was the sum of squared deviation between predicted and actual activity values for each molecule in test set [Pan X., et al., 2010].

4.2.5. External statistical validation

To evaluate the true predictive abilities of the established models, it was necessary to perform external validation. On basis of literature [Lu P., *et al.*, 2010; Basu A., *et al.*, 2009; Golbraikh A., *et al.*, 2002; Roy P.P., *et al.*, 2008; Pratim Roy P., *et al.*, 2009; Roy K., *et al.*, 2009; Roy K., *et al.*, 2009] revelations, 3D QSAR models could be accepted if they satisfy all of the following conditions of external validation parameters:

$r_{cv}^2 > 0.5$, $r^2 > 0.6$, R_0^2 or $R_0'^2$ close to r^2 , i.e. $[(r^2 - R_0^2)/r^2] < 0.1$ or $[(r^2 - R_0'^2)/r^2] < 0.1$, the corresponding $0.85 \leq k \leq 1.15$ or $0.85 \leq k' \leq 1.15$, $r_m^2 > 0.5$, and $R_p^2 > 0.5$.

The r^2 value was calculated by the following formula:

$$R = \frac{\sum(Y_i - \bar{Y}_o)(\tilde{Y}_i - \bar{Y}_p)}{\sqrt{\sum(Y_i - \bar{Y}_o)^2 \sum(\tilde{Y}_i - \bar{Y}_p)^2}} \dots\dots\dots (5)$$

Where, Y_i and \tilde{Y}_i were the observed and predicted activities, \bar{Y}_o and \bar{Y}_p were the average values of the observed and predicted pIC50 values of the test set molecules respectively. For an ideal QSAR model, correlation coefficient R between the actual Y and predicted \tilde{Y} activities should be close to 1 for high predicted activities and regressions in scatter plots of Y_i against \tilde{Y}_i or \tilde{Y}_i against Y_i through the origin, i.e. $Y^{r0} = k\tilde{Y}$ and $\tilde{Y}^{r0} = k'Y$ (with the intercept set to 0) respectively, and the slopes should be characterized by at least either k or k' close to 1 [Golbraikh A., *et al.*, 2002]. Slopes k and k' were calculated as follows:

$$k = \frac{\sum Y_i \tilde{Y}_i}{\sum \tilde{Y}_i^2} \dots\dots\dots (6a)$$

$$k' = \frac{\sum Y_i \tilde{Y}_i}{\sum Y_i^2} \dots\dots\dots (6b)$$

Both the correlation coefficients for the regression lines through the origin (Y^{r0}) could be defined by R_0^2 and $R_0'^2$, which were calculated as follows:

$$R_0^2 = 1 - \frac{\sum(\tilde{Y}_i - Y_i^{r0})^2}{\sum(\tilde{Y}_i - \bar{Y}_p)^2} \dots\dots\dots (7a)$$

$$R_0'^2 = 1 - \frac{\sum(Y_i - \bar{Y}_i^{r_0})^2}{\sum(Y_i - \bar{Y}_0)^2} \dots\dots\dots (7b)$$

For better external predictive potential of the model, a parameter of modified r^2 (r_m^2) was used for the whole set considering LOO-predicted values for the training set and predicted values of the test set compounds. The r_m^2 statistic equation for overall test and training set values, were generally used for selection of the best predictive models [Pratim Roy P., *et al.*, 2009]. Substantiation of the particular QSAR models with r_m^2 value was defined by the following equation:

$$r_m^2 = r^2 \left(1 - \sqrt{|r^2 - R_0'^2|} \right) \dots\dots\dots (8)$$

Where r^2 was the non-cross-validated correlation coefficient obtained from the PLS process, and the $R_0'^2$ was calculated from equation 7a.

Another important parameter for an acceptable 3D QSAR model was that the average correlation coefficient (R_r) of randomized models should be less than the correlation coefficient (R) of the non-randomized model. A parameter R_p^2 [Roy K., *et al.*, 2009] was used to penalize the model R^2 accounting for the difference between squared mean correlation coefficient (R_r^2) of randomized models and squared correlation coefficient (R^2) of the non-randomized model. R_p^2 was calculated by the following equation:

$$R_p^2 = R^2 \left(\sqrt{R^2 - R_r^2} \right) \dots\dots\dots (9)$$

This parameter R_p^2 ensures that the model thus developed is not obtained by chance, where the value of R_p^2 should be greater than 0.5 for an acceptable model.

4.3. Structure based pharmacophore modelling

4.3.1. e-Pharmacophore model development

For structure-based energy dependent pharmacophore model generation for noncovalent CatS inhibitors, the crystallographic data of eight PDB noncovalent ligand complexes (2F1G, 2G7Y,

2H7J, 2HH5, 2R9M, 3IEJ, 3KWN) were analyzed within the software Maestro 9.3. PDB complex 2F1G was finalized based on its low K_i value (29 nm) and resolution (1.90 Å). Raw crystallographic protein ligand complexes were prepared using protein preparation wizard, the co-crystal ligand molecule was duplicated, and prepared using Ligprep application. Binding energy descriptors were generated using the Glide extra precision (XP) docking module. XP energy descriptor file was utilized by PHASE script to generate energy based pharmacophore models.

4.3.2. Pharmacophore validation

Enrichment calculation was performed to validate the reliability and robustness of the best four e-pharmacophore hypotheses. A decoy set consisting of 1150 molecules including 150 known active molecules of CatS inhibitors was developed and was used to check the hypothesis ability to discriminate the active CatS inhibitors from other molecules. Enrichment factor (EF) and goodness of hit (GH) was calculated using equations 10 and 11 [Sakkiah S., *et al.*, 2012]:

$$EF = \frac{(H_a \times D)}{(H_t \times A)} \dots\dots\dots (10)$$

$$GH = \left(\left(\frac{H_a}{4H_tA} \right) \times (3A + H_t) \right) \times \left(1 - \left(\frac{H_t - H_a}{D - A} \right) \right) \dots\dots\dots (11)$$

Where, ‘ H_t ’ was total number of compounds in the hit list; ‘ H_a ’ was the total number of actives molecules in the hit list ‘ A ’ was the total number of actives in the decoy set and ‘ D ’ was the total number of molecules in the decoy set.

Enrichment calculator script provided by Schrodinger application package was utilized for the internal validation properties such as EF1%, 10%, BEDROC, RIE. EF(X)% inferred the ability of the e-pharmacophore to select the active molecules in the first X% of the match find. Boltzman enhanced discrimination receiver operating characteristic (BEDROC) and robust initial enhancement (RIE) were good metrics which have advantage to discriminates between early and late recognition problem of true positives as described by Wei Zhao *et al* [Wei Zhao., *et al.*, 2009]. In this study, exponential weighting scheme of $\alpha=20$ was used for BEDROC, corresponding to 80% of the score from the top 8% of the list. Validated pharmacophore hypothesis with above parameters was considered to utilize for the virtual screening.

4.3.3. Atom based 3D QSAR

An atom based 3D QSAR mapping was performed for the synthesized compounds, with help of enzymatic inhibition assay IC_{50} values. All 32 molecules were prepared and conformer generated to build atom based QSAR. All the IC_{50} values were converted into pIC_{50} values and utilized to generate correlation factors. Molecules were divided into training and test set, and performed LOO method for the optimization of the correlation factors (R^2 and Q^2). Molecules were restricted to 60% of in training set and remaining 40% in test set. PLS factors until five were used and later, based on scatter plot analysis contour maps were generated.

4.4. Docking based virtual screening and ADME prediction studies

The best validated pharmacophore hypotheses from both ligand based and structure based methods were subjected to screen against large public compound libraries from Asinex (www.asinex.com) for docking based virtual screening. Glide module was used to carry out virtual screening of the compound library. The crystal structure of CatS (2F1G) was downloaded and prepared for geometric optimization using protein preparation wizard of Schrodinger, LLC. Primarily, favorable interactions between screened ligand hits (from pharmacophore screening) and the CatS in the flexible mode of docking were examined by using module Glide. Three different levels of docking precision modes were used for Glide, i.e., HTVS (high throughput virtual screening), SP (standard precision) and XP (extra precision) (Glide 5.7, Schrodinger, LLC, New York, USA). At first HTVS was used to carry out initial docking calculations and further refinement of good ligand poses was done in SP and XP mode. All the confirmations of final docked molecules were visually examined for the pocket occupancy and crucial amino acid interactions to get apparently promising ligands. Finally, top list compounds were subjected to ADME property predictions, where further checked predicted druggability and pharmacokinetic properties using QikProp module provided by Schrodinger, LLC.

4.5. Enzymatic assay

CatS enzyme inhibition studies were carried out using SensoLyte 440 Cathepsin S Assay Kit Fluorimetric (from AnaSpec corporate, Canada.). The activity of purified recombinant human CatS (from human spleen) was measured using benzyloxycarbonyl- valine- valine-arginine-7-amido-4-methylcoumarin (ZVVR-AMC) as the substrate provided in assay kit. All the test compounds were dissolved in DMSO and later diluted with assay buffer (DMSO concentration

was below 1%) and incubated with recombinant activated enzyme at 37 °C for 10 min in the assay buffer. The assay buffer consisted of 0.1 M sodium acetate (pH 7.0), 1 mM EDTA, 0.01% Triton X-100, 1 mM DDT. Fluorescence generated by the release of methylcoumarin (nMec) within 30 minutes of reaction after addition of substrate was read in Perkin Elmer VICTOR X3 (Perkin Elmer, Shelton, CT, USA) with excitation and emission wavelengths of 354 nm and 442 nm, respectively. Auto fluorescence was checked and subtracted from the respective samples including the positive and negative controls.

4.6. Cell culture

The human cell lines U-87 MG (glioblastoma) and HEK293 (Human embryonic kidney cells) were used for the growth inhibition screening studies to screen CatS inhibitors as anticancer agents selective towards cancer cells (U-87 MG) deprived of normal cell (HEK293) cytotoxicity. Cells were obtained from National Center for Cell Science (NCCS, Pune, India) and U-87 MG was cultured in Eagle's minimum essential medium with Earle's salt containing 2 mM L-glutamine, 1.5 g/l sodium bicarbonate (Himedia) supplemented with 10% new-born calf serum (NBCS, Himedia), 100 µg/ml streptomycin, and 100 U/ml penicillin. While the HEK293 cells were cultured in RPMI-1640 with L-glutamine (Himedia) supplemented with 10% fetal bovine serum (FBS, Himedia) and 100 µg/ml streptomycin, and 100 U/ml penicillin. Cell culture treated culture flasks (Corning) and 96 well assay plates (Corning) were used for the entire studies in humid atmosphere containing 5% CO₂ at 37°C temperature.

4.6.1. Growth inhibition and cell viability assay

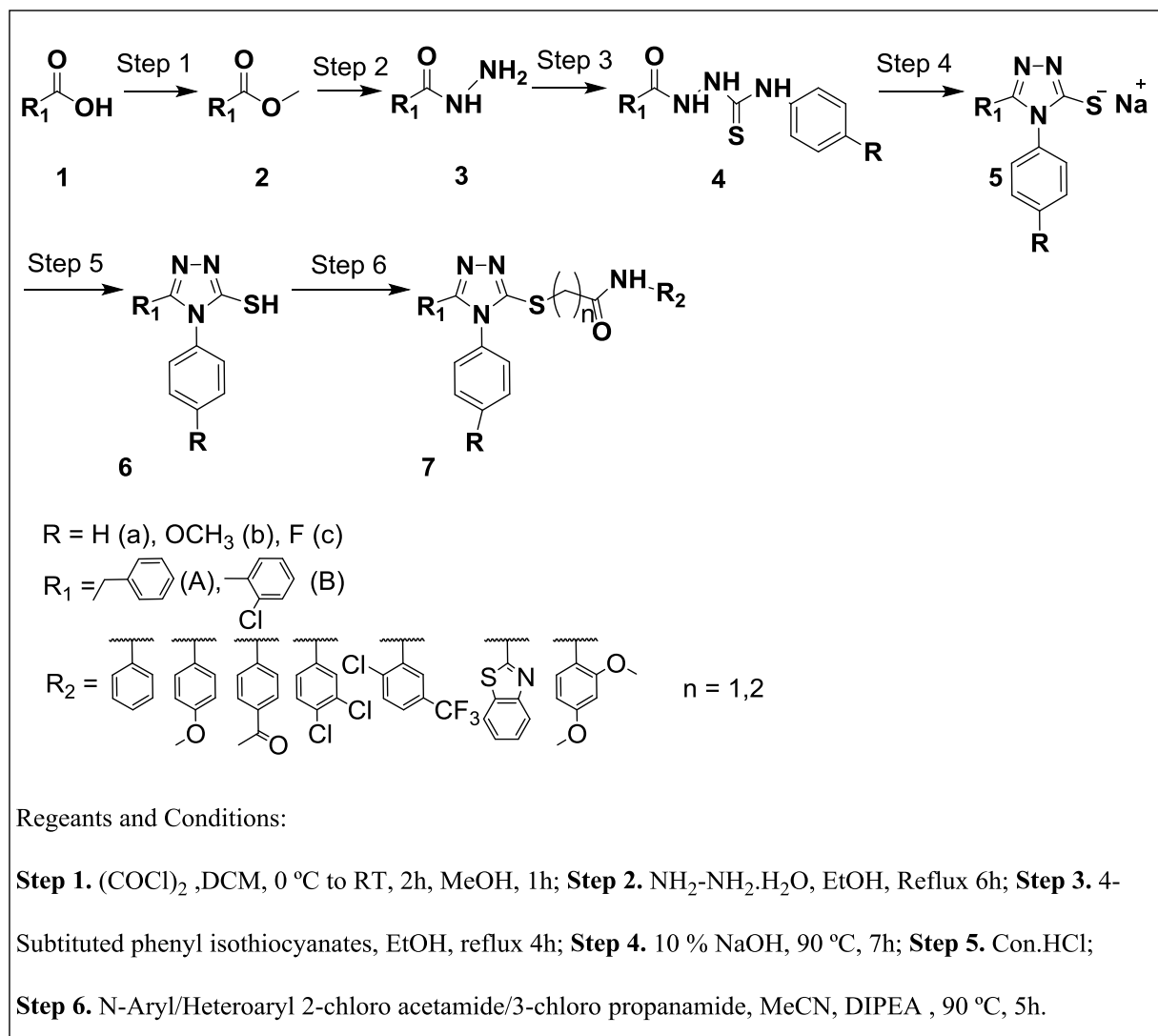
Cells were grown in 96-well plates at an initial concentration of approximately 3500 cells followed by proper treatment. Morphological change was examined under the upright type phase-contrast microscopy (Olympus). Triplicate wells were treated with six logarithmic concentrations of the each test compounds and DMSO concentration was constantly maintained at 1% in final dilution. Initial reading at non treated state and the final reading after 72 hr drug incubation were measured with Vector X3 2030 multi label reader (Perkin Elmer). Ten microliters of 5 mg/ml 3-[4,5-dimethylthiazol-2-yl]-2,5-diphenyltetrasolium bromide (MTT) (Sigma-Aldrich Co. LLC. USA) in growth medium was added to each well. After incubation for 4 h at 37 °C with MTT, cell medium was removed. The precipitated formazan, a product of MTT

tetrazolium ring by the action of mitochondrial dehydrogenases, was solubilized with DMSO and quantified spectrophotometrically at 540 nm.

4.7. Chemistry

4.7.1. General procedure for the synthesis

All commercially available chemicals and solvents were used without further purification. Melting points of the synthesized compounds were determined by Buchi B-540 open capillary instrument and were uncorrected. The homogeneity of the compounds was monitored by TLC (Thin layer chromatography) on silica gel 40 F254 coated on aluminum plates, visualized by UV or iodine chamber and KMnO_4 treatment. All ^1H and ^{13}C NMR spectra were recorded on a Bruker AM-300 (300.12 MHz, 75.12 MHz) NMR spectrometer and Bruker BioSpin Corp, Germany respectively. Molecular weights of the synthesized compounds were checked by SHIMADZU LCMS-2020 series in ESI mode. Chemical shifts are reported in ppm (δ) with reference to the internal standard TMS. The signals were designated as follows: s, singlet; d, doublet; dd, doublet of doublets; t, triplet; m, multiplet. Elemental analyses were carried out on elemental vario MICRO CUBE CHN Analyser. Detailed scheme for the synthesis of series of compounds is represented in Scheme 4.1.



Scheme 4.1 Synthetic protocol for 1,2,4-triazol thiol arylacetamide analogues [Cretu OD., et al., 2010; Khan I., et al., 2010; Mali R., et al., 2009].

Step 1.

Procedure for the preparation of methyl 2-phenylacetate/methyl 2-chlorobenzoate (2A/B):

Phenyl acetic acid (**1A**) or 2-chloro benzoic acid (**1B**) (150 mmol) was dissolved in dichloromethane (100 mL) followed by addition of oxalyl chloride (19 ml, 220 mmol) and 2-3 drops of N,N-dimethylformamide was added at $0-5^\circ C$. The reaction was stirred for 2 h and monitored by TLC. After completion of the reaction, methanol (60 mL) was added slowly to the reaction mixture and stirred for 1 hour. The reaction mixture was vacuum evaporated and was

further purified by flash column chromatography using 5 % ethylacetate in hexane as eluent to get **2A** and **2B**.

Step 2.

Procedure for the preparation of 2-phenylacetohydrazide (3A):

Compound **2A** (18g, 120 mmol) was dissolved in ethanol (100 mL) and 35% hydrazine hydrate (34.2 ml, 240 mmol) was added and refluxed for 6 h and monitored by TLC. The organic layer was vacuum evaporated and purified by washing with 10% ethylacetate/hexane (100 mL) and ethylacetate (50 mL) to get **3A**.

Procedure for the preparation of 2-chlorobenzohydrazide (3B):

Compound **2B** (18g, 105 mmol) was dissolved in ethanol (100 mL) and 35% hydrazine hydrate (30 ml, 240 mmol) was added and refluxed for 6 h and monitored with TLC. The organic layer was vacuum evaporated and purified by washing with 10% ethylacetate/hexane (100 mL) and ethylacetate (50 mL) wash to get **3B**.

Step 3.

General procedure for the preparation of N-(phenyl/4-Fluorophenyl/4-methoxyphenyl)-2-(2-phenylacetyl) hydrazinecarbothioamide (4Aa-4Ac) and 2-(2-Chlorobenzoyl)-N-(phenyl/4-Fluorophenyl/4-methoxyphenyl) hydrazinecarbothioamide (4Ba-4Bc):

To the intermediates (**3A/3B**) prepared in step 2 (35 mmol) in ethanol (60 mL) corresponding aryl isothiocyanates (35 mmol) were added and refluxed for 4 h. Subsequently, ethanol layer was vacuum evaporated and purified by washing with hexane (2*30 mL), diethylether (2*30 mL) and ethyl acetate (2*20 mL) to give corresponding desired compound.

N-Phenyl-2-(2-phenylacetyl) hydrazinecarbothioamide (4Aa): According to the above general procedure **3A** (5.3g, 35 mmol), phenylisothiocyanate (4.7g, 35mmol) were utilised to afford desired compound **4Aa** as an off-white solid.

N-(4-Fluorophenyl)-2-(2-phenylacetyl) hydrazinecarbothioamide (4Ab): According to above the general procedure **3A** (5.3g, 35 mmol), 4-fluorophenylisothiocyanate (5.4g, 35mmol) were employed to afford desired **4Ab**.

N-(4-Methoxyphenyl)-2-(2-phenylacetyl) hydrazinecarbothioamide (4Ac): According to above the general procedure **3A** (5.3g, 35 mmol) and 4-methoxyphenylisothiocyanate (5.8g, 35mmol) were utilized to afford desired **4ac**.

2-(2-Chlorobenzoyl)-N-phenylhydrazinecarbothioamide (4Ba): According to the above general procedure **3B** (6g, 35 mmol) and phenylisothiocyanate (4.7g, 35mmol) were utilized to afford desired **4Ba**.

2-(2-Chlorobenzoyl)-N-(4-fluorophenyl) hydrazinecarbothioamide (4Bb): According to the above general procedure **3B** (6g, 35 mmol), 4-fluorophenylisothiocyanate (5.4g, 35mmol) were used to afford desired **4Bb**.

2-(2-Chlorobenzoyl)-N-(4-methoxyphenyl) hydrazinecarbothioamide (4Bc): According to the above general procedure **3B** (6g, 35 mmol), 4-methoxyphenylisothiocyanate (5.8g, 35mmol) were used to afford desired compound **4Bc**.

Step 4.

General procedure for the preparation of sodium salt of 1,2,4- triazole-3-thiol derivatives (5Aa-5Ac and 5Ba-5Bc):

The compounds with general formula represented by compound **4** (30 mmol) were dissolved in 10% Sodium hydroxide solution and refluxed at 90 °C for 7 h. The reaction was monitored by TLC.

Step 5.

General procedure for the preparation of 1,2,4- triazole-3-thiol derivatives (6Aa-6Bc):

The Step **4** reaction mixture was neutralized by addition of conc. HCl to a pH in range from 5 to 6. The precipitate formed was filtered, washed with water and recrystallized in ethanol to get desired compounds.

5-Benzyl-4-phenyl-4H-1,2,4-triazole-3-thiol (6Aa): According to the general procedure **4Aa** (8.5g, 30 mmol) were used to afford desired compound **6Aa** (6.4g, 81 %) as off-white solid.

5-Benzyl-4-(4-fluorophenyl)-4H-1,2,4-triazole-3-thiol (6Ab): According to the general procedure **4Ab** (9.1g, 30 mmol) was used to afford desired compound **6Ab** .

5-Benzyl-4-(4-methoxyphenyl)-4H-1,2,4-triazole-3-thio (6Ac): According to the general procedure **4Ac** (9.5g, 30 mmol) was employed to afford desired compound **6Ac** .

5-(2-Chlorophenyl)-4-phenyl-4H-1,2,4-triazole-3-thiol (6Ba): According to the general procedure **4Ba** (9.1g, 30 mmol) was employed to afford desired compound **6Ba** .

5-(2-Chlorophenyl)-4-(4-fluorophenyl)-4H-1,2,4-triazole-3-thiol (6Bb): According to the general procedure **4Bb** (9.7g, 30 mmol) was employed to afford desired compound **6Bb** .

5-(2-Chlorophenyl)-4-(4-methoxyphenyl)-4H-1,2,4-triazole-3-thioli (**6Bc**): According to the general procedure **4Bc** (10g, 30 mmol) was used to afford desired compound **6Bc**.

Step 6.

General procedure for the preparation of substituted 1,2,4-triazol-3-yl-thio-N-substitutedphenylacetamide derivatives 7 (compounds **8-a** to **8-o**, **8-2a** to **8-2o** and **8-3n&8-4j**):

To 1 mmol of compound **6** in acetonitrile (15 mL), 3 mmol of N,N-di-isopropylethylamine (DIPEA) was added and the reaction mixture was heated upto 70 °C. 1 mmol of 2-chloro-N-substituted aryl/heteroaryl acetanilide was added drop wise. The reaction was continued at the same temperature for 5 h along with monitoring of TLC to check that the reaction was complete. The acetonitrile was vacuum evaporated and remaining mixture was diluted with 20 mL ethylacetate. The organic layer was washed with saturated sodiumbicarbonate solution (3*15 mL), separated and dried over anhydrous sodiumsulphate followed by purification using flash column chromatography with ethylacetate in n-hexane as eluent (25%-35%) to get desired compounds with general formula **7** (**8-a** to **8-o**, **8-2a** to **8-2o** and **8-3n&8-4j**) described in detail in chapter 6.

4.7.2. HPLC method development for the purity analysis

All the final compounds were checked for purity with a common method for detection was developed using a Shimadzu HPLC system (Shimadzu Corporation, Kyoto, Japan). Chromatographic separation was achieved on an end capped Phenomenex Luna C8 analytical column (150 × 4.6 mm i.d., 5 µm) with pore size 100 Å, maintained at 40°C at a flow-rate of 1 mL/ min. The mobile phase consisted of acetonitrile and 10mM ammonium acetate (30:70 isocratic), pH 6.6. For all samples, injection volume and run time were fixed as 50 µL and 15 min, respectively and the detection wavelength was at 235 & 240nm.

4.8. Pharmacology

4.8.1. Animals

Wistar rats of either sex (200–250g) were utilized for the neuropathic pain models were kept under a 12h/12 h light-dark cycle regimen, with free access to food and water. The Institutional Animal Ethics Committee approved all experiments. All the animals were acclimatized to the housing conditions for a period of one week before the start of experiments. For all experiments,

animal groups were divided into vehicle control, naïve, standard drug control and test drug groups were included for optimal comparison analysis, where each group comprised of five animals.

4.8.2. Chronic constriction injury (CCI) method

Chronic constriction nerve injury method was utilized to produce unilateral mononeuropathy in rats performed essentially as described by Bennett & Xiao [Bennett GJ., *et al.*, 1988]. The rats were anesthetized with an i.p. dose of ketamine (55 mg/kg) and xylazine (5 mg/kg) with additional doses of the anesthetic given if needed. Under aseptic conditions, a 2 cm incision was made on the lateral aspect of the left hind limb at the mid-thigh level. The left paraspinal muscles were then separated from the spinous processes and the common left sciatic nerve was exposed just above the trifurcation point. Four loose ligatures were made with a 4-0 braided silk suture around the sciatic nerve with about 1 mm spacing. The wound was then closed by suturing the muscle using chromic catgut with a continuous suture pattern. Finally, the skin was closed using silk thread with horizontal mattress suture pattern.

4.8.3. Drug administration

All the test compounds including synthesized compounds and standard drug GBP, were administered i.p. CCI rats. Test compounds injected were given in a volume of 1 ml per each animal. All the test compounds were dissolved in 0.5% carboxymethyl cellulose sodium salt (S D Fine-Chem Limited) as vehicle to get the desired dilution and volume range of doses of 30, 10 and 3 mg/kg. For the percentage change of locomotor activity studies, normal rats were administered with 100 mg/kg test drug dose in i.p.

4.8.4. Cold allodynia behavioral assessment

Unilateral mononeuropathy induced rats were assessed for acute cold allodynia (CA) sensitivity using the acetone drop application technique as described by Caudle et al. [Caudle RM., *et al.*, 2001]. The operated rat were placed inside an observation cage that was kept 5 cm from the ground level and were allowed to acclimatize for 10 min or until exploratory behavior ceased. A total number of five rats (n=5) were assigned to each group. Few drops (100-200 µL) of freshly dispensed acetone were squirted as a fine mist onto the mid plantar region of the affected paw. A cold allodynic response was assessed by noting down the duration of paw-withdrawal response. For each measurement, the paw was sampled three times and a mean was calculated. At least 3

minutes elapsed between each test. Paw withdrawal duration (PWD) of CCI rats were measured on both the ipsilateral (ligated) and contralateral (non-ligated as basal reading) paw prior to (pre-dose) and at several time points following compound or vehicle administration. Assessments were done after 30, 60 and 120 min of post injection of test compounds.

4.8.5. Mechanical hyperalgesia behavioral assessment

Mechanical paw withdrawal thresholds (PWT) were assessed with a slightly modified version of the Randall–Selitto method [Randall LO., et al., 1957] using analgesymeter (UGO Basile, Italy). The instrument exerted a force that increased at a constant rate. This force was applied to the hind paw of the rat, which was placed on a small plinth under a cone-shaped pusher with a rounded tip (1.5 mm in diameter) until the animal withdrew its paw. A cutoff of 250 g was used to avoid injury. Mechanical paw withdrawal thresholds were calculated as the average of two consecutive measurements. PWT of CCI rats were measured on both the ipsilateral (ligated) and contralateral (non-ligated as basal reading) paw prior to (pre-dose) and at several time points following compound or vehicle administration. Assessments were done after 30, 60 and 120 min of post injection of test compounds.

4.8.6. Tactile allodynia behavioral assessment

Tactile allodynia (TA) was assessed for the examination of the neuropathic pain state in rats by understanding PWT in response to mechanical stimuli as measured using calibrated Von Frey filaments [Eliav E., et al., 1999]. Animals were placed on a metallic grid floor covered with a plastic box giving access to the underside of their paws and allowed to acclimatize prior to the start of the experiment. A set of Von Frey monofilaments (0.4-15 g), with intensities of mechanical stimulation increasing in graded manner with successively greater diameter filaments, applied to the plantar surface of the hind paw five times at intervals of 1-2 s in the immediate vicinity. The lowest amount of force required to elicit a response was recorded as the PWT (in grams) and pattern of responses were tabulated using up down method of Dixon [Dixon WJ., et al., 1980]. Chaplan pain assessment statistical table was utilized to determine the 50% paw withdrawal threshold and was interpolated using the formula [Chaplan SR., et al., 1994]:

$$50\% \text{ g threshold} = (10^{[X_r + k\delta]})/10,000 \dots\dots\dots (12)$$

Where X_f was the value (in log units) of the final vonfrey hair used; k was tabular value [Chaplan SR., *et al.*, 1994] for the pattern of positive/negative responses; and δ was mean difference (in log units) between stimuli. 50% g threshold of initial reading (before administering the drug dose) was subtracted from the final reading (1 hour post administration) and finally compared with vehicle control (each group of animals $n=5$). Assessments are done after 30, 60 and 120 min of post injection of test compounds.

4.8.7. Locomotor activity assessment

Central nervous system depressant activity-locomotor activity was assessed to understand the percentage of neurotoxicity of the test compounds (100 mg/kg). In the experiment, rats were individually placed in an actophotometer for recording the activity score after 60 min of test drug administration. Rearing of locomotor activity of all synthesized compounds were recorded for 5 min using a digital locomotion detection system (actophotometer) equipped with photo sensor [Asakura W., *et al.*, 1993] and the percentage change in the activity was calculated.

4.8.8. RNA extraction and cDNA synthesis

Total RNA was extracted from the *in vivo* sample tissues of brain, spinal cord and sciatic nerve of vehicle treated, naïve, **GBP** treated and most active compound (**8-n**) treated groups each comprises of three animals. Tissue samples were collected between 60 to 120 minutes of post injection, where both **GBP** and **8-n** were given in a dose of 30 mg/kg. Total RNA was extracted using TRI reagent according to the protocol of the manufacturer (Sigma-Aldrich Co. LLC. USA). Concentrations and purity of RNA were quantified with Perkin Elmer VICTOR X3 (Perkin Elmer, Shelton, CT, USA) according to optical density. Purity of RNA was determined with A260/280 ratio (1.8–2.0 was considered pure).

cDNA synthesis of respective samples were acquired according to the Verso cDNA synthesis kit (Thermo Fisher Scientific Inc. USA) protocol. Equal amount of RNA (about 1 μ g) from the samples was suspended in 5 μ l of RNase-free water. RNA sample was further added to reaction mixture containing final volumes of 1X cDNA synthesis buffer, 500 μ M of dNTP Mix, 500 ng of Anchored Oligo-dT primers, 1 μ L of RT Enhancer (to remove contaminating DNA), Verso Enzyme Mix (includes Reverse transcriptase) and the final volume was adjusted with water (PCR grade). Reverse transcription cycling program was set at the temperature 42°C in 1 cycle of

30 min and at 95 °C for 2 min for reaction termination using MJ Mini Thermal Cycler (Bio-Rad Laboratories, Inc. USA.).

4.8.9. Real-time quantitative polymerase chain reaction

Real-time quantitative polymerase chain reaction (PCR) was performed with CFX CONNECT Real-Time System (Bio-Rad Laboratories, Inc.) in a 25 µl reaction mixture containing 10 µl KAPA SYBR FAST qPCR MasterMix Universal (Kapa Biosystems, Inc.), 1 µl of cDNA solution of all samples were diluted to attain 20 ng of final concentration, 200 nM final concentration of primer pairs, and volume was adjusted with water (PCR grade). All samples were run in triplicates. Rat forward (F) and reverse (R) primers were used for NFκB (gene accession number NM_199267.2) forward: 5'-CCTCTACACATAGCGGCTGG-3'; reverse: 5'-GCACCTTGGGATGCGTTTTT-3', for ERK1 (gene accession number NM_017347.2) forward: 5'-CACTGGCTTTCTGACCGAGT-3'; reverse: 5'-GTGATGCGCTTGTTTGGGTT-3', for IL-1β [Hagiwara N., *et al.*, 2005; Visnagri A., *et al.*, 2014] forward: 5'-ATAGCAGCTTTCGACAGTGAG-3'; reverse: 5'-GTCAACTATGTCCCGACCATT-3', for IL-6 [Huang Y., *et al.*, 2014] forward: 5'-GACTGATGTTGTTGACAGCCACTGC-3'; reverse: 5'-TAGCCACTCCTTCTGTGACTCTAACT-3', for TNF-α [Hagiwara N., *et al.*, 2005; Visnagri A., *et al.*, 2014] forward: 5'-CCACGTCGTAGCAAACCACCAAG-3'; reverse: 5'-CAGGTACATGGGTCATACC-3' and for GAPDH [Rantamäki T., *et al.*, 2013] forward: 5'-GGTGAAGGTCGGTGTGAACGG-3'; reverse: 5'-CATGTAGTTGAGGTCAATGAAGGG-3'. Primers for NFκB and ERK1 were designed using Primer Blast online tool (<http://www.ncbi.nlm.nih.gov/tools/primer-blast>) and remaining primers for IL-1β, IL-6, TNF-α and GAPDH were taken from recent published works [Hagiwara N., *et al.*, 2005; Visnagri A., *et al.*, 2014; Huang Y., *et al.*, 2014; Rantamäki T., *et al.*, 2013]. The thermal cycling conditions to run real time reaction was carried out with initial enzyme activation at 94 °C for 20 sec and 35 cycles of amplification with denaturation at 94°C for 15 sec, with 30 sec annealing at respective nearby temperatures (61°-69 °C) and 1 min extension at 72°C. All the PCR products from every sample were subjected to melting curve analysis (60–95 °C) for specificity. The amount of mRNA for all the target genes was normalized against the housekeeping gene GAPDH in the corresponding samples. Quantification of the samples was carried out with Sequence Detection CFX Manager 3.0 analysis software (Bio-Rad Laboratories, Inc.).

4.8.10. Western blotting analysis

The lumbosacral spinal cords of the rats were extracted and stored in liquid nitrogen. Tissue samples were homogenized in TRI Reagent (1 ml per 50–100 mg of tissue). Allowed the samples to stand for 5 min at room temperature and added 0.2 ml of chloroform at room temperature and later centrifuged to separate the mixture into 3 phases: a red organic phase (containing protein), an interphase (containing DNA), and a colorless upper aqueous phase (containing RNA). After separation of upper aqueous phase (RNA), remaining organic and interphases were mixed with 0.3 ml of 100% ethanol and centrifuged to get phenol-ethanol supernatant containing proteins (where pellet contained DNA) and later separated supernatant was added with 1.5 ml of 2-propanol and centrifuged to get protein pellet. All protein samples were dissolved in 1% SDS and concentrations were determined using the Bradford method and stored at -20 °C until use. Protein samples were dissolved in 5X sample buffer [Tris-HCl 0.2 μM, glycerol 20% v/v, DDT 10 mmol, 0.05% w/v bromo phenol blue, and 10% w/v sodium dodecyl sulfate (SDS), pH 6.8], and denatured at 95 °C for 5 min, then the equivalent amounts of proteins were separated by using 10% SDS-polyacrylamide gel electrophoresis (PAGE) and transferred onto a nitrocellulose membrane. The membranes were incubated overnight at 4 °C with mouse polyclonal anti-pERK primary antibody. The membranes were extensively washed with Tris-buffered saline Tween-20 (TBST) and incubated for 1 h with the secondary antibody conjugated with horse radish peroxidase (HRP) at room temperature. The immune complexes were detected by using an entry-level peroxidase substrate for enhanced chemiluminescence (ECL) kit (Thermo Scientific Pierce ECL Western Blotting substrate). The scanned images were imported into Image J software (<http://imagej.nih.gov/ij/index.html>) for band density was used for semi quantitative analysis and comparison of the test samples.

4.8.11. Brain slice preparation for *ex vivo* studies

Female wistar rats (200-250 g) were decapitated and brains were removed and submerged in ice-cold minimal essential medium (MEM). Each hemisphere of cerebral cortex was cut into coronal slice to attain approximate weight of 100mg and placed in 12-well p-lysine coated plate. Culture media consists of MEM with 10% fetal bovine serum, 100 μg/ml streptomycin and 100 U/ml penicillin. Slices were treated with 5 μg/ml Lipopolysaccharide (LPS) (Sigma-Aldrich Co. LLC. USA), **GBP** and **8-n** in combinations (LPS, LPS+**GBP**, LPS+**8-n**) and all are at 1μM individual concentration. All the combination of treatments incubated simultaneously for 3 hrs in a

humidified environment with 5% CO₂. Total number of three animals was utilized for the study and slices after test compound incubation were harvested to isolate total RNA using TRIzol reagent method explained in section 4.8.8. For cDNA synthesis and real-time quantitative polymerase chain reaction were performed with CFX CONNECT Real-Time System as explained in sections 4.8.8 and 4.8.9.

4.9. Statistical analysis

All the statistically compared pharmacological data were expressed as means \pm standard error of mean (SEM). The data were analyzed by one-way ANOVA in the case of neuropathic pain studies, statistical significance was determined for drug effects by Dunnett's multiple comparison post hoc test for individual comparisons with vehicle values. For gene expression studies, analyzed by a one-way ANOVA followed by post hoc Tukey's multiple range post hoc test. Significance was assigned to a p value of less than 0.05. The statistical software package PRISM 6 (Graphpad Software Inc., San Diego, CA) was used for the analysis.

CHAPTER 5

Lead identification: Drug design and biological evaluation

CHAPTER 5

Lead identification: Drug design and biological evaluation

Knowledge based drug discovery methods have been enduring in current times to understand theoretical predictions and to develop specific drug design strategy. To acquire favorable results, knowledge based CADD methods were followed for the current work, which are in two general categories: ligand-based and structure-based drug design methods. As the primary objective of current work is to design novel, non-peptidic, non-covalent CatS inhibitors, the CADD methodologies were employed to grab promising novel drug analogues.

Ligand-based drug design exploits the knowledge of known active and inactive molecules through chemical similarity searches and utilizes for the generation of pharmacophores, which possess median features of all the known active molecules. Further validation of pharmacophores with general validation methods and 3D QSAR mapping, gives the verdict to finalize the best pharmacophore hypothesis with high predictive molecular searching capacity. Construction and external statistical validations of 3D QSAR models gives range of predictions to proceed further in generation of structure activity relationships of particular novel molecules.

Structure-based drug design relies on the knowledge of the target protein structure to calculate interaction energies between the ligand molecule and the protein active site by utilizing high-resolution crystallized structural data. In current work, co-crystallized molecules in the active site were subjected to re-interact with the protein active site virtually, by retaining its original poses, with the help of docking based methods. Real time generation of energy descriptors while docking were utilized to recognize important interaction energies, which are responsible for binding interaction. Moreover, Pharmacophore hypothesis generation based on important interaction energies is a fruitful strategy to attain novel chemical analogues with a property of protein active site favored interactions.

Lead molecules obtained from the lead identification strategies using ligand based and structure based drug design methods, were further experimentally evaluated with *in vitro* enzymatic assays for estimating CatS inhibitory activity. Molecules with high enzymatic inhibitory activity were

screened for the cytotoxicity assays on glioblastoma cell lines to assess anti microglial cancer activity. Molecule, which displays good enzyme inhibition and anti-microglial cancer cell viability, were considered as final lead molecule.

5.1. Ligand based drug design

Ligand based drug design strategy is completely a chemoinformatics drug design strategy. Where, chemoinformatics provided a forum for the necessary dialogue between theoretical sciences, and experimental chemistry and biology. While, in current drug discovery we followed ligand based pharmacophore mapping methods for the generation of novel CatS inhibitors. A pharmacophore is an abstraction of the crucial features responsible for the binding of ligands to a binding site, which is typically (part of) a biological macromolecule [Farnum MA., *et al.*, 2003]. For pharmacophore-based drug design, initial step started with a collection of several compounds that were known to bind to a particular receptor (Figure 5.1). Next step would be the generation of pharmacophore by understanding the key structural features, which could be involved in biological activity. Among the generated pharmacophore hypotheses, to select the best hypothesis model, there is a need to undergo validation procedures. After internal, external decoy set validation and the 3D QSAR mapping analysis, the hypothesis, which can satisfy all the validation parameters, could be finalized for the database screening. Generated pharmacophore can then be used to generate a query, which in turn can be applied to search drug-like compound database. The pharmacophore further could be involved in the applications virtual screening and structure-based combinatorial library design, as well as 3D QSAR predictive activity analysis.

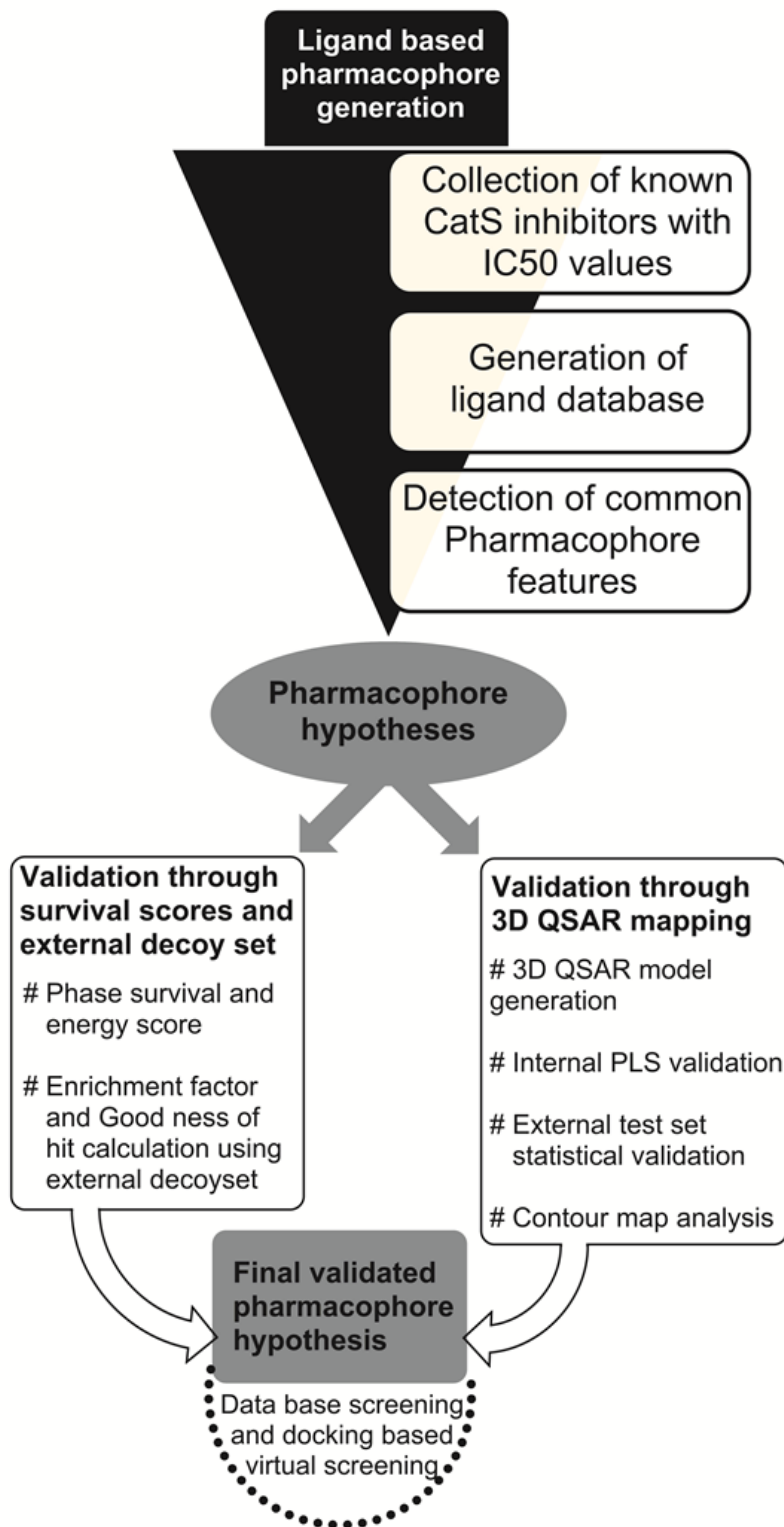


Figure 5.1 Schematic workflow of ligand based pharmacophore generation and validation

5.1.1. Determination of pharmacophore and validation

Several reported CatS inhibitor ligands ranging from 10 μM to 0.2 nM with diverse structural groups were collected and sorted to make a dataset for the generation of pharmacophore. Whole data set of 161 molecules was divided into active, moderately active and inactive sets to find the common pharmacophores. Molecules with pIC_{50} values higher than or equal to 9.5 were considered active and those with pIC_{50} values less than 5.0 were considered inactive. Whereas, pIC_{50} values in-between active and inactive were considered moderately active.

Twenty three hypotheses survived to the different phases of scoring procedure (survival, survival inactive, post-hoc) and we selected five best hypotheses based on good scores and those that satisfied the internal parameters (survival activity, vector, volume, energy scores, most active molecule alignment and number of matches) (Table 5.1). The five best hypotheses (Table 5.1 & 5.2) were subjected for validation using decoy set database, which included 60 known active CatS inhibitors and 990 compounds with unknown activity for CatS enzyme. Hypothesis 1, a five point model (AAADH. 1, Figure 5.2) containing three hydrogen bond acceptors (A), one hydrogen bond donor (D), and one hydrophobic group (H) displayed good EF, GH (using equations 1,2 described in Chapter 4) and satisfied all other validation parameters of a true pharmacophore model (Table 5.2). Number of hits (H_i) obtained with this model was 148 compounds accounting for 34.45% as total active yields (%Y) and 85% of actives were retrieved in the hit lists (%A) (Table 5.2). From the overall validations, we were assured that hypothesis 1 could predict most of the experimentally active kind of molecules than the remaining four comparable hypotheses. Molecules used in building of common pharmacophores with their structural representation are given in in Tables 5.3 to 5.20.

Table 5.1 Selected best pharmacophore hypotheses and their internal scores

ID	Survival active	Survival inactive	Site [†]	Vector [§]	Volume ^{\$}	Selectivity [#]	Matches [¥]	Energy [¢]
AAADH.1	2.705	1.202	0.51	0.855	0.342	1.352	6	0.798
AAADH.2	2.793	1.305	0.48	0.855	0.459	1.336	6	7.799
AAADH.3	2.604	1.088	0.42	0.837	0.352	1.369	6	0
AAADH.4	2.664	1.281	0.44	0.889	0.332	1.312	6	2.771
AAAH.5	2.512	1.296	0.36	0.772	0.379	1.638	6	2.469

† Site score range from 0.0 to 1.0

§ Vector score range from -1.0 to 1.0

\$ Volume score range from 0.0 to 1.0

Selectivity score range from 0.0 to ∞

¥ Number of actives that match the hypothesis.

¢ Reference ligand relative conformational energy 0.0 to ∞

Table 5.2 Pharmacophore statistical validation for top 5 hypotheses

Top 5 Hypotheses	AAADH. 1	AAADH. 2	AAADH. 3	AAADH. 4	AAAHH. 5
H_t [#]	148	203	188	215	95
H_a ^{\$}	51	51	51	50	29
%Y [¥]	34.46	25.12	27.13	23.26	30.53
%A [§]	85	85	85	83.33	48.33
EF [†]	6.04 [*]	4.40	4.76	4.08	5.35
Fn [‡]	9	9	9	10	31
Fp	97	152	137	164	66
GH [£]	0.42 [*]	0.33	0.35	0.31	0.32

Total number of hit molecules from the database; \$ Total number of active molecules in hit list; ¥ % yield of actives [$(H_a/H_t) \times 100$]; § % Ratio of actives [$(H_a/A) \times 100$]; † Enrichment Factor; ‡ False negatives [$A - H_a$]; || False Positives [$H_t - H_a$]; £ Goodness of fit score; * best EF and GH scores among five hypothesis

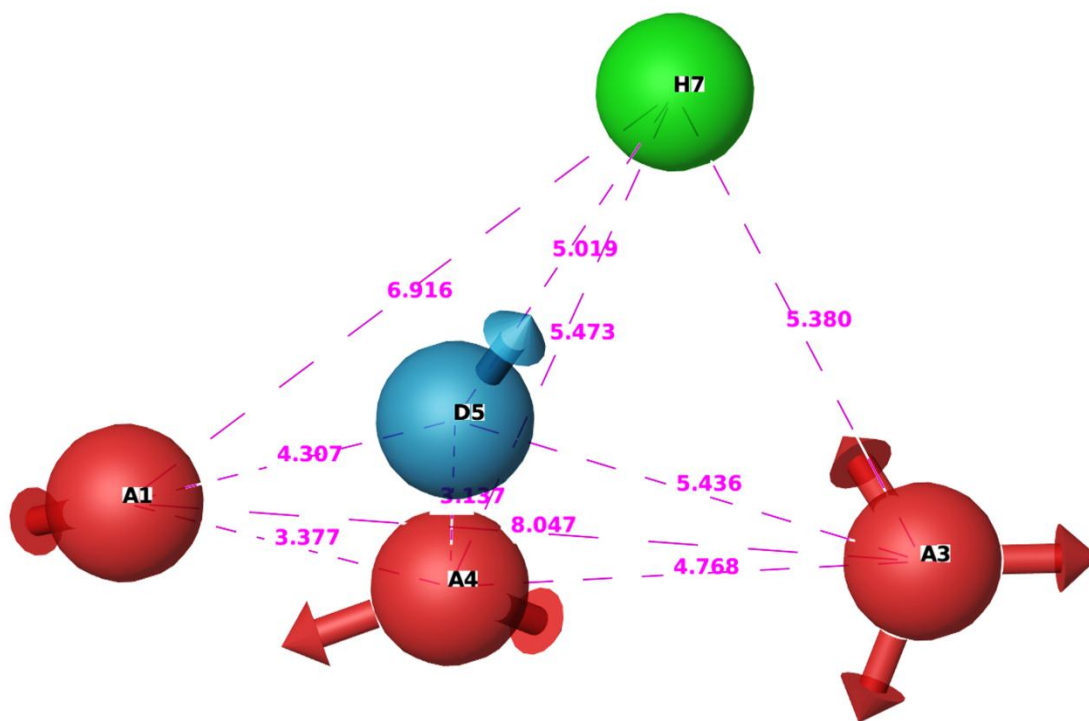
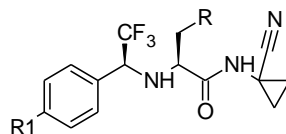


Figure 5.2 Pharmacophore hypothesis (Hypothesis 1) and distance between the pharmacophoric sites are in pink dotted lines. All the distances are in Å unit.

All the five-pharmacophore hypotheses were further validated for the best QSAR predictability by generating pharmacophore based 3D QSAR models and subjected to PLS analysis. Since, our purpose was to generate a common 3D QSAR map for the most active structurally diverse compounds; therefore, we chose the method of pharmacophore-based 3D QSAR development instead of atom-based method. The difference between atom and pharmacophore based 3D QSAR was based on all atoms would be taken into account, or the pharmacophoric sites would be matched to the entire ligand alignment pattern respectively. Indeed, the dataset structures were quite divergent, with many rotatable bonds; thus, we adopted pharmacophore-based 3D QSAR model. If the ligand structures had relatively small number of rotatable bonds and with some common structural framework, then, an atom-based model would work quite well [Dixon SL., et al., 2006]. Moreover, it was found that the major structural factors affecting the potency of most active compounds (used for pharmacophore development) were related to their basic scaffold where it was mapped with the respective features. For the generation of 3D QSAR model data set of known CatS inhibitor compounds (Used for the Pharmacophore generation) was split into training and test sets (Tables 5.3-5.20). 3D Alignment of data set molecules was assessed with statistical validation methods, where the shift of test and training set positions leads to the proper alignment of molecules. All the data set molecules used for pharmacophore generation and 3D QSAR study are given in Tables 5.3 to 5.20 with their structural information, experimental and predicted biological activity and dataset positions.

Table 5.3 Trifluoroethylamine compounds for 3D QSAR study and their experimental and predicted biological activity [Gauthier JY., *et al.*, 2007]

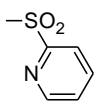
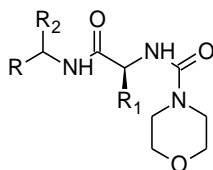
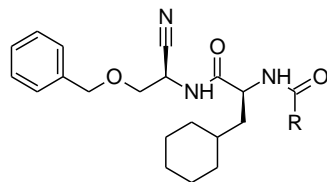
Comp. No	R	R ₁	pIC ₅₀ Experimental	pIC ₅₀ Predicted	Residual	Data set
1	-SO ₂ (3-Br)Ph	H	9.698	9.61	-0.088	training
2	-SCH ₃	Br	7.096	7.25	0.153	training
3	-SO ₂ CH ₃	(4-F)Ph	8	8.23	0.23	training
4	-SO ₂ CH ₃	F	8.744	8.46	-0.284	training
5	-SO ₂ CH ₃	3-F	8.193	8.58	0.386	test
6	-SO ₂ CH ₃	H	8.602	8.24	-0.362	test
7	-SO ₂ CH ₂ CH(CH ₃) ₂	F	9.397	9.03	-0.367	test
8	-SO ₂ CH ₂ -cyclopropyl	H	9.221	9.29	0.068	training
9	-SO ₂ CH ₂ (2,3-F)Ph	H	9.522	8.17	-1.352	test
10	-SO ₂ CH ₂ (2,3-F)Ph	F	9.522	8.16	-1.362	test
11	-SO ₂ CH ₂ (2,3-Cl)Ph	F	9.154	8.3	-0.854	test
12	-SO ₂ CH ₂ biPh	F	8.744	9.22	0.475	test
13	-SO ₂ 2-thiazolyl	H	8.301	8.64	0.338	test
14	-SO ₂ 2-benzothiazolyl	H	8.886	9.07	0.183	test
15	-SO ₂ (3,4-Cl)Ph	H	9.698	9.58	-0.118	training
16	-SO ₂ (3,4-Cl)Ph	H	9.698	9.19	-0.508	test
17		F	7	7.76	0.76	test

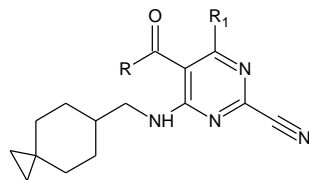
Table 5.4 Dipeptide nitriles with morpholine moiety for 3D QSAR study and their experimental and predicted biological activity [Ward YD., *et al.*, 2002; Asaad N., *et al.*, 2009]

Comp. No	R	R ₁	R ₂	pIC ₅₀ Experimental	pIC ₅₀ Predicted	Residual	Data set
18	n-Bu	i-Bu	····≡N	7.251	7.35	0.098	Training
19	CH ₂ OCH ₂ Ph	i-Bu	····≡N	7.721	7.62	-0.101	Training
20	CH ₂ OCH ₂ (o-Cl)Ph	i-Bu	····≡N	8.045	7.01	-1.035	Test
21	CH ₂ OCH ₂ Ph	i-Bu	····≡N	8.045	8.13	0.084	Training
22	CH ₂ CH ₂ Ph	CH ₂ Ph	←≡N	6.761	6.74	-0.021	Training
23	CH ₂ CH ₂ Ph	CH ₂ ^t -Bu	←≡N	7.638	7.61	-0.028	Training
24	CH ₂ CH ₂ Ph	CH ₂ ^c -Hex	←≡N	8.301	8.42	0.118	Test
25	CH ₂ CH ₂ Ph	i-Bu	←≡N	7.638	8.22	0.581	Test
26	CH ₂ CH ₂ Ph	c-Hex	←≡N	8.301	8.08	-0.221	Test
27	CH ₂ OCH ₂ Ph	i-Pr	←≡N	7.721	7.61	-0.111	Training
28	CH ₂ OCH ₂ Ph	i-Bu	←≡N	8.096	8.05	-0.046	Training
29	CH ₂ OCH ₂ Ph	c-Hex	····≡N	8.221	7.65	-0.571	Test
30	CH ₂ OCH ₂ (o-Me)Ph	i-Pr	←≡N	7.721	7.62	-0.101	Training
31	CH ₂ OCH ₂ (o-Me)Ph	i-Bu	←≡N	7.920	7.85	-0.070	Test
32	CH ₂ OCH ₂ (o-Me)Ph	c-Hex	····≡N	8.154	8.14	-0.014	Training
33	CH ₂ OCH ₂ (o-Cl)Ph	i-Pr	←≡N	8.045	7.23	-0.815	Test
34	CH ₂ OCH ₂ (o-Cl)Ph	c-Hex	····≡N	8.096	8.65	0.553	Test
35	c-Hex	c-Hex	····≡N	8.045	7.87	-0.175	Training
36	2Me	c-Hex	CN	7.769	7.71	-0.059	Training
37	CH ₂ OCH ₂ Ph	i-Bu	····≡N	8.045	6.83	-1.215	Test
38	=N-NHCOPh	i-Pr	····-CH ₂ Ph	7.958	7.97	0.011	Training
39	CH ₂ SSPh	i-Pr	····-CH ₂ Ph	5.346	5.41	0.063	Training
40	=N-NHCOPh	i-Pr	←-CH ₂ Ph	7.958	7.99	0.031	Training
41	←-CH ₂ Ph	i-Pr	CO	8	7.98	-0.02	Training
42	=N-NHCOPh(p-OH)	i-Pr	←-CH ₂ Ph	8.154	7.42	-0.734	Test
43	=N-NHCOPh(o-OH)	i-Pr	←-CH ₂ Ph	7.455	7.48	0.024	Training
44	-NHNHCOPh	i-Pr	←-CH ₂ Ph	6.247	6.85	0.602	Test

Table 5.5 Dipeptide nitrile compounds for 3D QSAR study and their experimental and predicted biological activity [Ward YD., *et al.*, 2002; Asaad N., *et al.*, 2009]

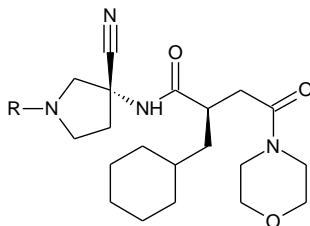


Comp. NO	R	pIC ₅₀ Experimental	pIC ₅₀ Predicted	Residual	Data set
45	Morpholin-2-yl	8.221	7.53	-0.691	Test
46	Pyridine-2-yl	8.221	8.04	-0.181	Test
47	Furan-2-yl	7.677	7.49	-0.187	Training
48	Thein-2-yl	8.301	8.31	0.008	Training
49	Pyrazinyl	8.045	7.39	-0.655	Test

Table 5.6 Cyanopyrimidine compounds for 3D QSAR study and their experimental and predicted biological activity [Irie O., *et al.*, 2008b]

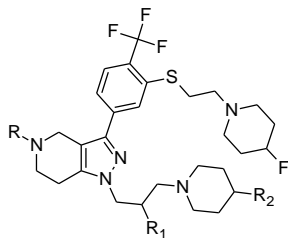
Comp. NO	R	R ₁	pIC ₅₀ Experimental	pIC ₅₀ Predicted	Residual	Data set
50		-	7.638	7.55	-0.088	Training
51		-	9	8.17	-0.83	Test
52		-	7.677	7.87	0.192	Training
53	-NHCH ₂ Ph		9	9.01	0.01	Training
54	-NHCH ₂ Ph		9.045	9.18	0.134	Training
55	-NHCH ₂ CH ₂ Ph		9.045	8.62	-0.425	Test

Table 5.7 Succinyl-nitrile compounds for 3D QSAR study and their experimental and predicted biological activity [Bekkali Y., *et al.*, 2007]

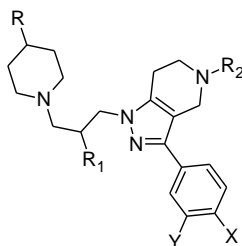


Comp. NO	R	pIC ₅₀ Experimental	pIC ₅₀ Predicted	Residual	Data set
56	Cyclopentyl	7.116	6.7	-0.416	Test
57	CH ₂ c-Hex	7.221	7.62	0.398	Test
58	Cycloheptyl	7.537	7.65	0.112	Training
59	CH ₂ Ph	7.522	7.05	-0.472	Test
60	CH ₂ CH ₂ Ph	7.651	6.73	-0.921	Test

Table 5.9 Tetrahydropyrido-pyrazole thioether amine compounds for 3D QSAR study and their experimental and predicted biological activity [JM Wiener J., *et al.*, 2010]



Comp. NO	R	R ₁	R ₂	pIC ₅₀ Experimental	pIC ₅₀ Predicted	Residual	Data set
64	-SO ₂ CH ₃	-OH		8	8.07	0.07	Training
65	-SO ₂ CH ₃	-OH	-	6.826	6.78	-0.046	Training
66	-SO ₂ CH ₃	-OH	-	7.236	7.13	-0.106	Training
67	-	-OH	-	5.017	5	-0.017	Training
68	CH ₃	-OH	-	5.045	4.97	-0.075	Training
69	-COCH ₂ NH ₂	-OH	-	6.091	6.02	-0.071	Training

Table 5.10 Ketobenzimidazole compounds for 3D QSAR study and their experimental and predicted biological activity [Gustin DJ., *et al.*, 2005]

Comp. NO	R	R ₁	R ₂	X	Y	pIC ₅₀ Experimental	pIC ₅₀ Predicted	Residual	Data set
70		...OH	-CONH ₂	Br	-	7.096	7.37	0.273	Test
71		...OH	-CONH ₂	CF ₃	-	7	6.91	-0.09	Test
72		←OH	-COCH ₃	Br	-	6.920	6.91	-0.010	Training
73		←OH	-COCH ₃	Br	-	6.958	6.95	-0.008	Training
74		←OH	-COCH ₃	Br	-	7.045	7.08	0.034	Test
75		-	-SO ₂ CH ₃	Cl	Cl	8	8.07	0.07	Training
76		-	-SO ₂ CH ₃	CF ₃	-	7.522	7.57	0.047	Training

Continued...

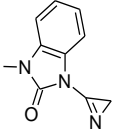
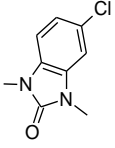
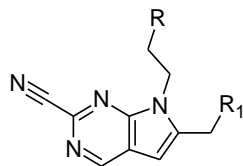
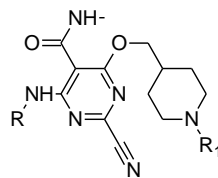
77		-	-SO ₂ CH ₃	CF ₃	-	7	6.94	-0.06	Training
78		-	-SO ₂ CH ₃	Cl	Cl	6.823	6.85	0.026	Training

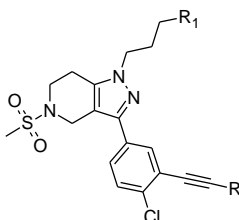
Table 5.11 Pyrrolopyrimidine compounds for 3D QSAR study and their experimental and predicted biological activity [Irie O., *et al.*, 2008a]

Comp. NO	R	R ₁	pIC ₅₀ Experimental	pIC ₅₀ Predicted	Residual	Data set
79	Ph	(p-Cl)Ph	7.193	7.26	0.066	Training
80			7.283	6.51	-0.773	Test
81			8	7.92	-0.08	Training
82			8.045	8.05	0.004	Training

Table 5.12 Cyanopyrimidine compounds for 3D QSAR study and their experimental and predicted biological activity [Irie O., *et al.*, 2008a]



Comp. NO	R	R ₁	pIC ₅₀	pIC ₅₀	Residual	Data set
			Experimental	Predicted		
83		CH ₃	8.522	8.72	0.197	Test
84		CH ₃	6	5.99	-0.01	Training
85		COCH ₃	8	8.04	0.04	Training

Table 5.13 Arylalkyne compounds for 3D QSAR study and their experimental and predicted biological activity [Ameriks MK., *et al.*, 2009]

Comp. NO	R	R ₁	pIC ₅₀ Experimental	pIC ₅₀ Predicted	Residual	Data set
86	c-Hex		5.173	5.14	-0.033	Training
87	Ph		6.214	6.21	-0.004	Training
88	H		5.130	5.22	0.089	Training
89	(1-Me)Ph		5.958	6.27	0.311	Test
90	(m-OH)Ph		6.124	6.13	0.005	training
91	(m,o-OH)Ph		6.036	6.24	0.203	test
92	CH ₂ CH ₂ OH		5.151	5.24	0.088	training
93	CH ₂ NHSO ₂ Ph		5.882	7.42	1.537	test
94			7.221	7.24	0.018	training
95			6.187	6.74	0.552	test
96			7.397	7.35	-0.047	training
97			7.522	7.52	-0.002	training
98			7.522	7.49	-0.032	training

Continued...

Lead identification

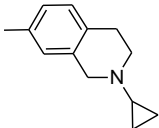
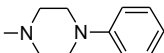
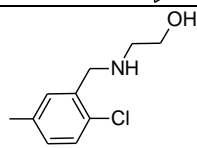
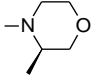
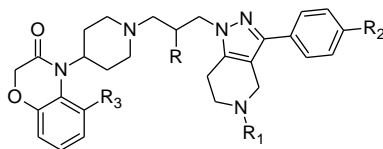
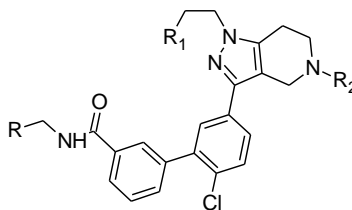
99			7.397	7.41	0.012	training
100			7.301	7.25	-0.051	training

Table 5.14 Bicyclic piperidine compounds for 3D QSAR study and their experimental and predicted biological activity [Grice C., *et al.*, 2006]

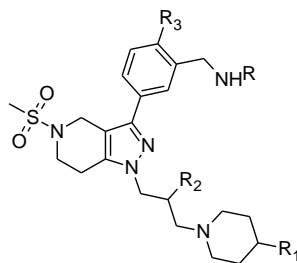


Comp. NO	R	R ₁	R ₂	R ₃	pIC ₅₀ Experimental	pIC ₅₀ Predicted	Residual	Data set
101	OH	H	CF ₃	H	5.715	5.72	0.004	training
102	H	H	CF ₃	H	7	6.92	-0.08	training
103	H	-SO ₂ CH ₃	CBr ₃	H	7.221	7.11	-0.111	training
104	H	-SO ₂ CH ₃	CBr ₃	CH ₃	6.769	6.75	-0.019	test

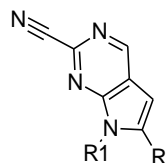
Table 5.15 Tetrahydropyrido pyrazole compounds for 3D QSAR study and their experimental and predicted biological activity [Allen D., *et al.*, 2008b]



Comp. NO	R	R ₁	R ₂	pIC ₅₀ Experimental	pIC ₅₀ Predicted	Residual	Data set
105			-SO ₂ CH ₃	6.145	6.12	-0.025	training
106			-SO ₂ CH ₃	7.387	7.43	0.042	training
107			H	7.337	7.31	-0.027	training
108			H	7.091	7.22	0.128	Test

Table 5.16 N-sulphonyl tetrahydropyridopyrazole compounds for 3D QSAR study and their experimental and predicted biological activity [Allen D., *et al.*, 2008a]

Comp. NO	R	R ₁	R ₂	R ₃	pIC ₅₀ Experimental	pIC ₅₀ Predicted	Residual	Data set
109			...OH	CF ₃	5.769	6.75	0.980	test
110			H	CF ₃	5.598	7.04	1.441	test
111		(m-Cl)Ph	H	Cl	6.119	7.08	0.960	test
112			...OH	CF ₃	7.522	7.49	-0.032	training
113		c-Hex	H	CF ₃	7.698	7.79	0.091	training

Table 5.17 Pyrimidopyrrolo nitrile compounds for 3D QSAR study and their experimental and predicted biological activity [Bailey A., *et al.*, 2003]

Comp. NO	R	R ₁	pIC ₅₀ Experimental	pIC ₅₀ Predicted	Residual	Data set
114		CH ₂ t-Bu	7	7.25	0.25	test
115		CH ₂ t-Bu	7	6.93	-0.07	training
116		CH ₂ t-Bu	7	6.93	-0.07	training
117		CH ₂ t-Bu	7	7.33	0.33	test
118		CH ₂ t-Bu	7.008	7.48	0.471	test
119		CH ₂ t-Bu	7.008	6.99	-0.018	training

Continued...

Lead identification

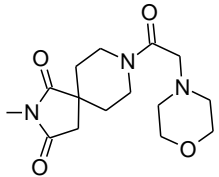
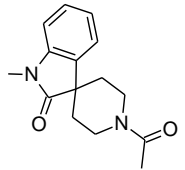
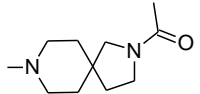
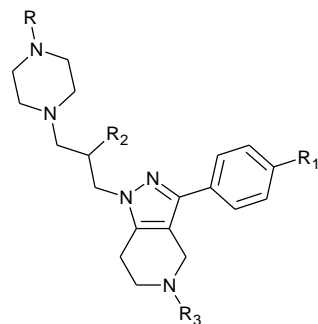
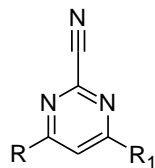
120		CH ₂ t-Bu	7.013	7.1	0.086	test
121		CH ₂ CH ₂ t-Bu	8	7.96	-0.04	training
122		CH ₂ CH ₂ c-Hex	7.346	7.47	0.123	training

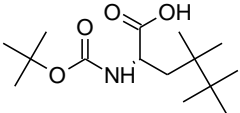
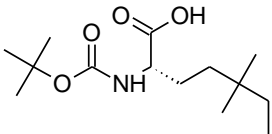
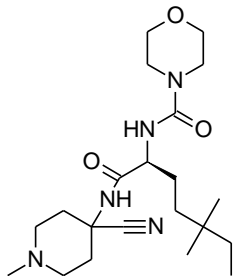
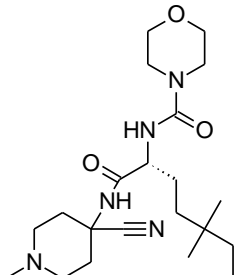
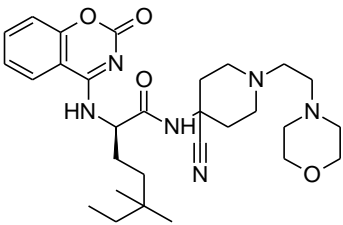
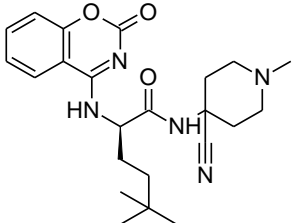
Table 5.18 N-substituted tetrahydropyrido pyrazole compounds for 3D QSAR study and their experimental and predicted biological activity [Beavers MP., *et al.*, 2007]

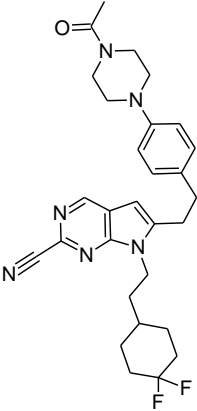
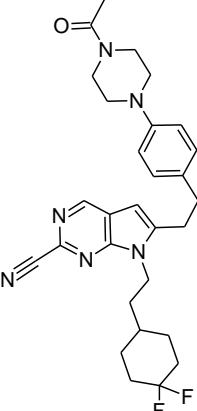
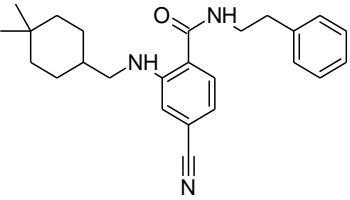
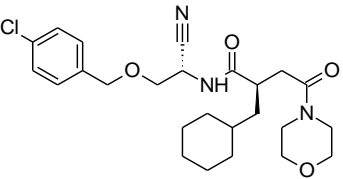
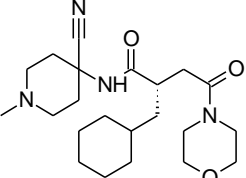
Comp. NO	R	R ₁	R ₂	R ₃	pIC ₅₀ Experimental	pIC ₅₀ Predicted	Residual	Data set
123	(2-CN)Ph	CF ₃	OH	COCH ₃	6.522	6.48	-0.042	training
124	(2-Me)Ph	CF ₃		COCH ₃	6.050	6.07	0.019	training
125	(2-NO ₂)Ph	CF ₃	H	SO ₂ CH ₃	7.221	7.28	0.058	training
126	(2-NH ₂ ,6-Cl)Ph	CF ₃	OH	SO ₂ CH ₃	7.154	7.1	-0.054	training
127		Br	H	CONH ₂	7	6.96	-0.04	training

Table 5.19 Pyrimido nitriles compounds for 3D QSAR study and their experimental and predicted biological activity [Rankovic Z., et al.,2008]

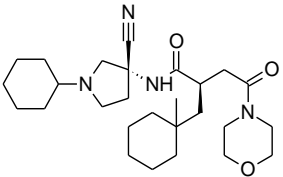
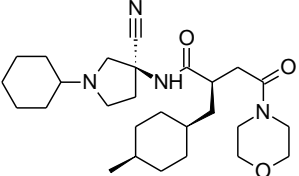
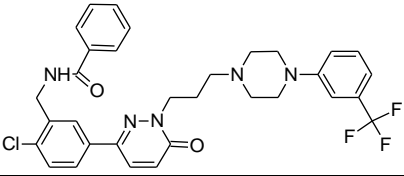
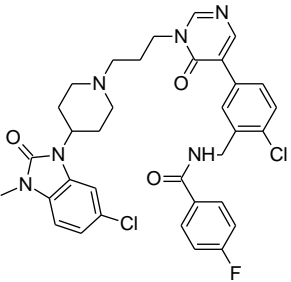
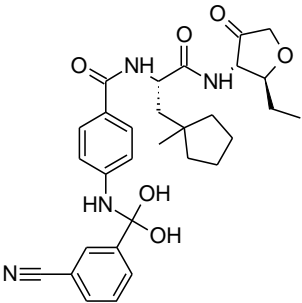
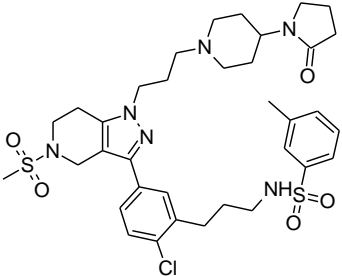
Comp. NO	R	R ₁	pIC ₅₀ Experimental	pIC ₅₀ Predicted	Residual	Data set
128	(2-CF ₃)Ph		7	6.91	-0.09	training
129	(2-CF ₃)Ph	NHCH ₂ CH ₂ OH	7	6.67	-0.33	test
130	(2-CF ₃)Ph	NHCH ₂ CH ₃	7	6.68	-0.32	
131	(2-CF ₃)Ph		6	6.16	0.159	training
132	(3-OCH ₃ ,2-CF ₃)Ph		6	6.88	0.879	test
133	(2-CF ₃)Ph		7	7.04	0.04	training

Table 5.20 Various CatS inhibitors from research and patent literature used for 3D QSAR study and their experimental and predicted biological activity [Bekkali Y., *et al.*, 2003; Hickey ER., *et al.*, 2006; Ameriks MK., *et al.*, 2008; Bekkali Y., *et al.*, 2007]

Comp. NO	Structure	pIC ₅₀ Experimental	pIC ₅₀ Predicted	Residual	Data set
134		7	7.17	0.17	Test
135		7	6.77	-0.23	Test
136		7.045	7.04	-0.005	training
137		7.045	7.18	0.134	Test
138		7.055	7.15	0.094	Test
139		7.075	7.21	0.134	training

140		8	8	0	training
141		7.22	6	1.22	Test
142		7.1	7.031	0.068	training
143		7.207	7.34	0.132	Test
144		6.347	6.4	0.052	training

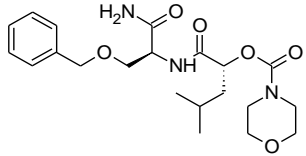
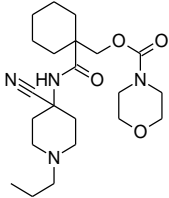
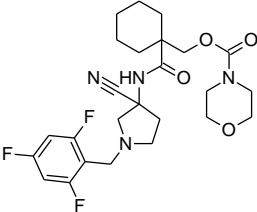
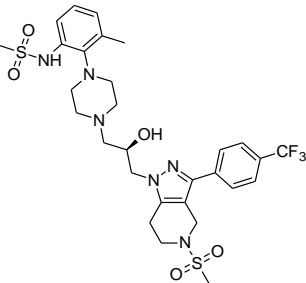
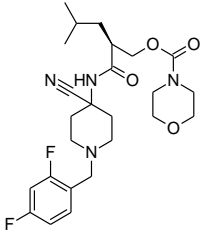
Continued...

145		7.263	7.09	-0.173	training
146		7.809	8.12	0.310	Test
147		5.795	7.32	1.524	Test
148		7.397	7.36	-0.037	training
149		5.853	6.71	0.856	Test
150		5.610	6.74	1.129	Test

Continued...

151		5.610	6.74	1.129	Test
152		5.772	5.72	-0.052	training
153		7.096	7.19	0.093	training
154		6.602	6.63	0.027	training
155		7.096	7.3	0.203	Test
156		8	7.92	-0.08	training

Continued...

157		5	4.86	-0.14	training
158		5.004	5.08	0.075	training
159		5.004	4.84	-0.164	training
160		6.886	7.02	0.133	training
161		5	5.2	0.2	training

5.1.2. 3D QSAR model generation and PLS analysis

Data set of known CatS inhibitor compounds was split into training and test sets, where the shift of test and training set positions leads to the proper alignment of molecules. Generated 3D QSAR model simultaneously generates predicted pIC_{50} values for each compound that involved in model building, their predicted pIC_{50} values and training and test set allocation was presented in tables 5.3 to 5.20. To develop superlative QSAR models, which were meant to exhibit reliable predictions both in internal and external statistical validation became mandatory as models that were capable of fulfilling various statistical validation parameter boundaries, could display more reliable predictions [Li Y., *et al.*, 2010]. Internal statistical validation by PLS analysis conferred important parameters as shown in Table 5.21, obtained through LOO method. In fact, LOO-cross validated value of training set (R^2) was expected to be greater than 0.6, LOO-cross validated value for test set (Q^2) should show a value greater than 0.55 to attain good predictive capacity, and standard deviation (SD) to be below 0.3, with a minimum value of root mean square error (RMSE), and a high value of variance ratio (F) which would provide conventional QSAR validation limits.

In our study, the predictive correlation coefficient (r_{pred}^2) value generated based on molecules of test set demonstrated real predictive capacity and robustness of QSAR model [Roy P., *et al.*, 2008]. Among the best five models, hypothesis 1 showed effective external predictive ability for each combination as compared to others. Hypothesis 1 showed a good R^2 value for the training set of 0.970, good predictive power with Q^2 of 0.633, with a lowest SD of 0.096, and a high F value of 2243. Further, the integrity of the model 1 was predicted by r_{pred}^2 for test set with a satisfactory value of 0.64 (Table 5.21).

Table 5.21 PLS internal validation of best five hypotheses, evolved after 3D QSAR model building.

PLS statistics (LOO)	AAADH. 1	AAADH. 2	AAADH. 3	AAADH. 4	AAAHH. 5
SD	0.0965	0.1187	0.089	0.1673	0.0881
R²	0.9919	0.9877	0.9931	0.9756	0.9932
F	2243.6	1478.2	2639.5	735	2695.9
r_{pred}²	0.637576	0.52244	0.54678	0.42789	0.4996
RMSE	0.682	0.7545	0.7575	0.8552	1.0871
Q²	0.6072	0.5193	0.5155	0.3825	0.0022
Pearson-R	0.7853	0.7318	0.7319	0.6312	0.2701

PLS statistic parameters: SD standard deviation of the regression, R² for the regression, F variance ratio, r_{pred}² predictive correlation coefficient value, RMSE root mean square error. Q-squared (Q²) value of Q² for the predicted activities. Pearson R correlation between the predicted and observed activity for the test set.

5.1.3. Analysis of external statistical validation

For a QSAR model, internal validation of LOO-cross-validated Q^2 was commonly used to assess predictive ability, where a high value of Q^2 was necessary but not sufficient to make a model with a high predictive ability. A reliable model should also be characterized by a high correlation coefficient R (or r^2) between the predicted and observed activities of compounds from an external test set [Golbraikh A., *et al.*, 2002]. Based on this postulation, our built QSAR model 1 (Pharmacophore hypothesis 1) was tested for external validation parameters where it gave an excellent r_{cv}^2 value of 0.991 (Table 5.22). The best predictive ability of the model was also revealed by correlation coefficient R of 0.92 ($r^2 = 0.84$) being near to 1. High slope of regression lines through the origin k value of 0.997 and k' value of 0.999 (either k or k' should be close to 1) gave substantial values of R_0^2 value 0.9996 and the $R'_0{}^2$ value 0.9995, which were obtained by calculating correlation coefficient of regression lines of the scatter plot obtained by means of actual activity versus predicted activity and vice versa (Figure 5.3). Scatter plots with respective best fit lines of predicted vs actual pIC50 for training and test set are shown in Figure 5.3. The calculated relation between r^2 , R_0^2 and $R'_0{}^2$ gave $(r^2 - R_0^2 / r^2)$ values of -0.18 and second relation $(r^2 - R'_0{}^2 / r^2)$ value -0.189 indicating optimum values within the statistical limits (Table 5.22). A parameter of modified r^2 (r_m^2) considered as a better external predictive potential for the whole set of compounds was found to be 0.53 (>0.5 optimal) defined through scatter plot best fit line values (Figure 5.3). The developed models were further validated by the process of randomization techniques where the values of R_f^2 (0.322) and R^2 were determined and were used for calculating the value of R_p^2 which was 0.812 (>0.5). Thus, the 3D QSAR model 1 (Hypothesis 1) emerged as a true predictive, statistically robust and highly accommodating model which fulfilling the requirements of various parameters in the external statistical validation (Table 5.22). Hence, the hypothesis 1 with three hydrogen bond acceptors (A), one hydrogen bond donor (D) and one hydrophobic (H) feature was retained for further design studies. Illustration of hypothesis 1 and the distance between the pharmacophoric features are depicted in Figure 5.2. All 161 diverse compounds alignment during the 3D QSAR model building with test and training set alignment is depicted in the Figure 5.4.

Table 5.22 External statistical validation results of 3D QSAR model for the Hypothesis 1 (AAADH. 1).

Validation parameter [§]	Parameter calculated	Limitations
r_{cv}^2	0.992	$r_{cv}^2 > 0.5$
R	0.920	Must close to 1
r^2	0.840	$r^2 > 0.6$
k value	0.9975	$0.85 \leq k \leq 1.15$
k' value	0.9990	$0.85 \leq k' \leq 1.15$
R_0^2	0.9996	R_0^2 or $R_0'^2$ close to r^2
$R_0'^2$	0.9995	R_0^2 or $R_0'^2$ close to r^2
$[(r^2 - R_0^2) / r^2]$	-0.1892	$[(r^2 - R_0^2) / r^2] < 0.1$
$[(r^2 - R_0'^2) / r^2]$	-0.1895	$[(r^2 - R_0'^2) / r^2] < 0.1$
r_m^2	0.530	$r_m^2 > 0.5$
R_p^2	0.812	$R_p^2 > 0.5$

[§] r_{cv}^2 is a cross validated coefficient. **R** (or r^2) is a correlation coefficient between the actual and predicted activities. **k** and **k'** are the slope values of regression lines. R_0^2 and $R_0'^2$ are correlation coefficients for the regression lines through the origin. $[(r^2 - R_0^2) / r^2]$ and $[(r^2 - R_0'^2) / r^2]$ are to calculate relation between r^2 , R_0^2 and $R_0'^2$. r_m^2 a modified squared correlation coefficient. R_p^2 is a parameter to calculate statistical significance of Random and non-random models

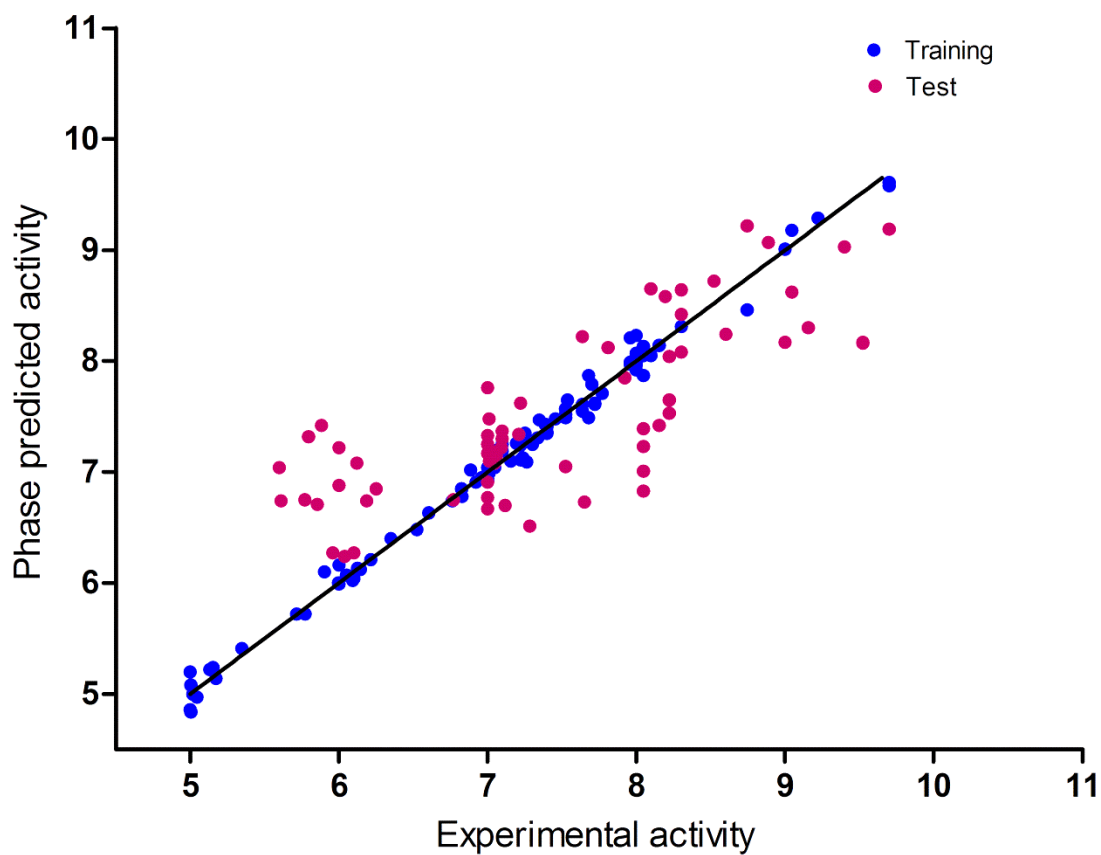


Figure 5.3 Scatter plot between predicted vs. experimental activity of CatS inhibition by the 3D QSAR model, obtained using compounds 98 as the training set and validated using compounds 63 as the test set. Inclination of the best fit line from the origin was considered in the context of calculating values of external r^2 , R_0^2 and $R_0'^2$.

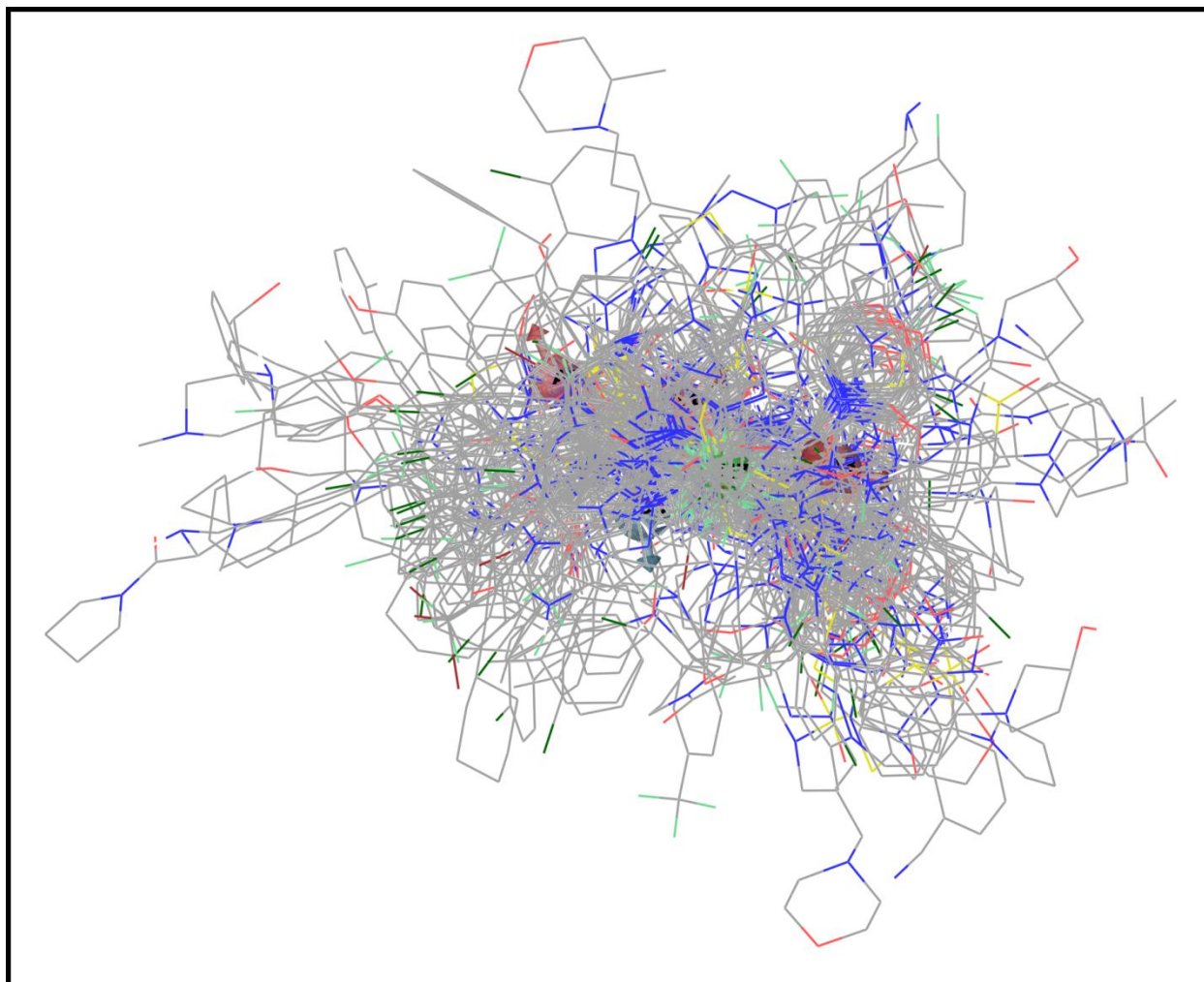


Figure 5.4 Illustration of alignment pattern of 161 diverse scaffold molecules on ligand based pharmacophore hypothesis while building 3D QSAR model.

5.1.4. Analysis of 3D contour maps

Generation of contour maps from the final validated hypothesis 1 by 3D QSAR method outlined clear positions of important atoms that could enhance the bioactivity. Additional insight into the CatS inhibitory activity was gained by visualizing the 3D QSAR model in the context of most active compound **1** (Table 5.1) and least active compound **161** (Table 5.18). Illustrations of ligand based contour maps on most and least active compounds were generated as shown in Figures 5.5 and 5.6. The blue cubes indicated favorable regions while red cubes indicated unfavorable regions for hydrogen bond acceptor activity as represented in Figure 5.5a1 and 5.5a2, while in Figure 5.5b1 and 5.5b2, the red cubes indicated favorable regions (conflict with 5.5a1 & 5.5a2) while blue cubes indicated unfavorable regions (conflict with 5.5a1 & 5.5a2) for hydrogen bond donor activity. The green cubes in Figure 5.6a1 and 5.6a2 indicated favorable regions while yellow cubes indicate unfavorable regions for hydrophobic groups. Figure 5.5a1 and 5.5a2 compares the most significant favorable and unfavorable electron withdrawing features that emerged when the 3D QSAR model was applied to the most active compound **1** (Figure 5.5a1) and least active compound **161** (Figure 5.5a2) respectively (in Tables 5.1 - 5.18). The favored red cubes were observed near the hydrogen bond acceptors along with respective acceptor hypothesis features at sulphonyl, ethanamide, and cyano cyclopropyl groups of most active compound (Figure 5.5a1) suggesting that these features were important for activity of the molecule and these groups should be unsubstituted. In the least active compound red cubes were mostly observed on carbamoyl and slightly at piperidine group (Figure 5.5a2) whereas disfavored blue cubes for hydrogen bond acceptor map was observed at morpholine carboxylic acid moiety, indicating that substitution of morpholine with alkyl acetamido group could increase the bioactivity of the least active compound **161**.

While, hydrogen bond donor mapping that raised when 3D QSAR model was applied to the most active compound **1** and least active compound **161** represented in Figure 5.5b1 and 5.5b2. Hydrogen bond donor mapping showed favored blue cube regions near the nitrogens of ethanamide, and cyano cyclopropyl amide of most active compound **1** (Figure 5.5b1), indicating their importance for activity in contrast to the least active compound **161**. We could understand the importance of alkyl amide as backbone scaffold with favored mapping seem to be necessary for the bioactivity. Blue favored cubes were absent in morpholine, piperidine and difluoro benzyl moiety of least active compound (Figure 5.5b2) but present near to the nitrogen of carbamoyl

group. Wherever, these findings clearly explain that the hydrogen bond donor groups such as benzyl sulphonyls, carbomoyls and alkylamide chain kind of substitutions increase the bioactivity of the compound **161** in place of existing functional groups.

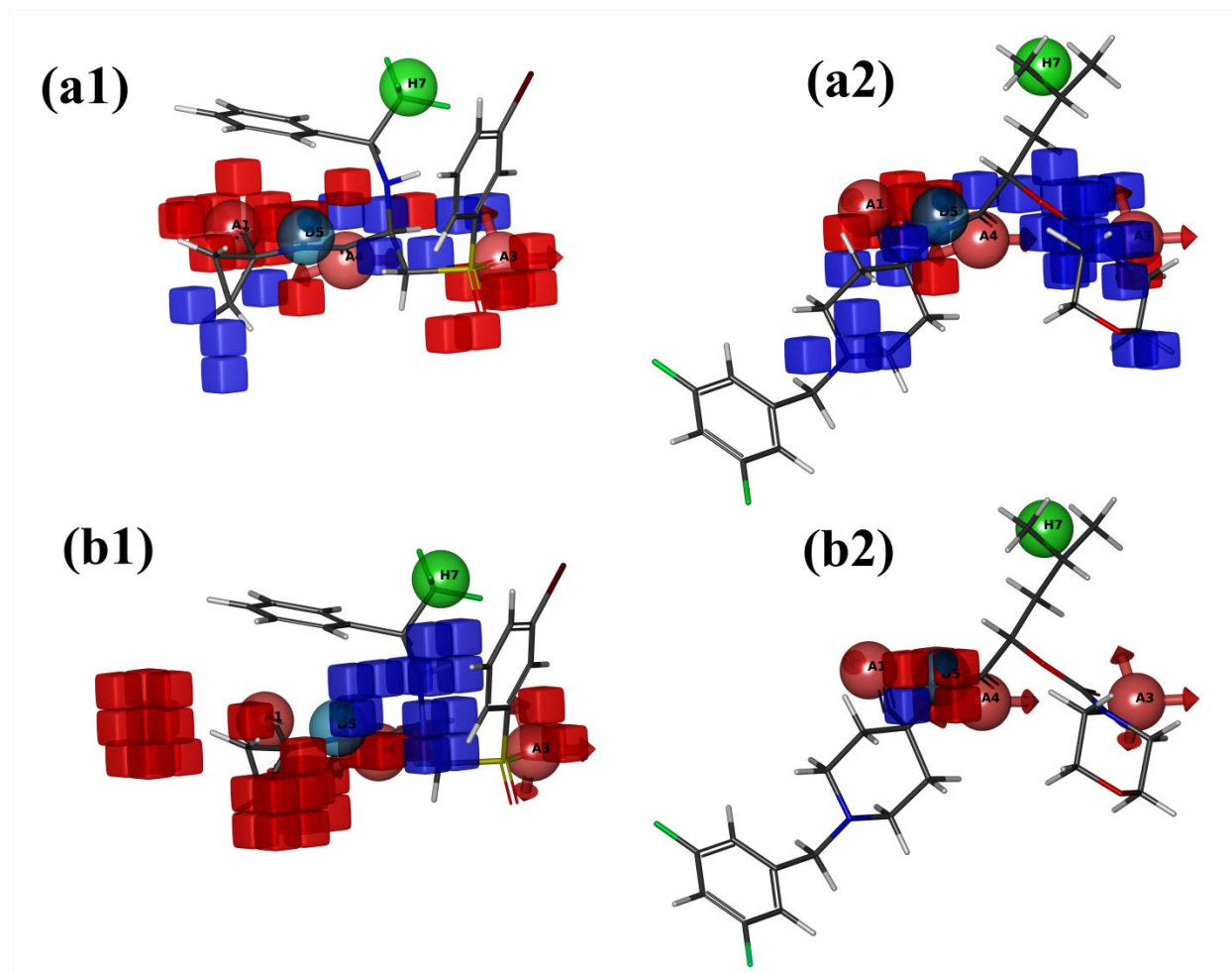


Figure 5.5 Illustration of 3D QSAR contour map on most (a1, b1) and least active (a2, b2) compounds. Hydrogen bond acceptor positive and negative contour map on most active compound **1** at (a1) and on least active compound **161** at (a2). Hydrogen bond donor positive and negative map on most active compound **1** at (b1) and on least active compound **161** at (b2).

Finally, we mapped 3D QSAR contours on the most active compound **1** and least active compound **161** in respect to hydrophobic favorable and unfavorable illustrations as depicted in Figure 5.6. In this case, we scrutinized the results with molecular docking (Glide XP) hydrophobic interactions of the most active and least active compounds to 3D QSAR hydrophobic contours of the most and least active compounds respectively. Auspiciously, hydrophobic binding patterns of compounds **1** and **161** at CatS active site were consistently allied with the 3D QSAR contour map predictions. When we carefully examine the active site of CatS, it mostly surrounded with hydrophobic amino acid side chains, which can greatly allow any kind of ligand with hydrophobically interacting groups. Therefore, we performed a comparative analysis with the contour maps and the docking pose interactions to understand the correlation and necessary hydrophobic interactions.

While in verifying 3D QSAR contours, favorable hydrophobic regions (green cubes) of most active compound (Figure 5.6a1) was involved in hydrophobic interactions within the active site of the CatS (2F1G) lined by highly hydrophobic amino acid residues Val162, Phe211, Phe70, Trp26, Met71 and Cys25 demonstrating that the cause of good bioactivity of the most compound **1**. In particular, bromophenyl and sulphonyl groups interact well with Phe211, Met71 and Val162. The cyclopropyl group was found to interact with Cys25 (necessary for activity of cysteine proteases), while trifluoroethyl benzene group with Phe70 and backbone scaffold ethanamide methyl group with Trp26 which profoundly were mapped as favorable (green cubes) hydrophobic contours. In fact, all these hydrophobic amino acid residues were reported earlier to be important for hydrophobic interaction with several ligands at the S1' and S2 subsites of CatS active site [Markt P., *et al.*, 2008].

Based on these observations it appeared that the bromophenyl group involved in hydrophobic interaction with in the CatS active site could be an essential moiety for the retainment of good activity of compound **1**. Replacement of bromine group attached to phenyl, with other halogens might lead to minor changes in the activity as reported in earlier study [Gauthier J., *et al.*, 2007]. Also, replacement of phenyl group with bulky alkyl hydrophobic groups might increase the activity as suggested in earlier report [Gauthier J., *et al.*, 2007], which was consistent with our 3D QSAR mapping inferring the reliability and mapping accuracy of our 3D QSAR model. Favorable hydrophobic mapping on trifluoroethyl benzene group was found to be responsible for

the activity where the benzene ring was involved in strong hydrophobic interaction with Phe70; substitution and replacement of trifluoro group might show improvement in the activity.

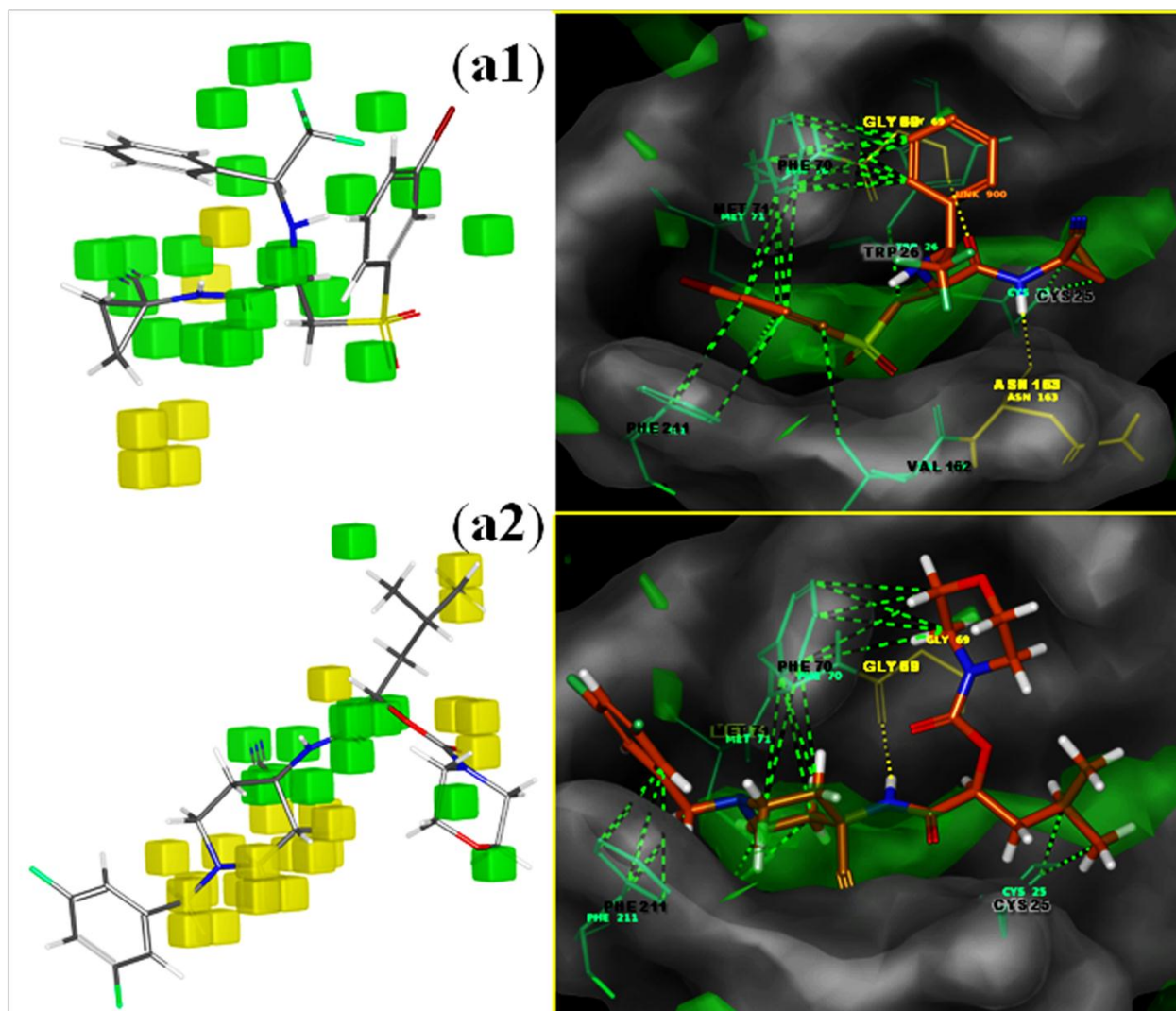


Figure 5.6 Illustration of the 3D QSAR contour map for hydrophobic visualization and docking poses of most (a1) and least active compound (a2). Green cubes represent favorable hydrophobic regions and yellow cubes represent disfavorable hydrophobic region and in the docking images, green and yellow dotted lines indicate hydrophobic and hydrogen bond interactions respectively.

Inevitably, structure-activity relationship predictions of the least active compound **161** demonstrated the negative aspects, which were impelled towards least activity. Morpholine carboxylic acid group, difluorobenzyl group, piperidine group and methylbutyl ester group were

found to interact hydrophobically with the residues Phe70, Phe211, Met71 and Cys25 respectively that were found to be comparable with predictions of 3D QSAR map. On the contrary, interactions with hydrophobic amino acid residues of Trp26, Val162 were found to be missing with least active compound **161** when compared to that of the most active compound **1**. Besides, hydrogen bond interaction with important amino acids were also found to be missing with least active compound **161** which retained a single hydrogen bond with Gly69. In addition, disfavored regions (yellow cube aggregation in Figure 5.6a2) were mapped by 3D QSAR contours on the molecule exposed to the hydrophobic surface (Green surface of active site in Figure 5.6a2) within the binding site was one of the down side of compound **161** in losing its activity. However, replacement of piperidine group with simple non-bulky alkyl amide chains might possibly improve the activity.

In summary, 3D QSAR contour map predictions on both the compounds were well correlated with the active site binding patterns, indicating the accuracy and robustness of the model to forecast novel molecule design for CatS inhibition. Therefore, the model was validated in all the stages and could be the best ligand based predictive model to commence novel drug discovery specifically for CatS.

5.2. Structure-based drug design

Structure-based drug design relies on the knowledge of the target protein crystal structure to calculate binding energies between the co-crystal ligand molecule and the protein active site, utilizes for generation of energy-based pharmacophore models. In current work, we have been selected 2FIG crystal structure among several CatS crystal structures, based on its resolution (1.9 Å), co-crystallized ligand's enzyme inhibition ($K_i = 29$ nM) and non-covalent binding interaction. Bounded crystal ligand in the active site was subjected to re-interact with the active site virtually, by retaining its original pose, with the help of docking based methods. Retaining its original pose by limiting the RMSD poses is a crucial step for the e-pharmacophore generation, where the actual idea is to understand and utilize the original binding interactions between the protein and ligand complex. Generation of energy descriptors while docking were utilized to recognize important interaction energies, which are responsible for binding interaction. All the features generated due to e-pharmacophore model building were shuffled to attain combinations of hypotheses to validate the features in understanding of predictive capacities (Figure 5.7). Hypothesis, which could with stand and satisfy the validation properties

was further useful for the database searching to dig out novel structural analogues for the drug design. Schematic representation of e-pharmacophore generation and its validation steps are depicted in the Figure 5.7.

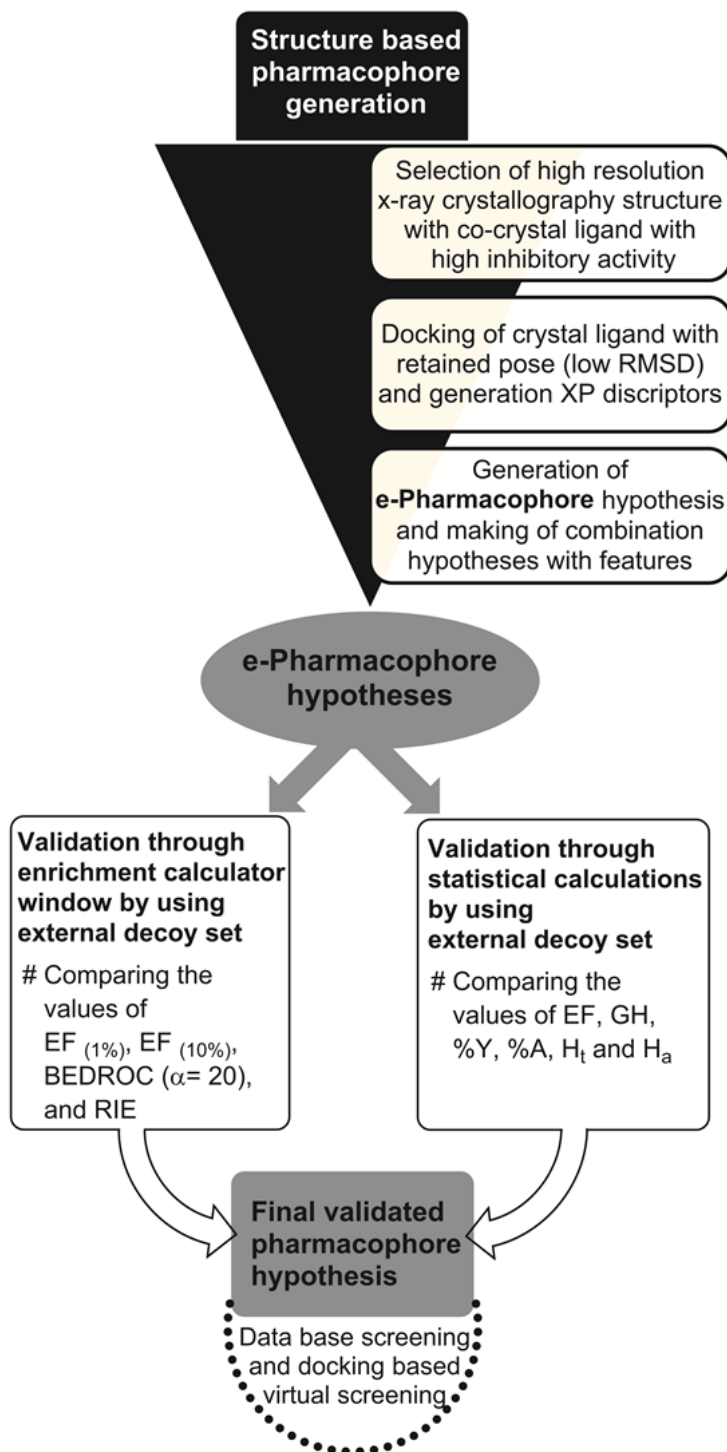


Figure 5.7 Schematic workflow of structure based pharmacophore generation and validation

5.2.1. e-Pharmacophore modeling and validation

The crystallographic data of CatS PDB complex (2F1G) was selected and analyzed within the software package Maestro (Maestro v9. Schrödinger, LLC, New York, NY, 2012) to attain structure based pharmacophore (e-pharmacophore). Template protein-ligand complex (2F1G) was energetically optimized and generated energetic terms computed by the Glide XP scoring function (Glide, version 5.8, Schrödinger, LLC, New York, NY, 2012) to rank the important pharmacophore features. A co-crystal ligand (2F1G) with arylaminoethyl amide moiety (Figure 5.8) was taken as reference ligand to generate e-Pharmacophore, since it was known to be a non-covalent inhibitor of CatS and had a low K_i value of 29 nM. [Tully DC., *et al.*, 2006] Final hypothesis generated with five pharmacophoric features of one hydrogen bond acceptor (A), one hydrogen bond donor (D), two aromatic ring features (R), and one hydrophobic group (H). Three more combinations of four point hypotheses were generated by shuffling features RRH but not AD, (Figure 5.8) where the features A and D are most important interactions must needed for CatS inhibition. All hypotheses were subjected for validation by using decoy set database, which included 150 known active CatS inhibitors and 1000 decoy compounds. Hypothesis 4 (DARH. 4) (Figures 5.8 and 5.9) displayed a good Enrichment Factor (EF) value of 5.31 and consistent GH value of 0.616. Enrichment in the top 1% of the decoys for hypotheses 2,3,4 were shown similar value of 7.7, but EF in top 10% shown highest value of 5.6 for hypothesis 4. Further, the hypothesis DARH.4 is also persisted in problem of "early recognition" by BEDROC ($\alpha=20$) value of 0.829 and with good RIE value of 6.34 (Table 5.23). Although RIE and BEDROC produce different values, their distributions identical in provide good "early recognition" of actives.

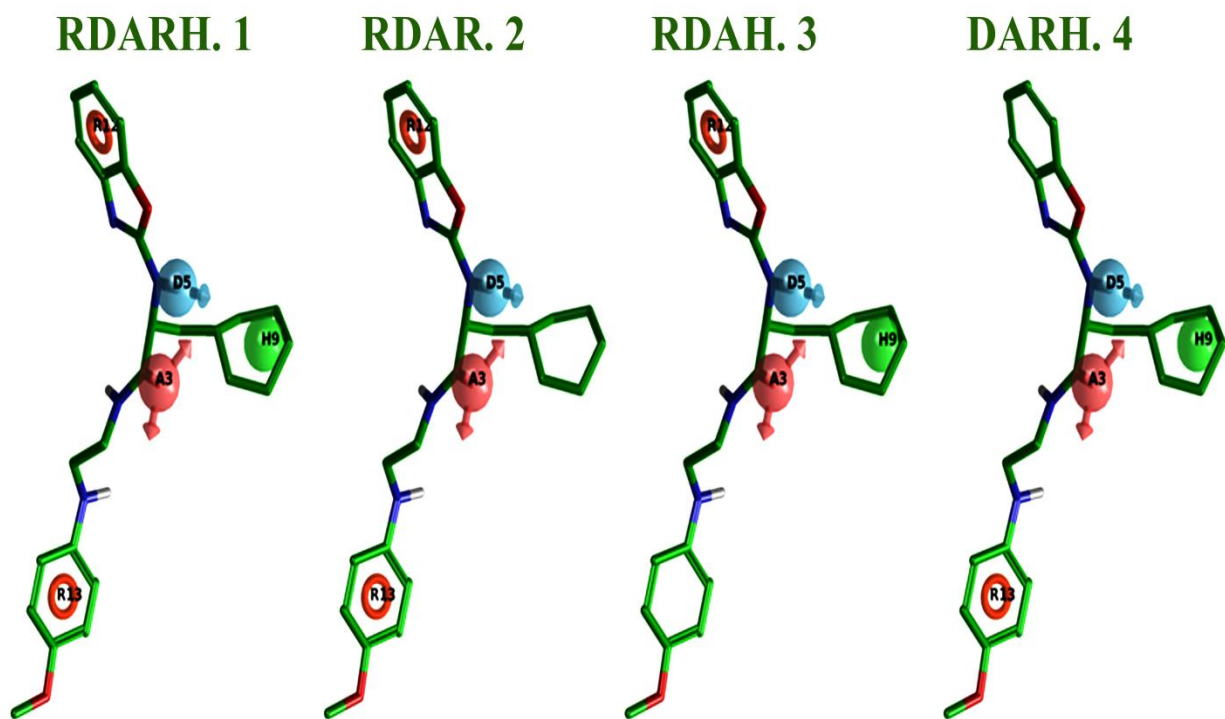


Figure 5.8 Possible four-combination hypotheses from the evolved e-pharmacophore model

Table 5.23 Pharmacophore enrichment validation of all four-combination hypotheses.

Parameters	RDARH. 1	RDAR. 2	RDAH. 3	DARH. 4
H_t	6	113	339	101
H_a	4	29	86	70
%Y	66.66	25.66	25.36	69.30
%A	2.66	19.33	57.33	46.66
EF	5.11	1.96	1.94	5.31*
GH	0.505	0.220	0.249	0.616*
EF_(1%)	2.6	7.7	7.7	7.7
EF_(10%)	0.27	1.7	4.5	5.6
BEDROC ($\alpha=20$)	0.073	0.393	0.749	0.829
RIE	0.52	2.79	5.89	6.34

H_t - Total number of hit molecules from the database

H_a - Total number of active molecules in hit list

%Y - Percentage yield of actives $[(H_a/H_t) \times 100]$

%A - Percentage ratio of actives $[(H_a/A) \times 100]$

EF - Enrichment Factor

GH Goodness of fit score

EF(1%) - The enrichment in the top 1% of the decoys.

EF(10%) - The enrichment in the top 10% of the decoys.

BEDROC ($\alpha=20$) - Recovery rate of actives against the ranked decoy database.

RIE Indicates good early recognition.

* Best EF and GH scores among four hypotheses.

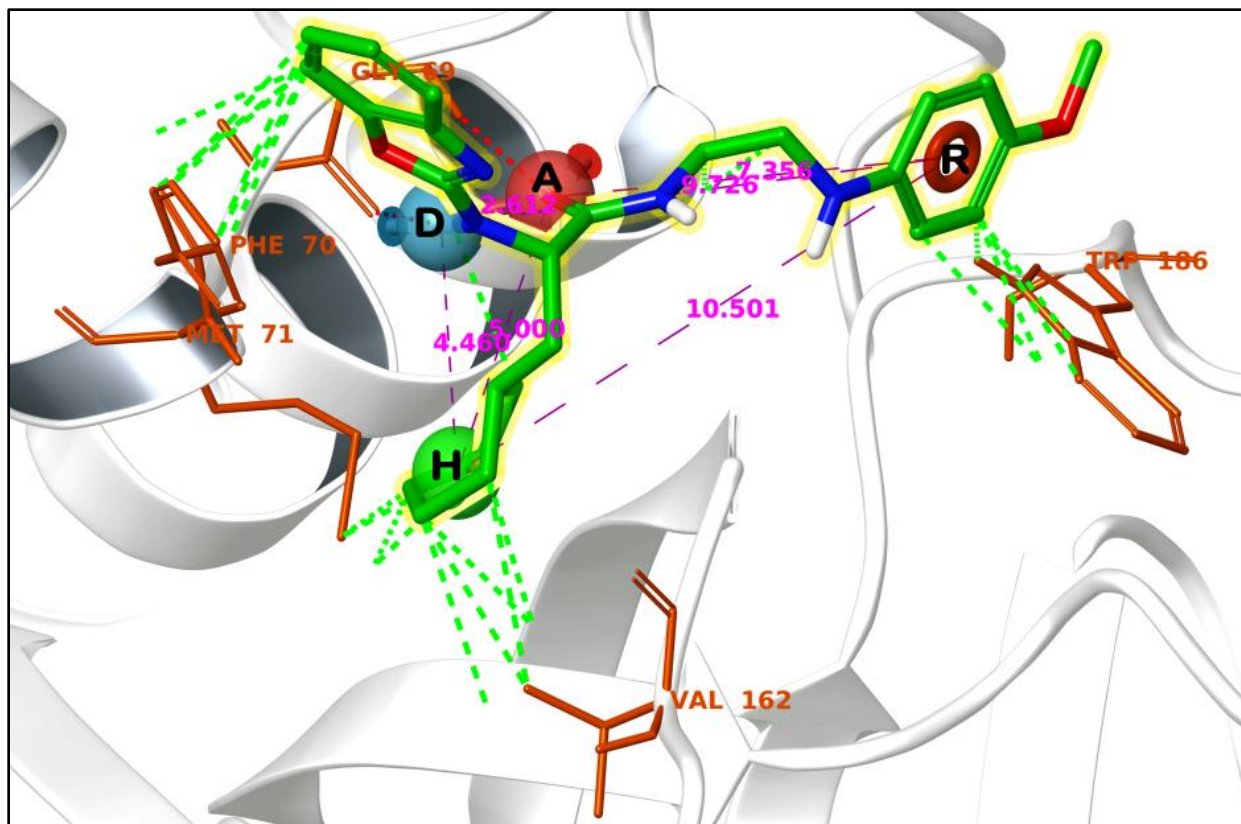


Figure 5.9 Illustration of four point e-pharmacophore hypothesis (DARH. 4) derived from CatS crystal structure data (2F1G). Green dotted lines indicate the hydrophobic interactions, Red dotted lines indicate the H-bond interactions with respective amino acid residues and pink dotted lines indicate the length between pharmacophore's each hypothesis features.

5.3. Virtual screening and docking

Virtual screening studies of the compound database could retrieve novel active molecules after filtering out the inactive molecules. Both ligand based and structure based pharmacophores were operated for ligand find match database screening. The validated pharmacophore hypotheses from ligand based (AAADH. 1) and structure based (DARH. 4) were operated individually for ligand find match database screening of 5,00,000 compounds (Asinex database). Co-crystal ligand (arylaminoethyl amide compound from pdb id: 2F1G) with K_i 29nm [Tully DC., *et al.*, 2006] was taken as reference ligand, since it was showed non-covalent interactions with the CatS and has low K_i value among all the CatS crystal structure ligands and especially it was utilized for the generation of e-pharmacophore hypothesis. From both pharmacophore hypotheses, compounds with fitness more than 1.5 were taken as initial cut-off to shortlist, hit compounds. Subsequently, in case of ligand based pharmacophore has an advantage of getting predicted activity scores to screen out some more low-scored molecules. Furthermore, interpretation of the ligand-based pharmacophore with 3D QSAR maps provided insights to crucial structural requirements for inhibition of CatS, could be utilized as a guide for further selection prerequisite to pick out hit molecules.

From ligand-based pharmacophore, around 50246 hit molecules with good fitness (> 1.5) and with predicted activity, more than 5.0 were selected and from structure based e-pharmacophore, around 38372 hit molecules with good fitness were selected for further virtual screening (Figure 5.10). Molecules (around 88618) from both the pharmacophores were combined and made as a single database and taken for HTVS (High throughput virtual screening) as primary docking. 5222 compounds from HTVS with a Glide score less than -6.0 were further refined using SP (standard precision) docking module and then 320 ligand molecules were identified with good Glide score (< -6.0). The cut off value was taken as -6.0 as the reference crystal ligand of 2F1G Glide score was found to be -5.63. Molecules from SP docking (320) were further subjected to highly precise XP (extra precision) docking study where we acquired 106 compounds were shown good Glide score than crystal ligand (< -5.48). Further, repetitions of molecules were corrected from the hit molecules after XP docking, and were visually inspected with manual observations of crucial amino acid binding within the surface consisted CatS active site (Figure 5.11) and finally 52 molecules were finalized for the preliminary enzyme inhibition studies.

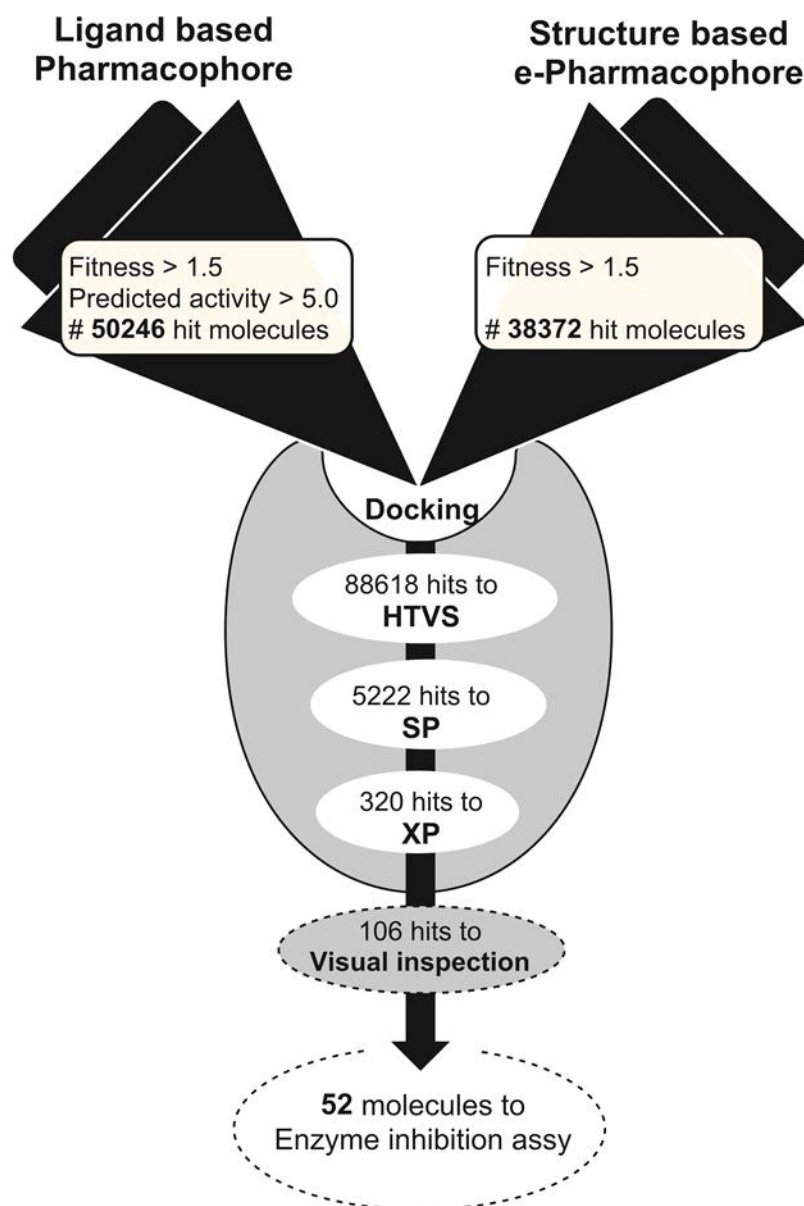


Figure 5.10 Virtual-screening workflow from both ligand and structure based drug designing.

The important amino acid residues for good binding were found to be Asn163, Gly69, Gln19, Met71, Trp186 and His164 based on previous literatures [Markt P., *et al.*, 2008] and the crystal ligand interactions in 2F1G (Figure 5.11). After corrected repetitions and visual inspection, 52 molecules (Table 5.24) were finally shortlisted for the biological assays to screen as CatS inhibitors.

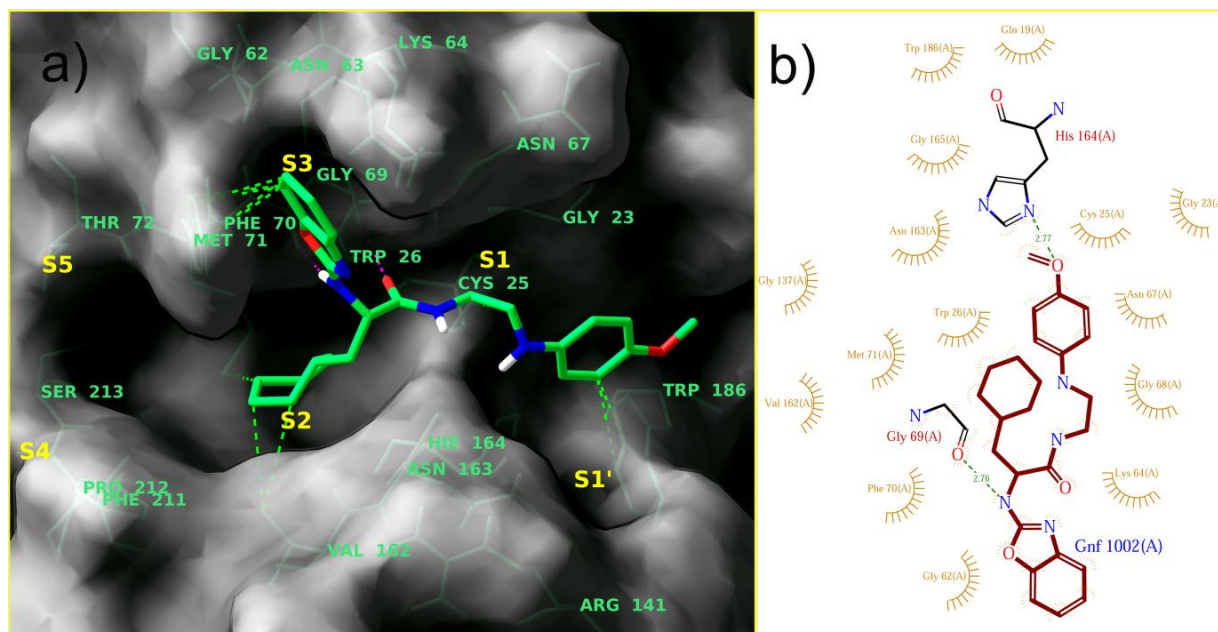


Figure 5.11 Illustration of the co-crystal ligand (2F1G) interacted with active site of CatS represented in three dimensional binding pose. (a) where, green dotted lines indicated hydrophobic interaction and pink dotted lines indicated the hydrogen bond interaction. Two-dimensional representation of interaction picture was depicted in (b).

5.3.1. ADME predictions

All the 52 hits from Glide were verified for the pharmaceutically relevant properties (ADME) to check drug likeliness, which could avoid imminent troubles while conducting experimental work. QikProp module was used for evaluation of drug-like behavior through analysis of pharmacokinetic parameters required for absorption, distribution, metabolism and excretion (ADME). All the hit compounds (Table 5.24) showed good partition coefficient (QPlogPo/w) values which were critical for understanding the absorption and distribution of test compounds, ranging from 0.33 to 6.33. Other drug likeliness factor ‘rule of five’ is an estimation of rule of five violations, where all 52 compounds were shown lesser than three violated rules (Maximum is 4). QPPCaco for 52 hit compounds ranged from 12.04 to 2868.46, where QPPCaco was a predicted apparent Caco-2 cell permeability in nm/sec value (Caco-2 cells represented as a model for gut-blood barrier), a key factor for estimation of cell permeability in biological membranes and its metabolism. In context of CatS physiological location and activity in certain disease conditions like neuropathic pain and other neurological disorders, we examined the factor QPlogBB (predicted brain/blood partition coefficient) and were found to be in range from -3.03 to -0.53. The percentage of human oral absorption for the compounds ranged from 29.16 to 100% and 38 compounds (Table 5.24) showed more than 80% indicating high oral absorption. All the 52 compounds passed all the predicted pharmacokinetic parameters, were within the acceptable range displaying drug likeliness, and defined for human use (Table 5.24).

5.4. Preliminary enzymatic assay studies

All the 52 hit compounds were screened at 50 μ M for CatS enzyme inhibition to understand the inhibitory activity and to screen efficient molecules for further studies. According to the protocol discussed earlier in section 4.5 all test compounds were incubated with enzyme substrate complex in triplicate samples. Blank, enzyme controls, substrate controls and auto fluorescence samples were thoroughly maintained for the entire assay. Eventually, 26 compounds among 52 showed more than 50% inhibition at 50 μ M concentration against CatS enzyme and were considered as lead compounds and further studied for IC₅₀ calculations (Table 5.24). Propitiously, all 26 lead compounds showed promising results with the values of IC₅₀ ranging from 3-100 μ M (Table 5.25). Structural representation of selected lead molecules was represented in Figure 5.12. As part of biological evaluation, lead molecules were forwarded to the next step of cytotoxicity assays.

Table 5.24 Hit molecules found from both ligand and structure based pharmacophores with their Glide and QikProp scores and the selected final lead molecules.

Hit number	> 50% inhibition at 50 μ M Leads	XP GScore	QPlogPo/w	Rule Of Five	QPPCaco	QPlogBB	% Human Oral Absorption
Hit-1		-8.402	1.206	0	65.091	-2.485	66.464
Hit-2		-8.013	5.429	1	757.292	-0.835	100
Hit-3		-7.879	4.416	0	695.595	-1.199	100
Hit-4		-7.839	4.84	0	1434.189	-0.532	100
Hit-5		-7.713	3.566	1	49.595	-2.767	65.212
Hit-6		-7.702	5.189	1	701.222	-0.995	95.304
Hit-7		-7.662	4.535	0	711.292	-1.493	100
Hit-8		-7.652	1.503	2	12.042	-1.441	29.168
Hit-9		-7.531	4.55	0	523.489	-1.227	100
Hit-10		-7.476	4.926	0	751.797	-0.927	100
Hit-11		-7.424	4.516	0	590.578	-0.969	100
Hit-12		-7.400	3.394	0	157.616	-1.945	86.152
Hit-13		-7.385	3.045	0	277.694	-1.474	88.51
Hit-14		-7.372	3.884	0	309.46	-1.738	94.264
Hit-15	Lead -1	-7.333	5.235	3	33.457	-3.048	46.009
Hit-16	Lead -2	-7.248	3.931	0	667.799	-1.289	100
Hit-17	Lead -3	-7.242	4.697	0	198.705	-1.809	95.584
Hit-18		-7.223	5.05	1	779.129	-1.124	95.309
Hit-19	Lead -4	-7.187	1.264	0	67.547	-1.986	67.093
Hit-20	Lead -5	-7.167	3.905	0	2034.083	-0.464	100
Hit-21		-7.039	6.271	2	143.909	-2.417	76.373
Hit-22		-6.929	0.332	0	70.196	-1.277	61.936
Hit-23	Lead -6	-6.922	1.166	0	182.857	-1.431	74.262
Hit-24		-6.879	1.959	0	125.141	-1.722	75.953
Hit-25	Lead -7	-6.865	2.533	2	42.106	-3.036	44.933
Hit-26		-6.851	4.058	0	491.847	-1.085	100
Hit-27	Lead -8	-6.840	5.665	1	1459.944	-0.874	100
Hit-28	Lead -9	-6.823	4.061	0	205.801	-1.844	92.128
Hit-29	Lead -10	-6.814	6.332	2	481.914	-1.099	86.126
Hit-30	Lead -11	-6.802	2.89	1	13.794	-1.572	51.308
Hit-31	Lead -12	-6.726	3.766	0	362.318	-1.564	94.797
Hit-32	Lead -13	-6.690	4.442	0	400.368	-1.164	100
Hit-33	Lead -14	-6.681	3.153	1	160.119	-1.913	71.904
Hit-34	Lead -15	-6.666	3.599	0	941.178	-0.851	100
Hit-35		-6.634	4.998	0	685.772	-1.338	100
Hit-36	Lead -16	-6.396	3.989	0	1081.821	-0.533	100

Continued...

Hit-37	Lead -17	-6.388	4.887	0	2868.466	-0.185	100
Hit-38		-6.345	2.896	0	1004.272	-0.787	100
Hit-39	Lead -18	-6.333	2.693	0	197.565	-1.443	83.804
Hit-40	Lead -19	-6.295	2.128	1	18.919	-3.035	49.3
Hit-41	Lead -20	-6.258	3.162	0	230.265	-1.786	87.741
Hit-42	Lead -21	-6.220	4.522	0	197.491	-1.783	94.508
Hit-43	Lead -22	-6.173	5.113	2	739.18	-1.015	82.311
Hit-44	Lead -23	-6.011	2.976	0	109.469	-2.076	80.867
Hit-45	Lead -24	-6.001	2.145	0	70.288	-2.199	72.56
Hit-46	Lead -25	-5.916	1.693	0	70.115	-2.287	69.893
Hit-47	Lead -26	-5.861	2.964	0	101.13	-1.801	80.187
Hit-48		-5.820	3.303	0	373.721	-0.744	92.328
Hit-49		-5.786	2.374	0	218.916	-1.349	82.732
Hit-50		-5.777	4.616	0	833.362	-0.941	100
Hit-51		-5.761	4.812	0	1645.821	-0.615	100
Hit-52		-5.186	4.523	0	595.405	-0.946	100

QPlogPo/w Predicted octanol/water partition co-efficient log p (acceptable range from -2.0 to 6.5).

QplogHERG Predicted IC₅₀ value for blockage of HERG K⁺ channels (concern below -5.0).

QPPCaco Predicted Caco-2 cell permeability in nm/s (acceptable range: <25 is poor and >500 is great).

QPlogBB Predicted brain/blood partition coefficient (acceptable range from -3.0 to 1.2)

% Human oral absorption Percentage of human oral absorption (<25% is poor and >80% is high).

Rule of five Number of violations of Lipinski's rule of five (Maximum is 4)

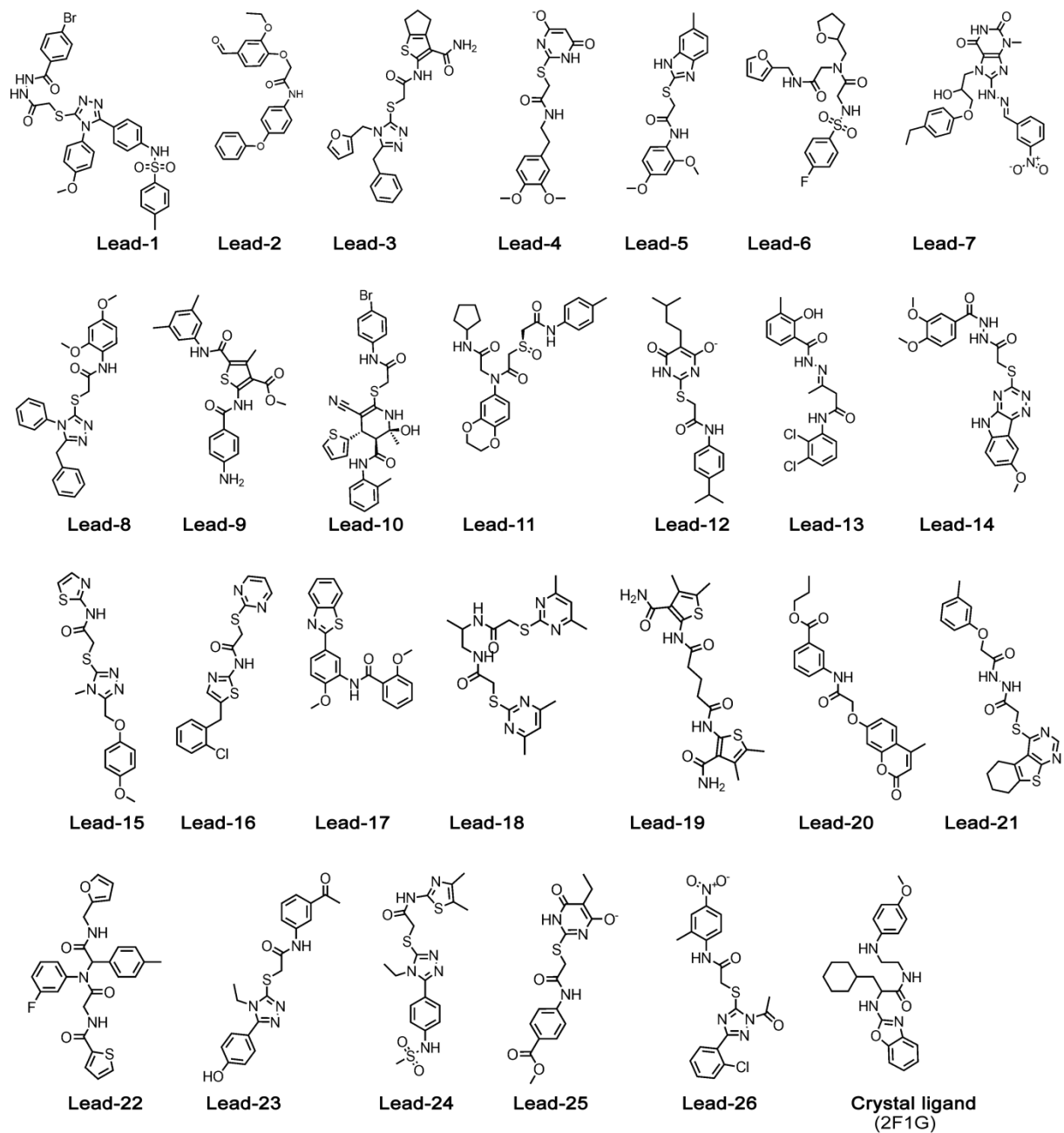


Figure 5.12. Structures of 26 lead molecules identified after virtual screening and enzymatic assay along with structure of crystal ligand (2F1G)

5.5. Cell-based assays for lead molecules

Identified lead molecules were estimated for growth inhibition and cytotoxicity assays to understand the potency of CatS enzyme inhibitors with growth inhibitory activity on human glioblastoma cell lines (U-87 MG). As the selection of glioblastoma cell lines was based on the recent reports [Zhang L., *et al.*, 2014; Flannery T., *et al.*, 2006], that revealed, the inhibition of would CatS induce autophagy and apoptosis in human glioblastoma cell lines and reduced the progression of cancer. Moreover, in current work, deliberate selection of human glioblastoma cell lines (U-87 MG) for the biological evaluation studies was to explore the potent CatS inhibitors, which could concurrently work on inflammatory cancerous mediators as well as to get activity on cancer induced neuropathic pain. Human Embryonic Kidney cells (HEK 293) were also utilized to carry out the normal cell cytotoxicity and to estimate the selectivity towards the cancerous glioblastoma cells than the normal cells. GIC₅₀ (Growth inhibitory concentration 50) and CC₅₀ (Cytotoxicity concentration 50) were calculated for all the 26 lead compounds. Propitiously, all 26 compounds were shown promising results with the values of GIC₅₀ range from 0.001-100 μ M (Table 5.25). Leads **14** and **15** were displayed low GIC₅₀ of 0.001 with good selectivity index.

Table 5.25 All lead compound's IC₅₀ values of enzyme inhibition, glioblastoma cell growth inhibition (GIC₅₀) and cytotoxicity (CC₅₀) and their selectivity index.

Lead compound	IC₅₀ (μM) ±SEM	GIC₅₀ (μM) ±SEM	CC₅₀ (μM) ±SEM	Selectivity Index (CC₅₀/GIC₅₀)
Lead -1	18.14±0.27	>100.000	0.305±0.06	--
Lead -2	15.60±0.36	0.189±0.09	0.510±0.17	2.702
Lead -3	12.07±0.63	22.42±0.86	0.300±0.03	0.013
Lead -4	9.63±0.52	>100.000	0.466±0.04	--
Lead -5	21.99±0.39	11.160±1.63	0.004±0.00	<0.001
Lead -6	10.11±0.45	10.460±0.64	0.007±0.00	<0.001
Lead -7	10.21±0.44	10.060±0.78	4.525±0.94	0.450
Lead -8	6.58±0.56	0.477±0.05	>100.000	>100.000
Lead -9	3.09±0.68	15.990±1.06	0.001±0.00	<0.001
Lead -10	8.20±0.59	5.661±1.41	15.690±1.50	2.772
Lead -11	14.74±0.49	82.410±2.47	>100.000	>100.000
Lead -12	15.55±0.48	15.340±1.21	0.106±0.01	0.007
Lead -13	12.63±0.37	86.290±5.03	7.380±0.64	0.086
Lead -14	23.61±0.34	0.001±0.00	59.240±0.85	59240
Lead -15	23.20±0.29	0.001±0.00	1.122±0.55	1122
Lead -16	26.48±0.28	11.620±1.53	0.635±0.01	0.055
Lead -17	76.42±0.34	46.540±1.67	>100.000	>100.000
Lead -18	14.03±0.38	>100.000	>100.000	--
Lead -19	>100.000	4.549±0.94	1.784±0.50	0.392
Lead -20	17.59±0.26	21.460±0.91	0.012±0.04	<0.001

Continued...

Lead -21	22.06±0.36	97.870±0.35	3.927±0.45	0.040
Lead -22	30.49±0.27	0.135±0.05	0.346±0.05	2.566
Lead -23	64.22±0.25	3.722±0.86	>100.000	>100.000
Lead -24	75.50±0.12	88.840±0.50	0.439±0.09	0.005
Lead -25	49.59±0.21	0.053±0.02	0.019±0.02	0.359
Lead -26	>100.000	0.025±0.01	0.012±0.01	0.487
E-64	0.013±0.01	>100.000	>100.000	--
Bendamustin	nd	0.073±0.02	>100.000	>100.000
Temazolamide	nd	11.560±0.21	>100.000	>100.000

nd- not determined

5.6. Relationships between the binding poses and the activity

Interpretation of ligand interaction poses in relation with enzymatic inhibitory activity, could give the knowledge regarding key specifications and structural features in building specific target's drug design strategy. 2D ligand interaction pictures were generated for the docked lead molecules and represented in Figures 5.13 and 5.14. Initially, when observed the interaction picture of crystal ligand (Figure 5.14), there were two important hydrogen bonds with Gly69 and Asn163 and an aromatic hydrophobic interaction with Phe70. If we compared the interaction pictures of active lead molecules, exhibited $\leq 10 \mu\text{M}$ IC_{50} (**Lead 4, 6, 7, 8, 9, 10**) showed several relations in binding to CatS active site. Particularly all these leads with $\leq 10 \mu\text{M}$ IC_{50} , had common interaction with Asn163 as like crystal ligand. Except **Lead 7**, remaining leads (**4, 6, 8, 9 and 10**) (Figure 5.13) interacted with Gly69, but lead 7 has a peculiar interaction with positively charged flexible amino acid Lys64 located at S3 site. **Leads 8, 9 and 10** were found to hydrophobically interacted with Phe70 as like crystal ligand. Very importantly, **Lead 10** showed all other important interactions such as H-bond with Gly69, Asn163, Lys64 and hydrophobically with Hie164, Phe70, but reason were not known for the most active lead (8.20 μM).

However, lead compounds with low IC_{50} values i.e. near and below 50 μM (**Lead 17, 19, 23, 24, 25, 26**) (Figure 5.14), commonly showed one or no hydrophobic interaction with Phe70 and others. In contrast, **Lead 19** exhibited interaction with Phe70, but missed the interaction with Gly69. Absence of crucial amino acid H-bond interaction and hydrophobic interaction as well as site-specific pocket occupancy of the molecule could be the reasons behind the loss of activity.

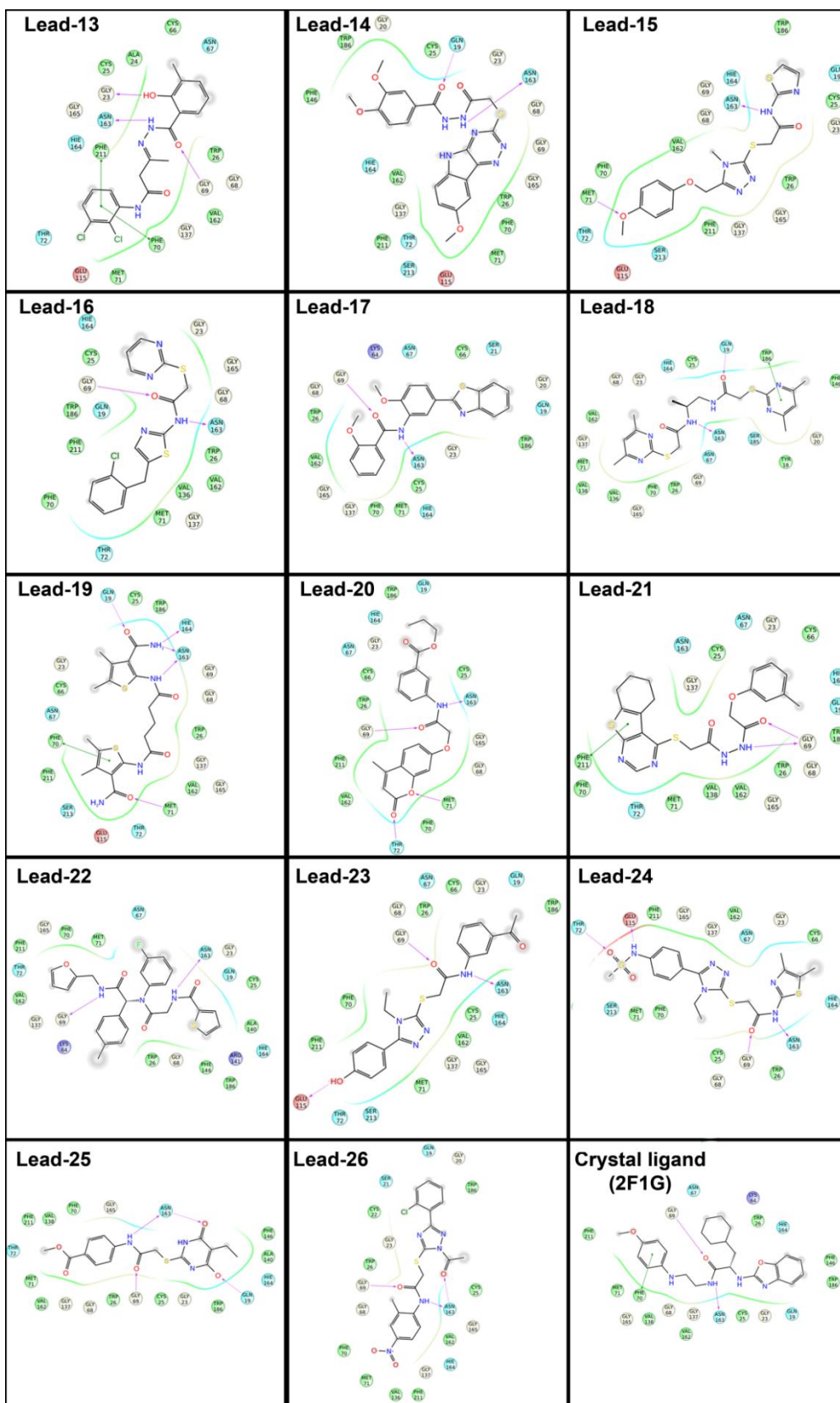


Figure 5.14 Ligand interaction pictures of lead molecules from Lead 13 to 26.

5.7. Summary and conclusions

Lead molecules obtained from the lead identification strategies using ligand based and structure based drug design methods, were further experimentally evaluated *in vitro* enzymatic assays, where, the most active lead compound was found to be **Lead 9** with IC_{50} of 3.09 μ M. However, compound, which displayed good enzyme inhibition and anti-microglial cancer cell viability with low cytotoxicity, were considered for cell-based assays. After cytotoxicity analysis (MTT assays) **Lead 9** was found to be cytotoxic compound, and its selectivity index towards cancer cells was < 0.001 . Moreover, **Lead 9** showed low GIC_{50} of 15.99 μ M and highly cytotoxic to the normal cells with CC_{50} of < 0.001 μ M. Due to this reason, we investigated another potent lead compound for further structure optimization. Among lead molecules with IC_{50} below and near 10 μ M (**Lead 4, 6, 7, 8, 10**), compound **Lead 8** with good enzyme inhibition (6.58 μ M) and glioblastoma inhibition of GIC_{50} value 0.477 μ M and with >100 fold selectivity index as well as low cytotoxicity on normal cells. Other compounds **Leads 14** and **15** (Table 5.25) displayed high GIC_{50} with good selectivity index, but due to low enzymatic inhibition (23.61 and 23.20 μ M respectively), were not considered important compounds. Therefore, compound **Lead 8** was selected as final lead molecule to proceed for lead optimization by medicinal chemistry approach.

CHAPTER 6

Lead optimization and structure activity relationships

The synthetic route followed for the synthesis of 1,2,4 triazole-3-thiol derivatives is illustrated in the scheme 4.1. Aromatic esters (**2A-B**) were synthesized by reacting corresponding acids **1A** and **1B** (150 mmol) with oxalylchloride in methanol as pale yellow oil. ESI-MS was found at m/z 151.19 $[M+H]^+$ and 171.62 $[M+H]^+$ respectively. Esters (**2A-B**) were converted to acid hydrazides (**3A-B**) by refluxing with hydrazine hydrate (30%) in ethanol. Hydrazinecarbothioamide derivatives (**4Aa-4Bc**) were prepared by condensation of acid hydrazides (**3A-B**) with substituted phenylisothiocyanates in ethanol. The physical and chemical characterization of intermediate **4** are presented below.

N-Phenyl-2-(2-phenylacetyl) hydrazinecarbothioamide (**4Aa**): Compound **4Aa** was a white solid (8.7g, 87%). ESI-MS was found at m/z 286.36 $[M+H]^+$. 1H NMR (DMSO- d_6)-300 MHz) δ_H . 4.13 (s, 2H), 7.40-7.22 (m, 10H), 9.82 (bs, 2H), 10.07 (s, 1H).

N-(4-Fluorophenyl)-2-(2-phenylacetyl) hydrazinecarbothioamide (**4Ab**): Compound (**4Ab**) was a white solid (9.6g, 90%). ESI-MS was found at m/z 316.47 $[M+H]^+$. 1H NMR (DMSO- d_6)-300 MHz) δ_H . 4.10 (s, 2H), 7.45-7.89 (m, 9H), 9.89 (bs, 2H), 10.07 (s, 1H).

N-(4-Methoxyphenyl)-2-(2-phenylacetyl) hydrazinecarbothioamide (**4Ac**): Compound (**4Ac**) was a white solid (9.7g, 88%). ESI-MS was found at m/z 304.39 $[M+H]^+$. 1H NMR (DMSO- d_6)-300 MHz) δ_H . 3.84 (s, 3H), 4.08 (s, 2H), 7.57-7.83 (m, 9H), 9.86 (bs, 2H), 10.07 (s, 1H).

2-(2-Chlorobenzoyl)-*N*-phenylhydrazinecarbothioamide (**4Ba**): Compound (**4Ba**) was a white solid. ESI-MS was found at m/z 306.32 $[M+H]^+$. 1H NMR (DMSO- d_6)-300 MHz) δ_H . 7.57-7.90 (m, 9H), 9.89 (bs, 2H), 10.12 (s, 1H).

2-(2-Chlorobenzoyl)-*N*-(4-fluorophenyl) hydrazinecarbothioamide (**4Bb**): Compound (**4Bb**) was a white solid. ESI-MS was found at m/z 304.39 $[M+H]^+$. 1H NMR (DMSO- d_6)-300 MHz) δ_H . 7.60-7.91 (m, 8H), 9.91 (bs, 2H), 10.11 (s, 1H).

2-(2-Chlorobenzoyl)-*N*-(4-methoxyphenyl) hydrazinecarbothioamide (**4Bc**): Compound (**4Bc**) was a white solid. ESI-MS was found at m/z 316.47 $[M+H]^+$. 1H NMR (DMSO- d_6)-300 MHz) δ_H . 3.87 (s, 3H), 7.68-7.92 (m, 8H), 9.87 (bs, 2H), 10.05 (s, 1H).

Further, These hydrazinecarbothioamide derivatives (**4Aa-4Bc**) were used as key intermediates for the synthesis of 1,2,4 triazol-3-thiol derivatives. The 1,2,4 triazol-3-thiol derivatives (**6Aa-6Bc**) were synthesized by intramolecular dehydrative cyclisation of carbothioamides when refluxed with 10 % sodium hydroxide solution , followed by neutralization with concentrated HCl. The physical and chemical characterization of intermediate 4 are presented below.

5-Benzyl-4-phenyl-4H-1,2,4-triazole-3-thiol (6Aa): According to the general procedure **4Aa** prepared compound was in white solid (6g, 75%). ESI-MS was found at m/z 268.39 $[M+H]^+$. 1H NMR (DMSO- d_6)-300 MHz) δ_H . 4.10 (s, 2H), 7.40-7.87 (m, 10H), 12.12 (s, 1H).

5-Benzyl-4-(4-fluorophenyl)-4H-1,2,4-triazole-3-thiol (6Ab): According to the general procedure **4Ab** prepared compound was in white solid (6.5g, 77%). ESI-MS was found at m/z 286.64 $[M+H]^+$. 1H NMR (DMSO- d_6)-300 MHz) δ_H . 4.09 (s, 2H), 7.35-7.88 (m, 10H), 12.14 (s, 1H).

5-Benzyl-4-(4-methoxyphenyl)-4H-1,2,4-triazole-3-thio (6Ac): According to the general procedure **4Ac** prepared compound was in white solid (6.6g, 74%). ESI-MS was found at m/z 298.27 $[M+H]^+$. 1H NMR (DMSO- d_6)-300 MHz) δ_H . 4.11 (s, 2H), 7.33-7.84 (m, 10H), 12.10 (s, 1H).

5-(2-Chlorophenyl)-4-phenyl-4H-1,2,4-triazole-3-thiol (6Ba): According to the general procedure **4Ba** prepared compound was in white solid (6.3 g, 74%). ESI-MS was found at m/z 288.72 $[M+H]^+$. 1H NMR (DMSO- d_6)-300 MHz) δ_H . 7.36-7.89 (m, 9H), 12.10 (s, 1H).

5-(2-Chlorophenyl)-4-(4-fluorophenyl)-4H-1,2,4-triazole-3-thiol (6Bb): According to the general procedure **4Bb** (9.7 g, 30 mmol) to afford desired compound as an off-white solid (6.8 g, 75%). ESI-MS was found at m/z 306.52 $[M+H]^+$. 1H NMR (DMSO- d_6)-300 MHz) δ_H . 7.32-7.90 (m, 8H), 12.13 (s, 1H).

5-(2-Chlorophenyl)-4-(4-methoxyphenyl)-4H-1,2,4-triazole-3-thiol (6Bc): According to the general procedure **4Bc** prepared compound was in white solid (6.8g, 72). ESI-MS was found at m/z 318.80 $[M+H]^+$. 1H NMR (DMSO- d_6)-300 MHz) δ_H . 7.29-7.89 (ms, 8H), 12.03 (s, 1H).

The resulted 1,2,4 triazole-3-thiol derivatives were S-alkylated with different substituted α -chloroacetanilides using DIPEA (N,N Diisopropylethylamine) as a base in acetonitrile as solvent to get the desired compounds **8-a** to **8-o**, **8-2a** to **8-2o** and **8-3n**&**8-4j** (Table 6.1 and 6.2) in good yields. Synthesized compounds were estimated for melting points and spectroscopic analysis to conform to confirm the occurrence of desired compounds. Further, all the compounds purity were checked by HPLC method. Preparation, yield, melting point and spectroscopical data of individual compounds were given below:

2-(5-Benzyl-4-phenyl-4H-1,2,4-triazol-3-ylthio)-N-phenylacetamide (8-a): The compound was synthesized according to the general procedure using 5-benzyl-4-phenyl-4H-1,2,4-triazole-3-thiol (0.3g, 1.1 mmol), DIPEA (0.434g, 3.4 mmol) and 2-chloro-N-phenylacetamide (0.209g, 1.2 mmol) to afford as an off-white solid (0.3g, 66%). m.p : 139-140 °C. ^1H NMR (CDCl_3): δ_{H} . 3.88 (s, 2H), 4.03 (s, 2H), 6.91-7.21 (m, 6H), 7.41-7.65 (m, 9H), 10.25 (s, 1H). ^{13}C NMR (CDCl_3): δ_{C} . 169.1, 154.0, 147.7, 146.3, 139.5, 136.8, 130.9, 129.8(2C), 129.3(2C), 128.8(2C), 128.6(3C), 128.4(2C), 128.1, 126.3, 121.5, 40.4, 31.6. EI-MS m/z (Calcd. for $\text{C}_{23}\text{H}_{20}\text{N}_4\text{OS}$: 400.14); Found: 401.17 ($\text{M}+\text{H}$)⁺. Anal Calcd. for $\text{C}_{23}\text{H}_{20}\text{N}_4\text{OS}$: C, 68.98; H, 5.03; N, 13.99; Found: C, 69.02; H, 4.97; N, 13.93.

2-(5-Benzyl-4-phenyl-4H-1,2,4-triazol-3-ylthio)-N-(4-methoxyphenyl)acetamide (8-b): The compound was synthesized according to the general procedure using 5-benzyl-4-phenyl-4H-1,2,4-triazole-3-thiol (0.3g, 1.1 mmol), DIPEA (0.434g, 3.4mmol) and 2-chloro-N-(4-methoxyphenyl) acetamide (0.246g, 1.2 mmol) to afford as an off-white solid (0.287g, 59%). m.p : 161-162 °C. ^1H NMR ($\text{DMSO}-d_6$): δ_{H} . 3.81 (s, 3H), 3.99 (s, 2H), 4.03 (s, 2H), 6.93(d, 2H, $J= 7.5\text{Hz}$), 7.24-7.34 (m, 5H), 7.48-7.55 (m, 7H), 10.26 (s, 1H). ^{13}C NMR ($\text{DMSO}-d_6$): δ_{C} . 169.0, 160.1, 155.2, 147.6, 145.9, 136.7, 130.6, 130.1(2C), 129.2(2C), 129.9 (2C), 128.7(2C), 126.2, 122.8(2C), 115.5(2C), 56.7, 39.3, 30.7. EI-MS m/z (Calcd. for $\text{C}_{24}\text{H}_{22}\text{N}_4\text{O}_2\text{S}$: 430.15); Found: 429.09 ($\text{M}-\text{H}$)⁻. Anal Calcd. for $\text{C}_{24}\text{H}_{22}\text{N}_4\text{O}_2\text{S}$: C, 66.96; H, 5.15; N, 13.01; Found: C, 66.91; H, 5.19; N, 13.05.

2-(5-Benzyl-4-phenyl-4H-1,2,4-triazol-3-ylthio)-N-(3,4-dichlorophenyl)acetamide (8-c): The compound was synthesized according to the general procedure using 5-benzyl-4-phenyl-4H-1,2,4-triazole-3-thiol (0.3g, 1.1 mmol), DIPEA (0.407g, 3.2mmol) and 2-chloro-N-(3,4-dichlorophenyl)acetamide (0.294g, 1.2 mmol) to afford as an off-white solid (0.280g, 53%). m.p

: 146-147 °C. ¹H NMR (DMSO-d₆): δ_H. 3.91 (s, 2H), 4.03(s, 2H), 7.23-7.34 (m, 5H), 7.49-7.62 (m, 7H), 7.92 (s, 1H), 10.18 (s, 1H). ¹³C NMR (DMSO-d₆): δ_C. 169.3, 161.5, 147.9, 138.6, 137.4, 133.9, 130.6, 130.1(3C), 129.8, 129.5(2C), 129.2(3C), 128.9(2C), 126.4, 124.8, 121.6, 39.5, 29.7. EI-MS m/z (Calcd. for C₂₃H₁₈Cl₂N₄OS: 468.06); Found: 469.11(M+H)⁺. Anal Calcd. for C₂₃H₁₈Cl₂N₄OS: C, 58.85; H, 3.87; N, 11.94; Found: C, 58.89; H, 3.81; N, 11.95.

N-(Benzo[d]thiazol-2-yl)-2-(5-benzyl-4-phenyl-4H-1,2,4-triazol-3-ylthio)acetamide (**8-d**): The compound was synthesized according to the general procedure using 5-benzyl-4-phenyl-4H-1,2,4-triazole-3-thiol (0.3g, 1.1 mmol), DIPEA (0.390g, 3.0mmol) and *N*-(benzo[d]thiazol-2-yl)-2-chloroacetamide (0.280g, 1.2 mmol) to afford as an off-white solid (0.3g, 58%). m.p : 279-280 °C. ¹H NMR (DMSO-d₆): δ_H. 3.79 (s, 2H), 3.85 (s, 2H), 7.22-7.33 (m, 5H), 7.48-7.59 (m, 7H), 8.04 (d, *J* = 7.3 Hz, 1H), 8.17 (d, *J* = 7.5, 1H), 9.89 (s, 1H). ¹³C NMR (DMSO-d₆): δ_C. 175.1, 168.7, 153.9(2C), 149.5, 147.8, 137.2, 130.9, 130.3(2C), 130.0(2C), 129.7(3C), 129.4(2C), 126.6(2C), 125.9, 122.5, 122.0, 39.5, 29.1. EI-MS m/z (Calcd. for C₂₄H₁₉N₅OS₂: 457.1); Found: 458.01(M+H)⁺. Anal Calcd. for C₂₄H₁₉N₅OS₂: C, 63.00; H, 4.19; N, 15.31; Found: C, 63.09; H, 4.15; N, 15.27.

2-(5-Benzyl-4-phenyl-4H-1,2,4-triazol-3-ylthio)-*N*-(2-chloro-5-(trifluoromethyl)phenyl)acetamide (**8-e**): The compound was synthesized according to the general procedure using 5-benzyl-4-phenyl-4H-1,2,4-triazole-3-thiol (0.3g, 1.1 mmol), DIPEA (0.434g, 3.4mmol) and 2-chloro-*N*-(2-chloro-5-(trifluoromethyl)phenyl)acetamide (0.336g, 1.2 mmol) to afford as an off-white solid (0.289g, 51%). m.p : 177-178 °C. ¹H NMR (DMSO-d₆): δ_H. 3.82 (s, 2H), 3.86 (s, 2H), 7.22-7.34 (m, 6H), 7.39-7.57 (m, 6H), 7.97 (s, 1H), 9.99 (s, 1H). ¹³C NMR (DMSO-d₆): δ_C. 168.9, 160.7, 146.6, 138.3, 136.8, 134.5, 130.7(2C), 130.2(2C), 129.7(2C), 129.3(2C), 128.9(3C), 126.4(2C), 124.8, 122.6, 119.3, 39.5, 29.2. EI-MS m/z (Calcd. for C₂₄H₁₈ClF₃N₄OS: 502.08); Found: 501.45(M-H)⁻. Anal Calcd. for C₂₄H₁₈ClF₃N₄OS: C, 57.31; H, 3.61; N, 11.14; Found: C, 57.26; H, 3.65; N, 11.09.

2-(5-Benzyl-4-(4-fluorophenyl)-4H-1,2,4-triazol-3-ylthio)-*N*-phenylacetamide (**8-f**): The compound was synthesized according to the general procedure using 2-((5-benzyl-4-(4-fluorophenyl)-4H-1,2,4-triazol-3-yl)thio)-*N*-phenylacetamide (0.3g, 1.0 mmol), DIPEA (0.406g, 3.1 mmol) and 2-chloro-*N*-phenylacetamide (0.196g, 1.2 mmol) to afford as an off-white solid (0.285 g, 65%). m.p : 157-158 °C. ¹H NMR (DMSO-d₆): δ_H. 3.96 (s, 2H), 4.02 (s, 2H), 7.20-7.32

(m, 8H), 7.47-7.64 (m, 6H), 10.27 (s, 1H). ^{13}C NMR (DMSO- d_6): δ_{C} . 168.5, 162.8, 153.4, 147.6, 141.3, 139.0, 136.4, 130.9(2C), 129.8(2C), 128.7(2C), 128.4(2C), 127.9, 125.9, 121.4(2C), 116.1(2C), 39.5, 31.7. EI-MS m/z (Calcd. for $\text{C}_{23}\text{H}_{19}\text{FN}_4\text{OS}$: 418.13); Found: 419.11 ($\text{M}+\text{H}$) $^+$. Anal Calcd. for $\text{C}_{23}\text{H}_{19}\text{FN}_4\text{OS}$: C, 66.01; H, 4.58; N, 13.39; Found: C, 65.98; H, 4.55; N, 13.41.

2-(5-Benzyl-4-(4-fluorophenyl)-4H-1,2,4-triazol-3-ylthio)-N-(4-methoxyphenyl)acetamide (**8-g**):

The compound was synthesized according to the general procedure using 5-benzyl-4-(4-fluorophenyl-4H)-1,2,4-triazole-3-thiol (0.3g, 1.0 mmol), DIPEA (0.434g, 3.4mmol) and 2-chloro-N-(4-methoxyphenyl) acetamide (0.231g, 1.2 mmol) to afford as an off-white solid (0.288g, 61%). Melting point. 177-178 °C. ^1H NMR (DMSO- d_6): δ_{H} . 3.79 (s, 3H), 3.95 (s, 2H), 4.01 (s, 2H), 6.95 (d, $J = 7.3$, 2H), 7.24-7.32 (m, 7H), 7.48 (d, $J = 7.4$ Hz, 2H), 7.63 (d, $J = 7.5$ Hz, 2H), 10.29 (s, 1H). ^{13}C NMR (DMSO- d_6): δ_{C} . 168.9, 163.6, 162.0, 159.7, 148.2, 142.1, 136.8, 131.6, 130.9(2C), 129.7(2C), 129.2(2C), 126.5, 123.7(2C), 115.8(2C), 114.7(2C), 56.6, 39.8, 30.4. EI-MS m/z (Calcd. for $\text{C}_{24}\text{H}_{21}\text{FN}_4\text{O}_2\text{S}$: 448.14); Found: 449.11 ($\text{M}+\text{H}$) $^+$. Anal Calcd. for $\text{C}_{24}\text{H}_{21}\text{FN}_4\text{O}_2\text{S}$: C, 64.27; H, 4.72; N, 12.49; Found: C, 64.31; H, 4.69; N, 12.51.

2-(5-Benzyl-4-(4-fluorophenyl)-4H-1,2,4-triazol-3-ylthio)-N-(3,4-dichlorophenyl)acetamide (**8-h**):

The compound was synthesized according to the general procedure using 5-benzyl-4-(4-fluorophenyl-4H)-1,2,4-triazole-3-thiol (0.3g, 1.0 mmol), DIPEA (0.434g, 3.4mmol) and 2-chloro-N-(3,4-dichlorophenyl)acetamide (0.276g, 1.2 mmol) to afford as an off-white solid (0.289g, 56%). m.p : 163-164 °C. ^1H NMR (DMSO- d_6): δ_{H} . 3.83 (s, 2H), 3.91(s, 2H), 7.24-7.35(m, 7H), 7.52-7.61(m, 4H), 8.05(s, 1H), 10.11 (s, 1H). ^{13}C NMR (DMSO- d_6): δ_{C} . 168.7, 163.4, 161.2, 148.1, 138.7, 137.3, 133.9, 131.8(2C), 131.1(2C), 129.3(3C), 126.5(2C), 125.2, 123.9, 121.6, 116.2(2C), 39.2, 29.3. EI-MS m/z (Calcd. for $\text{C}_{23}\text{H}_{17}\text{Cl}_2\text{FN}_4\text{OS}$: 486.05); Found: 485.66($\text{M}-\text{H}$) $^-$. Anal Calcd. for $\text{C}_{23}\text{H}_{17}\text{Cl}_2\text{FN}_4\text{OS}$: C, 56.68; H, 3.52; N, 11.50; Found: C, 56.62; H, 3.55; N, 11.48.

N-(Benzo[d]thiazol-2-yl)-2-(5-benzyl-4-(4-fluorophenyl)-4H-1,2,4-triazol-3-ylthio)acetamide (**8-i**):

The compound was synthesized according to the general procedure using 5-benzyl-4-(4-fluorophenyl)-4H-1,2,4-triazole-3-thiol (0.3g, 1.0 mmol), DIPEA (0.390g, 3.0mmol) and N-(benzo[d]thiazol-2-yl)-2-chloroacetamide (0.262g, 1.2 mmol) to afford as an off-white solid (0.316g, 63%). m.p. 278-279 °C. ^1H NMR (DMSO- d_6): δ_{H} . 3.79 (s, 2H), 3.83 (s, 2H), 7.22-7.30 (m, 7H), 7.51-7.59 (m, 4H), 8.01(s, 1H), 8.21 (s, 2H), 9.98 (s, 1H). ^{13}C NMR (DMSO- d_6): δ_{C} .

175.1, 168.9, 163.5, 161.7(2C), 149.5, 147.8, 137.4, 131.9, 130.7(2C), 129.7(2C), 129.0(2C), 126.5(2C), 125.8, 124.7, 122.1, 115.9 (2C), 39.2, 29.5. EI-MS m/z (Calcd. for $C_{24}H_{18}FN_5OS_2$: 475.09); Found: 476.23(M+H)⁺. Anal Calcd. for $C_{24}H_{18}FN_5OS_2$: C, 60.61; H, 3.82; N, 14.73; Found: C, 60.67; H, 3.85; N, 14.68.

2-(5-Benzyl-4-(4-fluorophenyl)-4H-1,2,4-triazol-3-ylthio)-N-(2-chloro-5-(trifluoromethyl)phenyl)acetamide (8-j): The compound was synthesized according to the general procedure using 5-benzyl-4-phenyl-4H-1,2,4-triazole-3-thiol (0.3g, 1.0 mmol), DIPEA (0.407g, 3.2mmol) and 2-chloro-N-(2-chloro-5-(trifluoromethyl)phenyl)acetamide (0.315g, 1.2 mmol) to afford as an off-white solid (0.320g, 58%). m.p : 205-206 °C. ¹H NMR (DMSO-d₆): δ_H. 3.80 (s, 2H), 3.88 (s, 2H), 7.24-7.4 (m, 9H), 7.59 (d, J = 7.5 Hz, 2H), 8.03 (s, 1H), 10.21 (s, 1H). ¹³C NMR (DMSO-d₆): δ_C. 168.6, 163.4, 160.8, 148.0, 138.3, 136.9, 134.5, 130.5(2C), 129.7(2C), 129.5(2C), 129.1(2C), 126.3(2C), 125.6, 122.4, 119.1, 116.4(2C), 39.3, 29.6. EI-MS m/z (Calcd. for $C_{24}H_{17}ClF_4N_4OS$: 520.07); Found: 521.14(M+H)⁺. Anal Calcd. for $C_{24}H_{17}ClF_4N_4OS$: C, 55.34; H, 3.29; N, 10.76; Found: C, 55.37; H, 3.32; N, 10.71.

N-(3-Acetylphenyl)-2-(5-benzyl-4-(4-fluorophenyl)-4H-1,2,4-triazol-3-ylthio)acetamide (8-k): The compound was synthesized according to the general procedure using 5-benzyl-4-(4-fluorophenyl)-4H-1,2,4-triazole-3-thiol (0.3g, 1.0 mmol), DIPEA (0.407g, 3.2mmol) and N-(3-acetylphenyl)-2-chloroacetamide (0.245g, 1.2 mmol) to afford as an off-white solid (0.315g, 65%). m.p : 133-134 °C. ¹H NMR (DMSO-d₆): δ_H. 2.58 (s, 3H), 3.79 (s, 2H), 3.86 (s, 2H), 7.24-7.37 (m, 7H), 7.55-7.79 (m, 5H), 8.04 (s, 1H), 9.27 (s, 1H). ¹³C NMR (DMSO-d₆): δ_C. 199.6, 168.8, 163.5, 161.3, 147.9, 141.5(2C), 137.5(2C), 133.7, 131.0(2C), 129.7(2C), 129.1(2C), 126.5(2C), 125.2, 119.3, 115.8(2C), 39.4, 29.8, 29.1. EI-MS m/z (Calcd. for $C_{25}H_{21}FN_4O_2S$: 460.14); Found: 461.12(M+H)⁺. Anal Calcd. for $C_{25}H_{21}FN_4O_2S$: C, 65.20; H, 4.60; N, 12.17; Found: C, 65.21; H, 4.65; N, 12.14.

2-(5-Benzyl-4-(4-methoxyphenyl)-4H-1,2,4-triazol-3-ylthio)-N-(3,4-dichlorophenyl)acetamide (8-l): The compound was synthesized according to the general procedure using 5-benzyl-4-(4-methoxyphenyl)-4H-1,2,4-triazole-3-thiol (0.3g, 1.0 mmol), DIPEA (0.407g, 3.2mmol) and 2-chloro-N-(3,4-dichlorophenyl)acetamide (0.265g, 1.1 mmol) to afford as an off-white solid (0.290g, 58%). m.p : 231-232 °C. ¹H NMR (DMSO-d₆): δ_H. 3.75 (s, 3H), 3.78 (s, 2H), 3.85(s, 2H), 6.94 (d, J = 7.3 Hz, 2H), 7.26-7.37(m, 5H), 7.50-7.64 (m, 4H), 8.01 (s, 1H), 10.23 (s, 1H).

^{13}C NMR (DMSO- d_6): δ_{C} . 168.9, 161.5, 153.6, 147.7, 138.5(2C), 136.8, 135.5(2C), 131.5, 130.9, 129.7(3C), 129.0(2C), 126.1, 123.8, 121.3, 114.7(2C), 56.4, 39.1, 29.5. EI-MS m/z (Calcd. for $\text{C}_{24}\text{H}_{20}\text{Cl}_2\text{N}_4\text{O}_2\text{S}$: 498.07); Found: 499.4(M+H) $^+$. Anal Calcd. for $\text{C}_{24}\text{H}_{20}\text{Cl}_2\text{N}_4\text{O}_2\text{S}$: C, 57.72; H, 4.04; N, 11.22; Found: C, 57.76; H, 4.01; N, 11.25.

N-(Benzo[d]thiazol-2-yl)-2-(5-benzyl-4-(4-methoxyphenyl)-4H-1,2,4-triazol-3-ylthio)acetamide (**8-m**): The compound was synthesized according to the general procedure using 5-benzyl-4-(4-methoxyphenyl)-4H-1,2,4-triazole-3-thiol (0.3g, 1.1 mmol), DIPEA (0.434g, 3.4mmol) and *N*-(benzo[d]thiazol-2-yl)-2-chloroacetamide (0.252g, 1.1 mmol) to afford as brown solid (0.314g, 64%). m.p : 275-276 °C. ^1H NMR (DMSO- d_6): δ_{H} . 3.77 (s, 3H), 3.78 (s, 2H), 3.84 (s, 2H), 6.89 (d, $J = 7.5$ Hz, 2H), 7.23-7.33 (m, 5H), 7.50-7.55 (m, 4H), 8.05 (d, $J = 7.3$ Hz, 1H), 8.20 (d, $J = 7.6$, 1H), 10.12 (s, 1H). ^{13}C NMR (DMSO- d_6): δ_{C} . 175.3, 168.5, 160.9, 153.5(2C), 149.7, 138.3, 136.5, 136.7(2C), 131.4, 129.9(2C), 129.1(2C), 126.6(2C), 126.4, 122.1, 119.4, 114.7(2C), 56.3, 39.6, 29.2. EI-MS m/z (Calcd. for $\text{C}_{25}\text{H}_{21}\text{N}_5\text{O}_2\text{S}_2$: 487.11); Found: 456.65 (M-H) $^-$. Anal Calcd. for $\text{C}_{25}\text{H}_{21}\text{N}_5\text{O}_2\text{S}_2$: C, 61.58; H, 4.34; N, 14.36; Found: C, 61.63; H, 4.36; N, 14.44.

2-(5-Benzyl-4-(4-methoxyphenyl)-4H-1,2,4-triazol-3-ylthio)-*N*-(2-chloro-5-(trifluoromethyl)phenyl)acetamide (**8-n**): The compound was synthesized according to the general procedure using 5-benzyl-4-(4-methoxyphenyl)-4H-1,2,4-triazole-3-thiol (0.3g, 1.0 mmol), DIPEA (0.407g, 3.2mmol) and 2-chloro-*N*-(2-chloro-5-(trifluoromethyl)phenyl)acetamide (0.302g, 1.1 mmol) to afford as an off-white solid (0.310g, 58%). m.p : 171-172 °C. ^1H NMR (DMSO- d_6): δ_{H} . 3.71 (s, 3H), 3.79 (s, 2H), 3.89 (s, 2H), 6.96 (d, $J = 7.6$ Hz, 2H), 7.19-7.38 (m, 7H), 7.59 (d, $J = 7.2$ Hz, 2H), 8.05 (s, 1H), 10.08 (s, 1H). ^{13}C NMR (DMSO- d_6): δ_{C} . 168.9, 161.5, 161.0, 147.8, 138.3 (2C), 136.6, 134.6(2C), 130.0(2C), 129.8(2C), 129.3(2C), 126.5(2C), 124.8, 122.6, 119.4, 114.8(2C), 56.5, 39.7, 29.4. EI-MS m/z (Calcd. for $\text{C}_{25}\text{H}_{20}\text{ClF}_3\text{N}_4\text{O}_2\text{S}$: 532.09); Found: 531.01(M-H) $^-$. Anal Calcd. for $\text{C}_{25}\text{H}_{20}\text{ClF}_3\text{N}_4\text{O}_2\text{S}$: C, 56.34; H, 3.78; N, 10.51; Found: C, 56.30; H, 3.81; N, 10.47.

N-(3-Acetylphenyl)-2-(5-benzyl-4-(4-methoxyphenyl)-4H-1,2,4-triazol-3-ylthio)acetamide (**8-o**): The compound was synthesized according to the general procedure using 5-benzyl-4-(4-methoxyphenyl)-4H-1,2,4-triazole-3-thiol (0.3g, 1.0 mmol), DIPEA (0.390g, 3.0mmol) and *N*-(3-acetylphenyl)-2-chloroacetamide (0.235g, 1.1 mmol) to afford as brown solid (0.316g, 66%). m.p : 100-101 °C. ^1H NMR (DMSO- d_6): δ_{H} . 2.53 (s, 3H), 3.75 (s, 3H), 3.80 (s, 2H), 3.89 (s, 2H),

6.94 (d, $J = 7.3$ Hz, 2H), 7.23-7.33 (m, 5H), 7.53-7.83 (m, 5H), 8.12 (s, 1H), 9.26 (s, 1H). ^{13}C NMR (DMSO- d_6): δ_{C} . 200.3, 168.9, 161.5, 147.8, 139.1, 137.9, 137.3, 136.3(2C), 135.6(2C), 133.6, 129.9(2C), 129.0(2C), 126.8(2C), 124.7, 119.3, 114.6(2C), 56.5, 39.2, 29.7, 29.3. EI-MS m/z (Calcd. for $\text{C}_{26}\text{H}_{24}\text{N}_4\text{O}_3\text{S}$: 472.16); Found: 473.17(M+H) $^+$. Anal Calcd. for $\text{C}_{26}\text{H}_{24}\text{N}_4\text{O}_3\text{S}$: C, 66.08; H, 5.12; N, 11.86; Found: C, 66.02; H, 5.15; N, 11.89.

2-(5-(2-Chlorophenyl)-4-phenyl-4H-1,2,4-triazol-3-ylthio)-N-phenylacetamide (**8-2a**): The compound was synthesized according to the general procedure using 5-(2-chlorophenyl)-4-phenyl-4H-1,2,4-triazole-3-thiol (0.3g, 1.0 mmol), DIPEA (0.403g, 3.1mmol) and 2-chloro-N-phenylacetamide (0.195g, 1.3 mmol) to afford as an off-white solid (0.255g, 58%). m.p : 193-194 °C. ^1H NMR (DMSO- d_6): δ_{H} . 3.89 (s, 2H), 7.37-7.69 (m, 14H), 10.01 (s, 1H). ^{13}C NMR (DMSO- d_6): δ_{C} . 169.1, 153.8, 148.3, 143.7, 139.2(2C), 132.9, 130.7, 130.4, 129.8(3C), 129.3(3C), 128.9, 127.7, 126.0(2C), 122.3(2C), 39.4. EI-MS m/z (Calcd. for $\text{C}_{22}\text{H}_{17}\text{ClN}_4\text{OS}$: 420.08); Found: 421.02(M+H) $^+$. Anal Calcd. for $\text{C}_{22}\text{H}_{17}\text{ClN}_4\text{OS}$: C, 62.78; H, 4.07; N, 13.31; Found: C, 62.75; H, 4.12; N, 13.27.

2-(5-(2-Chlorophenyl)-4-phenyl-4H-1,2,4-triazol-3-ylthio)-N-(4-methoxyphenyl)acetamide (**8-2b**): The compound was synthesized according to the general procedure using 5-(2-chlorophenyl)-4-phenyl-4H-1,2,4-triazole-3-thiol (0.3g, 1.0 mmol), DIPEA (0.430g, 3.1mmol) and 2-chloro-N-(4-methoxyphenyl)acetamide (0.229g, 1.3 mmol) to afford as an off-white solid (0.257g, 55%). m.p : 237-238 °C. ^1H NMR (DMSO- d_6): δ_{H} . 3.75 (s, 3H), 3.99(s, 2H), 6.91 (s, $J = 7.6$ Hz, 2H), 7.36-7.7 (m, 11H), 9.82 (s, 1H). ^{13}C NMR (DMSO- d_6): δ_{C} . 168.7, 157.1, 153.9, 148.3, 138.8, 132.6, 131.4, 131.0(2C), 129.7, 129.4, 129.1(3C), 128.0, 125.9(2C), 123.1(2C), 114.9(2C), 56.6, 39.3. EI-MS m/z (Calcd. for $\text{C}_{23}\text{H}_{19}\text{ClN}_4\text{O}_2\text{S}$: 450.09); Found: 449.12 (M-H) $^-$. Anal Calcd. for $\text{C}_{23}\text{H}_{19}\text{ClN}_4\text{O}_2\text{S}$: C, 61.26; H, 4.25; N, 12.42; Found: C, 61.35; H, 4.27; N, 12.33.

2-(5-(2-Chlorophenyl)-4-phenyl-4H-1,2,4-triazol-3-ylthio)-N-(3,4-dichlorophenyl)acetamide (**8-2c**): The compound was synthesized according to the general procedure using 5-(2-chlorophenyl)-4-phenyl-4H-1,2,4-triazole-3-thiol (0.3g, 1.0 mmol), di-isopropyl ethylamine (DIPEA) (0.403g, 3.1mmol) and 2-chloro-N-(3,4-dichlorophenyl) acetamide (0.273g, 1.3 mmol) to afford as an off-white solid (0.260g, 51%). m.p : 201-202 °C. ^1H NMR (DMSO- d_6): δ_{H} . 3.89 (s, 2H), 7.37-7.63 (m, 11H), 8.01 (s, 1H), 9.89 (s, 1H). ^{13}C NMR (DMSO- d_6): δ_{C} . 169.0, 153.8,

148.5, 139.3, 138.7(2C), 134.2, 133.5, 131.0(2C), 130.8(2C), 129.7, 129.5(3C), 127.9, 126.1(2C), 124.8, 121.5, 39.4. EI-MS m/z (Calcd. for $C_{22}H_{15}Cl_3N_4OS$: 488); Found: 489.01 ($M+H$)⁺. Anal Calcd. for $C_{22}H_{15}Cl_3N_4OS$: C, 53.95; H, 3.09; N, 11.44; Found: C, 53.98; H, 3.04; N, 11.47.

2-(5-(2-Chlorophenyl)-4-phenyl-4H-1,2,4-triazol-3-ylthio)-N-(benzo[d]thiazol-2-yl) acetamide (8-2d): The compound was synthesized according to the general procedure using 5-(2-chlorophenyl)-4-phenyl-4H-1,2,4-triazole-3-thiol (0.3g, 1.0 mmol), DIPEA (0.403g, 3.1mmol) and N-(benzo[d]thiazol-2-yl)-2-chloroacetamide (0.260g, 1.3 mmol) to afford as an off-white solid (0.285g, 57%). m.p : 280-281 °C. ¹H NMR (DMSO-d₆): δ_H. 3.81 (s, 2H), 7.40-7.66 (m, 11H), 8.03 (d, $J = 7.2$ Hz, 1H), 8.20 (d, $J = 7.4$ Hz, 1H), 10.31 (s, 1H). ¹³C NMR (DMSO-d₆): δ_C. 174.9, 169.3, 153.8(2C), 149.6, 148.4, 139.1, 132.9, 131.1(2C), 130.5(2C), 129.5(3C), 127.6, 126.5(3C), 125.1, 122.6, 119.2, 39.0. EI-MS m/z (Calcd. for $C_{23}H_{16}ClN_5OS_2$: 477.05); Found: 476.02 ($M-H$)⁻. Anal Calcd. for $C_{23}H_{16}ClN_5OS_2$: C, 57.79; H, 3.37; N, 14.65; Found: C, 57.83; H, 3.39; N, 14.61.

2-(5-(2-Chlorophenyl)-4-phenyl-4H-1,2,4-triazol-3-ylthio)-N-(2-chloro-5-(trifluoromethyl)phenyl)acetamide (8-2e): The compound was synthesized according to the general procedure using 5-(2-chlorophenyl)-4-phenyl-4H-1,2,4-triazole-3-thiol (0.3g, 1.0 mmol), DIPEA (0.403g, 3.1mmol) and 2-chloro-N-(2-chloro-5-(trifluoromethyl)phenyl)acetamide (0.312g, 1.3 mmol) to afford as an off-white solid (0.280g, 51%). m.p : 147-148 °C. ¹H NMR (DMSO-d₆): δ_H. 3.99 (s, 2H), 7.19-7.77 (m, 11H), 8.04 (s, 1H), 10.21 (s, 1H). ¹³C NMR (DMSO-d₆): δ_C. 169.4, 153.8, 148.5, 139.1, 138.5, 134.3, 132.9, 130.7, 130.4, 130.0, 129.8, 129.4(3C), 128.5(3C), 124.9(3C), 122.7, 119.5, 39.9. EI-MS m/z (Calcd. for $C_{23}H_{15}Cl_2F_3N_4OS$: 522.03); Found: 523.25 ($M+H$)⁺. Anal Calcd. for $C_{23}H_{15}Cl_2F_3N_4OS$: C, 52.78; H, 2.89; N, 10.71; Found: C, 52.69; H, 2.92; N, 10.75.

2-(5-(2-Chlorophenyl)-4-(4-fluorophenyl)-4H-1,2,4-triazol-3-ylthio)-N-phenylacetamide (8-2f): The compound was synthesized according to the general procedure using 5-(2-chlorophenyl)-4-(4-fluorophenyl)-4H-1,2,4-triazole-3-thiol (0.3g, 1.0 mmol), DIPEA (0.380g, 2.9mmol) and 2-chloro-N-phenylacetamide (0.183g, 1.2 mmol) to afford as an yellow sticky (0.260g, 60%). m.p : 176-177 °C. ¹H NMR (DMSO-d₆): δ_H. 3.86 (s, 2H), 7.23 (d, $J = 7.6$ Hz, 2H), 7.25-7.61 (m, 11H), 9.81 (s, 1H). ¹³C NMR (DMSO-d₆): δ_C. 168.9, 163.6, 153.8, 148.3, 139.0(3C), 132.7, 131.9,

130.5(3C), 129.8(3C), 128.5, 127.9, 121.9(2C), 116.2(2C), 39.5. EI-MS m/z (Calcd. for $C_{22}H_{16}ClFN_4OS$: 438.07); Found: 439.12 ($M+H$)⁺. Anal Calcd. for $C_{22}H_{16}ClFN_4OS$: C, 60.20; H, 3.67; N, 12.77; Found: C, 60.22; H, 3.65; N, 12.79.

2-(5-(2-Chlorophenyl)-4-(4-fluorophenyl)-4H-1,2,4-triazol-3-ylthio)-N-(4-methoxyphenyl)acetamide (8-2g): The compound was synthesized according to the general procedure using 5-(2-chlorophenyl)-4-(4-fluorophenyl)-4H-1,2,4-triazole-3-thiol (0.3g, 1.0 mmol), DIPEA (0.380g, 2.9 mmol) and 2-chloro-N-(4-methoxyphenyl) acetamide (0.215g, 1.2 mmol) to afford as an off-white solid (0.247g, 54%). m.p : 234-235 °C. ¹H NMR (DMSO-d₆): δ_H. 3.71 (s, 3H), 3.85 (s, 2H), 6.94 (d, $J = 7.4$ Hz, 2H), 7.25 (d, $J = 7.6$ Hz, 2H), 7.38-7.74 (m, 8H), 9.79 (s, 1H). ¹³C NMR (DMSO-d₆): δ_C. 168.9, 163.5, 157.1, 153.7, 148.4, 139.2(2C), 132.8, 132.3, 131.5(3C), 129.7(2C), 128.1, 123.3(2C), 116.0(2C), 115.4(2C), 56.2, 39.5. EI-MS m/z (Calcd. for $C_{23}H_{18}ClFN_4O_2S$: 468.08); Found: 469.14 ($M+H$)⁺. Anal Calcd. for $C_{23}H_{18}ClFN_4O_2S$: C, 58.91; H, 3.87; N, 11.95; Found: C, 58.95; H, 3.92; N, 11.86.

2-(5-(2-Chlorophenyl)-4-(4-fluorophenyl)-4H-1,2,4-triazol-3-ylthio)-N-(3,4-dichlorophenyl)acetamide (8-2h): The compound was synthesized according to the general procedure using 5-(2-chlorophenyl)-4-(4-fluorophenyl)-4H-1,2,4-triazole-3-thiol (0.3g, 1.0 mmol), DIPEA (0.380g, 2.9 mmol) and 2-chloro-N-(3,4-dichlorophenyl)acetamide (0.257g, 1.2 mmol) to afford as an off-white solid (0.270g, 54%). m.p : 205-206 °C. ¹H NMR (DMSO-d₆): δ_H. 3.85 (s, 2H), 7.28 (d, $J = 7.4$ Hz, 2H), 7.38-7.68 (m, 8H), 7.99 (s, 1H), 10.12 (s, 1H). ¹³C NMR (DMSO-d₆): δ_C. 168.9, 163.4, 153.7, 148.3, 139.1(3C), 132.7, 131.9, 130.8, 130.5(3C), 129.6(2C), 129.1, 127.7, 124.5, 121.7, 116.2(2C), 39.1. EI-MS m/z (Calcd. for $C_{22}H_{14}Cl_3FN_4OS$: 505.99); Found: 504.87 ($M-H$)⁻. Anal Calcd. for $C_{22}H_{14}Cl_3FN_4OS$: C, 52.04; H, 2.78; N, 11.03; Found: C, 51.99; H, 2.82; N, 11.05.

2-(5-(2-Chlorophenyl)-4-(4-fluorophenyl)-4H-1,2,4-triazol-3-ylthio)-N-(benzo[d]thiazol-2-yl)acetamide (8-2i): The compound was synthesized according to the general procedure using 5-(2-chlorophenyl)-4-(4-fluorophenyl)-4H-1,2,4-triazole-3-thiol (0.3g, 1.0 mmol), DIPEA (0.380g, 2.9mmol) and N-(benzo[d]thiazol-2-yl)-2-chloroacetamide (0.245g, 1.2 mmol) to afford as an off-white solid (0.270g, 55%). m.p : 270-271 °C. ¹H NMR (DMSO-d₆): δ_H. 3.81 (s, 2H), 7.26-7.59 (m, 10H), 8.04 (d, $J = 7.6$ Hz, 1H), 8.21 (d, $J = 7.4$, 1H), 9.98 (s, 1H). ¹³C NMR (DMSO-d₆): δ_C. 175.1, 168.8, 163.5, 154.0(2C), 149.9, 139.4(2C), 132.7, 131.6, 130.7(3C), 129.8(2C),

128.1, 125.9, 125.3, 124.8, 122.5, 116.0(2C), 39.4. EI-MS m/z (Calcd. for $C_{23}H_{15}ClFN_5OS_2$: 495.04); Found: 496.25 ($M+H$)⁺. Anal Calcd. for $C_{23}H_{15}ClFN_5OS_2$: C, 55.70; H, 3.05; N, 14.12; Found: C, 55.63; H, 3.01; N, 14.16.

2-(5-(2-Chlorophenyl)-4-(4-fluorophenyl)-4H-1,2,4-triazol-3-ylthio)-N-(2-chloro-5-(trifluoromethyl)phenyl)acetamide (8-2j): The compound was synthesized according to the general procedure using 5-(2-chlorophenyl)-4-(4-fluorophenyl)-4H-1,2,4-triazole-3-thiol (0.3g, 1.0 mmol), DIPEA (0.380g, 2.9mmol) and 2-chloro-N-(2-chloro-5-(trifluoromethyl)phenyl)acetamide (0.294g, 1.2 mmol) to afford as pale yellow solid (0.3g, 56%). m.p : 106-107 °C. ¹H NMR (DMSO-*d*₆): δ_H. 3.99 (s, 2H), 7.26-7.68 (m, 10H), 8.23 (s, 1H), 9.86 (s, 1H). ¹³C NMR (DMSO-*d*₆): δ_C. 169.3, 163.7, 153.9, 148.1, 139.3(2C), 138.2, 132.8, 131.1(3C), 129.7(3C), 128.3, 127.5, 126.3, 125.1, 122.9, 119.6, 116.4(2C), 39.7. EI-MS m/z (Calcd. for $C_{23}H_{14}Cl_2F_4N_4OS$: 540.02); Found: 539.12 ($M-H$)⁻. Anal Calcd. for $C_{23}H_{14}Cl_2F_4N_4OS$: C, 51.03; H, 2.61; N, 10.35; Found: C, 51.04; H, 2.57; N, 10.38.

2-(5-(2-Chlorophenyl)-4-(4-fluorophenyl)-4H-1,2,4-triazol-3-ylthio)-N-(3-acetylphenyl)acetamide (8-2k): The compound was synthesized according to the general procedure using 5-(2-chlorophenyl)-4-(4-fluorophenyl)-4H-1,2,4-triazole-3-thiol (0.3g, 1.0 mmol), DIPEA (0.380g, 2.9 mmol) and N-(3-acetylphenyl)-2-chloroacetamide (0.228g, 1.2 mmol) to afford as an off-white solid (0.273g, 58%). m.p : 165-166 °C. ¹H NMR (DMSO-*d*₆): δ_H. 2.57 (s, 3H), 3.98 (s, 2H), 7.25 (d, $J = 7.1$ Hz, 2H), 7.37-7.79 (m, 9H), 8.23 (s, 1H), 9.96 (s, 1H). ¹³C NMR (DMSO-*d*₆): δ_C. 198.4, 168.8, 163.5, 154.0, 148.4, 139.2, 138.9(3C), 132.8, 132.1, 130.5(3C), 129.4, 129.0, 128.1, 126.5, 125.3, 124.9, 119.2, 116.0, 39.6, 29.8. EI-MS m/z (Calcd. for $C_{24}H_{18}ClFN_4O_2S$: 480.08); Found: 481.12 ($M+H$)⁺. Anal Calcd. for $C_{24}H_{18}ClFN_4O_2S$: C, 59.94; H, 3.77; N, 11.65; Found: C, 59.99; H, 3.74; N, 11.61.

2-(5-(2-Chlorophenyl)-4-(4-methoxyphenyl)-4H-1,2,4-triazol-3-ylthio)-N-(3,4-dichlorophenyl)acetamide (8-2l): The compound was synthesized according to the general procedure using 5-(2-chlorophenyl)-4-(4-methoxyphenyl)-4H-1,2,4-triazole-3-thiol (0.3g, 1.0 mmol), DIPEA (0.365g, 2.8mmol) and 2-chloro-N-(3,4-dichlorophenyl)acetamide (0.248g, 1.1 mmol) to afford as a yellow solid (0.246g, 50%). m.p : 184-185 °C. ¹H NMR (DMSO-*d*₆): δ_H. 3.75 (s, 3H), 3.87 (s, 2H), 7.01 (d, $J = 7.2$ Hz, 2H), 7.38-7.69 (m, 8H), 8.03 (s, 1H), 10.21 (s, 1H). ¹³C NMR (DMSO-*d*₆): δ_C. 169.2, 161.5, 159.1, 148.4, 139.6(2C), 136.1, 134.3(2C), 132.9,

131.7, 131.0(2C), 130.2(3C), 127.7, 124.3, 121.9, 114.6(2C), 56.2, 39.5. EI-MS m/z (Calcd. for $C_{23}H_{17}Cl_3N_4O_2S$: 518.01); Found: 519.13 (M+H)⁺. Anal Calcd. for $C_{23}H_{17}Cl_3N_4O_2S$: C, 53.14; H, 3.30; N, 10.78; Found: C, 53.19; H, 3.27; N, 10.81.

2-(5-(2-Chlorophenyl)-4-(4-methoxyphenyl)-4H-1,2,4-triazol-3-ylthio)-N-(benzo[d]thiazol-2-yl)acetamide (8-2m): The compound was synthesized according to the general procedure using 5-(2-chlorophenyl)-4-(4-methoxyphenyl)-4H-1,2,4-triazole-3-thiol (0.3g, 1.0 mmol), DIPEA (0.365g, 2.8 mmol) and N-(benzo[d]thiazol-2-yl)-2-chloroacetamide (0.235g, 1.1 mmol) to afford as an off-white solid (0.260g, 54%). m.p : 263-264 °C. ¹H NMR (DMSO-d₆): δ_H. 3.71 (s, 3H), 3.85 (s, 2H), 6.89 (d, *J* = 7.4 Hz, 2H), 7.36-7.69 (m, 8H), 8.09-8.20 (m, 2H), 9.99 (s, 1H),. ¹³C NMR (DMSO-d₆): δ_C. 175.3, 168.9, 161.5, 153.8(2C), 148.2, 139.0, 136.3, 135.7(2C), 132.5, 131.1(2C), 129.4(2C), 126.7, 126.3, 125.0, 122.5, 122.3, 114.8(2C), 56.4, 39.7. EI-MS m/z (Calcd. for $C_{24}H_{18}ClN_5O_2S_2$: 507.06); Found: 508.25 (M+H)⁺. Anal Calcd. for $C_{24}H_{18}ClN_5O_2S_2$: C, 56.74; H, 3.57; N, 13.79; Found: C, 56.79; H, 3.52; N, 13.85.

2-(5-(2-Chlorophenyl)-4-(4-methoxyphenyl)-4H-1,2,4-triazol-3-ylthio)-N-(2-chloro-5-(trifluoromethyl)phenyl)acetamide (8-2n): The compound was synthesized according to the general procedure using 5-(2-chlorophenyl)-4-(4-methoxyphenyl)-4H-1,2,4-triazole-3-thiol (0.3g, 1.0 mmol), DIPEA (0.365g, 2.8 mmol) and 2-chloro-N-(2-chloro-5-(trifluoromethyl)phenyl) acetamide (0.283g, 1.1 mmol) to afford as an off-white solid (0.255g, 50%). m.p : 239-240 °C. ¹H NMR (DMSO-d₆): δ_H. 3.86 (s, 3H), 4.05 (s, 2H), 6.98 (d, *J* = 7.6 Hz, 2H), 7.33-7.75 (m, 8H), 8.02 (s, 1H), 9.99 (s, 1H). ¹³C NMR (DMSO-d₆): δ_C. 169.5, 161.3, 153.8, 148.4, 139.1, 138.4, 134.6, 132.9(2C), 131.5, 131.0, 129.8(3C), 128.1, 126.4, 124.7, 122.9, 122.3, 119.5, 114.8(2C), 56.4, 39.7. EI-MS m/z (Calcd. for $C_{24}H_{17}Cl_2F_3N_4O_2S$: 552.04); Found: 553.12 (M+H)⁺. Anal Calcd. for $C_{24}H_{17}Cl_2F_3N_4O_2S$: C, 52.09; H, 3.10; N, 10.12; Found: C, 52.12; H, 3.15; N, 10.07.

2-(5-(2-Chlorophenyl)-4-(4-methoxyphenyl)-4H-1,2,4-triazol-3-ylthio)-N-(3-acetylphenyl)acetamide (8-2o): The compound was synthesized according to the general procedure using 5-(2-chlorophenyl)-4-(4-methoxyphenyl)-4H-1,2,4-triazole-3-thiol (0.3g, 1.0 mmol), DIPEA (0.365g, 2.8 mmol) and N-(3-acetylphenyl)-2-chloroacetamide (0.220g, 1.1 mmol) to afford as a yellow sticky (0.264g, 57%). m.p : 118-119 °C. ¹H NMR (DMSO-d₆): δ_H. 2.52 (s, 3H), 3.77 (s, 3H), 3.89 (s, 2H), 6.97 (d, *J* = 7.6 Hz, 2H), 7.40-7.82 (m, 9H), 8.30 (s, 1H),

9.75 (s, 1H). ^{13}C NMR (DMSO- d_6): δ_{C} . 200.2, 168.9, 161.4, 153.9, 148.3, 139.1, 138.9, 137.7, 133.0, 131.6(2C), 131.2, 130.8, 130.1, 129.6(2C), 127.9, 126.9, 125.2, 119.4, 114.8(2C), 56.3, 39.7, 30.1. EI-MS m/z (Calcd. for $\text{C}_{25}\text{H}_{21}\text{ClN}_4\text{O}_3\text{S}$: 492.1); Found: 493.15 ($\text{M}+\text{H}$) $^+$. Anal Calcd. for $\text{C}_{25}\text{H}_{21}\text{ClN}_4\text{O}_3\text{S}$: C, 60.91; H, 4.29; N, 11.36; Found: C, 60.93; H, 4.25; N, 11.31.

3-(5-Benzyl-4-(4-methoxyphenyl)-4H-1,2,4-triazol-3-ylthio)-N-(2-chloro-5-(trifluoromethyl)phenyl)propanamide (8-3n): The compound was synthesized according to the general procedure using 5-benzyl-4(4-methoxyphenyl)-4H-1,2,4-triazole-3-thiol (0.3g, 1.0 mmol), DIPEA (0.365g ,2.8 mmol) and N-(2-chloro-5-(trifluoromethyl) phenyl) propanamide (0.261g, 1.0 mmol) to afford as a brownish yellow solid (0.265g, 51%). m.p : 122-123 °C. ^1H NMR (DMSO- d_6): δ_{H} . 2.62 (t, $J = 6.9$ Hz, 2H), 3.43 (t, $J = 6.9$ Hz, 2H), 3.86 (s, 3H), 3.99 (s, 2H), 6.96 (d, $J = 7.6$ Hz, 2H), 7.25-7.73 (m, 9H), 8.08 (s, 1H), 10.12 (s, 1H). ^{13}C NMR (DMSO- d_6): δ_{C} . 174.4, 161.9, 161.2, 147.8, 138.5, 137.0, 134.7, 131.4, 130.2, 129.9, 129.5(3C), 129.0(2C), 125.6(2C), 124.0, 122.3, 119.6, 115.7(2C), 56.5, 34.2, 30.8, 30.0. EI-MS m/z (Calcd. for $\text{C}_{26}\text{H}_{22}\text{ClF}_3\text{N}_4\text{O}_2\text{S}$: 546.11); Found: 547.25 ($\text{M}+\text{H}$) $^+$. Anal Calcd. for $\text{C}_{26}\text{H}_{22}\text{ClF}_3\text{N}_4\text{O}_2\text{S}$: C, 57.09; H, 4.05; N, 10.24; Found: C, 57.04; H, 4.11; N, 10.19.

3-(5-(2-Chlorophenyl)-4-(4-fluorophenyl)-4H-1,2,4-triazol-3-ylthio)-N-(2-chloro-5-(trifluoromethyl)phenyl)propanamide (8-4j): The compound was synthesized according to the general procedure using 5-(2-chlorophenyl)-4-(4-fluorophenyl)-4H-1,2,4-triazole-3-thiol (0.3g, 1.0 mmol), DIPEA (0.380g ,2.9 mmol) and N-(2-chloro-5-(trifluoromethyl)phenyl)propanamide (0.271g, 1.0 mmol) to afford as an off-white solid (0.276g, 51%). m.p : 119-120 °C. ^1H NMR (DMSO- d_6): δ_{H} . 2.65 (t, $J = 6.9$ Hz, 2H), 3.35 (t, $J = 6.9$ Hz, 2H), 7.23-7.73 (m, 10H), 8.09 (s, 1H), 10.01 (s, 1H). ^{13}C NMR (DMSO- d_6): δ_{C} . 174.5, 163.2, 153.9, 148.4, 139.1, 138.6, 134.3, 132.8, 132.2, 130.9, 130.0(2C), 129.5(2C), 129.1, 128.3, 125.5(2C), 122.8, 119.5, 116.3(2C), 34.1, 30.4. EI-MS m/z (Calcd. for $\text{C}_{24}\text{H}_{16}\text{Cl}_2\text{F}_4\text{N}_4\text{OS}$: 554.04); Found: 553.12 ($\text{M}-\text{H}$) $^-$. Anal Calcd. for $\text{C}_{24}\text{H}_{16}\text{Cl}_2\text{F}_4\text{N}_4\text{OS}$: C, 51.90; H, 2.90; N, 10.09; Found: C, 51.87; H, 2.92; N, 10.14.

2-((5-Benzyl-4-phenyl-4H-1,2,4-triazol-3-yl)thio)-N-(2,4-dimethoxyphenyl)acetamide (Lead-8): The compound was synthesized according to the general procedure using 5-benzyl-4(4-methoxyphenyl)-4H-1,2,4-triazole-3-thiol (0.3g, 1.0 mmol), DIPEA (0.365g, 2.8 mmol) and N-(2-chloro-5-(trifluoromethyl) phenyl) propanamide (0.260g, 1.0 mmol) to afford as a brownish yellow solid (0.361g, 69%). m.p : 128-130 °C. ^1H NMR (DMSO- d_6): δ_{H} . 3.86 (s, 6H), 3.99 (s,

2H), 4.17 (s, 2H), 6.69-7.79 (m, 13H), 10.12 (s, 1H). ^{13}C NMR (DMSO- d_6): δ_{C} . 170.4, 168.3, 153.6(2C), 147.8, 145.1, 136.5, 129.6(2C), 129.0(2C), 128.8(3C), 128.4(2C), 125.6, 123.7, 120.2, 106.9, 100.3, 55.7(2C), 38.7, 30.8. EI-MS m/z (Calcd. for $\text{C}_{25}\text{H}_{24}\text{N}_4\text{O}_3\text{S}$: 460.55); Found: 461.67 ($\text{M}+\text{H}$) $^+$. Anal Calcd. for $\text{C}_{25}\text{H}_{24}\text{N}_4\text{O}_3\text{S}$: C, 62.72; H, 5.16; N, 11.70; Found: C, 63.02; H, 5.10; N, 11.18.

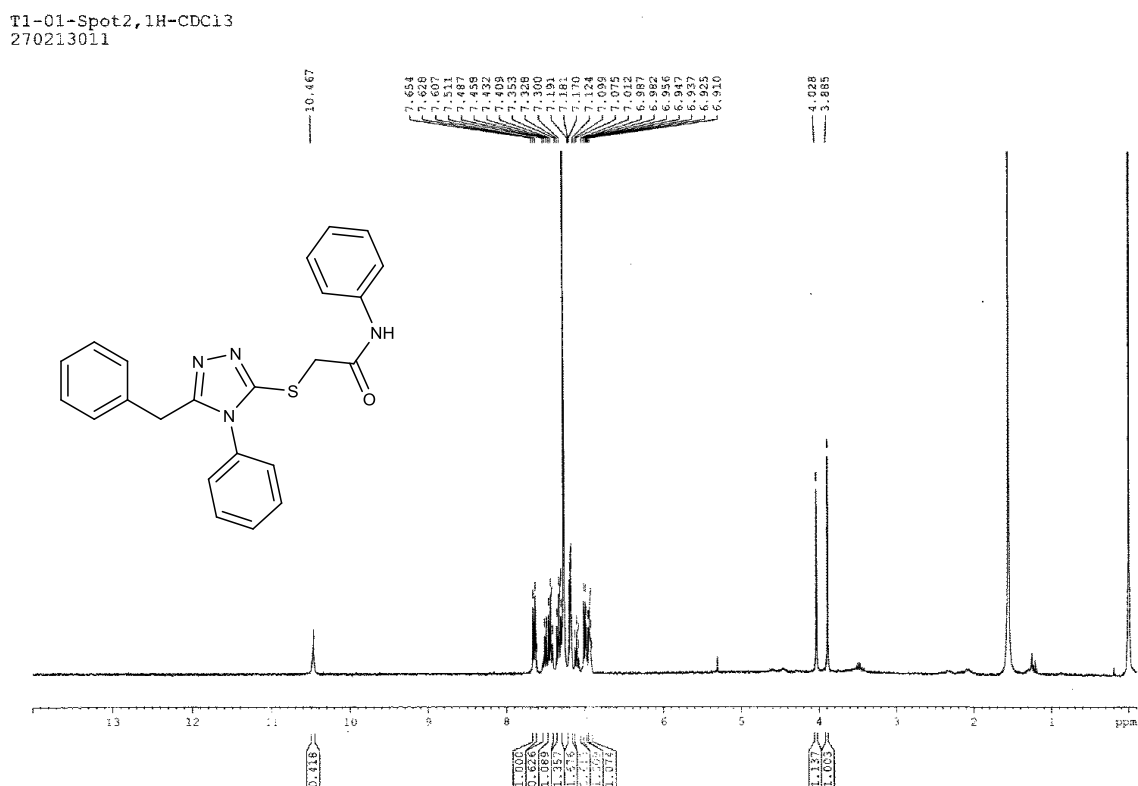
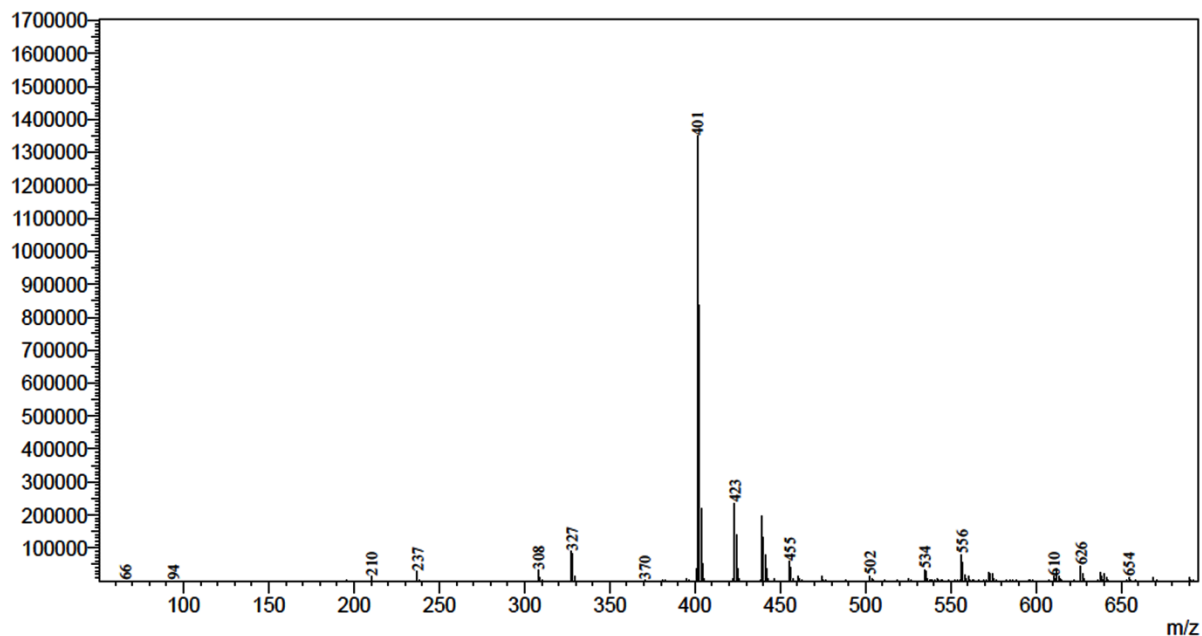


Figure 6.1 Spectral representation ^1H NMR spectra of compound **8-a**

<Spectrum>

Line#:1 R.Time:1.030(Scan#:207)
MassPeaks:178
RawMode:Averaged 0.670-1.810(135-363) BasePeak:401(1349263)
BG Mode:Averaged 0.000-0.660(1-133) Segment 1 - Event 1



Line#:2 R.Time:1.025(Scan#:206)
MassPeaks:304
RawMode:Averaged 0.675-1.815(136-364) BasePeak:400(50347)
BG Mode:Averaged 0.005-0.665(2-134) Segment 1 - Event 2

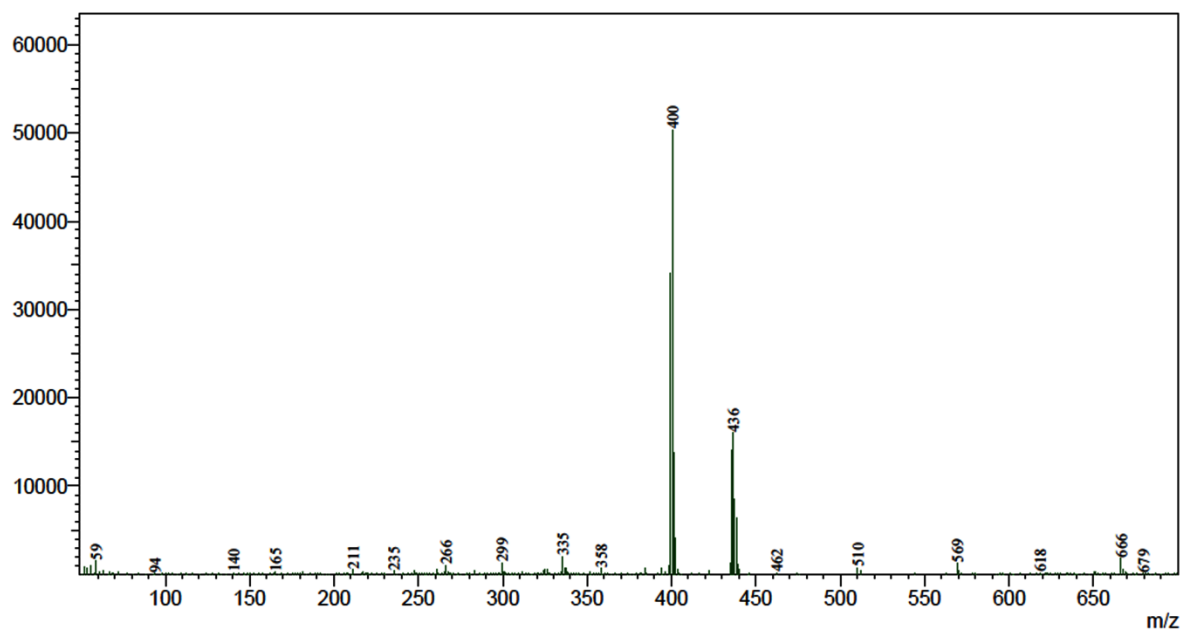


Figure 6.2 MASS spectra of compound 8-a

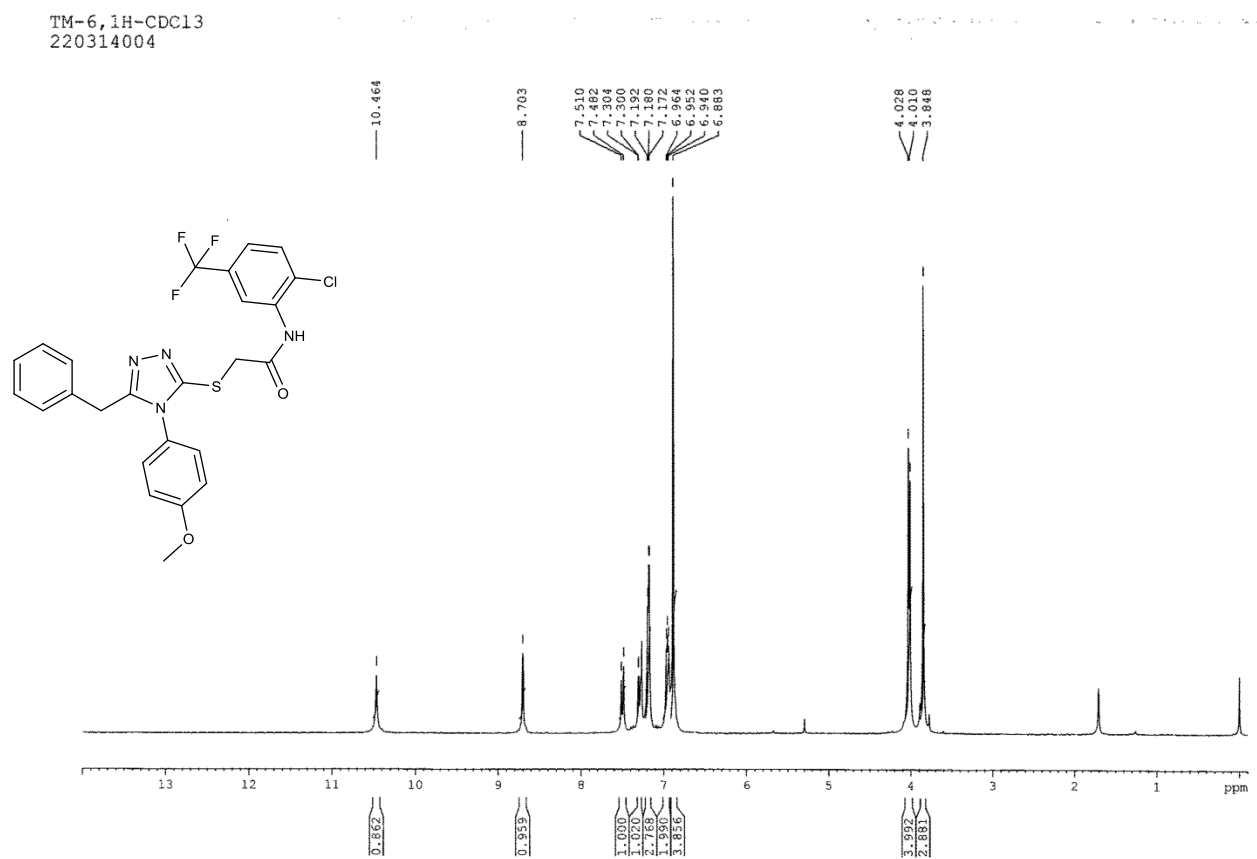


Figure 6.3. Spectral representation ^1H NMR spectra of most active compound **8-n**

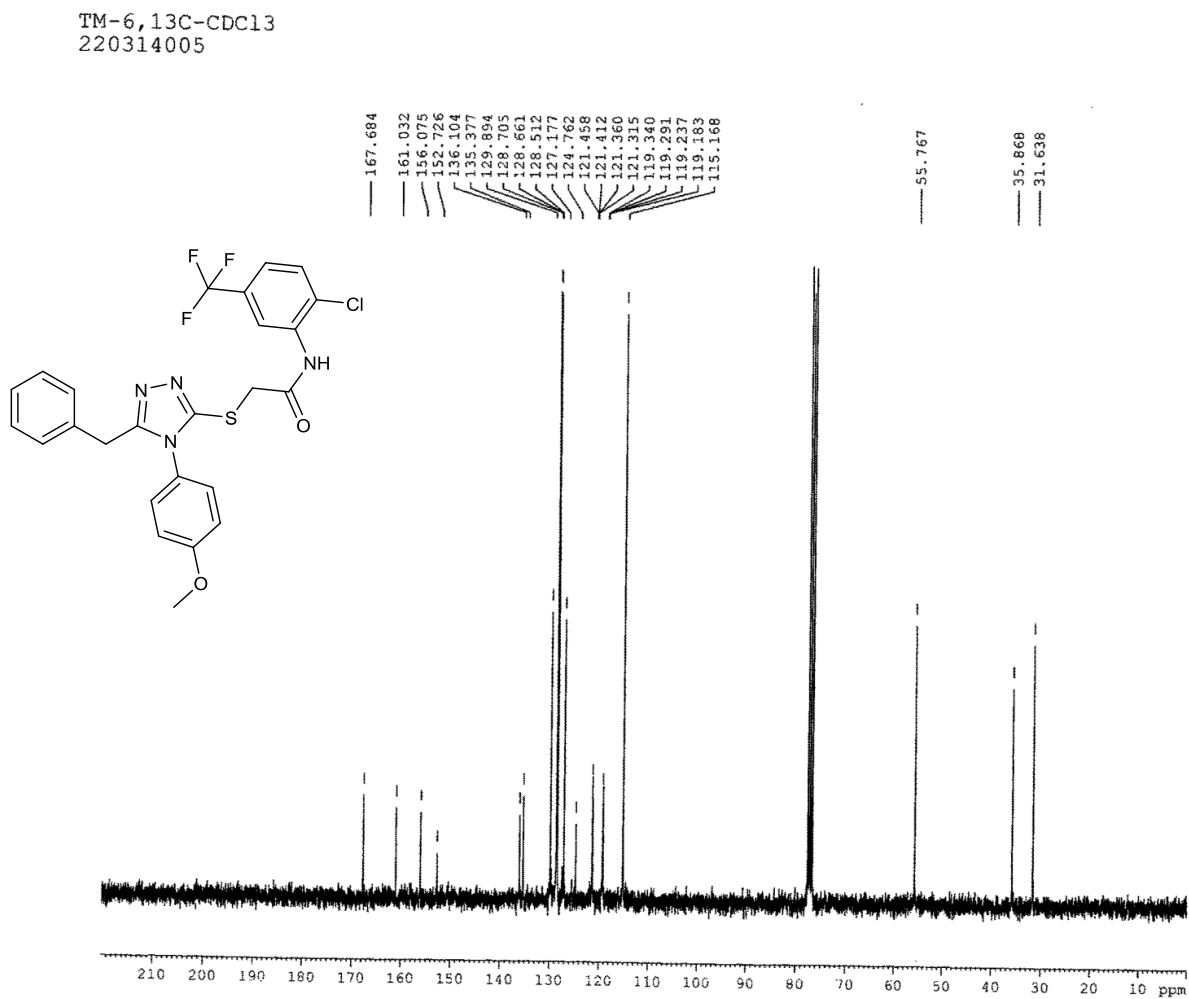
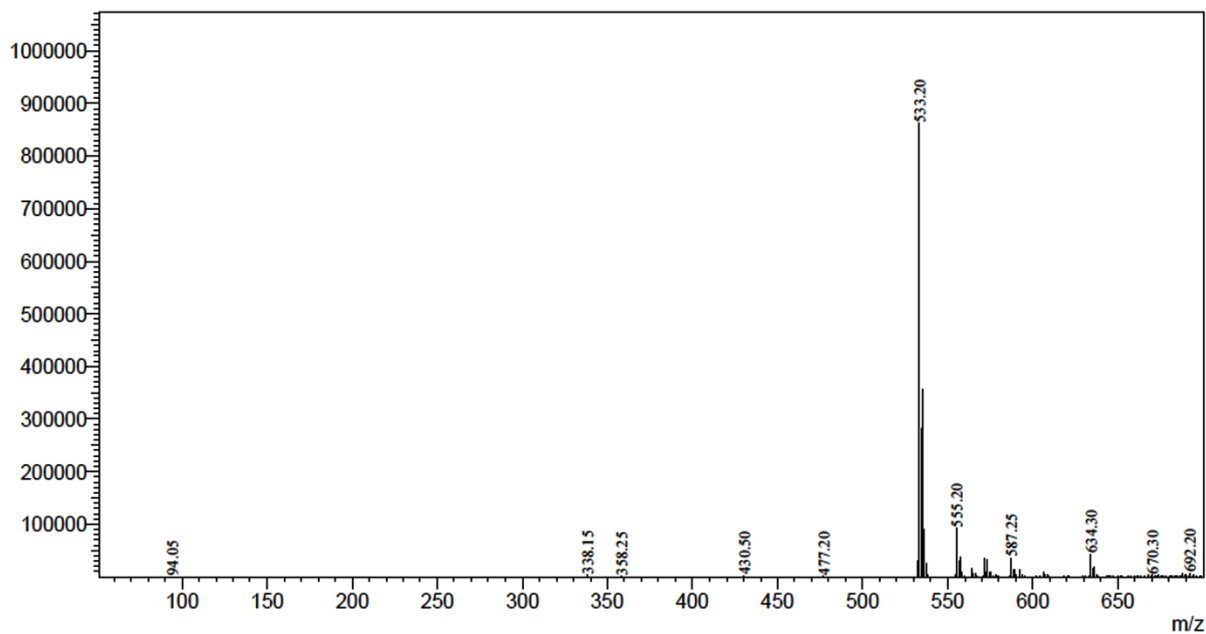


Figure 6.4 Spectral representation ^{13}C NMR spectra of most active compound **8-n**

<Spectrum>

Line#:1 R.Time:1.050(Scan#:211)
MassPeaks:155
RawMode:Averaged 0.660-1.750(133-351) BasePeak:533.20(861953)
BG Mode:Averaged 1.750-1.990(351-399) Segment 1 - Event 1



Line#:2 R.Time:0.995(Scan#:200)
MassPeaks:425
RawMode:Averaged 0.665-1.755(134-352) BasePeak:531.35(76242)
BG Mode:Averaged 1.755-1.995(352-400) Segment 1 - Event 2

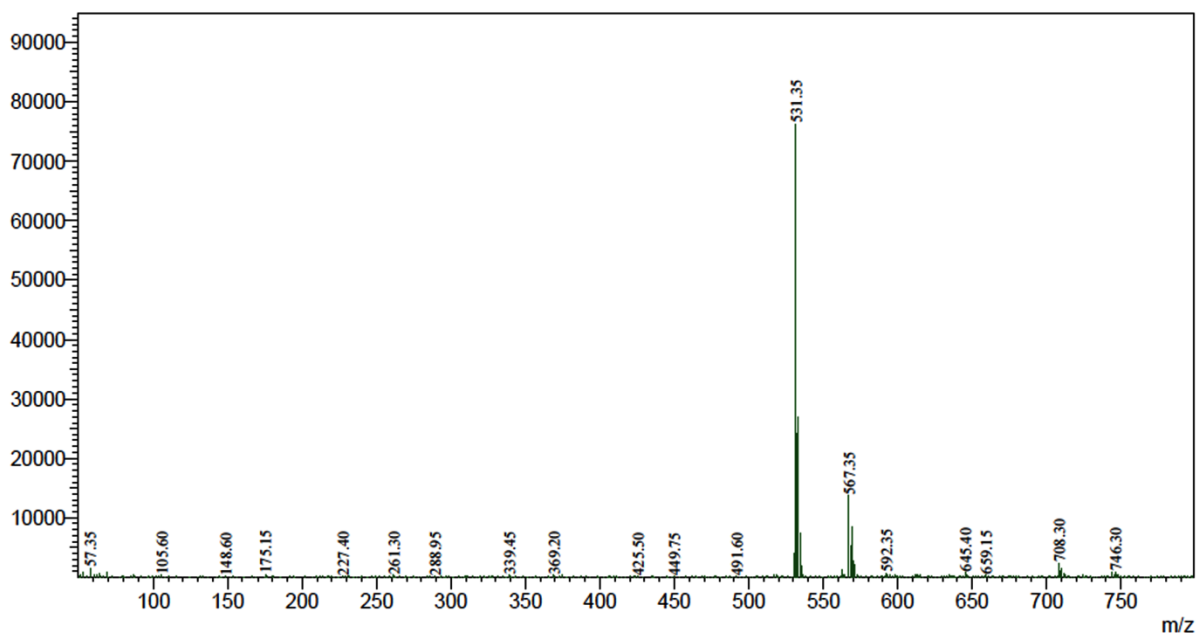


Figure 6.5 MASS spectra of compound **8-n**

6.1.2. Purity analysis

All the final compounds were checked for purity with a common method for detection was developed using a Shimadzu HPLC system. Chromatographic separation procedure was achieved on basis of method development protocol described in detail in materials and methods section. HPLC chromatogram of a representative compound **8-n** is displayed in Figure 6.6 where, the drug peak in aqueous method was resolved at retention time 4.79 minutes and the other impurity peak was resolved at 3.97 minutes. Detector at channel 2 was kept at wavelength 240 nm (Figure 6.6a) and the detector at channel 1 was kept at wavelength 235 nm (Figure 6.6b). Peak length and area was more at wavelength 240 than 235 nm, where the considerable single impurity was resolved at 3.97 minutes (Figure 6.6a). All the areas of the visible peaks were added manually and estimated the whole area to assess the purity of the single drug peak. The compound **8-n** has been shown 98.986% purity with low impurity, which was less than 1% of the whole sample. All the remaining compounds were estimated at the same aqueous methods with little pH adjustments of the samples, and were on an average found above 95% purity.

<Chromatogram>

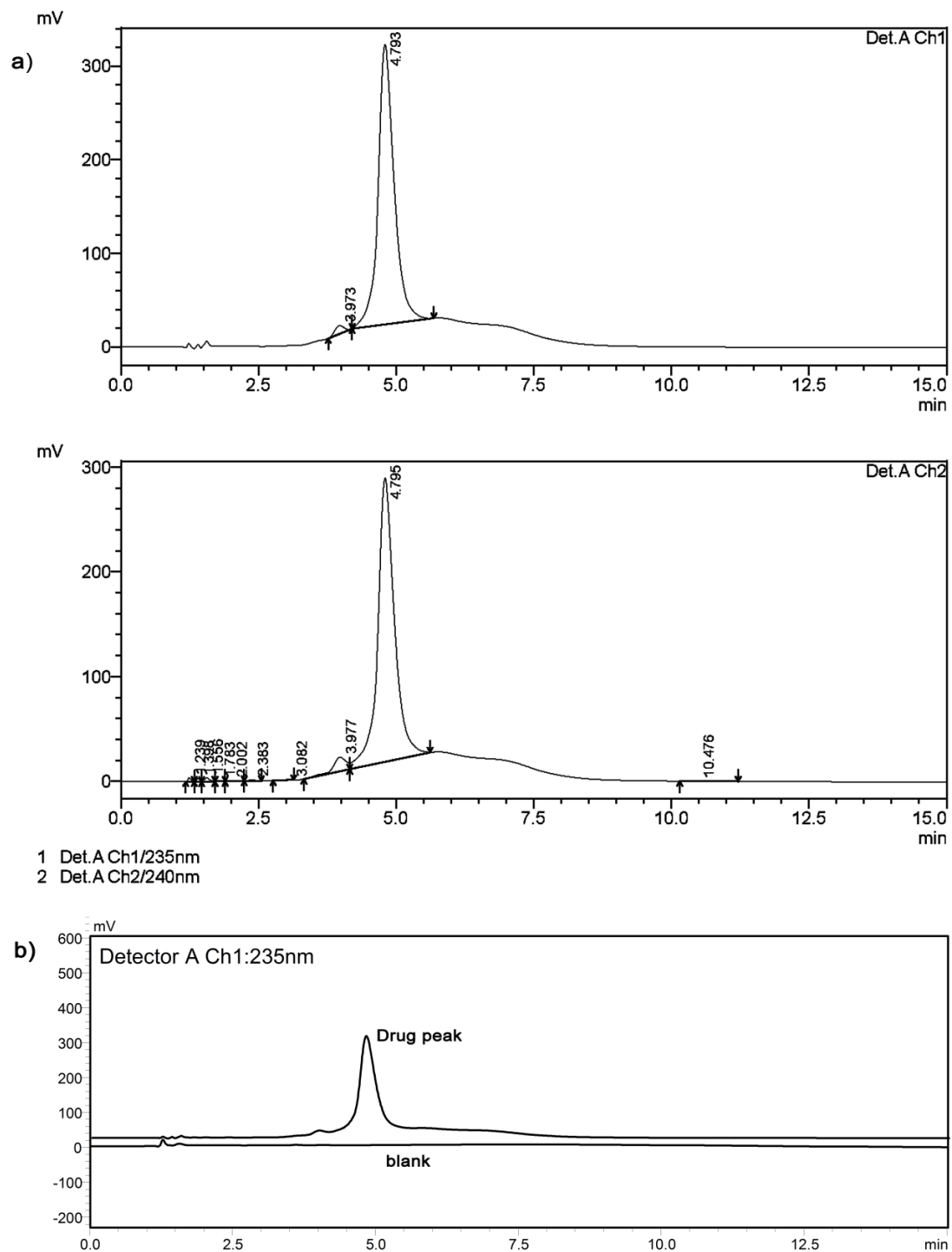


Figure 6.6 HPLC chromatogram of most active compound **8-n** with 98.986% purity, generated by chromatograph system with channels 1&2 (a) and overlay picture (b) of compound **8-n** and blank (ACN)

6.2. Biological evaluation.

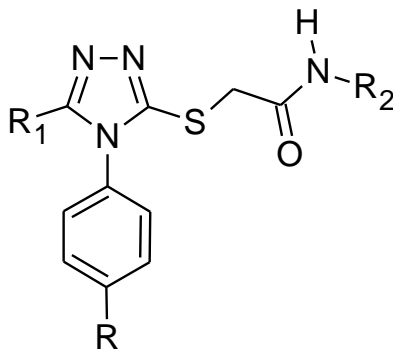
Chief strategy to prefer experimental methods of enzyme assay and tissue culture assays for lead identification and optimization was to inhibit CatS both *in vitro* and in biological cells. Preferably, CatS fluorimetric enzymatic assay and growth inhibition cell viability assays were performed to identify potent CatS enzyme inhibitors with growth inhibitory activity on human glioblastoma cell lines (U-87 MG). Recent immunofluorescence evidences from the works of Zhang L., *et al.*, [Zhang L., *et al.*, 2014] revealed that, the inhibition of CatS induced autophagy and apoptosis in human glioblastoma cell lines through ROS-mediated PI3K/AKT/mTOR/p70S6K and JNK signaling pathways, and they particularly tested in U87 MG cell lines. Plausibly, several other *in vitro* and immunohistochemical studies demonstrated that CatS was over expressed in astrocytomas and glioblastomas in contrast to its low level from astrocytes in normal brain [Flannery T., *et al.*, 2003, Flannery T., *et al.*, 2006]. Active CatS (stable at wide pH range 5.0 to 7.5) in the extracellular environment of astrocytoma may contribute to degradation of extra cellular matrix components thereby facilitating the invasive process in brain tumor as well as additionally functions in progression of neuropathic pain by cleaving of extracellular domain of FKN. However, several diagnostic methods also markedly reported that the chronic cancer pain was caused by nerve compression and immunoreactive and pronociceptive substances (such as CatS and BDNF) released from tumors, [Ueda H., *et al.* 2006] but the profound molecular mechanisms of this kind of pain remain to be studied. Evidently, several reports from rodent model studies had demonstrated that the cancer invasion pain model induced by implantation of Meth A sarcoma cells around the sciatic nerve in BALB/c mice [Shimoyama., *et al.*, 2002], led to development of allodynia, thermal hyperalgesia, and spontaneous pain [Shimoyama., *et al.*, 2002, Walker K., *et al.*, 2002, Wacnik P., *et al.*, 2001]. Moreover, in the current work, deliberate selection of human glioblastoma cell lines (U-87 MG) for the biological evaluation studies was to explore the potent CatS inhibitors, which could concurrently work on inflammatory cancerous mediators as well as inflammatory neuropathic pain.

Prior to the commencement of molecule series synthesis from parent compound **lead-8**, plan of SAR was made primarily based on knowledge based drug design techniques, where the necessity of functional groups to attain essential binding interactions with the active site of CatS was the chief consideration. Methodical checking of drug likeliness, ADME property predictions and

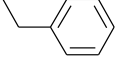
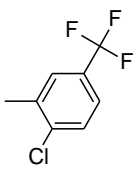
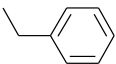
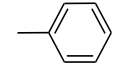
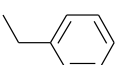
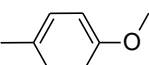
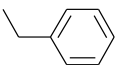
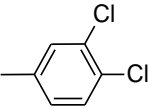
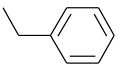
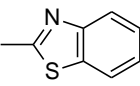
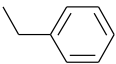
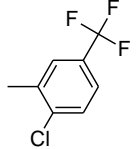
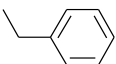
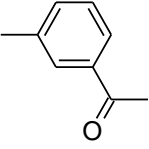
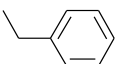
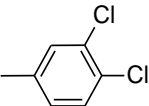
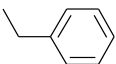
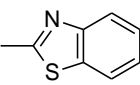
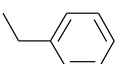
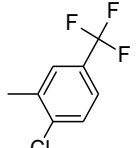
docking energy scores were helpful us to withdraw a series of 15 molecules as a 1st generation, as summarized in Table 6.1. Compounds were screened for human CatS enzyme inhibition, glioblastoma cell viability and cytotoxicity studies. Promisingly, all 15 molecules were found to be active in their IC₅₀ and GIC₅₀ in the ranges from 2.5-100 μM and 0.002-55 μM respectively. Whereas, 1st generation molecules were modified with help of biological activity data and their respective binding patterns, for the origin of a further 2nd generation series of compounds with a presumption to enhance the enzyme inhibitory activity. In particular, 2nd generation series were developed based on critical modification of replacing benzyl group with 2-chlorophenyl group at R₁ position (Table 6.1) and with an unchanged core moiety 4-phenyl-1,2,4-triazol sulfanyl acetamide (PTSA). Successively, the molecules from 2nd generation were found to be better in enzyme inhibition and similarly in growth inhibition than the 1st generation compounds. The molecules after modification were hoisted with enhanced enzyme inhibition as well as growth inhibition and lower cytotoxicity. IC₅₀ and GIC₅₀ of the modified 2nd generation series ranged from 0.102-52.04 μM and 0.001-100 μM respectively.

Furthermore, as a part of final modification two compounds from 1st generation series (**8-n** and **8-j**) were modified by extending alkyl length between sulfur and amide carbon (**8-3n** and **8-4j**) and checked for both enzyme activity as well as glioblastoma growth inhibition (Table 6.2) to understand, whether the chain length of the molecules take part any role in SAR. Structure activity relationships in regard to enzyme activity and docked binding poses were discussed in detail in the next section.

Table 6.1. Structural representation and enzyme inhibition (IC_{50}), glioblastoma cell growth inhibition (GIC_{50}) and HEK293 cytotoxicity (CC_{50}) of synthesized, compound **Lead-8** and 1st and 2nd generation series compounds and their selectivity index.



S.n	Compound Code	R	R ₁	R ₂	IC ₅₀ (μ M) \pm SEM	GIC ₅₀ (μ M) \pm SEM	CC ₅₀ (μ M) \pm SEM	Selectivity Index (CC ₅₀ /GI C ₅₀)
1	Lead-8	-H			6.58 \pm 0.56	0.477 \pm 0.05	>100.000	>100
1st generation series of molecules								
2	8-a	-H			>100.00	20.13 \pm 0.56	51.11 \pm 0.74	2.54
3	8-b	-H			26.91 \pm 1.25	3.60 \pm 0.24	0.48 \pm 0.06	0.14
4	8-c	-H			13.53 \pm 0.62	55.09 \pm 0.48	47.69 \pm 0.43	0.87
5	8-d	-H			>100.00	0.01 \pm 0.00	0.50 \pm 0.18	38.60

6	8-e	-H			9.79±1.44	40.94±0.82	0.003±0.00	<0.001
7	8-f	-F			35.09±0.50	17.14±2.24	56.73±0.47	3.31
8	8-g	-F			32.70±0.82	0.36±0.03	33.93±0.17	93.57
9	8-h	-F			9.75±0.84	0.06±0.03	6.80±0.39	113
10	8-i	-F			20.74±0.65	4.59±0.36	1.64±0.43	0.36
11	8-j	-F			3.24±2.12	0.004±0.00	14.33±0.32	3582.5
12	8-k	-F			2.48±0.01	0.03±0.00	24.55±1.68	818.33
13	8-l	-O			44.60±1.09	27.79±0.21	0.38±0.04	0.01
14	8-m	-O			12.72±1.05	0.97±0.40	23.76±0.68	24.29
15	8-n	-O			5.21±1.03	0.002±0.00	64.99±0.55	32495

16	8-o			3.10 ± 0.17	5.14 ± 0.31	54.14 ± 0.41	10.51
2nd generation series of molecules							
17	8-2a	-H		13.79 ± 0.29	>100.00	>100.00	--
18	8-2b	-H		10.90 ± 0.33	89.72 ± 0.26	>100.00	>100
19	8-2c	-H		1.84 ± 0.17	16.46 ± 0.09	>100.00	>100
20	8-2d	-H		0.95 ± 0.14	55.12 ± 0.11	>100.00	>100
21	8-2e	-H		52.04 ± 1.91	51.37 ± 0.09	>100.00	>100
22	8-2f	-F		11.37 ± 0.23	0.001 ± 0.00	>100.00	>100
23	8-2g	-F		0.43 ± 0.34	0.009 ± 0.00	>100.00	>100
24	8-2h	-F		51.96 ± 1.67	33.16 ± 0.85	>100.00	>100

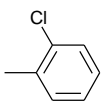
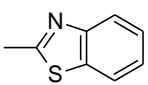
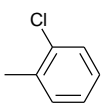
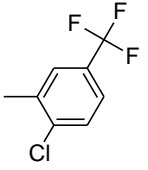
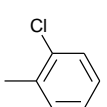
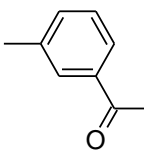
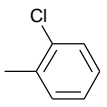
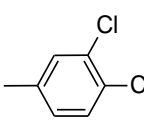
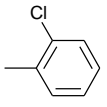
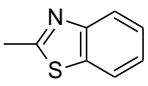
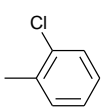
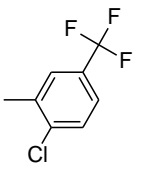
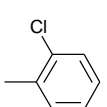
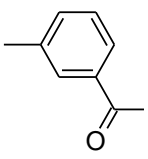
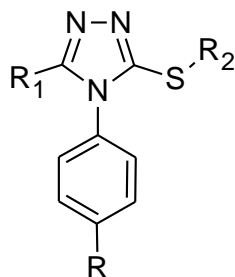
25	8-2i	-F			3.00 ± 0.37	>100.00	>100.00	--
26	8-2j	-F			18.07 ± 0.24	0.004 ± 0.00	>100.00	>100
27	8-2k	-F			0.16 ± 0.13	>100.00	>100.00	--
28	8-2l	-O			0.10 ± 0.06	0.52 ± 0.23	94.36 ± 18.11	181.46
29	8-2m	-O			0.86 ± 0.22	13.90 ± 0.17	>100.000	>100
30	8-2n	-O			0.32 ± 0.31	43.61 ± 0.33	>100.00	>100
31	8-2o	-O			0.16 ± 0.08	>100.00	>100.00	--

Table 6.2. Structural representation and enzyme inhibition (IC_{50}), glioblastoma cell growth inhibition (GIC_{50}) and HEK293 cytotoxicity (CC_{50}) of synthesized 2nd generation extension series compounds and standard drugs and their selectivity index.



S. no	Compound Code	R	R ₁	R ₂	IC ₅₀ (μM) ±SEM	GIC ₅₀ (μM) ±SEM	CC ₅₀ (μM) ±SEM	SI (CC ₅₀ /GIC ₅₀)
1	8-3n				0.39±0.24	>100.00	>100.00	--
2	8-4j	-F			0.20±0.12	0.028±0.0	>100.00	>100
3	E-64*				0.013±0.01	>100.00	>100.00	--
4	Bendamustin#				Nd	0.073±0.02	>100.00	>100
5	Temazolamide#				Nd	11.56±0.21	>100.00	>100

* Standard CatS inhibitor

Bendamustin commonly used drug for brain tumors and Temazolamide is a standard drug for microglial cancer

6.2.1. Structure activity relationships based on enzyme inhibition and docking interactions

Prior to the commencement of synthesis of entire set of analogs from parent compound **Lead-8**, plan of SAR was made using docking to attain improved CatS enzyme inhibition and biological activity. Utilization of docking calculations and interactive poses were guided towards, meticulous modifications and replacements of necessary functional groups to attain essential binding interactions with CatS active site. Core moiety PTSA (4-phenyl-1,2,4-triazol sulfanyl acetamide) of the parent compound **Lead-8** was modified at three positions R, R₁ and R₂ (Table 6.1) to attain precise amino acid binding interactions in the CatS active site. The binding interaction poses are illustrated in the Figures 6.7- 6.10, where, green dotted lines indicate hydrophobic interactions and pink dotted lines indicate H-bond interactions with important amino acid residues.

Initially, R substitution (Table 6.1) on 4-phenyl ring, were considered as -H, -F, -OCH₃. R₁ substitution was a simple substitution with benzyl group (1st generation) and 2-chlorophenyl group (2nd generation) (Table 6.1). R₂ substitutions were more prominently specific for each compound with three combinations of R subgroup substitutions. Simple substitution on phenyl group at R₂ position was shared by compounds **8-a**, **8-f**, **8-2a** and **8-2f**. Enzyme inhibition (IC₅₀) was found to have improvement with fluoro substitution at R position (R= -F) (**8-f** and **8-2f**) than -H substitution (**8-a** and **8-2a**) (R= -H). Alteration in 2-chlorophenyl group at R₁ position (from **8-a** to **8-2a**) modified the binding conformation a little (Figures 6.7 and 6.9) and improved the activity more than 5 fold (>100 to 13.8 μM), demonstrating the importance of the 2-chlorophenyl substitution rather than benzyl substitution. In fact, while observing binding patterns of the compounds (Figures 6.7 and 6.9), it was conferred that the hydrophobic interactions with hydrophobic amino acids and H-bond interactions (Asn163, Gly69) were more when R=fluoro substituted compounds (**8-f**, **8-2f**) than with no substitution i.e. R= -H (**8-a** and **8-2a**). Active site occupancy was extended with compounds **8-f** and **8-2f** due to unfolded conformational change, where molecule appeared to be interacting with amino acids Asn163, Gly69 and hydrophobic amino acids Phe211, Pro 212, Phe70, Met71, Trp26 and Val162 between sub sites S2, S3 and S1, which were important for CatS inhibition (Figures 6.7 and 6.9). Moreover, several theoretical observations and x-ray crystal structure analysis studies revealed that the interactions with highly hydrophobic amino acid residues such as Val162, Phe211, Phe70, Trp26, Met71 and Cys25 in the

sub-sites of S1, S2, S3, S4 at active site of CatS were crucial for activity (Figure 6.8) [Markt P., *et al.*, 2008; Tully DC., *et al.*, 2006].

Compounds **8-b**, **8-g**, **8-2b** and **8-2g** shared 4-methoxy phenyl as R₂ substitution (Table 6.1) among which compound **8-2g** showed adequate CatS inhibition IC₅₀ of 0.437 μM by obeying substantial binding interactions with Cys25 and other hydrophobic amino acids. 4-Methoxy phenyl at R-position in presence of benzyl (R₁) substitution (**8-b**, **8-g**) on PTSA showed moderate enzyme inhibition as it was correlated with the inappropriate binding patterns exhibited within the active site. But, with substitution of 2-chlorophenyl group at R₁ position along with fluoro group at R position (**8-2g**) showed improved activities in case of both enzyme and growth inhibition. Precisely, in case of compound **8-2b** (R₁ = 2-chlorophenyl and R = -H), positional orientation persisted within the sub sites of S3 and S2 but, missed the hydrophobic interactions of Cys25 and Trp186 at the sub site of S1 as shown by **8-2g**, which could perhaps be a reason behind decreased activity (Figure 6.9).

Further modification of R₂ position on PTSA with 3,4-dichlorophenyl group partaken in scheming of compounds **8-c**, **8-h**, **8-l**, **8-2c**, **8-2h** and **8-2l**. Among all, compound **8-2l** exhibited devastatingly improved potency against human CatS enzyme with the IC₅₀ value of 0.102 μM and emerged as most active compound among all compounds with more than 29 fold potency compared to the parent compound **Lead-8**. In particular, compound **8-2l** behaved in a distinct manner within the active site, where it showed hydrophobic interactions specifically with sub site S3 by R substituted 4-methoxy phenyl and R₁ substituted 2-chlorophenyl groups. Besides, compound **8-2l** also showed copious interactions with backbone of Cys25 that was important for cysteine protease inhibition (Figure 6.10). In addition to these, 3, 4-dichloro phenyl group at R₂ position was exposed to the S1' sub site particularly to hydrophobic indole side chain of Trp186 (Figure 6.10), perhaps adding to its role in bioactivity. Whereas, missing part in case of the remaining five compounds (**8-c**, **8-h**, **8-l**, **8-2c** and **8-2h**) was presumably due to persistent specificity towards S3 sub site with either hydrophobic interactions as well as molecular orientation to active site vicinity (Figures 6.7, 6.8 and 6.9). Several CatS active site analysis reports demonstrated that S3 sub pocket, which was well defined by the backbone of Gly69 and the flexible side chains of Phe70 and Lys64, was certainly responsible for the promising activity of molecules and for CatS specificity [Tully DC., *et al.*, 2006; Ayesa S., *et al.*, 2009,]. However, compound **8-l** showed similar kind of orientation as **8-2l**, within the active pocket, but presence

of simple benzyl group instead of 2-chlorophenyl could be a possible reason for considerable reduction in potency by 400 fold (with IC_{50} value 44.6 μ M) from **8-2l**.

Strategically, another set of compounds (**8-d**, **8-i**, **8-m**, **8-2d**, **8-2i** and **8-2m**) was modified with heterocyclic aromatic R_2 substitution of 1,3-benzothiazole rather than decorating with simple phenyl group. The 1,3-benzothiazole group partly tolerated and improved activity, while **8-2m** showed a moderate reduction in bioactivity (0.863 μ M) in contrast to compound **8-2l**. Yet again, 2-chlorophenyl R_1 substitution in compounds **8-2d**, **8-2i** and **8-2m** partaken its distinctive role to enhance potency compared to benzyl group at R_1 . For instance, compound **8-2d** exhibited more than 100 fold increase in activity (0.951 μ M) than **8-d** (100 μ M) and threefold more than parent compound **Lead-8**. Binding pattern orientations were relatively similar in all these six compounds, but the deep accommodation of R_1 substituted 2-chlorophenyl fragment into S2 sub site was persisted with **8-2d**, **8-2i** and **8-2m** compounds (Figures 6.9 and 6.10). Partial S3 site occupancy of R substituted with 4-methoxy phenyl compounds (**8-m** and **8-2m**) was found when compared to most active compound **8-2l** (Figures 6.8 and 6.10).

Furthermore, modifications of R_2 position was performed with N-substituted 2-chloro-5-(trifluoromethyl) phenyl group on core PTSA which was shared by compounds **8-e**, **8-j**, **8-n**, **8-2e**, **8-2j** and **8-2n**. Among these, compound **8-2n** showed adequate potency of 0.326 μ M with strong conformational drift, where molecule completely was involved in all S2 sub site hydrophobic amino acid residue interactions (Figure 6.9). Whereas, 2-chlorophenyl R_1 substitution in combination with R_2 substituted 2-chloro-5-(trifluoromethyl) phenyl group was considerably less potent as compared to benzyl (R_1) substitution.

In order to get additional attractive interaction with positively charged Arg141 (located at sub site S1'), an electronegative oxygen atom containing 3-acetylphenyl functional group was deliberately introduced to the R_2 position in combination with simple fluoro and methoxy R -substituted groups shared by compounds **8-k**, **8-o**, **8-2k** and **8-2o**. Conflictingly, none of the compounds showed H-bond interaction with Arg141, but surprising compound **8-2k** showed unique H-bond interaction with another positively charged flexible Lys64 residue (one of the important residue in S3 sub site) by displaying unexpected intense conformational drift (Figure 6.10), and exhibited good IC_{50} of 0.161 μ M. Other compounds **8-k** and **8-o** showed Cys25 and Trp186 interactions at S1 sub site (rather than Arg141 and Lys64), and exhibited satisfactory enzyme inhibition of 2.487 and 3.102 μ M respectively. However, the compound **8-2o** withstood

good potency (0.165 μM) though it did not possess any anticipated interactions (Arg141 and Lys64), but, perhaps may be due to H-bond interactions with Gly69 and Asn163 at narrow passage between sub sites S3 and S2 (Figure 6.10). Convincingly again, R substituted with 2-chlorophenyl group and R₂ substituted with 3-acetylphenyl group played major roles in enhancing the potency than R substituted with benzyl group.

Finally, as a part of 2nd generation series development, compounds **8-n** and **8-j** (from 1st generation) were modified by extending alkyl length between sulfur and amide carbon, based on docking calculations to derive binding patterns. Rationality behind the selection of compounds **8-n** and **8-j** were due to their high activity in both against enzyme (5.217 and 3.243 μM respectively) as well as in glioblastoma cancer cell growth inhibitions (0.002 and 0.004 respectively) among the 1st generation compounds. Along with the alkyl carbon extension, R₁ position that had benzyl group was replaced with 2-chlorophenyl in compound **8-j**, in order to understand the importance of alkyl chain modification (Table 6.2). The modified compounds namely **8-3n** (from compound **8-n**) and **8-4j** (from compound **8-j**) showed interesting binding orientations with stable and crucial H-bond interactions (Gly69 and Asn163) within the active site. In the first instance R substituted 4-methoxy phenyl group was found twisted into the S2 pocket instead of R₁ benzyl group of compound **8-3n** due to obvious alkyl rotations to form stable H-bond interactions (Figure 6.8). Whereas, in the case of compound **8-4j**, firm affinity due to R₁ substituted 2-chlorophenyl group towards deep hydrophobic S2 sub site was observed as there were no alkyl rotation as observed with **8-3n**, instead, alkyl chain conformation got crumpled in order to withstand the H-bond interaction with Gly69 and Asn163 (Figure 6.10). Analogously, compounds **8-3n** and **8-4j** enzyme inhibitory activity were relatively similar with IC₅₀ values of 0.392 and 0.205 μM respectively. Conclusively, extension of alkyl chain pretended to improved binding patterns and was successful in deriving enzyme inhibition. Therefore, reduction of an alkyl carbon at R₁ and extension of the other side between sulfur and amide mimicked the activity of PTSA derived compounds.

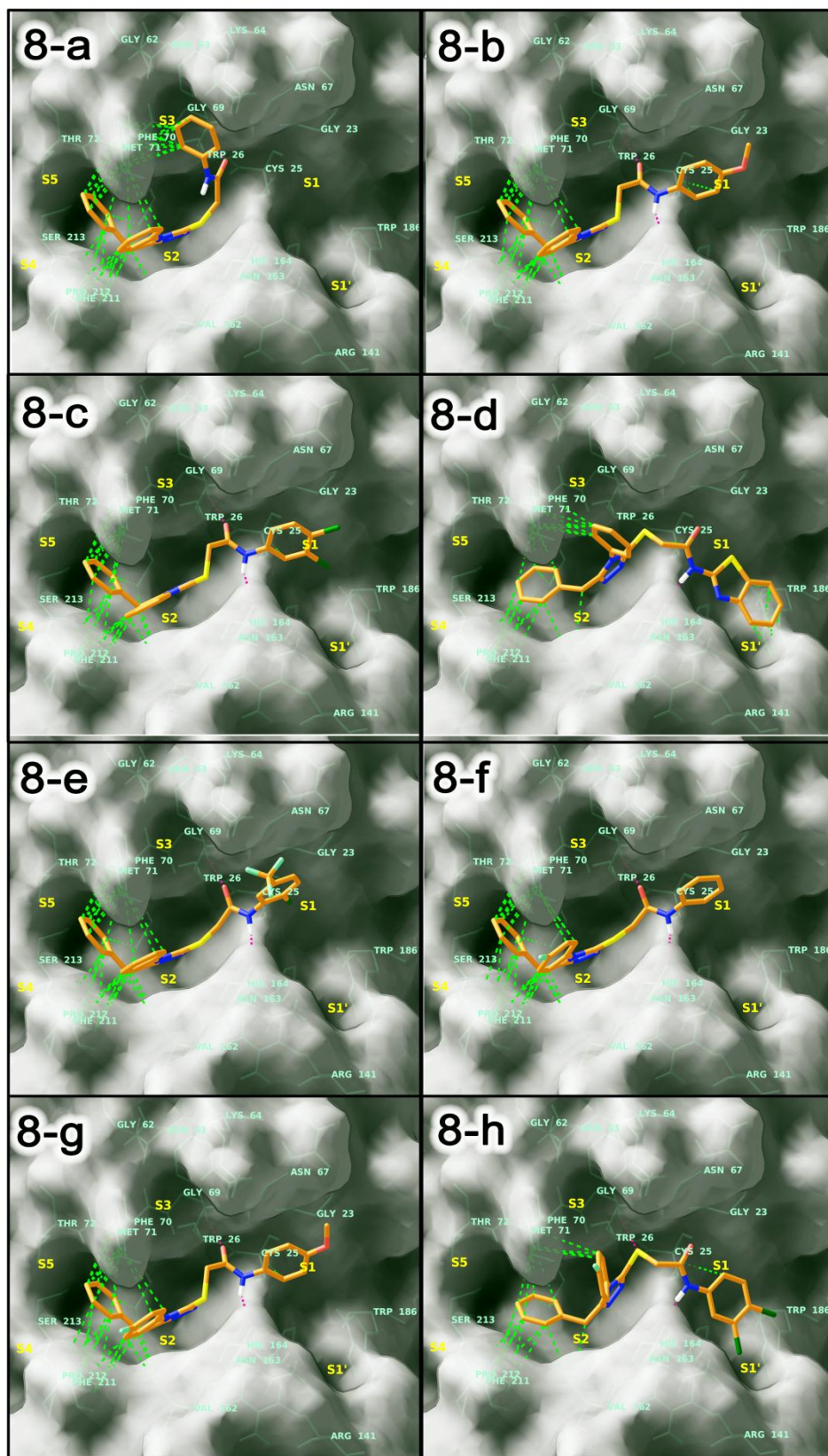


Figure 6.7 Binding poses with hydrogen and hydrophobic interactions of compounds from **8-a** to **8-h**

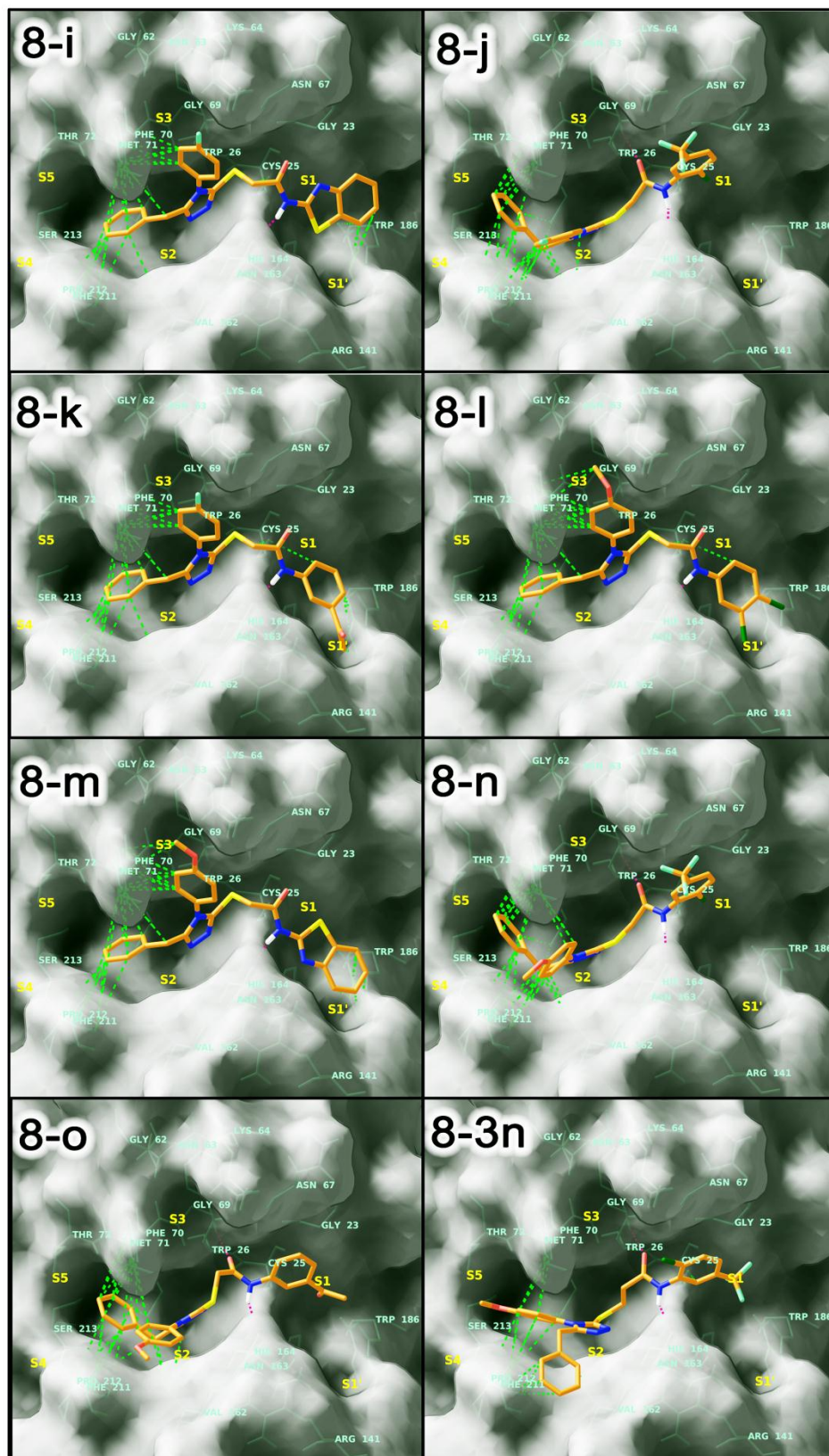


Figure 6.8 Binding poses with hydrogen and hydrophobic interactions of compounds **8-i** to **8-o** and **8-3n**

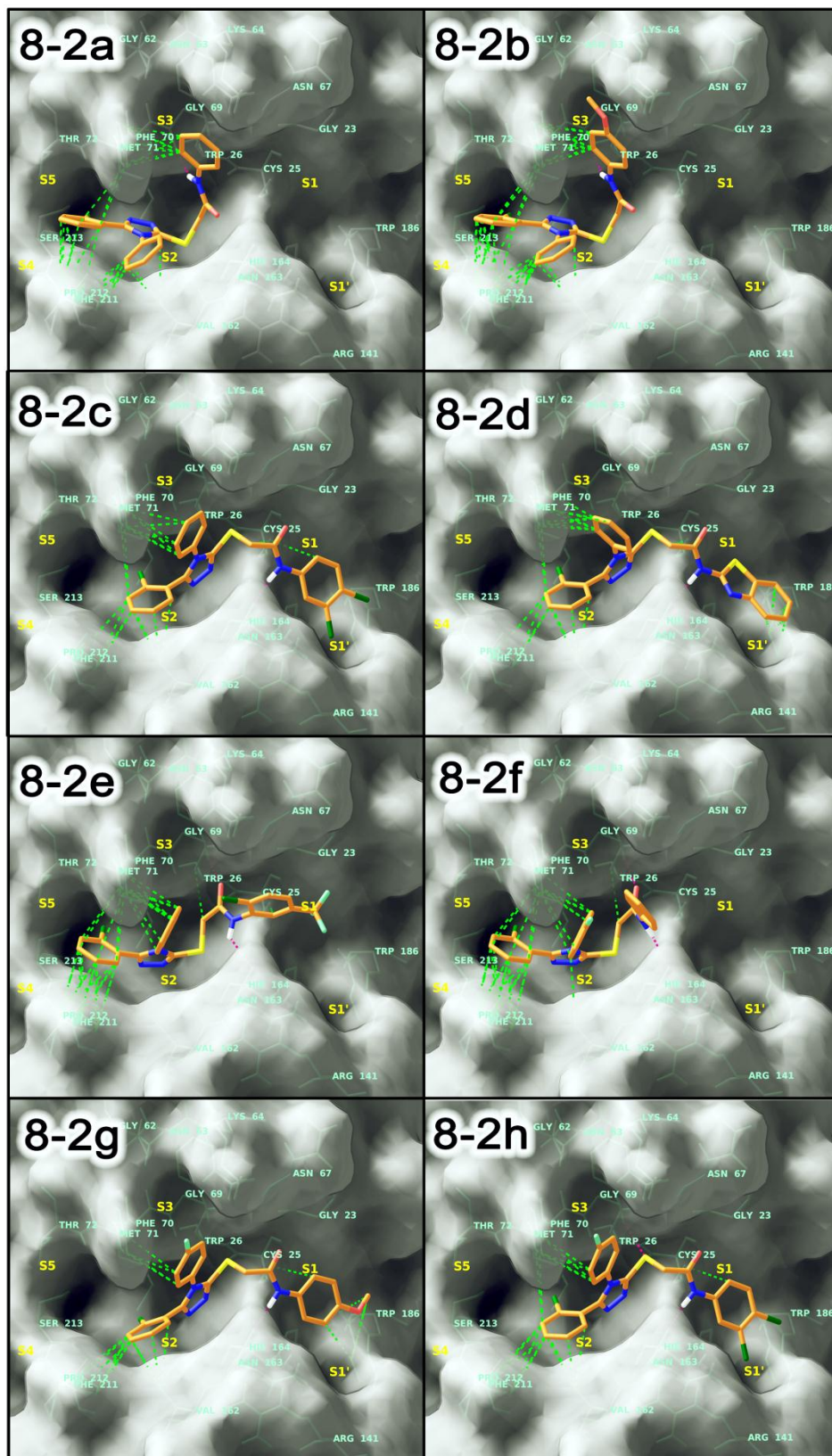


Figure 6.9 Binding poses with hydrogen and hydrophobic interactions of compounds from **8-2a** to **8-2h**

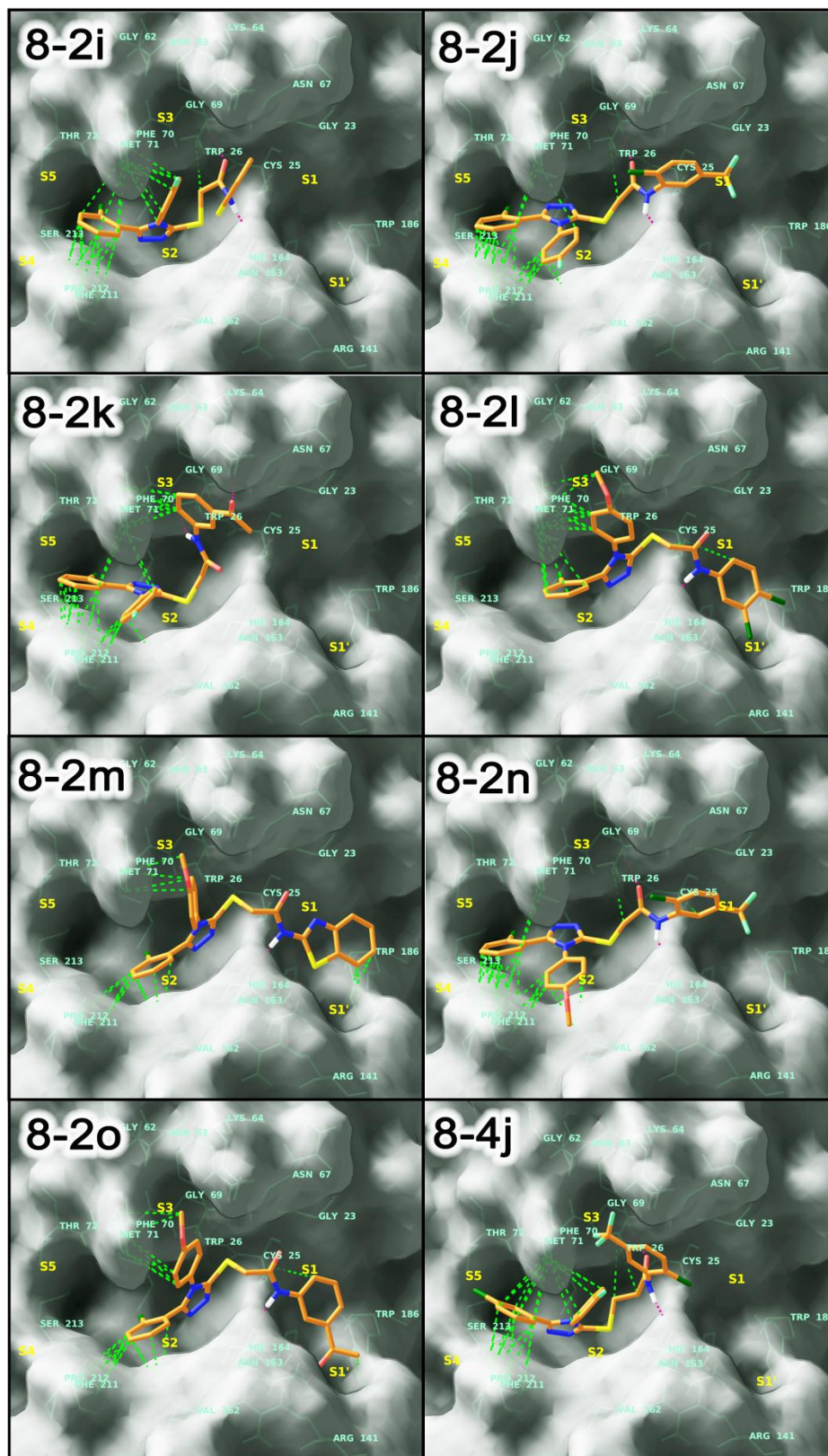


Figure 6.10 Binding poses with hydrogen and hydrophobic interactions of compounds from **8-2i** to **8-2o** and **8-4j**

6.2.2 Binding pattern relationships with co-crystal ligand

While comparing the compounds with co-crystal ligand (2F1G) binding patterns (Figure 6.11), were found to be in limited number of hydrophobic interactions with Cys25, Phe70, Met71, Val162 and Trp186 and also H-bond interactions with only Gly69 (Figure 6.11a) . In Figure 6.11 we tried to relate the binding analysis of compounds **Lead-8** (parent compound), **8-n** (best active compound in neuropathic pain and cancer growth) and **8-21** (most active compound in the enzyme activity) with the co-crystal ligand. S3 sub site occupancy and Cys25 interaction were the correlating factors to relate the most active compound **8-21** and crystal ligand that were found missing with **lead-8** and **8-n**. However, the hydrophobic interactions in deep S2 sub site were more in case of **lead-8** and **8-n** along with two crucial H-bond interactions (Asn163, Gly69). In contrast, spreading into S1' sub site and hydrophobic interaction with Trp186 has not been in case of compound **8-21** and other remaining compounds unlike crystal ligand. Substitution of different hydrophobic groups towards S1' sub site perhaps improved activity. In summary, most active compound **8-21** with good CatS inhibition showed similar orientation as to the crystal ligand orientation, which inferred the relation between the binding interaction poses and the enzyme inhibition to be a necessary part for the CatS inhibitor drug development.

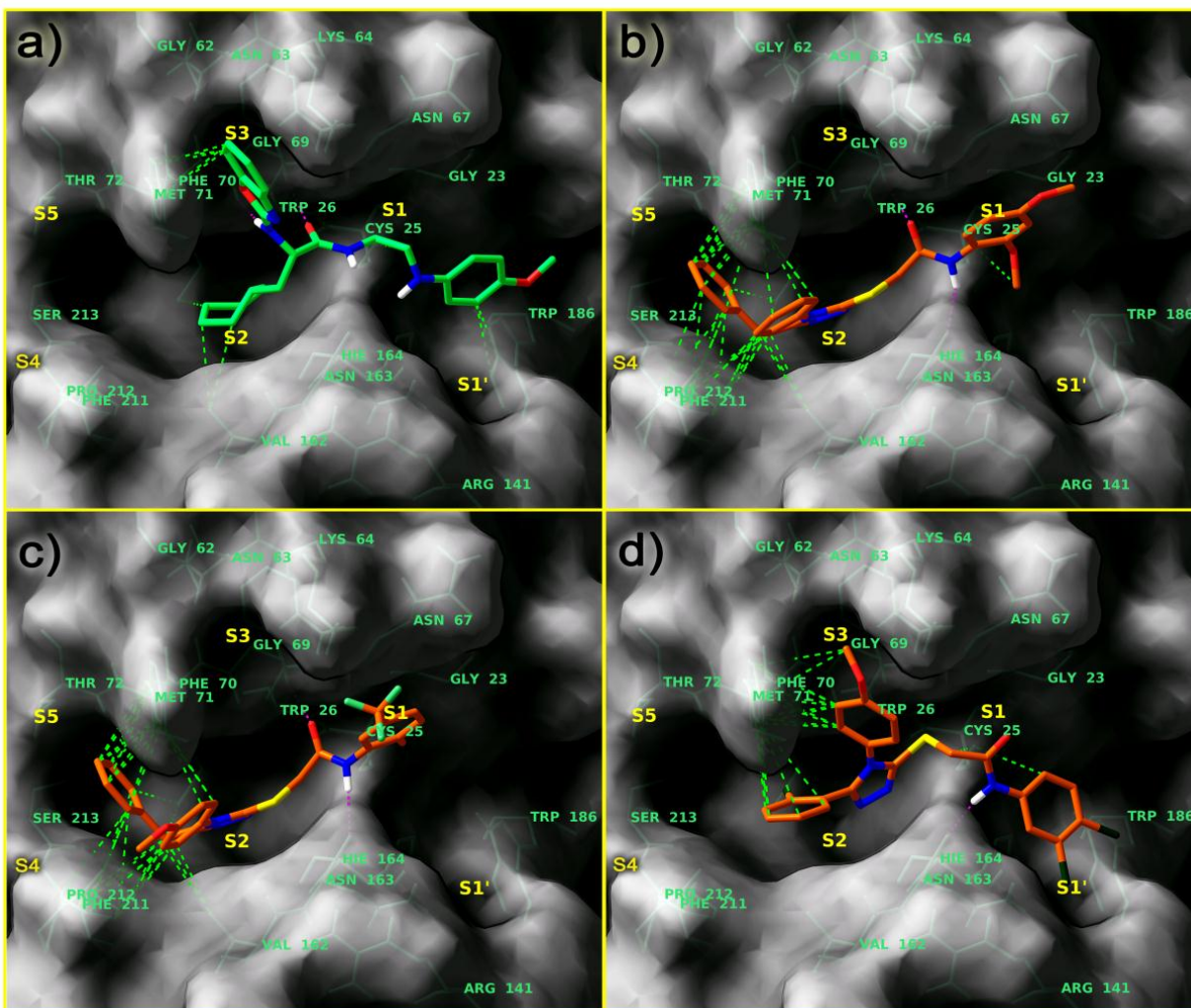


Figure 6.11 Illustrations of docking binding patterns of crystal ligand (a) compound **lead-8** (b) compound **8-n** (c) and compound **8-21** (d). Green dotted lines indicate the hydrophobic interactions; pink dotted lines indicate the H-bond interactions with respective amino acid residues.

6.2.3. Structure activity relationships based on growth inhibition of glioblastoma cell lines

In the 1st generation series of compounds, modifications at R₂ position with N-substituted 2-chloro-5-(trifluoromethyl) phenyl group with R substitution of fluoro and methoxy groups as in compounds **8-j** and **8-n** (Table 6.1) revealed high growth inhibition (GIC₅₀) in glioblastoma cells (0.004 μM and 0.002 μM respectively). Similarly, in the 2nd generation (R₁ with 2-chlorophenyl substitution) compounds, with N-substituted 2-chloro-5-(trifluoromethyl) phenyl group and with R substitution with fluoro group (compound **8-2j**) sustained the activity (showed 0.004 μM) whereas, R substituted with methoxy group (compound **8-2n**) lost the activity (showed 43.61 μM). Alkyl chain extension at R₂ position (Table 6.2) as in compound **8-4j** (modified from compound **8-j**) showed more than five-fold decrease in activity (0.028 μM). Among all the compounds, compound **8-2f** showed the promising GIC₅₀ value of 0.001 μM with the substitution of R-fluoro, R₁-2-chlorophenyl and R₂-phenyl moieties. Similarly, compound **8-2g** (from **8-2f**) with substituted methoxy group on R₂-phenyl ring led to nine-fold decrease in the activity (0.009 μM). Moreover, compounds **8-2f** and **8-2g** both from the 2nd generation series with R₁ substitution of 2-chloro phenyl group and the similar compounds from the 1st generation series compounds **8-f** and **8-g** with simple benzyl group did not show promising activities (17.14 μM and 0.363 μM respectively). In addition, some of the compounds from the 1st generation **8-d**, **8-h** and **8-k** showed good GIC₅₀ values of 0.013, 0.061 and 0.030 μM respectively. Few more compounds **Lead-8**, **8-m** and **8-2l** were considered to be moderately active in glioblastoma cell growth inhibition with GIC₅₀ values of 0.477, 0.978 and 0.520 μM respectively.

6.2.4. Selectivity index analysis

Rationality of the compounds to estimate cytotoxicity using human embryonic kidney cells (HEK 293) was performed for the estimation of the selectivity towards the cancerous glioblastoma cells than the normal cells. To comprehend the compound cancer selectivity and to sieve safer molecules we represented all the molecules in a four quadrant scattered plot by comparing log IC₅₀ values (Figure 6.12). The initial graph (Figure 6.12a) plotted between the log IC₅₀ of Cats enzyme (X-axis) and log GIC₅₀ of glioblastoma cells (Y-axis) to understand the potency status of each compound concerning CatS inhibitor as an anti-cancer agent. Compounds **8-2g**, **8-2l** and **8-4j** with R as fluoro and methoxy substitutions R₁ substituted as 2-chlorophenyl and R₂ substituted 4-methoxyphenyl, 3,4-dichlorophenyl and 2-chloro-5-(trifluoromethyl) phenyl

(with extended alkyl chain) groups respectively occupied most active quadrant III (low IC_{50} , low GIC_{50}) revealing the importance of respective modifications.

Compounds with lesser potency were circled within quadrant I (Figure 6.12a), were not to be considered as promising compounds for the activity in case of both enzyme inhibition and anti-cancer activity. Whereas, molecules in remaining quadrants (II, III and IV) were further checked for selectivity index (SI) towards cancer cells, than the normal cells (Figure 6.12-b, c, d). Here, X-axis was $\log IC_{50}$ (enzyme inhibition) and Y-axis was SI (CC_{50} / GIC_{50}), where the X-axis limited in each graph was based on the quadrant axis (from Figure 6.12a), but Y-axis remained same in all three plots (Figure 6.12-b, c, d). From the quadrant II, compounds **8-2k** and **8-2o** were found to fail to in exhibiting good SI by residing near to the zero dotted line in Figure 6.12b, displaying parallel inhibition towards both normal and cancer cells. Hence, compounds **8-2k** and **8-2o** were considered equally toxic on normal cells as well as cancer cells, descended into cytotoxic drug category. Except **8-2k** and **8-2o** remaining compounds near to log concentration 2 ($\geq 100 \mu M$) on Y-axis in Figure 6.12b, c and d, were considered to be in acceptable range. Compounds (**8-2g**, **8-2l** and **8-4j**) from most active quadrant III (Figure 6.12-a) were hence to be with high CatS inhibition and were highly selective towards cancerous microglial cells among current 1,2,4-triazole series of molecules (Figure 6.12-c). Many of the best active compounds from 1st generation series (**8-d**, **8-g**, **8-h**, **8-j**, **8-k**, **8-m** and **8-n**) were congregated at IVth quadrant (Figure 6.12-a) and were considered as adequately active inhibitors for CatS as well as microglial cancer growth with acceptable SI (Figure 6.12-d).

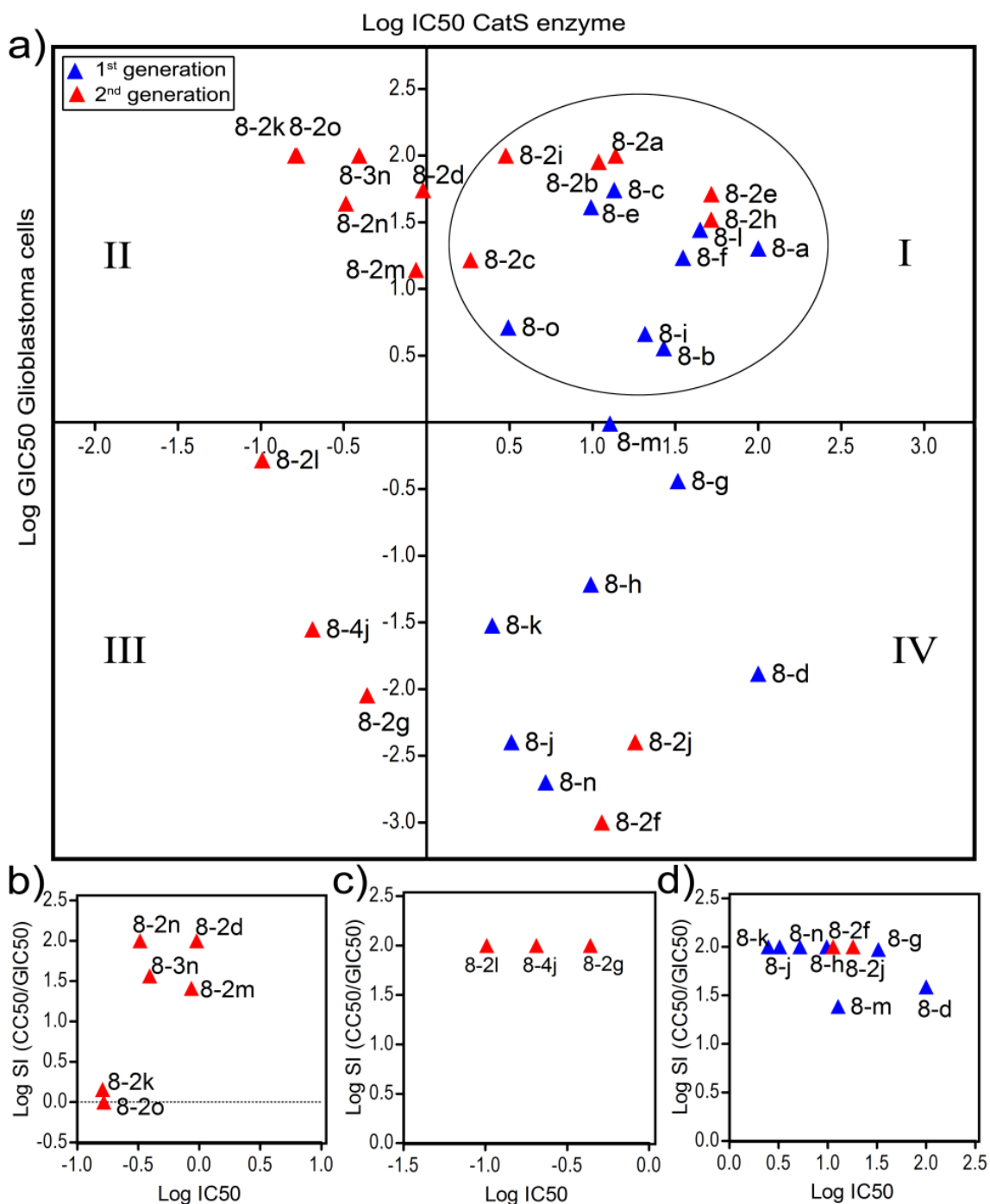


Figure 6.12 Scatter plot to locate the most and least active compounds lied in safety index.

(a) Graphical representation of xy column scatter plot of Log IC₅₀ vs Log GIC₅₀, X-axis is log IC₅₀ CatS enzyme, Y-axis is log GIC₅₀ glioblastoma cells. Compounds from quadrant II, III and IV (except circled quadrant I) were kept in a comparison with selectivity index towards glioblastoma in an anti-clock wise direction i.e. quadrant II= (b), III= (c), IV= (d).

All the series of compounds were compared with standard compounds E-64 (standard CatS inhibitor), bendamustin (commonly used for brain tumors) and temazolamide (standard drug for microglial cancer) (Table 6.2). Categorically, no molecule from the current series exceeded **E-64**, as it has been the most effective CatS inhibitor (0.013 μM) which did not show any activity in the glioblastoma cell viability (Table 6.2) while bendamustin and temazolamide successfully inhibited microglial cell viability (0.073 and 11.56 μM respectively) with higher SI (Table 6.2). Many of current series of compounds exceeded these two standard compounds with exceptional GIC_{50} values (Table 6.1 and 6.2).

All the synthesized derivatives of **Lead-8** were further examined for *in vivo* neuropathic pain pharmacological assessment, in order to assess and identify CatS inhibitors with neuropathic pain therapeutic potential.

6.3. Atom based QSAR and contour map analysis

Chief idea behind atom based QSAR analysis was to understand the ligand based QSAR of a series of analogues sharing single core moiety. In our current work, enzymatic inhibition IC_{50} values were considered for the generation of the atom based 3D QSAR mapping. After PLS analysis and LOO operation, correlation and regression coefficient values were found to be as R^2 was 0.983 and Q^2 was 0.741 respectively. Values of SD and RMSE were within the range of values 0.13 and 0.37 respectively. All the contour maps were generated on the basis of PLS factor 5, and mapping was done based on 'QSAR model based' mapping, on most active (**8-21**) and least active (**8-d**) compounds in the enzyme inhibition results.

Contour map analysis are illustrated in Figure 6.13, where, the most active compound **8-21** (Figure 6.13a, c and e) and least active compound **8-d** (Figure 6.13b, d, f) were mapped with hydrogen bond acceptor (Figure 6.13a and b), hydrogen bond donor (Figure 6.13c and d) and hydrophobic mapping (Figure 6.13e and f). Blue cubes represented positive mapping and the red cubes represented negative mapping in Figure 6.13. Analyses of hydrogen bond acceptor mapping (Figure 6.13a and b) on most active compound **8-21** (Figure 6.13a) revealed that the positive blue cubes were allocated at terminal part of methoxy group, suggesting that the increase in length of substitutions on phenyl group with different acceptor moieties improved the activity. Negative red cubes were found allocated at the acceptor oxygen of methoxy phenyl fragment indicating that the replacement of extended alkyl chain with terminal acceptor moieties could improve the activity. Whereas, in case of least active compound **8-d**, the hydrogen

acceptor mapping (Figure 6.13b) was observed with blue cubes allocated mostly away from the molecule and the important observation to consider was that the donor nitrogens of 1,2,4-triazole core moiety was conflictingly mapped with positive acceptor blue cubes indicating the cause of loss in activity. Replacements with different moieties according to the QSAR predictions could improve the activity by possibly changing compound **8-d**'s orientation.

Hydrogen bond donor mapping (Figure 13c and d) on most active compound **8-21** (Figure 6.13c) revealed positive blue cubes allocated at *para* position of phenyl ring attached to 1,2,4-triazole, indicating the possibility of a new substitution on the phenyl ring. Another group of blue cubes were found to have mapped on the donor nitrogen moiety of amide group attached to sulfur alkyl chain, displaying the importance of high activity of **8-21**. In case of least active compound **8-d** (Figure 6.13d), the negative red cubes were clearly found to be mapped on the donor nitrogen of 1,2,4-triazole and amide attached to sulfur alkyl chain, indicating that the loss in activity of the compound **8-d** could be attributed to it.

Analyses of the hydrophobic mapping in which (Figure 13e and f) green cubes represented positive hydrophobic mapping and yellow cubes represented a negative mapping. Contour map revealed that the positive green cubes on most active compound **8-21** (Figure 6.13e) were allocated majorly around the aromatic hydrophobic moieties of the whole molecule, indicating hydrophobicity of the molecule, which was a crucial factor for CatS active site binding. Conversely, in case of the least active compound **8-d** (Figure 6.13f) there were no specific mapping of positive green cubes on the aromatic as well as other hydrophobic groups, instead the negative yellow cubes were observed upon the hydrophobic moieties indicating for the loss inactivity of **8-d**.

On basis of these postulations, we developed an atom based QSAR model using compound **Lead-8** derivatives, and were able to get a complete picture of the key features responsible for bioactivity. The model was found to expediently useful in the generation SAR for newer modifications in the future.

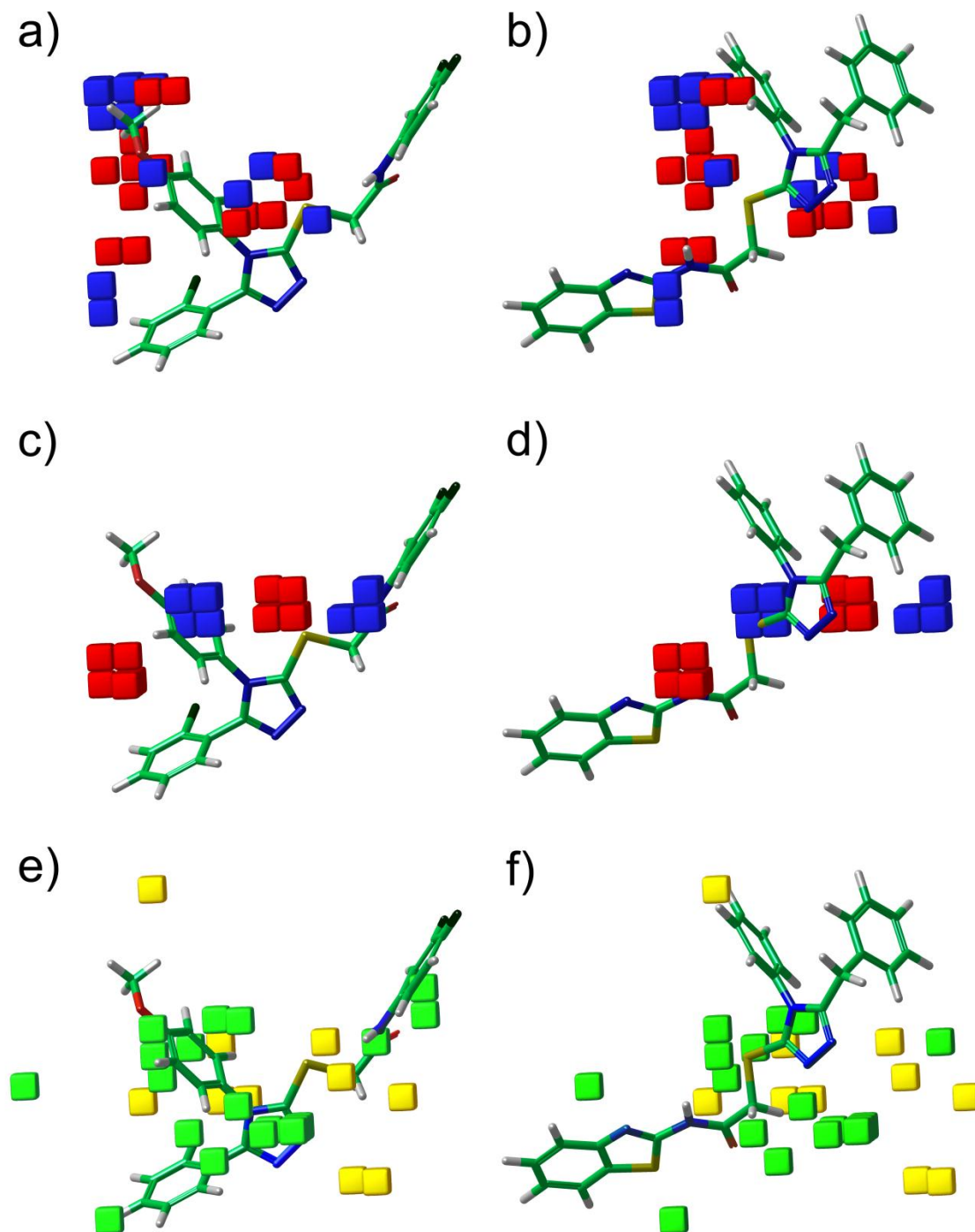


Figure 6.13 Contour mapping on most active compound **8-2l** (a, c, e) and least active compound **8-d** (b, d, f) based on atom based QSAR model. Mapping is hydrogen bond acceptor (a, b), hydrogen bond donor (c, d) and hydrophobic mapping (e, f).

6.4. Summary and conclusion

All the derivatives of **Lead-8** were synthesized and checked for structural elucidation and purity. Initially, 1st generation set of molecules were synthesized and evaluated for CatS enzyme inhibition, and later were modified with help of biological activity data and their respective binding patterns, with a set of 2nd generation series of compounds in presumption to enhance the enzyme inhibitory activity. In particular, 2nd generation series were developed by replacing benzyl group with 2-chlorophenyl group at R₁. Successively, the molecules from 2nd generation were found to show good enzyme inhibition and in growth inhibition compared to that of the 1st generation compounds. Molecules after modification emerged with enhanced enzyme inhibition as well as growth inhibition and lower cytotoxicity. IC₅₀s and GIC₅₀s of the modified 2nd generation series were found in the range from 0.102-52.04 μM and 0.001-100 μM respectively. All the compounds were interpreted with SAR studies with help of binding interaction patterns and an atom based QSAR model was developed and analyzed for SAR predictions. However, all the compounds were forwarded to the preliminary neuropathic pain *in vivo* animal screening to understand the efficacy of these molecules.

CHAPTER 7

Neuropharmacological and molecular interventions

CHAPTER 7

Neuropharmacological and molecular interventions

7.1. Pharmacology

The pathophysiologic and neurochemical characteristics of neuropathic pain are the principle considerations in the search for new treatment targets. Breakthroughs in the understanding of the structural and biochemical changes in neuropathy have opened up possibilities to explore novel exclusive molecular targets. Current enzyme target CatS is an exemplary mediator for the neuro-inflammatory mechanism in progression of nociceptive pathways of neuropathic pain. As discussed in earlier chapters, CatS released from activated microglia elicit cleavage and release of FKN, which, in turn, activates microglia via CXCR3 receptors leading to activation of NF κ B. Further, NF κ B promotes transcription of several inflammatory mediators such as IL-1 β IL-6 and TNF α . These, inflammatory mediators activates ERK through their respective receptors, leading to the central sensitization and pain [Benarroch EE., et al., 2010].

Designed CatS inhibitors after enzyme inhibition and cell based studies were further directed to pharmacological interventions to assess the anti-neuropathic pain potential. Since decades, several animal models were pivotal in understanding the mechanism of neuropathic pain and development of effective novel drug candidates for optimal therapy. In the current study, a sequence of pharmacological interventions was utilized to explore the drug activity on sensory behavioral responses of all synthesized compounds using the CCI model. Nervous tissues from *in vivo* samples from acute treatment groups were utilized to understand the molecular level of gene and protein expressions of neuro-inflammatory mediators.

Ex vivo based methods were also utilized for the molecular level of gene and protein expressions of neuroinflammatory mediators in brain samples. *Ex vivo* model offered an unique advantage over other *in vitro* platforms that they could replicate many aspects of the *in vivo* context. As *ex vivo* models preserved more of tissue architecture of brain regions, where they originated from and maintain neuronal activities intact with functional synaptic activity. Moreover, these assay systems provided easy experimental access and allowed precise control of extracellular

environments, which facilitated research establishing clear correlations between molecular changes with neuropathological outcomes [Cho S., *et.al.*, 2007; Huuskonen J., *et al.*, 2005]. In our current study, rationale behind employing *ex vivo* method was to understand the expression levels of neuro-inflammatory mediators released due to activation of microglia in live cells. In fact, resting ramified phenotype of microglia was intact and responded to the stimuli by retracting their projections minute to minute with a dynamic behavior in live brain and hippocampal slice cultures [Nimmerjahn A., *et.al.*, 2005; Grossmann R., *et.al.*, 2002; Petersen MA., *et.al.*, 2004] which could be effectively used for the study of neuroinflammation.

7.1.1. Behavioral assessment in chronic constriction injury (CCI) model

In the CCI rodent behavioral model, the left sciatic nerve proximal to the trifurcation point was constricted with four loose ligatures using 0-3 braided silk thread aimed to determine the severity of behavioral neuropathic responses. All the test compounds (**Lead-8** and its 32 derivatives) were assessed for three nociceptive assays CA, MH and TA. Main parameters included for pain assessment were percentage reversal of PWD in CA, percentage reversal of PWT in MH and 50% PWT (grams) in TA. Baseline sensory response values for both contralateral and ipsilateral paws were measured for each group of animals (n=5). Assessment was carried at pre and post administration of test compounds in a process of subsequent response examination at 30, 60 and 120 min post drug administration. Gabapentin (GBP) was employed as a standard drug for comparison.

Preliminary examination of the parent compound **lead-8** was checked for neuropathic pain inhibitory potential before synthesizing its analogues. **Lead-8** showed 70% reversal of CA, 55% reversal of MH (Figure 7.1) and in TA 50% paw withdrawal threshold (50% PWT) with a variation of 4.2 g at 30 mg/kg dose (Figure 7.2) after 1 h of drug administration. Compound **lead-8** sustained its significance ($p < 0.05$) at 1h and 2h time post injection in both CA and MH (Figure 7.1) and displayed good anti-nociceptive behavior compared to GBP (standard drug for neuropathic pain). Besides, **lead-8** also exhibited significant ($p < 0.05$) reversal of TA both at 30 and 10 mg/kg dose administration (Figure 7.2).

More than 50% reversal of pain sensitivity based on PWD with regard to CA and MH and more than 4g (not subtracted from basal readings) 50% PWT reversal readings in TA (determined using the up and down method of Dixon [Dixon WJ., *et al.*, 1980]) at 1 h post injection was the screening criteria to characterize worthy compounds at preliminary dose of 30 mg/kg.

Compounds which exhibited this screening criterion in not less than two behavioral methods among the three employed (CA, MH, TA) were further considered for testing at lower doses of 10 and 3 mg/kg. Consequently, among all of **Lead-8** derivatives, nine compounds from 1st generation (**8-a**, **8-d**, **8-e**, **8-f**, **8-i**, **8-j**, **8-k**, **8-n**, **8-o**) and eight compounds from 2nd generation (**8-2a**, **8-2b**, **8-2e**, **8-2h**, **8-2j**, **8-2m**, **8-2n**, **8-3n**) were selected as efficient compounds in reversal of neuropathic pain.

7.1.1.1. Cold allodynia (CA)

In CA assessments, some compounds from 1st generation (**8-e**, **8-j**, **8-k** and **8-n**) were found to ($p < 0.05$) significantly reverse the PWD at 1 h post injection similar to that of **Lead-8** and competitive when compared to GBP (Figure 7.1-a). Compound **8-k** was found to be efficient with a significance of $p < 0.01$ in comparison with vehicle treated group (Figure 7.1-a). At 0.5 h time point, compounds **8-a** and **8-f** were found to significantly reverse PWD, but failed at later time points (1 h and 2 h). In case of the 2nd generation compounds (Figure 7.1-c), compounds **8-2a**, **8-2b**, **8-2h**, **8-2n** and **8-3n** were found to significantly ($p < 0.05$) reverse the PWD at 1 h post injection, similar to **Lead-8** and compound **8-2h** was found to be more effective than the parent compound **Lead-8** ($p < 0.01$). Compound **8-3n** showed clear significance in increasing PWD in all time points (0.5, 1 and 2 h) and compound **8-2b** showed significant activity in two time points (0.5 and 1 h). Compound **8-2m** exhibited significant activity at the 2nd hour post injection similar to the standard, GBP. While finding the structural similarities among these significant anti-CA compounds, most of them had R₂ substitution with 2-chloro-5-(trifluoromethyl) phenyl group on core PTSA (**8-e**, **8-j**, **8-n**, **8-2n** and **8-3n**) and remaining were with varied substitutions. Percentage reversal of PWD values (Mean \pm SEM) of CA of compounds at 30 mg/kg post injection is presented in Table 7.1. All the tested compounds were considered for the quantification of ED50 calculations to pick a best compound for CA assessment.

Table 7.1 Percentage reversal of PWD values (Mean \pm SEM) of CA for compounds tested from 1st and 2nd generation series at 30 mg/kg post injection

Compound Code	CA % reversal for 30-120 min (30 mg/kg post injection)		
	0.5 h	1 h	2 h
Vehicle	2.0 \pm 1.3	5.4 \pm 2.1	2.5 \pm 1.0
8-a	72.7 \pm 10.9	62.9 \pm 10.7	36.1 \pm 10.2*
8-d	35.6 \pm 9.9	14.6 \pm 10.6	49.8 \pm 10.8
8-e	37.4 \pm 6.3	69.7 \pm 10.8*	65.8 \pm 5.1*
8-f	67.6 \pm 9.7	61.1 \pm 4.8	51.7 \pm 10.0
8-i	32.5 \pm 10.2	45.6 \pm 11.0	52.1 \pm 8.4
8-j	11.5 \pm 8.4	74.7 \pm 6.5*	73.8 \pm 10.0*
8-k	55.3 \pm 10.0	76.9 \pm 3.1*	84.3 \pm 1.6
8-n	34.4 \pm 9.45	69.7 \pm 2.4*	59.1 \pm 9.9
8-o	47.6 \pm 6.6	49.2 \pm 2.2	56.4 \pm 7.8
8-2a	36.3 \pm 10.2	74.0 \pm 6.6	46.9 \pm 9.9
8-2b	64.6 \pm 3.0	70.1 \pm 10.4*	22.8 \pm 1.7
8-2e	14.8 \pm 8.1	43.1 \pm 10.3	42.3 \pm 10.9
8-2h	62.5 \pm 7.8	82.8 \pm 7.0**	36.1 \pm 9.6
8-2j	61.1 \pm 7.7	55.6 \pm 6.2	57.3 \pm 8.3
8-2m	47.2 \pm 10.7	55.6 \pm 10.5	71.4 \pm 10.4*
8-2n	42.3 \pm 10.4	73.9 \pm 6.9*	44.2 \pm 3.4
8-3n	78.7 \pm 1.0	74.1 \pm 1.3*	89.9 \pm 1.9
Lead-8	84.1 \pm 3.9	70.9 \pm 2.5*	93.4 \pm 2.4*
GBP	33.8 \pm 4.1	52.3 \pm 4.5	66.9 \pm 2.1*

Significance values in comparison with vehicle group at 1st and 2nd hour post injection was shown in * $p < 0.05$, ** $p < 0.01$ calculated using Dunnett's multiple comparison test in one-way ANOVA.

7.1.1.2. Mechanical hyperalgesia (MH)

Behavioral assessment on MH revealed that the active compounds at 1 h were found to be **8-b**, **8-e** and **8-n** (Figure 7.1-b) from the 1st generation compounds. Among these, **8-n** showed significant enhancement of PWD in all the time points with values $p < 0.05$ at 0.5 h and with $p < 0.01$ at 1 and 2 h. In case of 2nd generation compounds, compounds **8-3n** and **8-2m** were found to show substantial activity, with compound **8-3n** that exhibited significant activity at all-time points at $p < 0.05$. Except compound **8-b**, the remaining four compounds (**8-e**, **8-n**, **8-3n** and **8-2m**) were found to be analogously active in CA and again three of them (**8-e**, **8-n** and **8-3n**) with 2-chloro-5-(trifluoromethyl) phenyl group as R₂ substitution displayed constructive structural features for anti-nociceptive activity. Percentage reversal of PWT values (Mean \pm SEM) in MH assessment for compounds at 30 mg/kg post injection is represented in Table 7.2. All the tested compounds were considered for the quantification of ED₅₀ calculations to pick a best compound for MH assessment.

Table 7.2 Percentage reversal of PWT values (Mean \pm SEM) in MH for compounds tested from 1st and 2nd generation series at 30 mg/kg post injection

Compound Code	MH % reversal for 30-120 min (30 mg/kg post injection)		
	0.5 hr	1 hr	2 hr
Vehicle	2.5 \pm 1.3	1.5 \pm 2.5	3.0 \pm 1.7
8-a	22.4 \pm 8.4	52.6 \pm 12.1*	34.3 \pm 16.0
8-d	25.0 \pm 7.1	21.0 \pm 6.2	21.0 \pm 6.2
8-e	36.1 \pm 7.3	68.5 \pm 10.6**	44.4 \pm 5.6
8-f	26.2 \pm 10.5	38.4 \pm 8.3	29.9 \pm 10.2
8-i	4.4 \pm 10.7	11.7 \pm 8.1	10.4 \pm 9.9
8-j	18.8 \pm 2.1	18.4 \pm 11.1	29.5 \pm 4.5
8-k	4.0 \pm 10.9	19.0 \pm 10.8	11.1 \pm 9.0
8-n	53.3 \pm 10.5	70.0 \pm 10.2**	75.0 \pm 2.9
8-o	15.1 \pm 6.7	20.7 \pm 4.0	9.9 \pm 5.0
8-2a	15.0 \pm 8.9	18.3 \pm 6.4	14.9 \pm 10.7
8-2b	13.1 \pm 3.0	20.8 \pm 3.3	2.8 \pm 2.8
8-2e	17.4 \pm 8.7	35.3 \pm 2.9	1.9 \pm 5.6
8-2h	9.4 \pm 5.8	29.9 \pm 5.0	9.4 \pm 5.8
8-2j	13.7 \pm 3.0	35.0 \pm 9.8	24.1 \pm 4.1
8-2m	38.7 \pm 2.8	52.4 \pm 2.4*	45.1 \pm 11.3
8-2n	28.8 \pm 6.1	42.9 \pm 5.0	23.2 \pm 11.6
8-3n	51.0 \pm 12.1	56.6 \pm 21.7*	61.0 \pm 13.3*
Lead-8	31.0 \pm 6.0	55.2 \pm 2.6*	67.1 \pm 17.1**
GBP	6.1 \pm 6.1	32.9 \pm 5.4	60.0 \pm 5.0*

Significance values in comparison with vehicle group at 1st and 2nd hour post injection was shown in * $p < 0.05$, ** $p < 0.01$ calculated using Dunnett's multiple comparison test in one-way ANOVA.

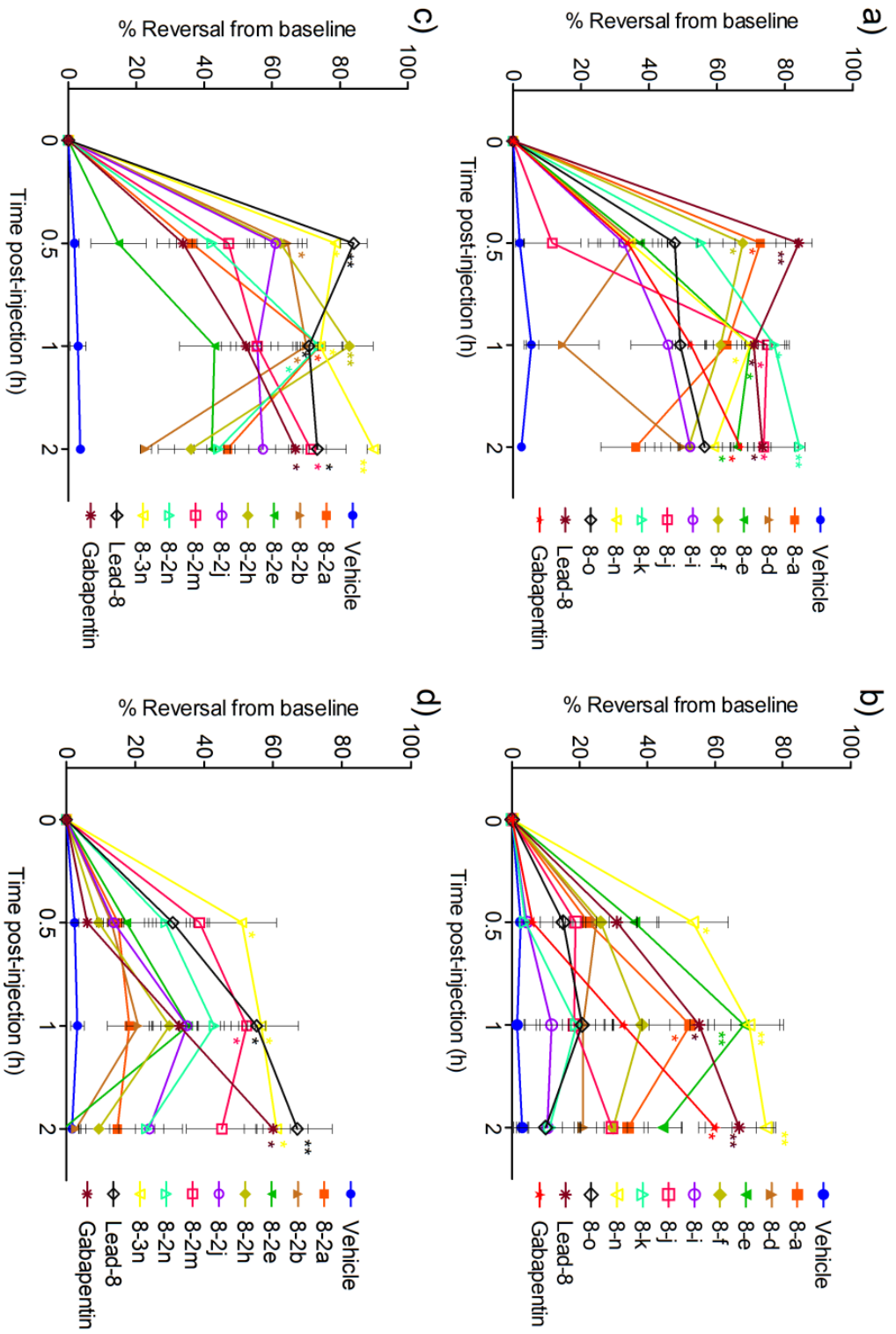


Figure 7.1 Efficacy of selected compounds in CA from 1st generation series (a) and 2nd generation series (c), MH from 1st generation series (b) and 2nd generation series (d) at dose 30 mg/kg. Results of post injection at time points 0.5, 1, and 2 hour are expressed in Mean \pm SEM (* p <0.05, ** p <0.01; Dunnett's multiple comparison test in 1 way ANOVA for non-parametric results undergone for test vs vehicle group $n=5$).

7.1.1.3. Tactile allodynia (TA)

TA assessment of all the compounds is represented in bar graphs (Figure 7.2) to display the 50% PWT in grams using chaplan quantitative statistical assessment method (explained in detail in experimental section). The variance of 50% PWT (g) from 0-1h is depicted in Figure 7.2, where all test compound were compared with vehicle control group to understand the confidence interval. Illustratively, TA was attenuated in a significant manner by 1st generation compounds that included (Figure 7.2-a) **8-e**, **8-i**, **8-k**, **8-n** and **8-o** at a dose of 30 mg/kg and compound **8-n** at 10 mg/kg and further compound **8-d** was effective at 3 mg/kg. In case of 2nd generation compounds (Figure 7.2-b), **8-2j**, **8-2m** and **8-2n** exhibited activity at 30 mg/kg, while compounds **8-2e** and **8-3n** at 10 mg/kg showed reversal of 50% PWT in CCI rats. Among all compounds, **8-i**, **8-n**, **8-o** and **8-2n** were highly effective with 99.9% confidence interval by acquiring significance value of $p < 0.001$ (Figure 7.2) similar to GBP and higher than the parent compound **Lead-8**. Furthermore, compound **8-i** exhibited even more significance level (about $p < 0.05$) when compared with GBP treated CCI group (data not shown). Compounds **8-n**, **8-2e** and **8-3n** at 10mg/kg exhibited enhanced 50% PWT significantly than **Lead-8** as well as GBP, but **8-2e** and **8-3n** were found to be significantly ineffective at 30 mg/kg dose and tumbled into ambiguous nociceptive behavior category. Yet, compound **8-d** at 3 mg/kg was also found to be ambiguous, where it was found ineffective in higher doses. Compounds **8-n** and **lead-8** were consistently significant in lower dose (10 mg/kg) treatment groups. 50% PWT (grams) variance values in TA by selected compounds from 1st and 2nd generation series at 1 h post injection in different doses (30, 10 and 3 mg/kg) are presented in Table 7.3.

Table 7.3 50% PWT (grams) variance values in TA for compounds tested from 1st and 2nd generation series at 1 h post injection in different doses (30, 10 and 3 mg/kg)

Compound Code	TA % reversal (grams) for 30-120 min		
	30 mg/kg	10 mg/kg	3 mg/kg
Vehicle	0.0 ± 0.1	0.0 ± 0.1	0.0 ± 0.0
8-a	1.6 ± 0.1	1.0 ± 0.3	0.0 ± 0.0
8-d	2.3 ± 1.6	1.0 ± 0.5	1.3 ± 1.0**
8-e	5.1 ± 1.5*	1.7 ± 0.7	0.3 ± 0.2
8-f	4.1 ± 0.7	0.3 ± 0.6	0.2 ± 0.2
8-i	10.4 ± 0.2****	2.0 ± 0.3	0.0 ± 0.0
8-j	0.7 ± 0.2	0.5 ± 0.3	0.0 ± 0.0
8-k	5.1 ± 1.5*	0.3 ± 0.1	0.3 ± 0.2
8-n	5.9 ± 1.2****	2.8 ± 0.8**	0.4 ± 0.3
8-o	6.9 ± 0.9****	0.3 ± 0.2	0.4 ± 0.2
8-2a	1.5 ± 0.6	1.1 ± 0.4	0.0 ± 0.0
8-2b	1.5 ± 0.4	1.1 ± 0.5	1.1 ± 0.3
8-2e	2.9 ± 0.5	3.1 ± 1.7****	0.4 ± 0.3
8-2h	0.7 ± 0.2	0.7 ± 0.0	0.2 ± 0.2
8-2j	5.0 ± 0.6**	1.1 ± 0.5	0.7 ± 0.3
8-2m	2.8 ± 0.2*	1.6 ± 0.3	0.9 ± 0.4
8-2n	5.7 ± 1.7****	1.1 ± 0.3	1.1 ± 0.5
8-3n	3.0 ± 0.7	2.8 ± 0.7**	1.3 ± 0.5
Lead-8	4.2 ± 0.2*	2.3 ± 1.1*	1.3 ± 0.6
GBP	5.8 ± 0.3****	0.9 ± 0.4	0.4 ± 0.2

Significance values in comparison with vehicle group at 30, 10 and 3 mg/kg shown in * $p < 0.05$, ** $p < 0.01$, **** $p < 0.001$ calculated using Dunnett's multiple comparison test in one-way ANOVA.

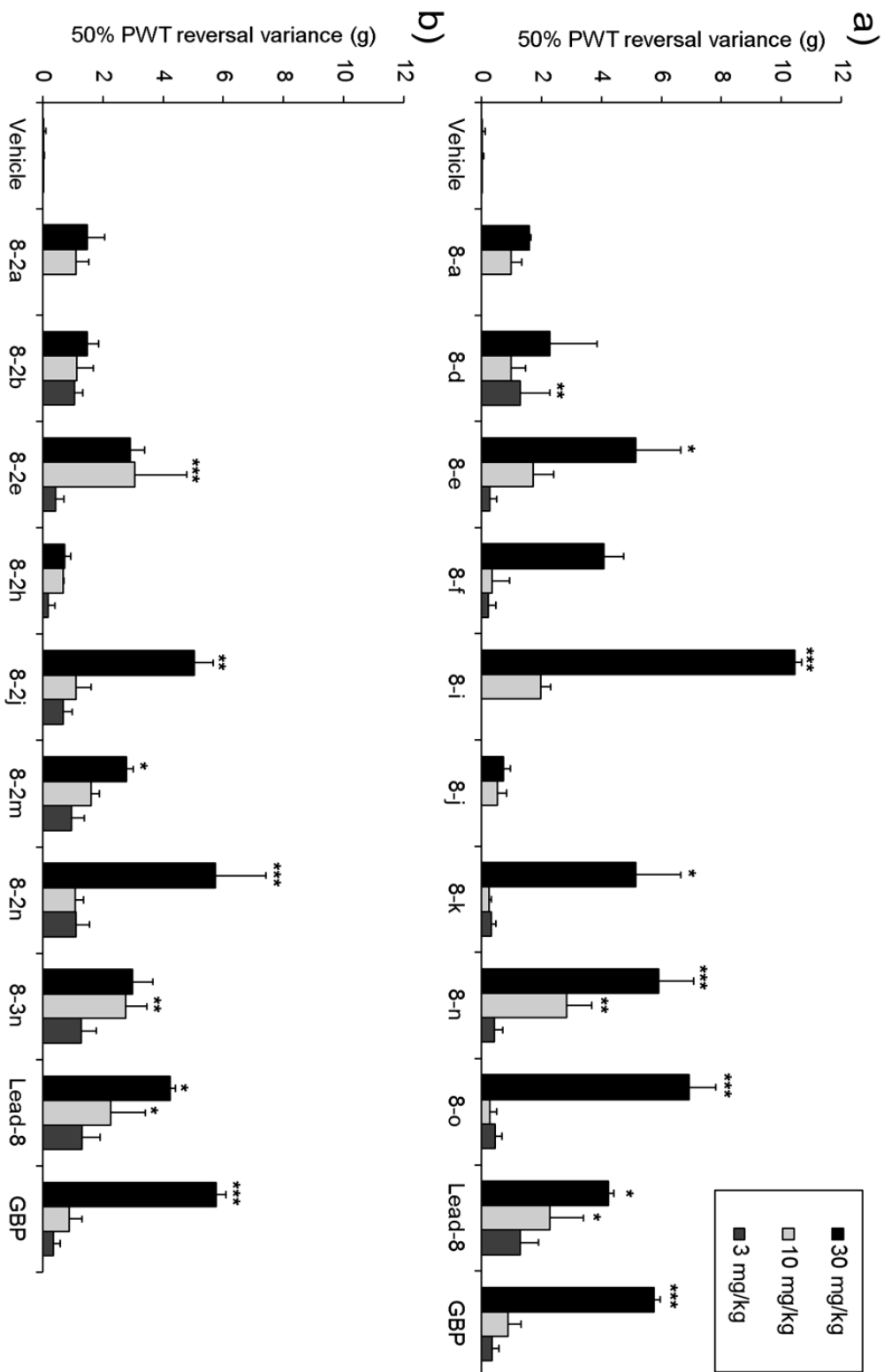


Figure 7.2 Efficacy of selected compounds in TA from 1st generation series (a) and 2nd generation series (b) compounds at 1hr post injection in different doses (30, 10 and 3 mg/kg). Results were 50% PWT variance from basal readings (pre dose injection) expressed in mean \pm SEM (* $p < 0.05$, ** $p < 0.01$, *** $p < 0.001$ Dunnett's multiple comparison post hoc test in one-way ANOVA for non-parametric results, comparison undergone for test vs vehicle group where $n=5$).

7.1.2. Neurotoxicity

Central nervous system depressant activity-locomotor activity of administered test compounds was assessed to understand the percentage of neurotoxicity at the dose of 100 mg/kg. The percentage change in the activity from pre to post administration of the test drugs was calculated while in comparison with vehicle treated group. Compounds **8-a**, **8-2a** and **8-2n** were showed more than 50% of the depressant of the locomotor activity, could be considered as neurotoxic to the rats at dose of 100 mg/kg. Compounds **8-f**, **8n**, **8-2b** and **8-2e** were showed the less than 20% of the depressant of the locomotor activity and which were safe drugs for the rats at 100 mg/kg dose. Remaining compounds (percentage locomotor activity between 20 and 50%) were considered to be moderately toxic at 100 mg/kg dosing in rats.

7.1.3. Structure activity relationships

To derive structure-activity relationship based on the *in vivo* anti-neuropathic pain assessment, we considered compounds which were quantified (ED_{50}). Many compounds with R_2 substitution with 2-chloro-5-(trifluoromethyl)phenyl group (**8-e**, **8-n**, **8-j**, **8-2j**, **8-2n**, **8-2e** and **8-3n**) were eventually found to show anti-nociceptive activity nearly in all three behavioural methods (CA, MH and TA). Replacing benzyl group with 2-chlorophenyl group at R_1 position did not help in improving the nocifensive behavior in CCI rats, rather led to a decrease in activity. However, simple substitutions such as phenyl group at R_2 position and unsubstitution (**8-a** and **8-2a**) were found to be effective and showed lower ED_{50} values in CA and MH, but exhibited more than 60% neurotoxicity at 100 mg/kg (Table 7.4). While comparing another set of compounds **8-k** and **8-0** with 3-acetylphenyl substitution at R_2 position in combination with R-substitution with either fluoro or methoxy respectively, showed similar activities as well as low neurotoxicity. Whereas, enhancement of the nociceptive behavior by good ED_{50} values (Table 7.4) and nociceptive behavior in TA method, by compound **8-0** inferred us that methoxy substitution at R position was favorable than the fluoro group. Compound **8-n** exhibited better ED_{50} value (< 3.000) in the reduction of CA and also in MH with a low ED_{50} value (8.407), but it was competent with compound **8-i**. Compound **8-i** exhibited remarkable bioactivity in TA assessment as well as in MH with low ED_{50} value (< 3.000) (Table 7.4). However, main criteria in the selection of single final compound for further studies, was based on overall activity profile that included both cell based activity as well as anti-nociceptive effects and also with adequate CatS inhibition. In fact, in central nervous system depressant locomotor activity assessment, compound **8-n** (7.56 %) is

more than 4 fold safe when compare to the compound **8-i** (37.20 %) at 100 mg/kg of the dosing (Table 7.4). Therefore, compound **8-n** was considered as best compound among all the series of compounds derived from compound **Lead-8**, where, it sustained its potency in all the chief considerations of neuropathic pain assessments. Finally, compound **8-n** was chosen for further evaluation of gene expression level studies of neuro-inflammatory mediators involved in neuropathic pain.

Table 7.4. ED₅₀ values of selected compounds based on methods CA and MH and their respective percentage of neurotoxicity values represented in Mean±SEM.

Compound code	Cold Allodynia ED₅₀ (mg/kg)	Mechanical Hyperalgesia ED₅₀ (mg/kg)	% Neurotoxicity (100 mg/kg)
8-a	9.58±0.09	28.50±0.03	68.96±2.65
8-d	9.91±0.19	> 30.00	45.99±3.85
8-e	11.61±0.67	20.65±0.09	32.46±1.86
8-f	21.04±0.14	> 30.00	19.80±1.38
8-i	12.75±1.09	3.01±0.60	37.20±1.12
8-j	9.19±0.02	>30.000	36.51±0.52
8-k	12.99±0.59	> 30.000	26.10±1.98
8-n	3.00±1.05	8.40±0.20	7.56±0.67
8-o	4.19±1.35	10.58±0.99	27.74±1.60
8-2a	8.91±0.16	>30.00	68.93±3.27
8-2b	9.16±0.21	>30.00	5.49±0.62
8-2e	>30.00	>30.00	0.78±0.53
8-2h	8.10±0.09	>30.00	27.85±2.46
8-2j	20.04±0.14	>30.00	22.89±1.79
8-2m	19.42±0.17	26.87±0.01	35.62±1.85
8-2n	10.29±0.12	>30.00	50.05±1.59
8-3n	10.08±0.13	20.40±0.08	35.29±1.43
Lead-8	10.06±0.13	21.51±0.13	23.82±0.35
GBP	>30.00	23.45±0.25	5.79±0.44

7.1.4. Gene expression studies from *in vivo* samples

Rationality behind choosing inflammatory mediators was due to their crucial role in progression of inflammatory neuropathic pain with association of neurons, microglia and dorsal horn sensitization following nerve injury. Activated microglia and astrocytes after nerve injury lead to mitogen-activated kinase p38 pathway activation which was involved in activation of nuclear factor kappa B (NFκB), which promoted transcription of several inflammatory mediators such as interleukin-1β (IL-1β), interleukin-6 (IL-6) and tumor necrosis factor α (TNFα) [Atremoliere A., *et al.*, 2009; Basbaum AI., *et al.*, 2009; Drdla R., *et al.*, 2008]. Due to activation of respective cytokine receptors by pro-inflammatory cytokines (IL-1β, IL-6 and TNFα) and over expression of extracellular signal-regulated kinase1 (ERK1) which was the main mediator in p38 MAPK nociceptive pathway finally contributed to central sensitization and neuropathic pain [Atremoliere A., *et al.*, 2009; Basbaum AI., *et al.*, 2009; Drdla R., *et al.*, 2008; Ciruela A., *et al.*, 2003]. GBP was employed as standard drug for comparisons of the gene expression of inflammatory mediators as recent reports revealed that intrathecal injection of GBP reduced the expression of pro-inflammatory cytokines TNF-α, IL-1β and IL-6 [Lee B., *et al.*, 2013] in rats. Moreover, GBP had also been reported to show a role in inhibition of NF-κB in rat spinal dorsal root ganglia cells [Park S., *et al.*, 2008] suggesting a role of GBP in the anti-inflammatory mechanisms in the attenuation of neuropathic pain.

As shown in the Figure 7.3, mRNA expression of NFκB, ERK1, IL-1β, IL-6 and TNFα were highly expressed in control group CCI rats as compared to normal naive rats in all the three nervous tissues (brain, spinal cord and sciatic nerve) studied. Quantitative mRNA, relative normalized expression (10^4) of NFκB, ERK1, IL-1β, IL-6 and TNF-α in brain, spinal cord and sciatic nerve were expressed as mean±SEM and are represented in Table 7.5. Treatment with best active compound **8-n** and standard compound GBP (30 mg/kg) down regulated mRNA expressions as compared to vehicle treated CCI control group. Compound **8-n** was found to significantly attenuate ($p<0.05$) mRNA expression of NFκB only in brain tissue, wherein GBP was found to be inefficient in any of the tissues (Figure 7.3a). In case of ERK1 gene expression, compound **8-n** exhibited remarkable down regulation similar to that of GBP (Figure 7.3b) both in brain and spinal cord tissues ($p<0.001$, $p<0.01$ respectively). With regard to the cytokine expression levels **8-n** regulated the levels of mRNA expression of IL-1β (Figure 7.3c) with high significance in brain ($p<0.001$) and in spinal cord tissues ($p<0.05$). Even the significance level

of reduction was similarly high ($p < 0.001$) when compared with GBP group, in which GBP did not show any activity with IL-1 β in any of the tissues (Figure 7.3c). IL-6 mRNA expression (Figure 7.3d) was reduced notably by GBP compared to compound **8-n** in spinal cord ($p < 0.01$) which showed equal significance of reduction in both brain and spinal cord tissues ($p < 0.05$). Finally, in case of TNF α , mRNA expression levels were found high in sciatic nerve (Figure 7.3-e) than other inflammatory mediators, and it was down regulated by GBP ($p < 0.05$) with unknown reasons. However, compound **8-n** displayed significant down regulation of TNF α expression similar to GBP in spinal cord ($p < 0.001$) and more significantly than GBP in case of brain ($p < 0.05$). Therefore, the mRNA expression studies could be inferred with the compound **8-n** being found to successfully down regulate the inflammatory mediators especially NF κ B (indirectly activated by CatS activity) *via* p38 MAPK pathway. As the crucial mediator among final cascade of MAPK pathway mediator was ERK1 we evaluated our compounds and **8-n** completely attenuated similar to the standard GBP. Conclusively, compound **8-n** thus evolved as the best active molecule from the parent **Lead-8** and showed adequate implications to treat inflammatory neuropathic pain.

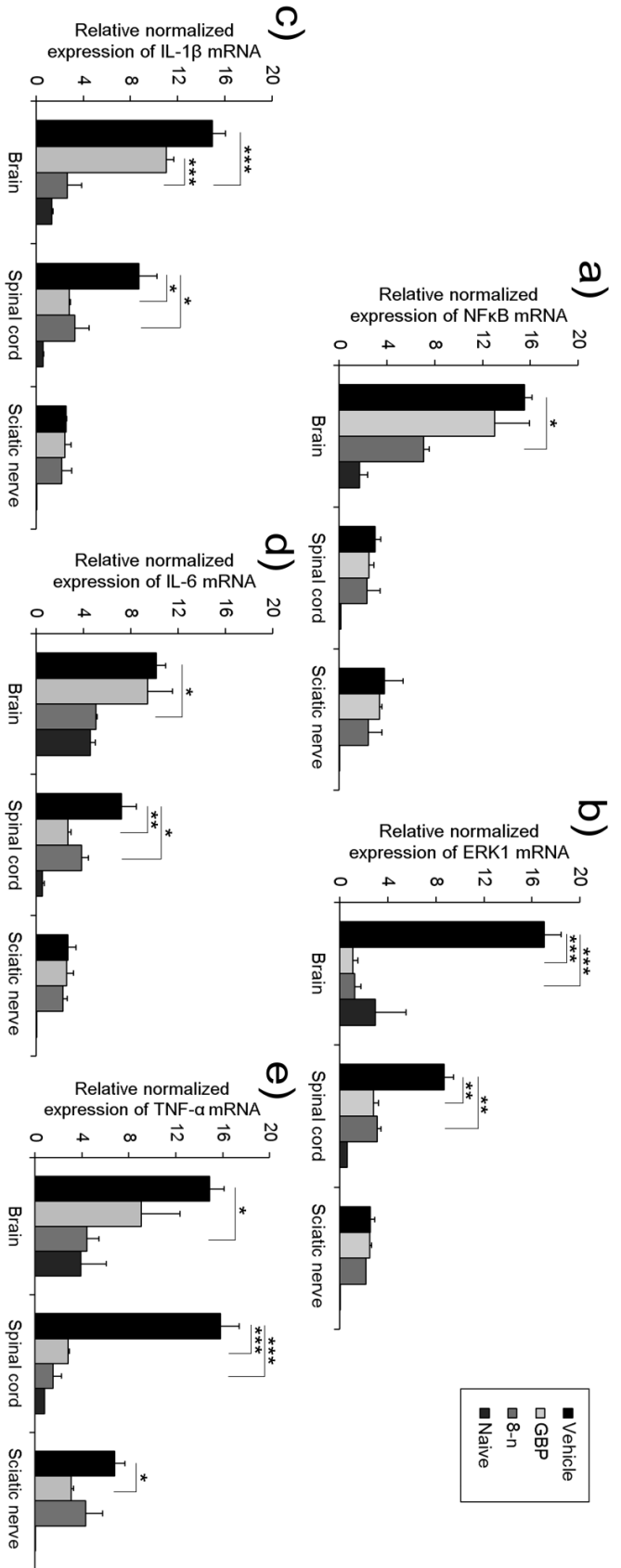


Figure 7.3 Effect of treatment of compound **8-n** and GBP on quantitative mRNA levels of NFκB (a) ERK1 (b) IL-1β (c) IL-6 (d) and TNF-α (e) in brain, spinal cord and sciatic nerve (ipsi lateral). Data are expressed as mean±SEM from n=3 rats and analyzed by a one-way ANOVA followed by post hoc Tukey's multiple range test. Significance values are represented as * $p < 0.05$, ** $p < 0.01$, *** $p < 0.001$.

Table 7.5. Quantitative mRNA relative to normalized expression (10^4) of NF κ B, ERK1, IL-1 β , IL-6 and TNF- α in brain, spinal cord and sciatic nerve expressed as Mean \pm SEM

Mediator	Tissue	Vehicle	GBP	8-n	Naive
NFκ-B	Brain	15.5 \pm 0.6	13.0 \pm 2.9***	7.1 \pm 0.5***	1.7 \pm 0.7
	Spinal cord	3.0 \pm 0.5	2.5 \pm 0.4**	2.4 \pm 0.4**	0.1 \pm 0.0
	Sciatic nerve	3.8 \pm 1.5	3.4 \pm 0.2	2.4 \pm 0.2	0.0 \pm 0.0
ERK1	Brain	17.0 \pm 1.4	1.1 \pm 0.4	1.2 \pm 0.6*	3.0 \pm 2.5
	Spinal cord	8.7 \pm 0.8	2.8 \pm 0.4	3.1 \pm 0.3	0.6 \pm 0.0
	Sciatic nerve	2.5 \pm 0.4	2.5 \pm 0.2	2.2 \pm 0.0	0.0 \pm 0.0
IL-1β	Brain	14.9 \pm 1.1	11.0 \pm 0.7***	2.7 \pm 1.2***	1.4 \pm 0.1
	Spinal cord	8.7 \pm 1.5	2.8 \pm 0.1*	3.3 \pm 1.2*	0.6 \pm 0.1
	Sciatic nerve	2.5 \pm 0.1	2.5 \pm 0.5	2.2 \pm 0.9	0.0 \pm 0.0
IL-6	Brain	10.2 \pm 0.8	9.4 \pm 2.1	5.0 \pm 0.1*	4.6 \pm 0.4
	Spinal cord	7.2 \pm 1.2	2.7 \pm 0.2**	3.8 \pm 0.6*	0.5 \pm 0.1
	Sciatic nerve	2.7 \pm 0.7	2.6 \pm 0.5	2.3 \pm 0.4	0.0 \pm 0.0
TNF-α	Brain	14.9 \pm 1.2	9.0 \pm 3.3	4.4 \pm 1.0*	3.9 \pm 2.1
	Spinal cord	15.8 \pm 1.6	2.8 \pm 0.1***	1.5 \pm 0.7***	0.8 \pm 0.0
	Sciatic nerve	6.8 \pm 0.9	3.1 \pm 0.2*	4.3 \pm 0.2	0.0 \pm 0.0

Significant mRNA expression levels in comparison with vehicle group shown in * $p < 0.05$, ** $p < 0.01$, *** $p < 0.001$ calculated using Dunnett's multiple comparison test in one way ANOVA.

7.1.5. Western blot analysis

Western blot analysis for the expression of inflammatory neuropathic pain mediator ERK1 was analyzed in *in vivo* samples of CCI animals. Wherein, ERK1 was found to mediate neuropathic pain through different inflammatory pathways, including CatS through induction of p38 MAPK pathway as reported earlier [Benarroch EE., *et al.*, 2010]. In this context, to understand the expression levels of the crucial mediator ERK1 we performed western blot analysis method. Acute dosing of compound **8-n**, GBP and vehicle to CCI animals and followed by collection of the lumbosacral spinal cords of the rats after 1 h of post injection was done. Normal naïve rats were taken as negative control. Protein samples and required buffers were prepared as described in materials and methods section 4.8.10. Scanned images generated after x-ray film transfer were analyzed using Image J software application, to understand the relative quantity. For relative quantity analysis, vehicle treated CCI animal sample was considered as 1, and relative expression of remaining samples was generated based on the vehicle sample (Figure 7.4). Compound **8-n** was found to exhibit relatively good activity in decreasing the level of pERK expression, where it was found near to the expression of naïve animal. In comparison with the standard compound **GBP**, compound **8-n** showed relatively low expression levels. This indicated an additional confirmation for the compound **8-n**'s efficacy after acute dosing to the CCI neuropathic rats.

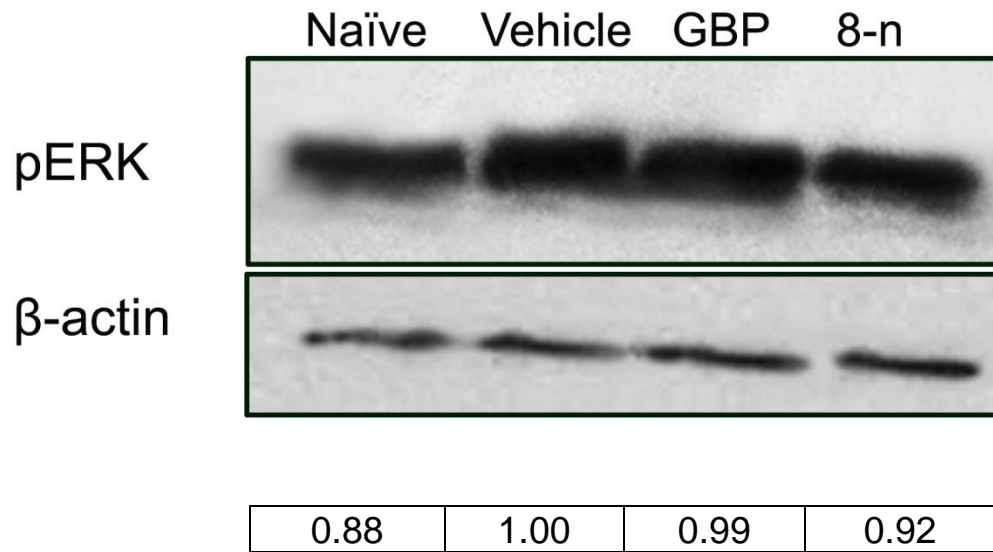


Figure 7.4 Western blot on the *in vivo* samples with their relative quantity of pERK expression measured by Image J application. Vehicle sample considered as 1, and remaining samples were relatively represented.

7.1.6. Gene expression studies in *ex vivo* samples

To estimate the efficacy of compound **8-n** further in inflammatory conditions, we also attempted in *ex vivo* model for inflammation. Lipopolysaccharide (LPS), an endotoxin derived from gram-negative bacteria was found to damage peripheral and central nervous system. LPS also induces inflammation in both *in vivo*, *ex vivo* conditions of brain tissues and was reported to cause progressive neuronal death overtime [Brian JE, Jr., *et al.*, 1998]. Hence was found to be toxic to the neighboring neurons, and further caused microglial activation and self-propelling progressive cycle of inflammation and neuronal damage. In the current study, estimation of proinflammatory cytokines (IL-6, IL-1 β , TNF- α), ERK1 and NF κ B gene expressions were analyzed using real time PCR studies in LPS treated tissues. mRNA expression was found to be high in LPS treated brain slices and conversely, significant decrease of mediators was observed when treated with GBP and **8-n** (Figure 7.5). Compound **8-n** was found to significantly reduce ($p < 0.001$) IL-6, TNF- α , NF κ B and ERK1. In case of TNF- α , compound **8-n** showed remarkable decrease in expression when compared to GBP. IL-6, IL-1 β , NF κ B and ERK1 mRNA expressions ($p < 0.001$) were reduced noticeably by GBP in comparison with naïve. However, compound **8-n** also showed significant ($p < 0.001$) decrease in expression in comparison with LPS treated vehicle control. Therefore, from this study we could infer that compound **8-n** was successful in down regulating the inflammatory mediators especially TNF- α more significantly than GBP. The crucial mediator in MAPK pathway being ERK1 was found to be decreased after treating with compound **8-n**.

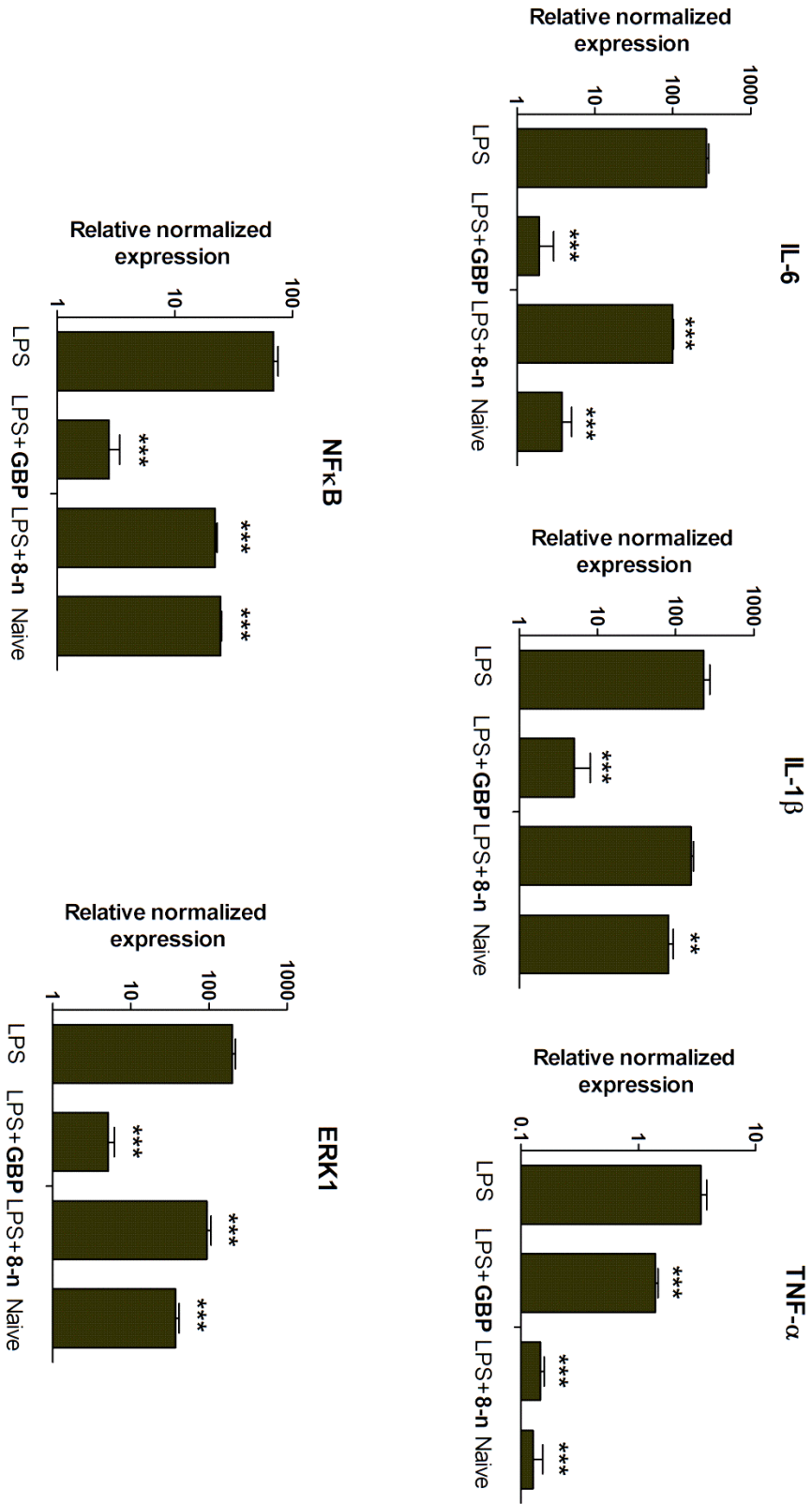


Figure 7.5 Quantitative mRNA level estimation of IL-6, IL-1β, TNF-α, NFκB and ERK1 in LPS treated *ex vivo* brain samples in the presence of compound **8-n** and **GBP**. Data are expressed as mean±SEM for n=3 rat samples and analyzed by a one-way ANOVA followed by post hoc Tukey's multiple range test. Significance values are represented as ** $p < 0.01$ and *** $p < 0.001$.

7.2. Summary and conclusion

A thorough biological evaluation of all the 32 compounds derived from parent compound **Lead-8** was conducted. Initially, compounds were tested for preliminary behavioral assessments along with parent compound **Lead-8**. Further 18 active compounds from 1st and 2nd series including **Lead-8** were chosen based on their activity in behavioral assessments and further analyzed in different doses to quantify ED₅₀ values. Among all the compounds, compound **8-n** exhibited lowest ED₅₀ value (3.00 mg/kg) in CA with adequate MH lower ED₅₀ value (8.41 mg/kg) and also showed significant reversal of TA at both 30 and 10 mg/kg doses ($p < 0.001$ and $p < 0.01$ respectively). Compound **8-i** showed good TA inhibition at 30 mg/kg ($p < 0.001$) and exhibited lowest ED₅₀ value in MH (3.01 mg/kg). In fact, compound **8-n** showed good enzymatic and cell based inhibitory activity compared to compound **8-i**. Finally, compound **8-n** was selected for the gene and protein expression studies, where it revealed a remarkable role in all biological and pharmacological activity assessments. Moreover, main criteria in the selection of a single final compound for further studies, was based on overall best activities such as anti-cancerous as well as anti-nociceptive behaviors and with adequate CatS inhibition. Compound **8-n** found to be successful CatS inhibitor in down regulation of the mRNA levels of inflammatory mediators as well as crucial mediators ERK1 and NFκB both in *in vivo* and *ex vivo* nervous tissue samples. Protein expression of pERK were found to be relatively reduced by compound **8-n** when compared to GBP in CCI neuropathic rat brain samples. Thus, compound **8-n** with all the chief priorities emerged as a potent compound useful in the treatment neuropathic pain.

CHAPTER 8

Recapitulation and Future perspectives

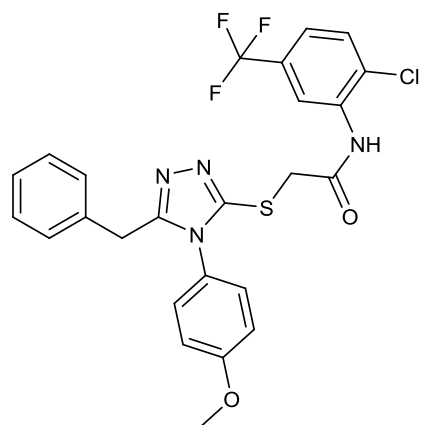
CHAPTER 8

Recapitulation and Future perspectives

- In the present work, we have attempted to design novel diverse inhibitors for the pleiotropic enzyme CatS, which has crucial role in inflammatory neuropathic pain and microglial cancer.
- Computer assisted drug design strategies such as ligand based and structure based drug designs were utilized to generate robust pharmacophore models to screen promising molecules from a large dataset of a commercial library as CatS inhibitors. Hit molecules attained were subjected for docking based virtual screening methods to predict the binding interactions between the enzyme active site and the molecule and to screen out the best hits.
- 52 molecules were shortlisted and were analyzed for the enzyme inhibition assay and the molecules with more than 50 % inhibition at 50 μM concentration were selected for the IC_{50} calculation.
- 26 Lead compounds out of 52 were biologically evaluated for the calculation of IC_{50} and GIC_{50} in cell based assay to find out the best CatS inhibitor with glioblastoma anticancer activity. Lead molecule was selected based on the glioblastoma cancer activity, where, CatS was found to be over expressed in extracellular regions of brain, both in cases of astrocyte cancers as well as in neuropathic conditions.
- Compound **Lead-8** with the IC_{50} value of 6.58 μM and the GIC_{50} of 0.477 μM was selected as best lead molecule for the lead optimization based on medicinal chemistry approach.
- A total of 32 analogues from parent compound **Lead-8** with different modifications were designed with computational methodologies and synthesized as a part of lead optimization.

- Synthesized and purified 32 analogues were subjected for the CatS enzyme inhibition, glioblastoma growth inhibition and cell cytotoxicity assessments, to postulate the structure activity relationships and selectivity index towards cancerous cells rather than normal cells.
- All the 32 synthesized compounds along with **Lead-8** were tested for preliminary *in vivo* neuropathic pain behavioral assays.
- From 32 compounds, 18 active compounds including **Lead-8** were selected and further analyzes in different doses to estimate ED₅₀ values.
- Among all the compounds, compound **8-n** exhibited lowest ED₅₀ value (3.00 mg/kg) in reduction of CA and with adequate MH lower ED₅₀ value (8.41 mg/kg) and showed significant reversal of TA at both 30 and 10 mg/kg doses ($p < 0.001$ and $p < 0.01$ respectively).
- Finally, compound **8-n** was selected for the gene and protein expression studies, where it showed remarkable role in all biological and pharmacological activity assessments. Apparently, compound **8-n** was found to successfully down regulate the mRNA levels of inflammatory mediators as well as crucial mediators ERK1 and NFκB both in *in vivo* and *ex vivo* nerve tissue samples.
- Protein expression of the pERK was relatively reduced by compound **8-n** when compared to the GBP in CCI neuropathic rat brain samples.

Our findings demonstrated that the journey of CatS inhibitor drug discovery had brought forward promising compounds especially compound **8-n** with good CatS inhibition and retained its potency in cancer inhibition and alleviated neuropathic pain. Significant attenuation of gene and protein expressions of inflammatory pain mediators (expressed in relation to CatS) in the nervous tissues was demonstrated by compound **8-n** and hence indicated its effectiveness in reducing the inflammatory mediators involved in neuropathic pain.



Compound **8-n**

Future insights:

- Structural modification based on developed atom based QSAR prediction models and binding interaction based SAR, could be useful for further molecular development with improved bioactivity.
- Immunofluorescence studies on both cancerous cells as well as neuropathic nervous tissues could be performed further to image and understand the allied expressions of particular molecular targets (CatS, FKN, CX3CR).
- Studies are still required to confirm the chronic pharmacodynamic and pharmacokinetic profile of the active molecules including safety profile.
- Development and utilization of brain cancer induced neuropathic pain animal models could be a novel domain to work, where, there are no such neuropathic pain animal models till date.
- Profound molecular pharmacological studies on specific molecular targets (ex: CatS) that causes brain cancers and concomitantly induces neuropathic pain, need to be studied further.
- Advancement of the candidate compounds presented in this thesis along a drug development path would require a significant investment in medicinal chemistry, preclinical and clinical studies.

References

References

- Aldous DJ, Leroy V, Thurairatnam S, Timm AP (2005). Novel keto-oxadiazole derivatives as cathepsin inhibitors. WO2005040142.
- Allen D, Ameriks MK, Axe FU, Burdett M, Cai H, Choong I, Edwards JP, Lew W, Meduna SP (2008a). Bicyclic aminopropyl tetrahydro-pyrazolo-pyridine modulators of cathepsin S. WO2008100620.
- Allen D, Choong I, Lew W (2008b). Biaryl-substituted tetrahydro-pyrazolo-pyridine modulators of cathepsin S. WO2008100622.
- Alper PB, Chatterjee A, Liu H, Mutnick D, Tully DC, Woodmansee DH (2005). Compounds and compositions as cathepsin S inhibitors. WO2005107464.
- Ameriks MK, Arienti KL, Edwards JP, Grice CA, Jones TK, Lee-Dutra A, Liu J, Mani NS, Neff DK, Wickboldt AT (2008). Tetrahydro-pyrazolo-pyridine thioether modulators of cathepsin s . WO2008100621.
- Ameriks MK, Axe FU, Bembenek SD, Edwards JP, Gu Y, Karlsson L, Randal M, Sun S, Thurmond RL, Zhu J (2009). Pyrazole-based cathepsin S inhibitors with arylalkynes as P1 binding elements. *Bioorg Med Chem Lett* 19: 6131-6134.
- Ameriks MK, Bembenek SD, Burdett MT, Choong IC, Edwards JP, Gebauer D, Gu Y, Karlsson L, Purkey HE, Staker BL (2010). Diazinones as P2 replacements for pyrazole-based cathepsin S inhibitors. *Bioorg Med Chem Lett* 20: 4060-4064.
- Asaad N, Bethel PA, Coulson MD, Dawson JE, Ford SJ, Gerhardt S, Grist M, Hamlin GA, James MJ, Jones EV (2009). Dipeptidyl nitrile inhibitors of cathepsin L. *Bioorg Med Chem Lett* 19: 4280-4283.
- Asakura W, Matsumoto K, Ohta H, Watanabe H (1993). Effect of alpha 2-adrenergic drugs on REM sleep deprivation-induced increase in swimming activity. *Pharmacol Biochem Behav* 46: 111-115.

- Ayasa S, Lindquist C, Agback T, Benkestock K, Classon B, Henderson I, Hewitt E, Jansson K, Kallin A, Sheppard D (2009). Solid-phase parallel synthesis and SAR of 4-amidofuran-3-one inhibitors of cathepsin S: Effect of sulfonamides P3 substituents on potency and selectivity. *Bioorg Med Chem* 17: 1307-1324.
- Bailey A, Pairaudeau G, Patel A, Thom S (2003). Novel purine- or pyrrolo[2,3-d]pyrimidine-2-carbonyls for treating diseases associated with cysteine protease activity. WO2004000843.
- Baron R (2006). Mechanisms of disease: neuropathic pain—A clinical perspective. *Nat Clin Prac Neurol* 2: 95-106.
- Basbaum AI, Bautista DM, Scherrer G, Julius D (2009). Cellular and molecular mechanisms of pain. *Cell* 139: 267-284.
- Basu A, Jasu K, Jayaprakash V, Mishra N, Ojha P, Bhattacharya S (2009). Development of CoMFA and CoMSIA models of cytotoxicity data of anti-HIV-1-phenylamino-1H-imidazole derivatives. *Eur J Med Chem* 44: 2400-2407.
- Beavers MP, Breitenbucher JG, Cai H, Edwards JP, Grice CA, Gustin DJ, Khatuya H, Medina SP, Pio BA, Tays KL (2007). Substituted pyrazoles useful for treating autoimmune diseases mediated by cathepsin S. US7309703.
- Beck H, Schwarz G, Schröter CJ, Deeg M, Baier D, Stevanovic S, Weber E, Driessen C, Kalbacher H (2001). Cathepsin S and an asparagine-specific endoprotease dominate the proteolytic processing of human myelin basic protein *in vitro*. *Eur J Immunol* 31: 3726-3736.
- Beers C, Burich A, Kleijmeer MJ, Griffith JM, Wong P, Rudensky AY (2005). Cathepsin S controls MHC class II-mediated antigen presentation by epithelial cells *in vivo*. *J Immunol* 174: 1205-1212.
- Bekkali Y, Thomson DS, Betageri R, Emmanuel MJ, Hao M, Hickey E, Liu W, Patel U, Ward YD, Young ER (2007). Identification of a novel class of succinyl-nitrile-based cathepsin S inhibitors. *Bioorg Med Chem Lett* 17: 2465-2469.

- Bekkali Y, Hickey ER, Patel UR, Spero DM, Sun S, Thomson DS, Ward YD, Weimin L, Young ERR (2003). Compounds useful as reversible inhibitors of cysteine proteases. WO2003029200.
- Benarroch EE (2010). Central neuron-glia interactions and neuropathic pain: overview of recent concepts and clinical implications. *Neurol* 75: 273-278.
- Bennett GJ and Xie Y (1988). A peripheral mononeuropathy in rat that produces disorders of pain sensation like those seen in man. *Pain* 33: 87-107.
- Bennett G (1997). Neuropathic pain: An overview. *Prog Pain Res Manag* 9: 109-114.
- Bouhassira D, Attal N, Fermanian J, Alchaar H, Gautron M, Masquelier E, Rostaing S, Lanteri-Minet M, Collin E, Grisart J (2004). Development and validation of the neuropathic pain symptom inventory. *Pain* 108: 248-257.
- Bowsher D (1999). The lifetime occurrence of herpes zoster and prevalence of post-herpetic neuralgia: a retrospective survey in an elderly population. *Eur J Pain* 3: 335-342.
- Bowsher D (1991). Neurogenic pain syndromes and their management. *Br Med Bull* 47: 644-666.
- Boycott HE, Wilkinson JA, Boyle JP, Pearson HA, Peers C (2008). Differential involvement of TNF α in hypoxic suppression of astrocyte glutamate transporters. *Glia* 56: 998-1004.
- Brian JE, Jr, Moore SA, Faraci FM (1998). Expression and vascular effects of cyclooxygenase-2 in brain. *Stroke* 29: 2600-2606.
- Brömme D and Wilson S (2011): Role of cysteine cathepsins in extracellular proteolysis. In: Anonymous Extracellular matrix degradation. Springer. Volume 2. pp 23-51.
- Cai J, Bennett DJ, Rankovic Z, Dempster M, Fradera X, Gillespie J, Cumming I, Finlay W, Baugh M, Boucharens S (2010). 2-Phenyl-9H-purine-6-carbonitrile derivatives as selective cathepsin S inhibitors. *Bioorg Med Chem Lett* 20: 4447-4450.

- Cardona AE, Li M, Liu L, Savarin C, Ransohoff RM (2008). Chemokines in and out of the central nervous system: much more than chemotaxis and inflammation. *J Leukoc Biol* 84: 587-594.
- Caudle RM, Mannes AJ, Benoliel R, Eliav E, Iadarola MJ (2001). Intrathecally administered cholera toxin blocks allodynia and hyperalgesia in persistent pain models. *J Pain* 2: 118-127.
- Chang WW, Wu H, Yeh C, Wu C, Chang J (2007). Lysosomal cysteine proteinase cathepsin S as a potential target for anti-cancer therapy. *J Cancer Mol* 3: 5-14.
- Chaplan S, Bach F, Pogrel J, Chung J, Yaksh T (1994). Quantitative assessment of tactile allodynia in the rat paw. *J Neurosci Methods* 53: 55-63.
- Cheng XW, Kuzuya M, Nakamura K, Di Q, Liu Z, Sasaki T, Kanda S, Jin H, Shi G, Murohara T (2006). Localization of cysteine protease, cathepsin S, to the surface of vascular smooth muscle cells by association with integrin $\alpha\beta 3$. *Am J Pathol* 168: 685-694.
- Cho S, Wood A, Bowlby MR (2007). Brain slices as models for neurodegenerative disease and screening platforms to identify novel therapeutics. *Curr Neuropharmacol* 5: 19-33.
- Choo PW, Galil K, Donahue JG, Walker AM, Spiegelman D, Platt R (1997). Risk factors for postherpetic neuralgia. *Arch Intern Med* 157: 1217-1224.
- Clark AK and Malcangio M (2012). Microglial signalling mechanisms: Cathepsin S and Fractalkine. *Exp Neurol* 234: 283-292.
- Clark AK, Wodarski R, Guida F, Sasso O, Malcangio M (2010). Cathepsin S release from primary cultured microglia is regulated by the P2X7 receptor. *Glia* 58: 1710-1726.
- Clark AK, Yip PK, Grist J, Gentry C, Staniland AA, Marchand F, Dehvari M, Wotherspoon G, Winter J, Ullah J, Bevan S, Malcangio M (2007). Inhibition of spinal microglial cathepsin S for the reversal of neuropathic pain. *Proc Natl Acad Sci U S A* 104: 10655-10660.

- Clark AK, Yip PK, Malcangio M (2009). The liberation of fractalkine in the dorsal horn requires microglial cathepsin S. *J Neurosci* 29: 6945-6954.
- Costigan M, Scholz J, Woolf CJ (2009). Neuropathic pain: A maladaptive response of the nervous system to damage. *Annu Rev Neurosci* 32: 1-32.
- Coull JA, Beggs S, Boudreau D, Boivin D, Tsuda M, Inoue K, Gravel C, Salter MW, De Koninck Y (2005). BDNF from microglia causes the shift in neuronal anion gradient underlying neuropathic pain. *Nature* 438: 1017-1021.
- Cretu OD, Barbuceanu SF, Saramet G, Draghici C (2010). Synthesis and characterization of some 1, 2, 4-triazole-3-thiones obtained from intramolecular cyclization of new 1-(4-(4-X-phenylsulfonyl) benzoyl)-4-(4-iodophenyl)-3-thiosemicarbazides. *J Serbian Chem Soc* 75: 1463-1471.
- Cruccu G, Sommer C, Anand P, Attal N, Baron R, Garcia-Larrea L, Haanpaa M, Jensen T, Serra J, Treede R (2010). EFNS guidelines on neuropathic pain assessment: Revised 2009. *Eur J Neurol* 17: 1010-1018.
- Cunha TM and Dias QM (2009). Glial modulation of pain: a step beyond. *J Neurosci* 29: 3340-3342.
- Cywin CL, Firestone RA, McNeil DW, Grygon CA, Crane KM, White DM, Kinkade PR, Hopkins JL, Davidson W, Labadia ME (2003). The design of potent hydrazones and disulfides as cathepsin S inhibitors. *Bioorg Med Chem* 11: 733-740.
- Dansereau M, Gosselin R, Pohl M, Pommier B, Mechighel P, Mauborgne A, Rostene W, Kitabgi P, Beaudet N, Sarret P (2008). Spinal CCL2 pronociceptive action is no longer effective in CCR2 receptor antagonist-treated rats. *J Neurochem* 106: 757-769.
- Davies M, Brophy S, Williams R, Taylor A (2006). The prevalence, severity, and impact of painful diabetic peripheral neuropathy in type 2 diabetes. *Diabetes Care* 29: 1518-1522.
- Dixon WJ (1980). Efficient analysis of experimental observations. *Annu Rev Pharmacol Toxicol* 20: 441-462.

- D'Mello R and Dickenson AH (2008). Spinal cord mechanisms of pain. *Br J Anaesth* 101: 8-16.
- Drdla R, Sandkuhler J (2008). Long-term potentiation at C-fibre synapses by low-level presynaptic activity in vivo. *Mol Pain* 4: 8069-8064.
- Eliav E, Herzberg U, Ruda M, Bennett GJ (1999). Neuropathic pain from an experimental neuritis of the rat sciatic nerve. *Pain* 83: 169-182.
- Elie BT, Gocheva V, Shree T, Dalrymple SA, Holsinger LJ, Joyce JA (2010). Identification and pre-clinical testing of a reversible cathepsin protease inhibitor reveals anti-tumor efficacy in a pancreatic cancer model. *Biochimie* 92: 1618-1624.
- Enyedy IJ, Egan WJ (2008). Can we use docking and scoring for hit-to-lead optimization? *J Comput Aided Mol Des* 22: 161-168.
- Fajardo I, Svensson L, Bucht A, Pejler G (2004). Increased levels of hypoxia-sensitive proteins in allergic airway inflammation. *Am J Respir Crit Care Med* 170: 477-484.
- Flannery T, Gibson D, Mirakhur M, McQuaid S, Greenan C, Trimble A, Walker B, McCormick D, Johnston PG (2003). The clinical significance of cathepsin S expression in human astrocytomas. *Am J Pathol* 163: 175-182.
- Flannery T, McQuaid S, McGoohan C, McConnell RS, McGregor G, Mirakhur M, Hamilton P, Diamond J, Cran G, Walker B (2006). Cathepsin S expression: an independent prognostic factor in glioblastoma tumours—A pilot study. *Int J Cancer* 119: 854-860.
- Galadari I, Sharif MO, Galadari H (2005). Psoriasis: a fresh look. *Clin Dermatol* 23: 491-502.
- Gauthier JY, Black WC, Courchesne I, Cromlish W, Desmarais S, Houle R, Lamontagne S, Li CS, Massé F, McKay DJ (2007). The identification of potent, selective, and bioavailable cathepsin S inhibitors. *Bioorg Med Chem Lett* 17: 4929-4933.
- Golbraikh A and Tropsha A (2002). Beware of q²! *J Mol Graph Model* 20: 269-276.
- Graupe M, Link JO, Roepel MG (2007). Alpha ketoamide compounds as cysteine protease inhibitors. EP2511257.

- Grice CA, Tays K, Khatuya H, Gustin DJ, Butler CR, Wei J, Sehon CA, Sun S, Gu Y, Jiang W (2006). The SAR of 4-substituted (6, 6-bicyclic) piperidine cathepsin S inhibitors. *Bioorg Med Chem Lett* 16: 2209-2212.
- Grossmann R, Stence N, Carr J, Fuller L, Waite M, Dailey ME (2002). Juxtavascular microglia migrate along brain microvessels following activation during early postnatal development. *Glia* 37: 229-240.
- Gunčar G, Klemenčič I, Turk B, Turk V, Karaoglanovic-Carmona A, Juliano L, Turk D (2000). Crystal structure of cathepsin X: a flip–flop of the ring of His23 allows carboxy-monopeptidase and carboxy-dipeptidase activity of the protease. *Structure* 8: 305-313.
- Gunčar G, Pungerčič G, Klemenčič I, Turk V, Turk D (1999). Crystal structure of MHC class II-associated p41 Ii fragment bound to cathepsin L reveals the structural basis for differentiation between cathepsins L and S. *EMBO J* 18: 793-803.
- Guo W, Wang H, Watanabe M, Shimizu K, Zou S, LaGraize SC, Wei F, Dubner R, Ren K (2007). Glial-cytokine-neuronal interactions underlying the mechanisms of persistent pain. *J Neurosci* 27: 6006-6018.
- Gupta S, Singh RK, Dastidar S, Ray A (2008). Cysteine cathepsin S as an immunomodulatory target: present and future trends. *Expert Opin Ther Targets* 12:291-299.
- Gustin DJ, Sehon CA, Wei J, Cai H, Meduna SP, Khatuya H, Sun S, Gu Y, Jiang W, Thurmond RL (2005). Discovery and SAR studies of a novel series of noncovalent cathepsin S inhibitors. *Bioorg Med Chem Lett* 15: 1687-1691.
- Hagiwara N, Ikeda K, Higashida H, Tomita K, Yokoyama S (2005). Induction of tumor necrosis factor- α in Schwann cells after gradual elongation of rat sciatic nerve. *J Ortho Sci* 10: 614-621.
- Harrison MJ, Burton NA, Hillier IH (1997). Catalytic mechanism of the enzyme papain: predictions with a hybrid quantum mechanical/molecular mechanical potential. *J Am Chem Soc* 119: 12285-12291.

- Hart TW, Hallett A, Yokokawa F, Hirao H, Ehara T, Iwasaki A, Sakaki J, Masuya K, Kishida M, Irie O (2006). Compounds and compositions useful as cathepsin S inhibitors. WO2006018284.
- Heidtmann HH, Salge U, Havemann K, Kirschke H, Wiederanders B (1993). Secretion of a latent, acid activatable cathepsin L precursor by human non-small cell lung cancer cell lines. *Oncol Res* 5: 441-451.
- Hickey ER, Bekkali Y, Patel UR, Spero DM, Thomson DS, Young ERR (2006). Peptidyl carbamates; treatments for osteoporosis and autoimmune diseases. US6982263.
- Hilpert H, Mauser H, Humm R, Anselm L, Kuehne H, Hartmann G, Gruener S, Banner DW, Benz J, Gsell B (2013). Identification of Potent and Selective Cathepsin S Inhibitors Containing Different Central Cyclic Scaffolds. *J Med Chem* 56: 9789-9801.
- Holsinger LJ, Elrod K, Link JO, Graupe M, Kim IJ (2009). Compounds that inhibit protease cathepsin S and HCV replication. WO2009055467.
- Huang Y, Lu Y, Zhang L, Yan J, Jiang J, Jiang H (2014). Perineural Dexmedetomidine Attenuates Inflammation in Rat Sciatic Nerve via the NF- κ B Pathway. *Int J Mol Sci* 15: 4049-4059.
- Hulsebosch CE, Hains BC, Crown ED, Carlton SM (2009). Mechanisms of chronic central neuropathic pain after spinal cord injury. *Brain Res Rev* 60: 202-213.
- Hutchinson MR, Zhang Y, Brown K, Coats BD, Shridhar M, Sholar PW, Patel SJ, Crysedale NY, Harrison JA, Maier SF (2008). Non-stereoselective reversal of neuropathic pain by naloxone and naltrexone: involvement of toll-like receptor 4 (TLR4). *Eur J Neurosci* 28: 20-29.
- Huuskonen J, Suuronen T, Miettinen R, Van Groen T, Salminen A (2005). A refined in vitro model to study inflammatory responses in organotypic membrane culture of postnatal rat hippocampal slices. *J Neuroinflam* 2: 25.

- Inagaki H, Tsuruoka H, Hornsby M, Lesley SA, Spraggon G, Ellman JA (2007). Characterization and optimization of selective, nonpeptidic inhibitors of cathepsin S with an unprecedented binding mode. *J Med Chem* 50: 2693-2699.
- Inoue K and Tsuda M (2009). Microglia and neuropathic pain. *Glia* 57: 1469-1479.
- Irie O, Ehara T, Iwasaki A, Yokokawa F, Sakaki J, Hirao H, Kanazawa T, Teno N, Horiuchi M, Umemura I (2008a). Discovery of selective and nonpeptidic cathepsin S inhibitors. *Bioorg Med Chem Lett* 18: 3959-3962.
- Irie O, Kosaka T, Ehara T, Yokokawa F, Kanazawa T, Hirao H, Iwasaki A, Sakaki J, Teno N, Hitomi Y (2008b). Discovery of orally bioavailable cathepsin S inhibitors for the reversal of neuropathic pain. *J Med Chem* 51: 5502-5505.
- Jain P, Chatterjee A, Choudhary AH, Sareen R (2009). Prevalence, etiology, and management of neuropathic pain in an Indian cancer hospital. *J Pain Palliat Care Pharmacother* 23: 114-119.
- Jänig W and Baron R (2003). Complex regional pain syndrome: mystery explained? *The Lancet Neurol* 2: 687-697.
- Jedeszko C and Sloane BF (2004). Cysteine cathepsins in human cancer. *Biol Chem* 385: 1017-1027.
- Jelassi B, Chantome A, Alcaraz-Perez F, Baroja-Mazo A, Cayuela M, Pelegrin P, Surprenant A, Roger S (2011). P2X7 receptor activation enhances SK3 channels-and cystein cathepsin-dependent cancer cells invasiveness. *Oncogene* 30: 2108-2122.
- Jensen TS, Baron R, Haanpää M, Kalso E, Loeser JD, Rice AS, Treede R (2011). A new definition of neuropathic pain. *Pain* 152: 2204-2205.
- Jensen TS and Finnerup NB (2014). Allodynia and hyperalgesia in neuropathic pain: clinical manifestations and mechanisms. *Lancet Neurol* 13: 924-935.
- Ji R, Xu Z, Wang X, Lo EH (2009). Matrix metalloprotease regulation of neuropathic pain. *Trends Pharmacol Sci* 30: 336-340.

- Jorgensen WL (2010). Drug discovery: Pulled from a protein's embrace. *Nature* 466: 42-43.
- Joyce JA, Hanahan D (2004). Multiple roles for cysteine cathepsins in cancer. *Cell cycle* 3: 1516-1519.
- Kalyaanamoorthy S, Chen YP (2011). Structure-based drug design to augment hit discovery. *Drug Discov Today* 16: 831-839.
- Khan I, Ali S, Hameed S, Rama NH, Hussain MT, Wadood A, Uddin R, Ul-Haq Z, Khan A, Ali S (2010). Synthesis, antioxidant activities and urease inhibition of some new 1, 2, 4-triazole and 1, 3, 4-thiadiazole derivatives. *Eur J Med Chem* 45: 5200-5207.
- Kirschke H, Wiederanders B, Bromme D, Rinne A (1989). Cathepsin S from bovine spleen. Purification, distribution, intracellular localization and action on proteins. *Biochem J* 264: 467-473.
- Koo J and Khera P (2005). Update on the mechanisms and efficacy of biological therapies for psoriasis. *J Dermatol Sci* 38: 75-87.
- Krepela E (2001). Cysteine proteinases in tumor cell growth and apoptosis. *Neoplasma* 48: 332-349.
- Laird B, Colvin L, Fallon M (2008). Management of cancer pain: basic principles and neuropathic cancer pain. *Eur J Cancer* 44: 1078-1082.
- Laird MH, Rhee SH, Perkins DJ, Medvedev AE, Piao W, Fenton MJ, Vogel SN (2009). TLR4/MyD88/PI3K interactions regulate TLR4 signaling. *J Leukoc Biol* 85: 966-977.
- Latremoliere A and Woolf CJ (2009). Central sensitization: a generator of pain hypersensitivity by central neural plasticity. *J Pain* 10: 895-926.
- Lautwein A, Kraus M, Reich M, Burster T, Brandenburg J, Overkleeft HS, Schwarz G, Kammer W, Weber E, Kalbacher H, Nordheim A, Driessen C (2004). Human B lymphoblastoid cells contain distinct patterns of cathepsin activity in endocytic compartments and regulate MHC class II transport in a cathepsin S-independent manner. *J Leukoc Biol* 75: 844-855.

- Lee B, Jun I, Kim S, Park JY (2013). Intrathecal gabapentin increases interleukin-10 expression and inhibits pro-inflammatory cytokine in a rat model of neuropathic pain. *J Korean Med Sci* 28: 308-314.
- Lee-Dutra A, Wiener DK, Sun S (2011). Cathepsin S inhibitors: 2004-2010. *Expert Opin Ther Patents* 21: 311-337.
- Leroy V and Thurairatnam S (2004). Cathepsin S inhibitors. *Expert Opin Ther Pat* 14: 301-311.
- Link JO (2005). Haloalkyl containing compounds as cysteine protease inhibitors. WO2005028454.
- Link JO (2006). Alpha ketoamide compounds as cysteine protease inhibitors. WO2006102423.
- Link JO and Zipfel S (2006). Advances in cathepsin S inhibitor design. *Curr Opin Drug Discov Devel* 9: 471-482.
- Liu H, Tully DC, Epple R, Bursulaya B, Li J, Harris JL, Williams JA, Russo R, Tumanut C, Roberts MJ (2005). Design and synthesis of arylaminoethyl amides as noncovalent inhibitors of cathepsin S. Part 1. *Bioorg Med Chem Lett* 15: 4979-4984.
- Liuzzo JP, Petanceska SS, Devi LA (1999a). Neurotrophic factors regulate cathepsin S in macrophages and microglia: A role in the degradation of myelin basic protein and amyloid beta peptide. *Mol Med* 5: 334-343.
- Liuzzo JP, Petanceska SS, Moscatelli D, Devi LA (1999b). Inflammatory mediators regulate cathepsin S in macrophages and microglia: A role in attenuating heparan sulfate interactions. *Mol Med* 5: 320-333.
- Lu P, Wei X, Zhang R (2010). CoMFA and CoMSIA 3D-QSAR studies on quionolone caroxylic acid derivatives inhibitors of HIV-1 integrase. *Eur J Med Chem* 45: 3413-3419.
- Mali R, Somani R, Toraskar M, Mali K, Naik P, Shirodkar P (2009). Synthesis of some antifungal and anti-tubercular 1, 2, 4-triazole analogues. *Int J Chem Tech Res* 1: 168-173.
- Markt P, McGoohan C, Walker B, Kirchmair J, Feldmann C, Martino GD, Spitzer G, Distinto S, Schuster D, Wolber G (2008). Discovery of novel cathepsin S inhibitors by

- pharmacophore-based virtual high-throughput screening. *J Chem Inf Model* 48: 1693-1705.
- Marrack P, Kappler J, Kotzin BL (2001). Autoimmune disease: Why and where it occurs. *Nat Med* 7: 899-905.
- Maryanoff BE and Costanzo MJ (2008). Inhibitors of proteases and amide hydrolases that employ an α -ketoheterocycle as a key enabling functionality. *Bioorg Med Chem* 16: 1562-1595.
- McMahon SB and Malcangio M (2009). Current challenges in glia-pain biology. *Neuron* 64: 46-54.
- Menard R, Carriere J, Laflamme P, Plouffe C, Khouri HE, Vernet T, Tessier DC, Thomas DY, Storer AC (1991a). Contribution of the glutamine 19 side chain to transition-state stabilization in the oxyanion hole of papain. *Biochem* 30: 8924-8928.
- Menard R, Feng R, Storer AC, Robinson VJ, Smith RA, Krantz A (1991b). Nature of papain products resulting from inactivation by a peptidyl O-acyl hydroxamate. *FEBS Lett* 295: 27-30.
- Menard R, Plouffe C, Laflamme P, Vernet T, Tessier DC, Thomas DY, Storer AC (1995). Modification of the electrostatic environment is tolerated in the oxyanion hole of the cysteine protease papain. *Biochem* 34: 464-471.
- Milligan ED and Watkins LR (2009). Pathological and protective roles of glia in chronic pain. *Nat Rev Neurosci* 10: 23-36.
- Mohamed MM and Sloane BF (2006). Cysteine cathepsins: multifunctional enzymes in cancer. *Nat Rev Cancer* 6: 764-775.
- Mohan V (2008). Burden of neuropathic pain in Indian patients attending urban, specialty clinics: results from a cross sectional study. *Pain Practice* 8: 362-378.
- Nakagawa TY, Brissette WH, Lira PD, Griffiths RJ, Petrushova N, Stock J, McNeish JD, Eastman SE, Howard ED, Clarke SR (1999). Impaired invariant chain degradation and

- antigen presentation and diminished collagen-induced arthritis in cathepsin S null mice. *Immunity* 10: 207-217.
- Nakagawa T, Roth W, Wong P, Nelson A, Farr A, Deussing J, Villadangos JA, Ploegh H, Peters C, Rudensky AY (1998). Cathepsin L: critical role in Ii degradation and CD4 T cell selection in the thymus. *Science* 280: 450-453.
- Nimmerjahn A, Kirchhoff F, Helmchen F (2005). Resting microglial cells are highly dynamic surveillants of brain parenchyma in vivo. *Science* 308: 1314-1318.
- Otto H and Schirmeister T (1997). Cysteine proteases and their inhibitors. *Chem Rev* 97: 133-172.
- Pan X, Tan N, Zeng G, Huang H, Yan H (2010). 3D QSAR studies on ketoamides of human cathepsin K inhibitors based on two different alignment methods. *Eur J Med Chem* 45: 667-681.
- Park S, Ahn ES, Han DW, Lee JH, Min KT, Kim H, Hong Y (2008). Pregabalin and gabapentin inhibit substance P-induced NF- κ B activation in neuroblastoma and glioma cells. *J Cell Biochem* 105: 414-423.
- Patterson AW, Wood WJ, Ellman JA (2007). Substrate activity screening (SAS): a general procedure for the preparation and screening of a fragment-based non-peptidic protease substrate library for inhibitor discovery. *Nat Prot* 2: 424-433.
- Pauly TA, Sulea T, Ammirati M, Sivaraman J, Danley DE, Griffor MC, Kamath AV, Wang I, Laird ER, Seddon AP (2003). Specificity determinants of human cathepsin S revealed by crystal structures of complexes. *Biochem* 42: 3203-3213.
- Petanceska S, Canoll P, Devi LA (1996). Expression of rat cathepsin S in phagocytic cells. *J Biol Chem* 271: 4403-4409.
- Petersen MA and Dailey ME (2004). Diverse microglial motility behaviors during clearance of dead cells in hippocampal slices. *Glia* 46: 195-206.

- Pettit AR and Thomas R (1999). Dendritic cells: the driving force behind autoimmunity in rheumatoid arthritis? *Immunol Cell Biol* 77: 420-427.
- Pratim RP, Paul S, Mitra I, Roy K (2009). On two novel parameters for validation of predictive QSAR models. *Molecules* 14: 1660-1701.
- Punturieri A, Filippov S, Allen E, Caras I, Murray R, Reddy V, Weiss SJ (2000). Regulation of elastolytic cysteine proteinase activity in normal and cathepsin K-deficient human macrophages. *J Exp Med* 192: 789-799.
- Randall LO and Selitto JJ (1957). A method for measurement of analgesic activity on inflamed tissue. *Arch Int Pharmacodyn Ther* 111: 409-419.
- Rankovic Z and Cai J (2008). 4-Phenyl-6-substituted-pyrimidine-2-carbonitrile derivatives. US7326715.
- Rantamäki T, Kemppainen S, Autio H, Staven S, Koivisto H, Kojima M, Antila H, Miettinen PO, Kärkkäinen E, Karpova N (2013). The impact of Bdnf gene deficiency to the memory impairment and brain pathology of APP^{swe}/PS1^{dE9} mouse model of Alzheimer's disease. *PLoS One* 8: e68722.
- Rasmussen PV, Sindrup SH, Jensen TS, Bach FW (2004). Symptoms and signs in patients with suspected neuropathic pain. *Pain* 110: 461-469.
- Riese RJ, Mitchell RN, Villadangos JA, Shi GP, Palmer JT, Karp ER, De Sanctis GT, Ploegh HL, Chapman HA (1998). Cathepsin S activity regulates antigen presentation and immunity. *J Clin Invest* 101: 2351-2363.
- Rodriguez J, Vazquez J, Corte MD, Lamelas M, Bongera M, Corte MG, Alvarez A, Allende M, Gonzalez L, Sanchez M, Vijande M, Garcia Muniz J, Vizoso F (2005). Clinical significance of cathepsin D concentration in tumor cytosol of primary breast cancer. *Int J Biol Markers* 20: 103-111.
- Rossi A, Deveraux Q, Turk B, Sali A (2004). Comprehensive search for cysteine cathepsins in the human genome. *Biol Chem* 385: 363-372.

- Roy PP, Roy K (2008). On some aspects of variable selection for partial least squares regression models. *QSAR Comb Sci* 27: 302-313.
- Roy K, Paul S (2009). Exploring 2D and 3D QSARs of 2, 4-Diphenyl-1, 3-oxazolines for Ovicidal Activity Against *Tetranychus urticae*. *QSAR Comb Sci* 28: 406-425.
- Rückrich T, Brandenburg J, Cansier A, Müller M, Stevanović S, Schilling K, Wiederanders B, Beck A, Melms A, Reich M (2006). Specificity of human cathepsin S determined by processing of peptide substrates and MHC class II-associated invariant chain. *Biol Chem* 387: 1503-1511.
- Rzychon M, Chmiel D, Stec-Niemczyk J (2004). Modes of inhibition of cysteine proteases. *Acta Biochim Pol* 51: 861-873.
- Saab CY and Hains BC (2009). Remote neuroimmune signaling: a long-range mechanism of nociceptive network plasticity. *Trends Neurosci* 32: 110-117.
- Sakkiah S, Meganathan C, Sohn Y, Namadevan S, Lee KW (2012). Identification of important chemical features of 11 β -hydroxysteroid dehydrogenase type1 inhibitors: application of ligand based virtual screening and density functional theory. *Int J Mol Sci* 13: 5138-5162.
- Schudok M, Wagner M, Bauer A, Kohlmann A (2007). Spirocyclic nitriles as protease inhibitors. WO2007137738.
- Schudok M, Wagner M, Bauer A, Kohlmann A (2009). Spirocyclic nitriles as protease inhibitors. US8039480.
- Shi GP, Bryant RA, Riese R, Verhelst S, Driessen C, Li Z, Bromme D, Ploegh HL, Chapman HA (2000). Role for cathepsin F in invariant chain processing and major histocompatibility complex class II peptide loading by macrophages. *J Exp Med* 191: 1177-1186.
- Shi GP, Sukhova GK, Grubb A, Ducharme A, Rhode LH, Lee RT, Ridker PM, Libby P, Chapman HA (1999). Cystatin C deficiency in human atherosclerosis and aortic aneurysms. *J Clin Invest* 104: 1191-1197.

- Shi GP, Sukhova GK, Kuzuya M, Ye Q, Du J, Zhang Y, Pan JH, Lu ML, Cheng XW, Iguchi A, Perrey S, Lee AM, Chapman HA, Libby P (2003). Deficiency of the cysteine protease cathepsin S impairs microvessel growth. *Circ Res* 92: 493-500.
- Shi GP, Webb AC, Foster KE, Knoll JH, Lemere CA, Munger JS, Chapman HA (1994). Human cathepsin S: chromosomal localization, gene structure, and tissue distribution. *J Biol Chem* 269: 11530-11536.
- Shimoyama M, Tanaka K, Hasue F, Shimoyama N (2002). A mouse model of neuropathic cancer pain. *Pain* 99: 167-174.
- Sliwoski G, Kothiwale S, Meiler J, Lowe EW, Jr (2013). Computational methods in drug discovery. *Pharmacol Rev* 66: 334-395.
- Sloane BF and Honn KV (1984). Cysteine proteinases and metastasis. *Cancer Metastasis Rev* 3: 249-263.
- Sukhova GK, Zhang Y, Pan JH, Wada Y, Yamamoto T, Naito M, Kodama T, Tsimikas S, Witztum JL, Lu ML, Sakara Y, Chin MT, Libby P, Shi GP (2003). Deficiency of cathepsin S reduces atherosclerosis in LDL receptor-deficient mice. *J Clin Invest* 111: 897-906.
- Tandon AK, Clark GM, Chamness GC, Chirgwin JM, McGuire WL (1990). Cathepsin D and prognosis in breast cancer. *N Engl J Med* 322: 297-302.
- Teupser D, Pavlides S, Tan M, Gutierrez-Ramos JC, Kolbeck R, Breslow JL (2004). Major reduction of atherosclerosis in fractalkine (CX3CL1)-deficient mice is at the brachiocephalic artery, not the aortic root. *Proc Natl Acad Sci U S A* 101: 17795-17800.
- Thacker MA, Clark AK, Bishop T, Grist J, Yip PK, Moon LD, Thompson SW, Marchand F, McMahon SB (2009). CCL2 is a key mediator of microglia activation in neuropathic pain states. *Eur J Pain* 13: 263-272.
- Thurmond RL, Sun S, Sehon CA, Baker SM, Cai H, Gu Y, Jiang W, Riley JP, Williams KN, Edwards JP, Karlsson L (2004). Identification of a potent and selective noncovalent cathepsin S inhibitor. *J Pharmacol Exp Ther* 308: 268-276.

- Thurmond RL, Sun S, Karlsson L, Edwards JP (2005). Cathepsin S inhibitors as novel immunomodulators. *Curr Opin Investig Drugs* 6: 473-482.
- Toomes C, James J, Wood AJ, Wu CL, McCormick D, Lench N, Hewitt C, Moynihan L, Roberts E, Woods CG, Markham A, Wong M, Widmer R, Ghaffar KA, Pemberton M, Hussein IR, Temtamy SA, Davies R, Read AP, Sloan P, Dixon MJ, Thakker NS (1999). Loss-of-function mutations in the cathepsin C gene result in periodontal disease and palmoplantar keratosis. *Nat Genet* 23: 421-424.
- Tully DC, Liu H, Alper PB, Chatterjee AK, Epple R, Roberts MJ, Williams JA, Nguyen KT, Woodmansee DH, Tumanut C (2006). Synthesis and evaluation of arylaminoethyl amides as noncovalent inhibitors of cathepsin S. Part 3: Heterocyclic P3. *Bioorg Med Chem Lett* 16: 1975-1980.
- Turk B, Bieth JG, Björk I, Dolenc I, Turk D, Cimerman N, Kos J, Čolič A, Stoka V, Turk V (1995). Regulation of the activity of lysosomal cysteine proteinases by pH-induced inactivation and/or endogenous protein inhibitors, cystatins. *Biol Chem* 376: 225-230.
- Turk V, Stoka V, Vasiljeva O, Renko M, Sun T, Turk B, Turk D (2012). Cysteine cathepsins: from structure, function and regulation to new frontiers. *Biochim Biophys Acta* 1824: 68-88.
- Ueda H (2006). Molecular mechanisms of neuropathic pain—phenotypic switch and initiation mechanisms. *Pharmacol Ther* 109: 57-77.
- Visnagri A, Kandhare AD, Chakravarty S, Ghosh P, Bodhankar SL (2014). Hesperidin, a flavanoglycone attenuates experimental diabetic neuropathy via modulation of cellular and biochemical marker to improve nerve functions. *Pharm Biol* 1-15.
- Wacnik PW, Eikmeier LJ, Ruggles TR, Ramnaraine ML, Walcheck BK, Beitz AJ, Wilcox GL (2001). Functional interactions between tumor and peripheral nerve: morphology, algogen identification, and behavioral characterization of a new murine model of cancer pain. *J Neurosci* 21: 9355-9366.

- Walker K, Medhurst SJ, Kidd BL, Glatt M, Bowes M, Patel S, McNair K, Kesingland A, Green J, Chan O (2002). Disease modifying and anti-nociceptive effects of the bisphosphonate, zoledronic acid in a model of bone cancer pain. *Pain* 100: 219-229.
- Wang B, Sun J, Kitamoto S, Yang M, Grubb A, Chapman HA, Kalluri R, Shi GP (2006). Cathepsin S controls angiogenesis and tumor growth via matrix-derived angiogenic factors. *J Biol Chem* 281: 6020-6029.
- Wang JK, Portbury S, Thomas MB, Barney S, Ricca DJ, Morris DL, Warner DS, Lo DC (2006). Cardiac glycosides provide neuroprotection against ischemic stroke: discovery by a brain slice-based compound screening platform. *Proc Natl Acad Sci U S A* 103: 10461-10466.
- Ward YD, Thomson DS, Frye LL, Cywin CL, Morwick T, Emmanuel MJ, Zindell R, McNeil D, Bekkali Y, Girardot M (2002). Design and synthesis of dipeptide nitriles as reversible and potent cathepsin S inhibitors. *J Med Chem* 45: 5471-5482.
- Watkins LR, Hutchinson MR, Rice KC, Maier SF (2009). The “toll” of opioid-induced glial activation: improving the clinical efficacy of opioids by targeting glia. *Trends Pharmacol Sci* 30: 581-591.
- Wei F, Guo W, Zou S, Ren K, Dubner R (2008). Supraspinal glial-neuronal interactions contribute to descending pain facilitation. *J Neurosci* 28: 10482-10495.
- White FA, Feldman P, Miller RJ (2009). Chemokine signaling and the management of neuropathic pain. *Mol Interv* 9: 188-195.
- Wiener DK, Lee-Dutra A, Bembenek S, Nguyen S, Thurmond RL, Sun S, Karlsson L, Grice CA, Jones TK, Edwards JP (2010). Thioether acetamides as P3 binding elements for tetrahydropyrido-pyrazole cathepsin S inhibitors. *Bioorg Med Chem Lett* 20: 2379-2382.
- Wiener JJ, Sun S, L Thurmond R (2010). Recent advances in the design of cathepsin S inhibitors. *Curr Top Med Chem* 10: 717-732.

- Wolters PJ and Chapman HA (2000). Importance of lysosomal cysteine proteases in lung disease. *Respir Res* 1: 170-177.
- Wood WJ, Patterson AW, Tsuruoka H, Jain RK, Ellman JA (2005). Substrate activity screening: a fragment-based method for the rapid identification of nonpeptidic protease inhibitors. *J Am Chem Soc* 127: 15521-15527.
- Yoshikawa M, Goto S, Okamura A, Hamasaki T, Ushio Y (1998). Neurotoxicity evoked by N-methyl-D-aspartate in the organotypic static slice cultures of rat cerebral cortices: effect of GABAA receptor activation. *Acta Neuropathol* 95: 592-596.
- Zhang L, Wang H, Xu J, Zhu J, Ding K (2014). Inhibition of cathepsin S induces autophagy and apoptosis in human glioblastoma cell lines through ROS-mediated PI3K/AKT/mTOR/p70S6K and JNK signaling pathways. *Toxicol Lett* 228:248-259.
- Zhao W, Hevener KE, White SW, Lee RE, Boyett JM (2009). A statistical framework to evaluate virtual screening. *BMC Bioinfo* 10: 225-238.

APPENDIX

APPENDIX

LIST OF PUBLICATIONS

FROM THESIS WORK

1. **Madhu Babu Battu**, Anchuri Madhuri Chandra, Dharmarajan Sriram, Perumal Yogeeswari, (2014). Pharmacophore-Based 3DQSAR and Molecular Docking Studies to Identify New Non-Peptidic Inhibitors of Cathepsin S. *Curr Med Chem* 21: 1910-1921.
2. Perumal Yogeeswari, Dharmarajan Sriram, **Madhu Babu Battu**, Brahmam Medapi, Indian patent application on “A compound for treating inflammatory neuropathic pain and cancer”. Indian patent application **2945/DEL/2014 dated 15/10/2014**.

OTHER PUBLICATIONS

1. Venkat Koushik Pulla, **Madhu Babu Battu**, Mallika Alvala, Dharmarajan Sriram, Perumal Yogeeswari (2012). Can targeting SIRT-1 to treat type 2 diabetes be a good strategy? A review. *Expert Opin Ther Targets* 16: 819-832.
2. Patrisha Joseph Theresa, Dinesh Manvar, Sridevi Kondepudi, **Madhu Babu Battu**, Dharmarajan Sriram, Amartya Basu, and Perumal Yogeeswari, Neerja Kaushik-Basu (2014). Multiple e-Pharmacophore Modeling, 3D-QSAR, and High-Throughput Virtual Screening of Hepatitis C Virus NS5B Polymerase Inhibitors. *J Chem Inf Model* 54: 539-552.

PAPERS PRESENTED AT NATIONAL/INTERNATIONAL CONFERENCES

1. **Madhu Babu Battu**, Anchuri Madhuri Chandra, Dharmarajan Sriram, Perumal Yogeewari, Discovery of new microglial Cathepsin S inhibitors for the treatment of neuropathic pain Pharmacophore modeling, 3D-QSAR and high-throughput virtual screening. **3rd World Congress on Biotechnology**, Sep13-15th, 2012 at Hyderabad, India.
2. Sridevi Kondepudi, **Madhu Babu Battu**, Dharmarajan Sriram, Perumal Yogeewari Pharmacophore based virtual screening and building of 3D-QSAR in the discovery of new Cathepsin K inhibitors. **3rd World Congress on Biotechnology**, Sep13-15th, 2012 at Hyderabad, India.
3. **Madhu Babu Battu**, Anchuri Madhuri Chandra, Dharmarajan Sriram, Perumal Yogeewari., Discovery of new microglial Cathepsin S inhibitors for the treatment of neuropathic pain Pharmacophore modeling. **Current Trends in Pharmaceutical Science (CTPS 2012)**, BITS-Pilani, Hyderabad campus., Hyderabad, Nov 2012.
4. **Madhu Babu Battu**, Dharmarajan Sriram, Perumal Yogeewari, Targeting microglial Cathepsin S to treat neuropathic pain: Drug design and biological evaluation. **European Federation of IASP Chapters (EFIC)**, October 2013, Florence, Italy.

BIOGRAPHY OF MADHU BABU BATTU

Madhu Babu Battu completed his Bachelor of Pharmacy from The Janagoan Institute of Pharmaceutical Sciences; Kakatiya University in the Year 2008 and M.S (Pharmacy) from National Institute of Pharmaceutical Education and Research (NIPER), Hajipur. He has been appointed as a Senior Research Fellow at Pharmacy department Birla Institute of Technology and Science at Birla Institute of Technology and Sciences (BITS-Pilani), Hyderabad campus, from 2011-2014 under the supervision of Prof. P. Yogeewari. He was awarded CSIR-Senior Research Fellow from HRDG-CSIR, New Delhi in February 2012. He has published three scientific publications in well-renowned international journals and applied for Indian patent. He had presented papers at various national and international conferences. He was recently awarded CSIR foreign travel grant (full air fare) from CSIR-HRDG, New Delhi, in August 2013, to present his research work on title “Targeting microglial cathepsin S to treat neuropathic pain” at European Federation of IASP Chapters (EFIC), Florence, Italy 9th to 12th October 2013.

BIOGRAPHY OF PROF.P.YOGESWARI

Prof.P.Yogeeswari is presently working in the capacity of professor and Associate Dean (Sponsored Research and Consultancy Division), Department of Pharmacy, Birla Institute of Technology and Science, Pilani, Hyderabad Campus. She received the Ph.D. degree in the year 2001 from Banaras Hindu University; Varanasi. She has been involved in research for the last 14 years and in teaching for 13 years. APTI honoured her with YOUNG PHARMACY TEACHER AWARD for the year 2007. In 2010, ICMR honoured her by awarding “Shakuntala Amir Chand Award” for her excellent biomedical research. She has also been granted IASP 2014 award for “Excellence in Pain Research and Management in Developing Countries” under the basic science research category received at the “15th World Congress on Pain” at Argentina in October 2014. She has collaborations with various national and international organizations that include National Institute of Mental Health and Neurosciences, Bangalore, Karolinska Institute, Stockholm, Sweden, National Institute of immunology, New Delhi, India, Pasteur Institute, University of Lille, France, Bogomoletz Institute of Physiology National Academy of Science, Ukraine and Faculty of Medicine of Porto, Portugal,. She has to her credit more than 200 research publications and one Indian Patent granted in November 2014. She is an expert reviewer of many international journals like Journal of Medicinal Chemistry (ACS), Journal of Chemical Information & Modelling (ACS, USA), Bioorganic Medicinal Chemistry (Elsevier), Recent Patents on CNS Drug Discovery (Bentham), etc. She has also co-authored a textbook on organic medicinal chemistry with Prof. D. Sriram titled “Medicinal Chemistry” published by Pearson Education and one book chapter in Jan 2013 by IGI Global. She is a lifetime member of Association of Pharmacy Teachers of India and Indian Pharmaceutical Society. She has successively completed many sponsored projects and currently on projects sponsored by DST, DBT, INDO-BRAZIL, ICMR-INSERM, and CSIR. She has guided seven Ph.D students and currently thirteen students are pursuing their Ph.D work.